UNIVERSITY OF READING

Department of Meteorology

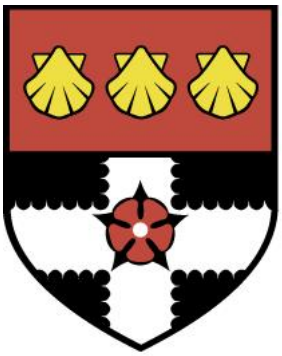

Downstream influence on Rossby wave breaking and blocking by extratropical cyclones

Jacob William Maddison

A thesis submitted for the degree of Doctor of Philosophy

July 2019

Declaration

I confirm that this is my own work and the use of all material from other sources has been properly and fully acknowledged.

Jacob William Maddison

Abstract

An atmospheric block is a weather event characterised by a large-amplitude tropospheric ridge of high pressure that is synoptic in scale and can persist over a region for several weeks. Such blocks, occur frequently in the midlatitudes of both hemispheres and can be associated with high-impact weather. The prediction of blocking events has been a well-known and frequently-studied problem in both weather and climate models for many decades. Medium-range forecasting of blocking in the northern hemisphere is assessed here, with a focus on improving the predictability of blocking originating from the representation of upstream cyclones and the impacts of improvements to numerical weather prediction models.

An improvement to the dynamical core of the Met Office Unified Model (MetUM) is proven to counteract the consistent underprediction of block frequency by weather and climate models. Implementing planned Met Office upgrades to various physical parameterisation schemes, and running the MetUM with updated sea surface temperatures (SST), are also shown to impact forecast evolution in a case study of upper-level ridge amplification and block development. The sensitivity of block development in the forecast results from different diabatic heating rates from parameterised processes: stronger diabatic heating in the warm conveyor belt of an extratropical cyclone led to a more-amplified ridge. Using updated SST does not distinguishably impact forecast skill when averaged over 54 forecasts initialised during autumn 2016, whereas using an improved representation of convection reduces forecast error. Accurate prediction of the intensities and locations of extratropical cyclones that feed air into blocking ridges via their warm conveyor belts is shown to be important for the most unpredictable blocking forecasts from the ECMWF. Together this work implies that improvements to weather models have the potential to further improve forecasts of blocking events which can cause of some of the worst forecasts produced at forecasting centres.

Acknowledgements

I owe biggest thanks to my supervisors, Sue Gray, Oscar Martínez-Alvarado and Keith Williams for their fantastic support and invaluable guidance in all aspects of my PhD research. I have benefited immensely from the time and effort they were eager to give to the project along the way. I thank John Methven and Matt Owens for their enthusiastic engagements in the biannual monitoring committees. Thanks also to John for encouraging my involvement in the NAWDEX campaign. It was a great experience and one from which I learned a lot. I would also like to thank Claudio Sanchez for his support setting up and running the diabatic tracers in the MetUM.

The friends I made at Reading during the PhD made the process a whole lot easier and much more enjoyable. Massive thanks in particular to Josh for making me (letting me?) follow him to athletics club the first week we started and his influence in my development into a running enthusiast, and to Hélène and Ben for our awesome house. I am also thankful to Reading for being so close to London and making it easy to party with my best friends there. Final thanks to all of my family because I would not have gotten to this point without you.

Contents

List of Figures

List of Tables

Chapter 1:

Introduction

Predicting the weather is a scientific experiment performed daily at many operational forecasting centres across the globe with the experimental results critically reviewed by the millions of users of the forecasts each day. Abbe (1901) and Bjerknes (1904) were the first to pose the weather forecast problem as an initial value problem of mathematical physics. Using the fundamental laws of physics we ought to be able to predict the weather into the future if we know the current state of the atmosphere. Herein lies the two elementary sources of error in numerical weather prediction (NWP): our numerical approximations of the fundamental equations of motion and our estimates of the atmosphere's current state. The two are commonly known as model and analysis error, respectively. Analysis error typically dominates over model error in short– to medium–range weather forecasts (e.g. Arpe et al., 1985; Rabier et al., 1996) because the atmosphere is a chaotic system in which small perturbations to the initial conditions can cause the rapid divergence of the model's trajectory (Lorenz, 1963). Steady improvements in producing analyses for initial conditions, helped in large part by the development of advanced data assimilation systems (e.g. Simmons and Hollingsworth, 2002) and improvements to the forecast models, has led to a steady increase in forecast skill in recent decades: see Bauer et al. (2015) for a review. Improvements to the forecast models can be gained from more realistic parameterisations of physical processes, resolution increases and dynamical core modifications. All of which have been shown to increase forecast skill (e.g. Jung et al., 2010; Walters et al., 2017b). The improvement in medium–range forecast skill from model improvements is the main focus of this thesis, with a particular focus on how dynamical core and parameterisation improvements affect forecasts of atmospheric blocking.

Atmospheric blocks are large-amplitude ridges of high pressure that are quasi-

stationary in space and can persist in time for up to several weeks. They are barotropic in structure with anticyclonic circulation dominating the entire troposphere. A blocking event interrupts the prevailing westerly winds and *blocks* the advance of storms over the region. Blocks occur year-round and most frequently in the Euro-Atlantic and Pacific regions of the northern hemisphere (Tyrlis and Hoskins, 2008) as well as in the Australasian region of the southern hemisphere (Lejenäs, 1984). There are two broad types of blocks that appear in the midlatitudes: the 'Rex' block and 'Ω' block. The flow at 500 hPa in the Rex–block consists of a meridional dipole in geopotential height and a split jetstream upstream of the blocked region. The blocking high pressure centre is flanked on the east and west by two low pressure centres in an Ω block, giving the streamlines an Ω shape and diverting the jetstream around the blocked region. These flow patterns are depicted schematically in Figure 1.1. Rex–type blocks are more common over Europe and Ω–type blocks more common over the Pacific. Atmospheric blocking has been an object of much study over the recent decades because of the profound effect it has on the surface weather (e.g. Rex, 1950; Green, 1977; Matsueda, 2011). Blocking over a region can be associated with severe heat waves in summer and extreme cold temperatures in winter due to clear skies in the high pressure centres of the blocking events. The effects of blocks are exacerbated by their persistence and can lead to large economic losses, the destruction of ecosystems and food sources, and many thousands of deaths (e.g. García-Herrera et al., 2010; Barriopedro et al., 2011).

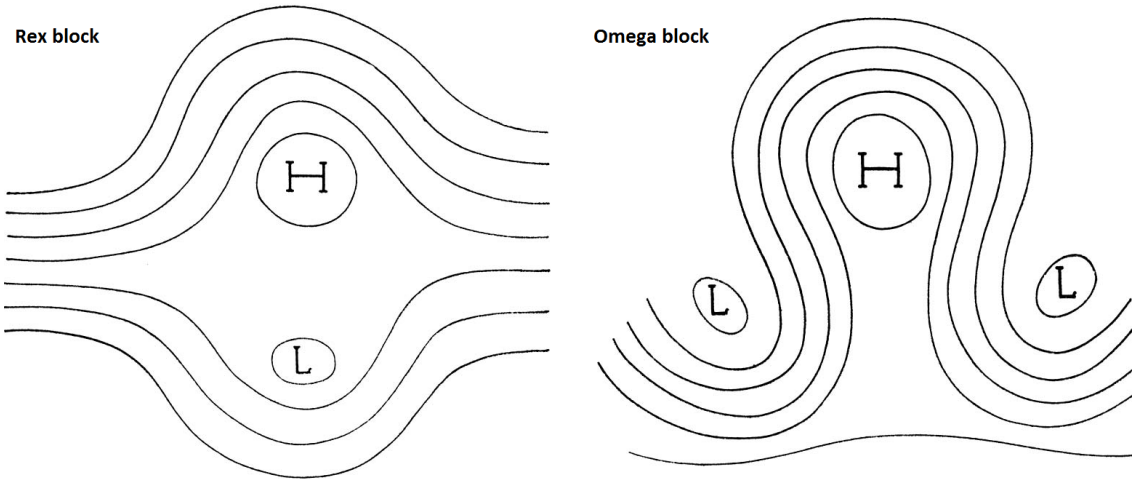

Figure 1.1: Schematic representations of the Rex– and Ω–type blocks. The contours represent upper–tropospheric streamlines. Adapted from Berry et al. (1953).

The influence they have on the weather and the potentially larger impacts they can have on society mean that it is crucial for us to predict atmospheric blocks as far

in advance as possible. However, the forecast of blocking is a well-known and long-standing problem for medium–range weather forecasts and future climate projections. Many studies (e.g. Tibaldi and Molteni, 1990; Pelly and Hoskins, 2003a; Matsueda, 2009; Davini and D'Andrea, 2016) have shown that several NWP models and longer climate simulations have a tendency to underestimate the observed frequency of blocking and exhibit a delay in the onset of a blocked flow. The role of upstream cyclones in the underestimation and delayed onset of blocking in NWP models is considered throughout this thesis. Since some of the earliest studies on atmospheric blocking (e.g. Berggren et al., 1949), it has been recognised that synoptic–scale transient weather systems might be important for the onset and maintenance of a blocking event. They have been observed to force geopotential height rises associated with developing blocks (Hoskins et al., 1983; Colucci, 1985; Shutts, 1986) and maintain blocks against dissipation and the background flow through vorticity advection (Shutts, 1983; Illari, 1984). Diabatic processes active within cyclones are also important for block development (Pfahl et al., 2015) and are known uncertainty in NWP model simulations of extratropical cyclones (Forbes and Clark, 2003; Forbes and Hogan, 2006; Joos and Wernli, 2012; Dearden et al., 2016; Martínez-Alvarado et al., 2016a). How this uncertainty relates to the development of blocks in medium–range forecasts is also explored in this thesis.

Concentrating on the role of extratropical cyclones in block representation in NWP models is also motivated by the known impact cyclones can have on the forecast of upper–level flow pattern and how this, in turn, is affected by model uncertainties relating to the parameterisation of diabatic processes. Errors in the representation of cyclones, originating from parameterisations of diabatic processes, can cause errors in the forecast of upper–level ridges (Davies and Didone, 2013; Martínez-Alvarado et al., 2016b). Furthermore, modifying the parameterisations of diabatic processes can have a big impact on the downstream Rossby wave development (Joos and Forbes, 2016). Diabatic processes can also be essential for highly amplified ridges developing downstream of ex–tropical cyclones (Grams et al., 2011). Gray et al. (2014) showed that the area of upper–tropospheric ridges decreases systematically with forecast lead time in several NWP models which could arise from a reduction in diabatically modified air reaching upper levels. It is clear that diabatic process, which need to be parameterised and hence are a source of model uncertainty, are important for upper–level flow evolution. But how does this, and other sources of model uncertainty, relate to error in forecasts of atmospheric blocking? And how does the systematic error in ridge area relate to forecasts of atmospheric blocking? This is investigated

in chapter 3. The specific aims of the work presented in this thesis that are designed to address these questions are now described.

1.1 Aims

The overall aim of this thesis is to improve the understanding of the link between errors in the forecast of atmospheric blocking and the upstream forecast of extratropical cyclones. In particular, it answers the question

- Do uncertainties in the representation of diabatic processes in extratropical cyclones lead to error in the downstream development of blocking?

To answer this question, each working chapter of this thesis (chapters 3–5) aims to answer several more specific research questions. The questions for each chapter are detailed below.

3. (a) What impact did the introduction of a new dynamical core in the Met Office Unified Model (MetUM) have on the forecast of atmospheric blocking?

   (b) How are the errors in the forecast of blocking related to the systematic errors in Rossby wave structure?

4. (a) How much of the difference seen in the ensemble forecast of block area can be attributed to the earlier forecast of an upstream cyclone?

   (b) What are the cyclone characteristics (in particular location and intensity) that are associated with the differing development of blocking in the ensemble?

5. (a) What is the impact of model physics uncertainty on medium–long range forecasts of atmospheric blocking and how does it compare to initial condition uncertainty?

   (b) Is block development sensitive to the heating structure and potential vorticity modification from parameterised diabatic processes near the tropopause?

Chapters 3–5 address the above research questions separately and are included in this thesis as articles that have been published or submitted during the PhD (see next section). The conclusions from each are synthesized and interpreted in light of the main research question in the conclusions.

1.2 Structure

The work in this thesis is presented as a collection of three articles that were completed during the PhD. The articles are included in Chapters 3–5 in the same version in which they were published or submitted. The articles included in this thesis, and the estimated percentage contribution of the author, are summarised in Table 1.1. Two of the articles have been published at the time of writing whilst the third has been submitted. All of the studies included in Table 1.1 were designed by, and had contributions to the writing from, all the listed authors. The analysis and main writing of the first paper listed was split evenly between J.W.M and O.M-A, with J.W.M completing all analysis and writing relating to atmospheric blocking and O.M-A all that related to upper–level Rossby waves. The analysis and main writing for the second and third papers was carried out by J.W.M.

Title	Journal	Status (date)	J.W.M Contribution
(a) Atmospheric blocking and upper-level Rossby wave forecast skill dependence on model configuration	Quart. J. Roy. Meteor. Soc.	Published (2018)	40%
(b) Upstream cyclone influence on the predictability of block onsets over the Euro-Atlantic region	Monthly Weather Review	Published (2019)	80%
(c) Impact of model upgrades on diabatic processes in extratropical cyclones and downstream forecast evolution	Quart. J. Roy. Meteor. Soc.	Submitted (2019)	80%

Table 1.1: Articles comprising chapters of this thesis. Together with their statuses and percentage contribution of the author.

In the next chapter, a literature review of midlatitude weather, especially that related to atmospheric blocking, is included. The primary literature reviewed is on the mechanisms behind atmospheric blocking and aspects of its predictability. A secondary focus on the structure, development and simulation of extratropical cyclones is also included as the interaction between extratropical cyclones and atmospheric blocking is an overarching theme of this thesis.

In chapter 3, the impact that a new dynamical core introduced in the MetUM had on the medium-range forecasts of atmospheric blocking and upper-level Rossby waves is analysed (Table 1.1(a)). The relationship between block forecasts and upstream cyclones in operational medium–range forecasts from ECMWF is addressed using ensemble sensi-

tivity analysis in chapter 4 (Table 1.1(b)). The relationship between upstream cyclones and atmospheric blocking in medium–range forecasts is further explored in chapter 5 (Table 1.1(c)): experiments with the MetUM modifying parameterisations of physical processes and a set of potential temperature tracers are used to this aim. The methods pertaining to each working chapter are included within the chapter in the same way as they were published or submitted. The conclusions from each working chapter are reflected on and suggestions are made for further work in chapter 6, the conclusions.

Chapter 2:

Literature Review

This chapter contains a review of literature that is relevant for the work included in the subsequent chapters of this thesis. The first section includes a broad overview of some of the main concepts in the study of the dynamics of midlatitude weather systems. Atmospheric blocking is comprehensively reviewed in the subsequent sections, from its definition, to the numerous theories proposed for the formation and maintenance of blocks and their predictability. Literature on extratropical cyclones and their representation in models is included at the end of the chapter as the impact of extratropical cyclones on the forecast of atmospheric blocking is considered throughout this thesis.

2.1 Midlatitude weather systems and regimes

The weather in the midlatitudes is governed by the passage of cyclones and anti-cyclones. Generally moving from west to east, steered by the predominantly westerly background flow, these weather systems are responsible for the weather we experience on a day to day basis. From a dynamical perspective, the distinguishing feature of the midlatitude circulation is the jet stream. The jet stream is a relatively thin, fast-flowing stream of air located at tropopause level. The structure of the jet stream is very variable across many timescales, meandering north and south as it flows around the globe, ranging from a zonal type flow, with low amplitude waves and high wind speeds, to a more wavy flow with weaker zonal winds. There is typically only one identifiable jet stream in the northern hemisphere flowing at high altitudes, though it is common to refer to two distinct jet streams when discussing its properties. The subtropical jet, located at the poleward edge of the Hadley cell in the upper troposphere where air is moving poleward, is a result of angular momentum transfer (Held and Hou, 1980) and local vorticity

balance (Woollings et al., 2010). The eddy-driven jet, driven by momentum and heat fluxes from transient synoptic-scale cyclones, is located further poleward in the baroclinic regions. It is the location and position of the jet that directs cyclones and anticyclones in different paths across the oceanic basins and over the continents (though the cyclones and anticyclones can also force changes in the jet stream location and structure (Lorenz and Hartmann, 2003)).

The jet stream and, in particular, its shape and location is thus closely related to the weather in midlatitude regions. For example, over the UK, a poleward shift in the jet stream brings warmer, generally wetter weather and vice versa. It is therefore useful to characterise the variability of the jet stream to understand weather variability in the midlatitudes. Woollings et al. (2010) showed that the jet stream in winter tends to exist in one of three latitudinal positions (southern, central and northern). Shifts in the jet stream are also commonly related to large–scale patterns of atmospheric variability, such as the North Atlantic Oscillation (NAO) and the East Atlantic pattern (EA) (Barnston and Livezey, 1987; Hurrell et al., 2003). The NAO and EA are the two dominant modes of low frequency variability over the North Atlantic and represent large–scale meridional pressure differences over the region. Switches between phases of the NAO and EA are associated with large changes in the wind speed and direction over the Atlantic (changes in the location of the jet stream). This drives changes in the heat and moisture transport from the subtropics towards the poles; the path, intensity and frequency of storms moving towards the continents; and ultimately the weather (Hurrell et al., 2001).

While the weather in midlatitudes is extremely variable, the atmospheric circulation in the midlatitudes can be broadly described in terms of *weather regimes*. A weather regime is a quasi-stationary period of "weather" (Reinhold and Pierrehumbert, 1982) that can be used to describe the variability of weather on synoptic scales (space and time). Over the North-Atlantic/European region, Vautard (1990) identified four distinct weather regimes in 37 years of 700 hPa geopotential height (Z700, equivalent notation also used hereafter for geopotential height at other pressure levels) analyses. The first is a European blocking dipole (BL), the second one an increased zonal flow (ZO), the third shows an anticyclone over Greenland (GA) and the final one is an East Atlantic ridge (AR). The day-to-day weather over the North-Atlantic/Europe can be neatly classified into one of these four regimes, usually identified using anomalies in Z500. The weather that is likely to follow can be intuited from the study of weather regime *transitions*. Vautard (1990) identified the preferred regime transitions as ZO to BL, BL to GA and

ZO to AR and the unlikely transitions as GA to BL, ZO to GA, GA to AR and self transitions. Other studies using different methods have identified similar weather regimes over the North Atlantic. Michelangeli et al. (1995) identified four similar regimes over the North Atlantic in a long time series Z700 anomalies. Kimoto and Ghil (1993b) find six distinct regimes in their Empirical Orthogonal Function (EOF) analysis of observed Z700, these included the four regimes described by Vautard (1990) plus a wave train extending from the East Coast of USA to Scandinavia and a regime resembling the EA pattern with low anomaly over Iceland. More recent studies have used Z500 to calculate weather regimes (normally using a clustering algorithm) over a range of periods and datasets and find the four regimes now commonly referred to as the North Atlantic weather regimes: the positive and negative phases of the NAO (NAO+/NAO-), European blocking and the Atlantic ridge (e.g. Cassou, 2008; Cattiaux et al., 2013; Dawson and Palmer, 2015; Ferranti et al., 2015). These four regimes are very similar to those identified in previous studies, with ZO equivalent to NAO+ and GA equivalent to NAO-. Reinhold and Pierrehumbert (1982) showed that forcing by transients is a key component of weather–regime dynamics. The planetary–scale waves that describe the weather regimes constrain the development of transient disturbances and, conversely, the transients can act as a forcing for the planetary scales.

Characterising atmospheric flow patterns as weather regimes is useful for medium–long range weather forecasts. If a prediction can be made that the large-scale atmosphere will closely resemble a particular weather regime the surface weather effects can be deduced. The focus in this thesis is on the prediction of atmospheric circulations resembling the European blocking regime (an extremely robust North Atlantic weather regime across studies) because blocking has a large influence on the midlatitude weather and is known to be hard to predict (e.g. Pelly and Hoskins, 2003a; Matsueda, 2009). Predicting atmospheric blocking of course requires an understanding of the dynamical processes responsible for its formation, maintenance and decay which can be understood using the potential vorticity framework.

2.1.1 The potential vorticity perspective on atmospheric dynamics

The dynamics of many midlatitude weather phenomena can be understood using potential vorticity (PV). The general form of PV and its tendency were first derived from the primitive equations by Ertel (1942), after its introduction by Rossby (1940). The

Rossby-Ertel PV is defined as

$$PV = \frac{1}{\rho}\boldsymbol{\zeta} \cdot \nabla\theta, \tag{2.1}$$

where PV is the potential vorticity ($\mathrm{Km^2kg^{-1}s^{-1}}$), ρ is the density ($\mathrm{kgm^{-3}}$), $\boldsymbol{\zeta}$ is the absolute vorticity ($\mathrm{s^{-1}}$) and θ is the potential temperature (K). The value of PV is normally given in potential vorticity units (PVU), where 1 PVU = $10^{-6}\mathrm{Km^2kg^{-1}s^{-1}}$. The rate of change of PV can then be derived as

$$\frac{DPV}{Dt} = \frac{1}{\rho}\left[\boldsymbol{\zeta} \cdot \nabla\left(\frac{D\theta}{Dt}\right) + \nabla \times \mathbf{F} \cdot \nabla\theta\right], \tag{2.2}$$

where $\frac{D}{Dt}$ is the Lagrangian derivative and $\mathbf{F}$ is the friction vector.

PV is a very useful variable because it is conserved for adiabatic $\left(\frac{D\theta}{Dt} = 0\right)$ and frictionless ($\mathbf{F}$=0) flow and is invertible under a defined balance condition and known boundary conditions. The conservation property approximately holds for upper-tropospheric flow on short time scales, where advection dominates over friction and diabatic heating, and allows PV to be used to trace air masses, study non-adiabatic processes and understand the dynamics of many midlatitude weather systems (Hoskins et al., 1985). The conservation of PV also demonstrates that the dynamical and thermodynamical aspects of a fluid parcel are not independent, and can only change such that the PV is conserved. The invertibility principle states that, under a certain balance condition (e.g. quasi-geostrophic balance), the distribution of wind, temperature and pressure fields can be obtained if the distribution of PV is known (provided boundary conditions are also known). Given a background state the flow induced by PV anomalies can also be derived. The strength of the circulation associated with a particular PV feature can be calculated using PV inversion and its influence on the development of other features can be ascertained (e.g. Davis and Emanuel, 1991; Davis, 1992; Stoelinga, 1996; Ahmadi-Givi et al., 2004).

PV is treated as one of the most fundamental meteorological variables as it combines the thermodynamical and dynamical aspects of the atmosphere into a single equation. From the PV perspective, the fundamental structures behind atmospheric dynamics and thermodynamics can be thought of as balls of PV (Hoskins et al., 1985) (spherically–shaped anomalous PV regions). The circulation induced by PV balls can be felt in regions away from the anomaly itself, through a concept known as 'action at a distance'. The PV

framework can be used to describe nearly the entirety of atmosphere and ocean dynamics, from the development of small amplitude perturbations to planetary–scale Rossby waves (Hoskins et al., 1985). PV thinking can also be exploited to study the role of diabatic and frictional processes in dynamical development, the concept of PV nonconservation (Stoelinga, 1996). Friction and diabatic heating can create PV anomalies that then have an effect on the flow (discussed further in section 2.4.3).

Large–scale undulations in the jet stream are known as Rossby waves (Rossby, 1940). Ridges and troughs in the upper-level flow develop frequently and propagate along regions of strong baroclinicity (Nakamura and Plumb, 1994) interacting with surface flow features (Hoskins et al., 1985) and driving midlatitude weather. These waves can be clearly visualised by looking at maps of PV on isentropic surfaces. On an upper-level isentropic map of PV, the tropopause can be identified as the location with the strongest gradient in PV (stratification increases dramatically in the stratosphere). The value of PV that divides tropospheric air and stratospheric air (the tropopause) is normally taken to be 2 PVU. The jet stream is co-located with the band of enhanced PV gradient (running parallel with the tropopause). This acts as a waveguide for the development of synoptic- and larger-scale flow (Martius et al., 2010). Rossby waves can then be visualised as undulations of the 2 PVU contour, with ridges characterised by low values of PV and troughs higher PV. An illustrative example of an isentropic map of PV, this case on 320 K, is provided in Figure 2.1.

Many fine–scale structures embedded in the flow are visible in the PV field, as are extrusions of cold and warm air from the north and south, respectively. Rossby wave breaking can also easily be visualised as overturnings (either cyclonically or anticyclonically) of the 2 PVU contour. Streamers of PV and regions of cut off high and low regions are ubiquitous in regions of the northern hemisphere. Analysis of subsequent isentropic PV maps allows for an investigation of the origin of air masses forming circulation features of interest (PV is quasi-conserved at upper levels far away from the Earth surface for a few days) and can show how they affect lower level weather system development.

2.2 Atmospheric blocking: definition and mechanisms

One of the most prominent features of the midlatitude flow is referred to as atmospheric blocking. The term ‘blocking’, or simply a block, originates from the most fundamental property of atmospheric blocking which is that it effectively blocks the prevailing

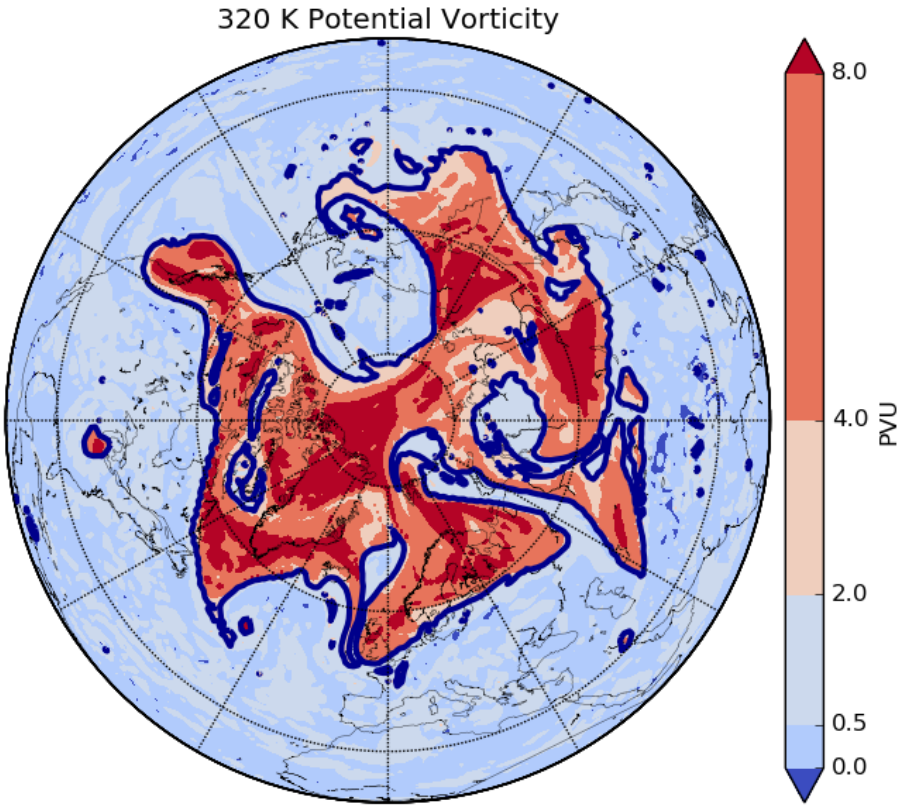

Figure 2.1: Illustrative example of an isentropic map of PV, the blue contour marks the dynamical tropopause.

westerly winds and redirects mobile systems to the north or south of the atmospheric blocking event. Typically, there is a reversal of the zonal winds so that there is net easterly winds in some region of the block. Garriott first discovered blocking in 1904 (Garriott, 1904; Rex, 1950). Blocking has been known to be an important phenomenon for midlatitude weather since the middle of the 20th century. In their pioneering studies, Berggren et al. (1949) and Rex (1950) described the effect of blocking on the local weather and climate in a couple of case studies and both suggested that transient synoptic-scale eddies may be important in initiating a blocking event. Berggren et al. (1949) provided a detailed description of the upper-level development of a blocking episode for the first time, using the increased availability of upper-air data following World War II. Rex (1950) gave the first widely accepted definition of a blocking event (described in section 2.2.2) that form the basis of many modern objective block detection algorithms.

2.2.1 Characteristics of atmospheric blocks

An atmospheric block is typically characterised by a synoptic-scale anticyclone (or ridge of high pressure) that is quasi-stationary in space and can persist for several weeks. Atmospheric blocks have a barotropic structure (Rex, 1950) with anticyclonic circulation dominating the troposphere: a surface high pressure centre located beneath the upper-level quasi-stationary warm ridge. There are, however, several flow patterns for which a block's defining features are satisfied. Woollings et al. (2018) highlighted five such different configurations, shown in Figure 2.2. The synoptic-scale anticyclones are in each case associated with a ridge (or cut-off high) in Z500 and locally higher values of potential temperature (θ) on the dynamical tropopause (2 PVU surface). Cyclonic regions are also present in a blocked configuration: one region located on the equatorward side of the block or two cyclonic regions flanking a blocks east and west. The onset of a block in each case is characterised by the poleward excursion of subtropical air and an amplified upper-level jet pattern. The timescale for block onset is quick, normally between 1–3 days, whereas the maintenance and eventual decay of a block occurs over longer timescales in many cases (several weeks). Broadly speaking, blocking occurs preferentially in three locations in the northern hemisphere: the Atlantic and Pacific regions at the end of the North Atlantic and North Pacific storm tracks and over Greenland. There are typically more blocking events (and more total days blocked) during winter and spring and a minimum in blocking frequency in summer (e.g. Tibaldi et al., 1994; Lupo and Smith, 1995). Atmospheric blocking also occurs in the southern hemisphere with a single longitudinal peak in blocking frequency (Lejenäs, 1984; Tibaldi et al., 1994) and two peaks in annual frequency in southern hemisphere autumn and winter. Northern hemisphere blocking is the focus throughout this section (and thesis), though many of the mechanisms and concepts discussed relate to southern hemisphere blocking as well.

The stationarity of a block can be understood by considering the flow signatures of the various θ or PV anomalies present in each type of block. The background distribution of θ on the dynamical tropopause equates to a near zonally-symmetric pattern with a negative meridional gradient. Ridges correspond to regions of anomalously high θ and troughs anomalously low, i.e. regions of potentially warm air intruding from the subtropics and potentially cold air intruding from the polar regions, respectively. These anomalies are associated with anticyclonic and cyclonic circulations, respectively. The configuration of these anomalies, and the net effect of their circulations in the different blocking types,

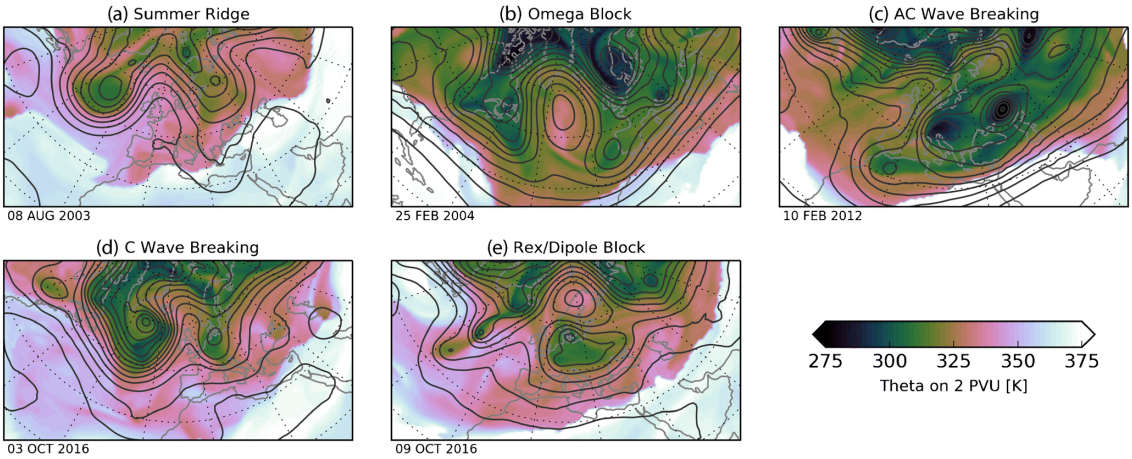

Figure 2.2: Different flow patterns that meet some of the commonly used criteria for blocking. Contours show Z500 (60 m contour spacing). From Woollings et al. (2018)

act to stop the blocking pattern being advected away by the background westerlies. For example, in the Rex/Dipole type block (Fig. 2.2e), the anticyclonic circulation to the north of the cyclonic circulation results in an easterly anomaly at the central latitude, counteracting the westerly flow. The stationarity achieved in the summer ridge cases (Fig 2.2a) occurs if the Rossby wave pattern has near zero phase speed. The range of flow structures that are referred to as blocks implies that there may be a variety of dynamical mechanisms that are associated with their onsets and persistence. This has resulted in many methods to identify them being introduced. Block identification methods are discussed in section 2.2.2 and the theories for the onset and maintenance of blocking are discussed in section 2.2.3. Important mechanisms have been studied that vary massively in scales, from transient eddies to planetary–scale waves. Though the onset and maintenance of atmospheric blocking have been shown to be closely related to migratory, synoptic-scale transient eddies (i.e. cyclones and anticyclones) (e,g, Rex, 1950; Shutts, 1983; Nakamura and Wallace, 1990). This is discussed further in section 2.2.3.1 and explored in the subsequent chapters of this thesis.

Atmospheric blocking has been a phenomenon of interest in much research since the studies of Berggren et al. (1949) and Rex (1950) because of the profound effect it has on the surface weather, both at the location of the block and in regions far away. This effect on the weather is caused mainly by the persistence and large amplitude of blocking events and is often associated with extreme temperatures and reduced precipitation in the blocking regions. Blocking can thus can contribute substantially to droughts. The nature and cause of the weather extremes is dependent on season. In summer, atmospheric blocking can drive extremely high temperatures in the location of the block. Clear skies in the

anticyclonic block drive surface heating mainly resulting from clear-sky radiative heating (Pfahl and Wernli, 2012). Many of the strongest and most damaging heatwaves on record, for example those of Europe in 2003 and Russia in 2010, were caused by atmospheric blocking events. In both cases the impacts were severe: there were thousands of deaths caused by the events (Robine et al., 2008; Matsueda, 2011); there were devastating effects on ecosystems and plant productivity (Ciais et al., 2005; Grumm, 2011); and widespread wildfires destroyed vast regions of crops and resulted in smog levels more than 5 times higher than usual (García-Herrera et al., 2010; Matsueda, 2011). The driver behind these impacts was the extreme temperatures that built up over the blocks lifecycle, resulting in average anomalies of $+4°C$ over Europe in 2003 (Black et al., 2004) and an anomaly of over $+15°C$ in Moscow for July and August 2010 (Grumm, 2011). In winter, the extreme cold temperatures associated with atmospheric blocking events (Buehler et al., 2011) are generally caused by thermal advection associated with easterly or northerly winds on the eastern flank of the blocking events (Sousa et al., 2018). Atmospheric blocking events can also cause extreme events in locations downstream. The atmospheric block behind the Russian heatwave of 2010 caused prolonged precipitation and flooding in Pakistan because of a cyclonic vorticity anomaly that was associated with the block. The anomaly was favourable for precipitation production in Pakistan because of the direction of the wind, which was persistent for the duration of the blocking event and hence resulted in flooding (Lau and Kim, 2012).

An objective algorithm, such as the blocking indices described in the next section, that identifies a block can be applied on many datasets to study blocking climatologies in the present, past and future. The prevalence of atmospheric blocking in the middle latitudes and its importance in driving extremes has led to much effort studying methods that are able to objectively identify a block in gridded datasets.

2.2.2 Blocking indices

Blocks have many defining features so the best way to objectively define them from a given dataset has been the subject of much research. Rex (1950) first established some characteristics that a typical blocking case has:

1. a split jet: the normal westerly jet must split into two branches with each branch of appreciable strength;

2. the split jet must extend over 45° of longitude;

3. zonal flow upstream of the block must be observed with a quick shift to meridional flow downstream;

4. the pattern must persist for at least 10 days.

These criteria are now widely accepted and used to subjectively define the so called 'Rex-type' blocking events (a high-low dipole structure with the blocking anticyclone to the north of a cyclone, Fig. 2.2e) and form the basis of many objective blocking indices. Indices must also capture the Ω-type blocking events (Fig. 2.2b) which do not always meet the split-jet requirement of Rex (1950). To capture both Rex- and Ω-type blocks in an algorithm is not easy. Barriopedro et al. (2010) provide a comprehensive review of blocking indices. PV and Z500 are the two most common variables used in blocking indices because they are able to describe features of the flow necessary to meet the criteria of Rex (1950). The Tibaldi and Molteni (1990) index is one of the most commonly used objective blocking indices. This index looks for reversals of the flow in Z500 by calculating meridional gradients at each longitude for a central latitude. A longitude is defined as blocked if the meridional gradient in Z500 from the south is negative and to the north is positive and larger than a given threshold. The index is popular because it is easy to apply to large datasets, but it is limited by its 1D description of blocking and necessary subjective parameters (e.g. latitude at which to calculate the index). Scherrer et al. (2006) extended the Tibaldi and Molteni (1990) index to 2D simply by calculating the meridional gradients in Z500 at every latitude between 35–75°N. 2D blocking indices account for the size of the blocking event and its location latitudinally and also allow for better linking of blocks temporally, which can be difficult in 1D indices. Anomaly based Z500 blocking indices, such as that introduced by Dole (1986), have also been used to define blocking events and are able to account for their spatial scale.

The index introduced in Pelly and Hoskins (2003b) emphasises the Rossby-wave breaking characteristic of atmospheric blocking when viewed from the PV perspective. Wave breaking can set up the large-scale reversals in the meridional gradient of θ on the dynamical tropopause (surface of 2 PVU) that is caused by the extrusion of subtropical air associated with an incipient block (Hoskins and Sardeshmukh, 1987; Vautard and Legras, 1988). Pelly and Hoskins (2003b) argue that a dynamical identification index based on PV is beneficial because it can exploit the conservation properties of θ on PV and is a more natural choice than Z500 because the PV-θ perspective can give a complete description of balanced midlatitude weather systems, and hence blocking (Hoskins et al.,

1985). Schwierz et al. (2004) also attest the benefits of using the PV-perspective to identify blocking events. The essential feature of a block that the index of Schwierz et al. (2004) attempts to identify is an upper-tropospheric 3D anomaly in PV. The use of an anomaly field allows for an easy definition of block amplitude, spatial scale, shape and evolution and removes the central-latitude restriction of earlier indices. The Rossby–wave breaking characteristics of blocking were further explored in Masato et al. (2012). Masato et al. (2012) extend the index of Pelly and Hoskins (2003b) to take into account the orientation of the wave breaking of θ on the 2–PVU surface and the dominant air mass excursions (cold or warm anomalies) of the blocking event. Blocks occurring over the oceans tend to be associated with cyclonic wave breaking, with anticyclonic being more frequent for continental Europe and Asia. Pacific blocks are dominated by warm air intrusions from the subtropics whilst European cases exhibit both cold and warm blocking cases.

Blocking indices can be used to compare many characteristics of blocks across many observational, reanalysis and modelled datasets. Climatologies of blocking produced using many of the indices, across a range of data sets, demonstrate that in the northern hemisphere winter blocking most frequently occurs in the Euro-Atlantic and Pacific regions (e.g. Tibaldi and Molteni, 1990; Tibaldi et al., 1994; D'Andrea et al., 1998; Pelly and Hoskins, 2003b; Schwierz et al., 2004; Scherrer et al., 2006). There is less agreement on the annual cycle: climatologies produced have Euro-Atlantic blocking maxima in spring (Lejenäs and Okland, 1983; D'Andrea et al., 1998), winter and spring (Tibaldi et al., 1994; Lupo and Smith, 1995) and the autumn (Pelly and Hoskins, 2003b). Blocking in the Pacific tends to have a less defined maximum in winter and spring (Lejenäs and Okland, 1983; Tibaldi et al., 1994; D'Andrea et al., 1998). The absolute value of blocking frequency in each region and season also changes between indices, with frequencies generally between 10–30% in the Euro-Atlantic in winter, spring and summer with less in the autumn and between 10–20% in the Pacific across all seasons. The disagreement between studies is likely in part due to the different data sets used, the differing periods covered by them and differing lengths of the climatologies produced. The disagreement also reflects the variety in flow configurations deemed atmospheric blocks and the inherent complexity of the phenomenon: different indices are better at identifying different block configurations and are based on different theories that describe block dynamics. Some of the theories that are commonly used to explain block dynamics are now reviewed.

2.2.3 Blocking theories

No complete dynamical theory currently exists for the onset, maintenance and decay of atmospheric blocking (e.g. Woollings et al., 2018). Many theories have been proposed and many are able to reproduce particular aspects of blocking observed in the real world. Theories of blocking can be classed into two categories: theories that view blocking as a global or planetary–scale phenomenon and those that emphasise more local processes.

2.2.3.1 Local theories

Local theories on blocking focus on processes occurring (or solutions of equations) near to the blocked location. Euro-Atlantic and Pacific blocking events can only be weakly correlated under local blocking theories (which has been found to be the case in some studies (e.g. Lejenäs and Okland, 1983)). Some local theories on blocking are described below. Many focus on the forcing from transient eddies (cyclones and anticyclones), and their interaction with the planetary–scale flow, which have been shown to be important in many cases of blocking (e.g. Shutts, 1983; Colucci, 1985; Lupo and Smith, 1995), and is an idea that will be explored further in this thesis, whilst others look for vortex-pair or wave solutions under quasi-geostrophic theory.

- Eddy forcing: Synoptic-scale eddies (cyclones and anticyclones) have been shown to be important for the maintenance of atmospheric blocking. Weather systems generated in the baroclinic zones move with the jet stream and upon arriving at the split jet on the western flank of the block are stretched and transfer momentum and vorticity to the flow in such a way that maintains the blocking dipole. The drought-inducing block of Western Europe in July 1976 was shown to be maintained by the transfer of momentum at near-tropopause levels by transient eddies by Green (1977). The momentum transfer was shown to result in anticyclonic vorticity forcing strong enough to produce the observed anticyclone. Shutts (1983) proposed an eddy-straining mechanism that can account for many observed features of an atmospheric block (described below). Illari and Marshall (1983) computed horizontal eddy fluxes of temperature and quasi-geostrophic (QG) PV during the month of July (the same block studied in Green (1977)) using twice daily synoptic charts. They proposed that the eddy forcing pattern is such that it stops the anomalous low PV air that constitutes the block from being advected downstream: the repeated transfer of low-PV air northwards and high-PV air southwards by transient

synoptic-scale systems maintains the blocking dipole, in accordance with the theory of Shutts (1983). Using QG theory, Mullen (1987) investigated the net forcing of time-mean blocking flows by synoptic-scale transient eddies in both observed blocks and blocks simulated in General Circulation Models (GCMs). He found that the vorticity forcing from the eddies tended to be located one quarter wavelength upstream of block, in agreement with previous studies (Austin, 1980). The QG temperature tendencies associated with the transient eddies also tended to be out of phase with the temperature perturbations of the block. Mullen (1987) also showed that the vorticity forcing by transient eddies differed between climatological and blocking flows. He suggested that barotropic processes associated with the deformation of the transient eddies are mainly responsible for the eddy forcing but that baroclinic processes are mainly responsible for generating the synoptic-scale transients. It was the interaction between the synoptic-scale eddies with planetary-scale waves that contributed substantially to block formation in a case study by Tsou and Smith (1990). The importance of transient eddies for block maintenance has been elucidated in many additional studies (e.g. Illari, 1984; Nakamura and Wallace, 1993; Nakamura et al., 1997) and remains a popular theory for explaining block dynamics. In their climatology of northern hemisphere wintertime blocking events, Lupo and Smith (1995) found that *all* of the 63 identified blocking events could be identified as having an upstream precursor cyclone.

- Eddy Straining Mechanism (ESM): (Shutts, 1983) proposed an eddy-feedback mechanism for block maintenance whereby synoptic-scale eddies act to maintain the blocking structure against dissipation: the vorticity forcing by the straining of eddies in the split jet stream maintains both the anticyclonic and cyclonic vortices of the block. Figure 2.3 shows the action of eddies on the flow when arriving at a split jet stream schematically. Synoptic-scale eddies (plus and minus contours) propagate into the split jet (background stream lines), are meridionally stretched and split into each branch of the jet. The vorticity forcing, calculated using the eddy enstrophy equation (Holland and Rhines, 1980), is denoted with the thick arrows and has the effect of producing anticyclonic forcing to the north and cyclonic forcing to the south just upstream of the block location. Shutts (1983) showed in idealised numerical experiments (using the barotropic vorticity equation) that dipole type blocking patterns can be created in a weak, uniform westerly flow by introducing a generator of eddies upstream. A stationary source of eddies was also

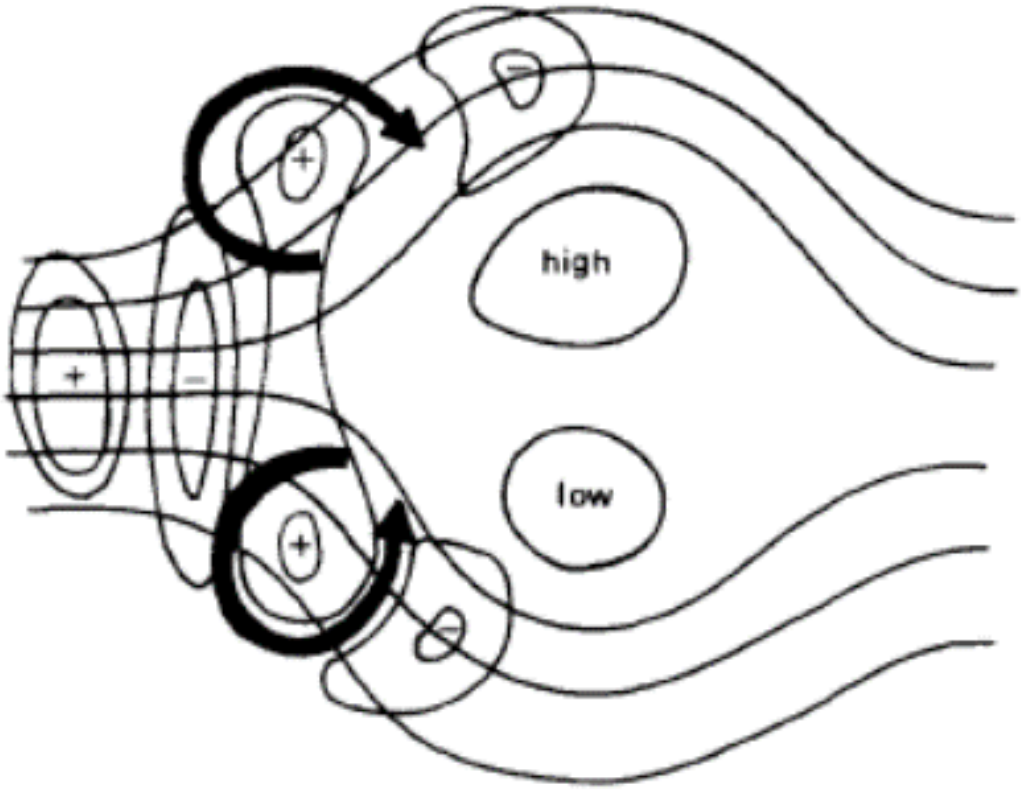

Figure 2.3: Schematic picture of the production and subsequent deformation of eddies propagating into a split jetstream (background contours) together with their associated vorticity forcing pattern (thick arrows). From Shutts (1983)

found to amplify the dipole meridional structure of a block. The generator of eddies used in Shutts (1983) was designed to mimic the production of eddies by baroclinic instability in the real atmosphere. The role of synoptic eddies was further explored in Shutts (1986) for a case study of blocking using the momentum, vorticity and Ertel PV equations. It was shown that the momentum and vorticity forcing of the eddies induced the upper-level anticyclone. Synoptic-scale disturbances were shown again to inject low PV air into the blocking anticyclone and high PV air into the equatorward cyclone, reinforcing the block structure.

Later studies showed that the ESM was very sensitive to storm track conditions (Yamazaki and Itoh, 2013), which are highly variable in the real atmosphere, and shifts in the location of the wavemaker in both the zonal and latitudinal direction comparable to those observed between blocking events resulted in a break down of the mechanism (Maeda et al., 2000; Arai and Mukougawa, 2002). The selective

absorption mechanism and nonlinear multiscale interaction model are newer eddy-feedback models, described below, that aim to describe block maintenance and the entire block lifecycle, respectively.

- Upstream cyclogenesis: another blocking theory associated with synoptic-scale eddies proposes that strong cyclogenesis upstream precedes block development. Two cases of explosive cyclogenesis over the Western Atlantic that were followed by blocks downstream were investigated by Colucci (1985). He showed that the $Z500$ rise in the blocking system were forced by both thermal and vorticity advections. Colucci (1987) examined a 17-day study period during November 1980, using analysed data, in which three cyclone events occurred. Two of the three events were associated with blocking events downstream. The QG-height tendencies were largest for the non-blocking event, but were not always of the same sign at the same location. The forcing (vorticity and differential temperature advection, or advection of PV) during the blocking events were of consistent sign suggesting that the forcing needs to not only be large but also persistent in space and time for a block to develop. Colucci (1987) hypothesise that the amplitude of existing planetary waves and their phase relative to the cyclone are what determine whether a blocking vortex develops. The strength of a block depends on both the amplitude of the planetary-scale ridge and the strength of synoptic eddies prior to block onset (Colucci, 1985), as well as the strength of the background westerly flow before block onset occurs (Kaas and Branstator, 1993).

  Colucci and Alberta (1996) explored the relationship (not proven to be causal) between blocking and explosive cyclogenesis in a 7-year climatology of winter Northern Hemisphere circulation. They found a 12% overall probability in the climatology that a block onset would occur in a 5-day period following a non-blocked day in both the Pacific and Atlantic sectors, regardless of upstream cyclogenesis. The occurrence of explosive cyclogenesis co-located with anomalously strong southerly and anomalously weak westerly planetary–scale geostrophic flow at 500 hPa increased the probabilities to 19% and 24% in the Atlantic and Pacific sectors, respectively. In total, 14 of the 25 blocking events were preceded by explosive cyclogenesis within 5 days and 60° zonally. Colucci and Alberta (1996) suggest anomalous planetary–wave amplification is important for block onset, though they note this does occur more frequently than blocking and so can at most be a part of the block onset

mechanism. Furthermore, no causation is proven in Colucci and Alberta (1996), i.e. the cyclone may develop as part of the block onset mechanism. Focusing on blocking events over Greenland occurring between 1979–2008 in the European Centre for Medium–range Weather Forecasts (ECMWF) Interim Re-analysis (ERA-I, Dee et al., 2011), McLeod and Mote (2015) found that across all seasons precursor cyclones are not significantly stronger and do not intensify more rapidly than non-precursor cyclones (cyclones that were not followed by a blocking event). Though not significant (except for spring), the maximum deepening rates of precursor cyclones across all seasons are less than those of non-precursor cyclones, which suggests explosive cyclogenesis may not be favourable to downstream formation of blocking events over Greenland. Konrad and Colucci (1988) also found that explosive cyclogenesis associated with downstream ridge-building tended to be relatively weak compared to the other explosively intensifying cyclones.

The role of extratropical cyclones (synoptic-scale cyclonic eddies) in the development of atmospheric blocking events in numerical weather prediction models is the main mechanism considered in this thesis.

- Selective absorption mechanism (SAM) (Yamazaki and Itoh, 2009, 2013): this mechanism is an update of the eddy-feedback mechanism described in Shutts (1983) to a vortex-vortex interaction between a blocking anticyclone and synoptic anitcyclones. According to the selective absorption mechanism, blocking anticyclones selectively absorb anticyclonic synoptic eddies as they are of the same polarity as the blocking anticyclone. The mechanism is based on the vortex–interaction theory of fluid dynamics (see, for example, chapter 18 of Cushman-Roisin and Beckers (2011)). Cyclonic eddies are repelled by the block as they are of the opposite polarity. The absorption of anticyclonic eddies (of low-PV) acts to maintain the blocking structure against dissipation. Yamazaki and Itoh (2013) argue that the selective absorption mechanism is more beneficial than earlier theories as it can be used to describe both dipole- and Ω-type blocks and has been verified against observed cases of blocking.

- The eddy-blocking matching mechanism (EBM) (Luo et al., 2014): combining ideas from the ESM and the SAM, and building on the nonlinear multiscale interaction model (Luo, 2005; Luo and Chen, 2006), the eddy-blocking matching mechanism aims to describe the causal relationship between eddy activity and blocking growth, maintenance and decay. This mechanism is a significant development from the ESM

and SAM which were limited to describing only block maintenance as they consider blocking events as steady state. Luo et al. (2014) find that the spatial distribution of the eddy vorticity forcing produced by upstream synoptic-scale eddies determines whether a blocking flow will intensify or decay. The block will intensify if the eddy vorticity forcing signature matches that of the developing block structure. The EBM also highlights the feedback of the block on the synoptic–scale eddies and Luo et al. (2014) argue that the preferred eddy vorticity forcing for block development is partially a response due to the blocked flow. Eddy straining and vortex interactions are not necessary in the EBM, but they do play an important role in the mature phase of a block.

- Instability theory: Frederiksen (1982, 1983) and Frederiksen and Bell (1990) view blocks, much like cyclones, as developing from an instability of the three-dimensional flow. Initially small perturbations can amplify and form blocking structures due to both baroclinic and barotropic instability (Frederiksen and Bell, 1990). Frederiksen (1983) used a two-layer quasi-geostrophic model to study the fastest-growing small-amplitude perturbations growing on the basic state (derived from the average northern hemisphere winter 300 and 850 hPa streamfunctions) for different static stabilities. Fast growing monopole structures were identified when the flow was most unstable and corresponded to cyclogenesis modes. Dipole structures, or block onset modes, were fastest growing when the stability increased. Frederiksen (1983) argue that the slow-moving dipoles structures found when the stability is increased equate to the onset of blocking in the same way that the monopole structures equate to cyclogenesis in the unstable case. Nonlinear processes would develop the dipole block onset modes into a mature block. Instability theory for blocking and other atmospheric teleconnection patterns is reviewed in Frederiksen and Webster (1988).

- Rossby-wave breaking mechanism: From the PV perspective, the defining feature of an atmospheric block is a negative PV anomaly located in the upper-troposphere and in the midlatitudes (Schwierz et al., 2004), typically with anomalously high PV air on the equatorward side. This anomalously low PV air originates in the subtropics and arrives in the midlatitudes ahead of a meridionally elongated trough (Hoskins and Sardeshmukh, 1987). This reversal of the equator to pole PV gradient can be set up via Rossby wave breaking. Hoskins et al. (1985) and Hoskins and Sardeshmukh (1987) show maps of isentropic PV that clearly demonstrate low-PV

air being advected from the subtropics, the breaking of Rossby waves (viewed as contours of isentropic PV) and the formation of the low-PV anomaly for case studies of blocking occurring in 1982 and 1996, respectively. Altenhoff et al. (2008) produced a climatological relationship between breaking Rossby waves and atmospheric blocking for the northern hemisphere winter during the period 1958–2002 in the ERA-40 reanalysis dataset (Uppala et al., 2005). They found that during the entire block lifecycle the spatial frequency of breaking synoptic-scale Rossby waves was significantly above the climatological value to the south of the block. Anticyclonic wave breaking tends to be associated with blocks forming over Europe and Asia whereas cyclonic wave breaking events drive blocks over the oceanic basins (Masato et al., 2012).

- Diabatic influence via warm conveyor belts (WCBs): Most of the theories discussed in this section are based on dry dynamics (e.g. Shutts, 1983; Frederiksen, 1983; Nakamura et al., 1997) with the role of diabatic processes discussed as a secondary factor. Though the theories involving cyclones or cyclogenesis (e.g. Colucci, 1987; Yamazaki and Itoh, 2013) are inherently dependent on diabatic processes, which can considerably affect cyclone development (Davis and Emanuel, 1991). Recently, Pfahl et al. (2015) showed that latent heat release in air ascending from lower levels to near the tropopause is of primary importance for the onset and maintenance of atmospheric blocking. Pfahl et al. (2015) used a combined PV and Lagrangian approach to analyse changes in block airmass properties in the days before block onset for northern hemisphere blocks in 21 years of ERA-I data. They found that between 30 and 45% of the blocked air mass is heated by more than 2 K in the three days before block onset (with a median heating of more than 7 K). In the seven days before block onset it is between 60 and 70% of the blocked air mass that is heated by more than 2 K. Accurate forecasts of blocking are thus likely to be dependent on the accurate representation of diabatic processes.

- Modons and solitons: A modon is an exact localised nonlinear solution of the quasi-geostrophic equations, or equivalent barotropic vorticity equation (McWilliams, 1980). It consists of a vortex pair (cyclone and anticyclone) embedded in background westerly winds reminiscent of a dipole block. McWilliams (1980) showed that modons were somewhat comparable to a dipole–like blocking event and many subsequent studies (e.g. Haines and Marshall, 1987; Yamazaki and Itoh, 2009) have

based their work on the modon solutions. However, the existence of modons in the real atmosphere requires conditions of the flow that are not easily attained (a too strong mean zonal wind) (Haines and Marshall, 1987) and it has been shown that composites of blocking events do not resemble modon vortex pairs (Higgins and Schubert, 1994). Soliton, or solitary wave, theories allow for wave solutions of the Korteweg–de Vries type solitary Rossby wave model (Malguzzi and Malanotte-Rizzoli, 1984) or eddy-forced envelope Rossby soliton model, based on a nonlinear Schrodinger equation (Luo, 2000, 2005). Rossby wave dispersion is then balanced by nonlinear advection and split jet, block-type flows are obtained for sensible atmospheric parameters and hence may capture the basis dynamics of blocking. Nezlin and Snezhkin (1993) review some of the implications of modon and soliton solutions for blocking.

2.2.3.2 Global theories

Global theories of blocking postulate that it is the interaction of large- or planetary-scale waves that is most important for block development. The three types of global theories of blocking can be summarised as follows:

1. Tropical forcing theories: Rossby wave trains triggered by tropical convection (forced by sea surface temperature (SST) anomalies) can produce block–like structures (Hoskins and Karoly, 1981; Hoskins and Sardeshmukh, 1987; Ferranti et al., 1994). Anomalous diabatic heating in the subtropical western Atlantic (Michel and Rivière, 2011) and the Caribbean (Hoskins and Sardeshmukh, 1987; Ferranti et al., 1994) can initiate blocking events in the Euro-Atlantic region. Pacific blocking has been shown to be strongly sensitive to the SSTs and convection over the Maritime continent (Ferranti et al., 1994).

2. Stationary wave theories: stationary waves of low wavenumber and large amplitude force the growth of ridges in the European and Pacific regions (Grose and Hoskins, 1979; Austin, 1980; Hansen and Sutera, 1993). Stationary Rossby wave trains induced by orography (Grose and Hoskins, 1979; Hoskins and Karoly, 1981) or thermal anomalies (Tung and Lindzen, 1979; Hoskins and Karoly, 1981) can undergo constructive interference, force the amplification of ridges and become blocking–like structures. Blocking in the Atlantic and Pacific occurs (a split jet forms upstream) when planetary waves of different wave numbers constructively interfere (Austin,

1980). Blocking typically occurs in the Atlantic when wave numbers one and two interact, whereas it is the interaction between wave numbers two and three that is dominant for Pacific blocking (Austin, 1980). Major mountain ranges provide the orographic forcing, whilst either land sea contrasts or tropical SSTs provide the thermal forcing. Since major mountain ranges, land-sea borders, and tropical SSTs are stationary, stationary wave theories are able to explain the favoured locations of block formation- i.e. the European and Pacific regions. The wave activity propagation across the North Atlantic through quasi-stationary wave-train can be a dominant driver of block onset over Europe (Nakamura et al., 1997). A precursor wave train was also found to be a common feature for the onset of blocking in the Atlantic by Altenhoff et al. (2008). Both Nakamura et al. (1997) and Altenhoff et al. (2008) suggest local signals are more important for the development of blocking in the Pacific.

3. Equilibria theories: these begin with the theory that there exists quasi-stable states in the atmosphere that give rise to observed circulation patterns. Blocking is then considered to be such a quasi-stable atmospheric state that is associated with the resonance of planetary waves. Charney and DeVore (1979) found two stable states in a barotropic channel model that resembled a blocking and zonal flow. Similar states have been found in more complex models (Malguzzi and Speranza, 1981; Charney et al., 1981) though their existence in the real atmosphere remains uncertain. Resonance can occur for a 'blocking wave' of zonal wavenumber four (Austin, 1980).

2.3 Predictability of atmospheric blocking and upper-level Rossby waves

The prediction of atmospheric circulation is a many faceted problem: the atmosphere has an 'intrinsic' level of predictability dependent on its base state (Lorenz, 1963; Palmer, 1993); initial condition uncertainty is important because of the chaotic nature of the atmosphere (Lorenz, 1993); and model formulation uncertainties can have a large impact on dynamical evolution (Ehrendorfer, 1997; Palmer, 2000). Forecast errors can propagate at the group speed of Rossby waves (Kelly et al., 2007), i.e. faster than the phase speed, so initial condition errors may impact forecast skill from far away (Magnusson, 2017).

Initial condition uncertainty is accounted for by running an ensemble of forecasts: the deterministic forecast model is evolved from a set of perturbed initial states giving a set of forecasts, each representing a possible state of the atmosphere at a given time. The spread in possible states of the atmosphere produced by the ensemble is taken as a measure of predictability of the atmosphere at that time. Model formulation uncertainties are commonly accounted for by applying stochastic perturbations to physical tendencies (e.g. Buizza et al., 1999) or by perturbing physical parameters (e.g. Doblas-Reyes et al., 2009).

Predicting the large-scale flow of the atmosphere has improved dramatically during recent years (e.g. Dee et al., 2014; Bauer et al., 2015): the number of forecast busts has decreased consistently and considerably since the 1990s (Rodwell et al., 2013) with five-day forecasts today as skilful as three-day forecasts from 20 years ago (Dee et al., 2014). Forecasts can still have errors, which can arise from initial condition uncertainty, any number of different model deficiencies (model physics uncertainty, dynamical core, resolution, etc), and the intrinsic unpredictability of certain atmospheric flows. The PV-perspective can be useful when studying the predictability of atmospheric flow because the fundamental properties of PV (conservation and inversion) have direct implications when considering forecast error (Dirren et al., 2003). The misrepresentation of diabatic or frictional processes, advection of error across a PV-gradient and/or error in the analysis field are the causes of PV-error non-conservation and can aid in the identification of systematic errors associated with model formulation.

The prediction of atmospheric blocking is reviewed in detail below as it is at the centre of the work included in this thesis. The ability of numerical weather prediction (NWP) models to forecast blocking during recent decades and its representation in GCMs is presented, and various sources of improvements highlighted, to provide context for the results discussed in subsequent chapters of this thesis.

2.3.1 Blocking

Predicting the occurrence of blocking events accurately is important for society because they can cause extended periods of harsh weather: heat waves during summer and extended cold spells during winter (e.g. Rex, 1951; Trigo et al., 2004), which can lead to severe societal impacts (Kirsch et al., 2012). Because of their stationarity, atmospheric blocking events also have the potential to influence weather in regions downstream of

the block location (e.g. Carrera et al., 2004; Galarneau Jr et al., 2012). The potential consequences of a blocking event, and their frequent appearance in the midlatitudes, has meant that there have been numerous studies assessing the ability of numerical weather prediction and climate models in predicting them. The predicted frequency of blocking during a season, which is crucial for surface weather impacts, has shown to be underestimated in several NWP models and GCMs for many years. Tibaldi and Molteni (1990) performed the first systematic assessment of the operational predictability of blocking in the ECMWF model. They showed that in forecasts from the winters between 1980 and 1987 inclusive blocking frequency is considerably underestimated in the medium range: only about 50% of blocked days in the analysis were forecast at 10 days lead time. In addition, the model tended to predict blocks of shorter duration and a delay in the transition to a blocked state compared to what were observed. Anderson (1993) studied the representation of blocking in the National Meteorological Center's Medium-Range Forecast Model (MRF) and found that there was a lack of blocking in the model climatology. An underestimation of the frequency of blocking during a given period in a given region has become a common finding when considering many models (both NWP and GCMs) across many timescales. Tibaldi et al. (1997) showed that in climate integrations of the ECHAM model (Roeckner et al., 2003) that the frequency of blocking in both the European and Pacific sectors is underpredicted. The underestimation was present at different horizontal resolutions and with different SST boundary conditions. This behaviour was found to be a common feature of many GCMs by D'Andrea et al. (1998). They found that the frequency of blocking was generally underestimated in 15 different GCMs. More recently, Matsueda (2009) analysed the performance of the ensemble prediction systems (EPSs) of 10 different operational NWP centres in predicting blocking in the northern hemisphere winter using data from The International Grand Global Ensemble (TIGGE) archive (Bougeault et al., 2010). They found that whilst most centres could accurately predict the frequency of blocking in winter in forecasts at five days lead time (several centres did still underestimate), many of the centres underestimated the peaks in blocking frequency at nine days lead time. The performance of the EPSs was consistent for blocks occurring in both the Atlantic and Pacific regions.

Another aspect of atmospheric blocking that has been proven to be difficult to predict is the onset of a blocked period. Tibaldi and Molteni (1990) found that the onset of blocking was almost always missed in forecasts of longer than four days in the ECMWF deterministic model. A "reluctance" of the ECMWF, National Meteorological Center

and Japanese Meteorological Agency (JMA) models to transition to a blocked state when forecasts were initialised more than five days prior to block onset was identified by Kimoto et al. (1992) during the winter of 1988/89, though the models were able to maintain a block once it was present in the initial conditions. The introduction of operational ensembles has added to the predictability of block onset. Pelly and Hoskins (2003a) showed that the operational ECMWF-EPS (mean) was more skilful than the deterministic control for all lead times in predicting blocking in the Euro-Atlantic region in a year's worth of forecasts; however the short time period used may affect the results of the study. The ensemble forecast of onset was skilful (when compared to a climatological forecast) out to day 6 whereas the deterministic forecast lost its skill past 3 days lead time. Pelly and Hoskins (2003a) also found that the forecasts were worse in predicting the onset of blocking in the Pacific, perhaps due to the different dominant dynamics triggering onset in the two regions (Nakamura et al., 1997). Matsueda (2009) also found that the prediction of block onset past 7–9 days lead time was uncertain, with only 25–50% of the ensemble frequently predicting the observed block onset at 9 days lead time. Matsueda (2009) found that block onset tended to be more difficult to predict in the Euro-Atlantic region than in the Pacific in medium-range forecasts from 10 operational NWP models, in contrast to Pelly and Hoskins (2003a).

Owing to the persistence and generality of the deficiencies of models in predicting atmospheric blocking, many avenues to improving block representation have been explored. The predicted frequency of blocking tends to improve with increased resolution in both NWP models (Matsueda, 2009) and GCMs (Tibaldi et al., 1997; Anstey et al., 2013; Schiemann et al., 2017) as increased resolution allows for better representation of large-scale variability that has been shown to be important for block dynamics (e.g. Shutts, 1986), though there generally remains an underestimation of block frequency even at high resolutions ($\sim$20 km). Many studies have shown that improving the parameterisation of sub-grid physical processes can also improve the representation of blocking (Palmer et al., 1986; Tibaldi et al., 1997; Jung et al., 2010; Dawson and Palmer, 2015; Pithan et al., 2016). For example, changes to the parameterisations of orographic gravity wave drag (Palmer et al., 1986) and convection (Jung et al., 2010) have been shown to improve block representation, as has adding stochasticity to the physics schemes (Dawson and Palmer, 2015). The error in block representation in a climate model was shown to be largely the result of the model mean bias by Scaife et al. (2010) and Zappa et al. (2014a). Removing the model bias can produce a large improvement in the representation of blocking (Scaife

et al., 2011). The representation of SST in a GCM, in particular the representation of the Gulf Stream SST front, was found to be important for the development of blocking over Europe in O'Reilly et al. (2016). They argue that the Gulf Stream SST gradient enables stronger meridional eddy heat transport in the storm track which results in increased upper–level eddy kinetic energy and the reinforcement of the quasi-stationary jet associated with the block. However, despite years of improvements to model resolution and physical parameterisations, current models still exhibit familiar errors of underestimation of block frequency and duration (Davini and D'Andrea, 2016).

Another approach to studying the predictability of blocking is by considering its inherent sensitivity to initial conditions. As many studies (e.g. Frederiksen, 1989; Frederiksen and Bell, 1990; Kimoto et al., 1992) suggest that there is a close association between instability of the flow, the growth of errors, and dynamical developments. Hence it is common practice to create ensemble forecasts using perturbations to the analysis that represent the fastest growing errors in the initial conditions (Toth and Kalnay, 1993). In this way the ensemble spread should provide an indication of the reliability of the forecasts and the truth should lie within the ensemble spread. Frederiksen et al. (2004) created an ensemble using a breeding method (e.g. Toth and Kalnay, 1993) to study the predictability of blocking regime transitions for forecasts initiated in October and November 1979. On average, the ensemble mean has lower error than the control for lead times longer than three or four days. Frederiksen et al. (2004) related variability in the skill of the forecasts to the instability regimes of particular synoptic events. In particular, the development, maturation and decay of blocking are occasions when forecast skill is reduced, with the highest errors present as early as four days into the forecast for those validating around block onsets/decays. Errors grow rapidly when dynamical development is rapid and are suppressed in the presence of large-scale equivalent barotropic waves such as mature blocks. Frederiksen et al. (2004) showed that forecast error and forecast spread become structurally organised in particular geographical regions and that these regions are focused around block development. All the regions of large ensemble variability were associated with maximum errors in the ensemble mean and the ECMWF analysis and there was a general relationship between spread, forecast variability and the formation of blocking dipoles.

The necessity to be able to forecast blocking accurately was recently highlighted in Rodwell et al. (2013). Looking at occasions when forecasts made with the ERA-I underlying model had very low skill (when a forecast has a large root mean square error

(RMSE) and low anomaly correlation coefficient (ACC) value in Z500) for forecasts over Europe during a 22-year period, they found that the composite Z500 field over all the cases was reminiscent of a dipole-type block over Europe. Rodwell et al. (2013) showed that the forecast error was associated with increased values of convective available potential energy over North-America and a trough over the Rocky Mountains. Considering the same set of forecasts as Rodwell et al. (2013), Lillo and Parsons (2017) used a clustering algorithm to split the forecasts into four subsets based on their six-day forecast evolution over the North Atlantic. Two of their subsets resembled blocking events over the USA and Europe at the time of forecast initiation and the remaining two subsets resembled blocking events at the time of forecast verification, implying that the transition to and from a blocked state can give rise to forecasts with unusually low skill.

The transition to and from a blocked state can also be viewed from the *regime transition* perspective. Weather regimes are used to describe the atmospheric circulation by a small number of recurrent, persistent and quasi-stationary states of the atmosphere (section 2.1). Weather regimes are generally constructed by using EOF analysis (e.g. Kimoto and Ghil, 1993a) or performing clustering algorithms (e.g. Michelangeli et al., 1995) on a circulation variable (commonly Z500). Zonal and blocked flow regimes are consistently identified as weather regimes. Realistic representations of zonal and blocking flow regimes were identified using a nonlinear barotropic model of the atmosphere by Legras and Ghil (1985). Statistics of the transitions between zonal and blocked flow were shown to be highly dependent on initial conditions and model parameters with neither transition robustly more predictable. The variability in response is possibly due to the models spectral truncation and absence of baroclinic processes (Legras and Ghil, 1985). Vautard (1990) constructed weather regimes from a 37-year set of 700 hPa geopotential height observations. The regime transition to a blocked flow was found to be the most rapidly occurring, and tends to succeed a zonal flow regime, and this results in the poor prediction of the transition to blocking. The transition to a blocked flow was shown to have higher than average sensitivity to initial conditions in two theoretical models by Oortwijn (1998), and stronger transitions to a blocked flow are associated with even larger sensitivity. Considering operation daily analyses of Z500 produced by ECMWF covering five extended winter seasons (Ferranti et al., 2015) identified the now commonly used Euro–Atlantic weather regimes: the positive and negative phases of the NAO; European blocking; and an Atlantic ridge regime. They show that among the large-scale weather regime transitions, the transition to a blocked state following a more zonal flow is the

most difficult to predict. The previously mentioned underestimation of blocking bias was present in the forecasts from ECMWF used by Ferranti et al. (2015) as was an overestimation of the persistence of zonal flows. Matsueda and Palmer (2018) examined the flow-dependent forecast skills of a larger set of NWP models using the TIGGE archive for the Euro-Atlantic weather regimes. The forecast performance was generally consistent across models and they suffered from poor forecast performance for the onset and persistence (or decay) of European blocking.

The theories for block onset and maintenance incorporating upstream cyclone activity are studied from a predictability perspective in this thesis. Are the mechanisms proposed in the theories evident in forecasts of atmospheric blocking in operational medium-range weather forecasts and do they provide a possible source of forecast improvement?

2.3.2 Upper-level Rossby waves

The representation of atmospheric blocking is closely related to that of upper-level Rossby waves (a block is a particular part of the hemispheric Rossby wave pattern) (e.g. Austin, 1980; Altenhoff et al., 2008). Errors in forecasts of upper-level Rossby waves should therefore be intimately related to errors in the forecast of atmospheric blocking. Dirren et al. (2003) found an apparent under-estimation of Rossby wave amplitude at tropopause height in forecasts from ECMWF in comparison with the analysis in a single winter season. PV streamers associated with Rossby wave breaking also appeared to be missed in the forecasts (Dirren et al., 2003). The use of PV diagnostics to study the dynamics of error growth was highlighted in Davies and Didone (2013). For a particular case study of forecast error, the predicted under amplification of Rossby waves was linked to both adiabatic effects and large cloud diabatic processes as well as a lack of interaction between lower and upper levels. The under-amplification of the Rossby-wave pattern was preceded by the missforecast of rapid cyclogenesis over the western North Atlantic and followed by the missforecast of Rossby wave breaking and block formation over Europe (Davies and Didone, 2013). Five mechanisms for tropopause-level wave disturbance generation and/or enhancement are proposed by Davies and Didone (2013): large-scale deformation; baroclinic development; lower-stratospheric PV anomaly; PV realignment and unshielding; and deep convection (see Davies and Didone (2013) for more details). Gray et al. (2014) found that upper-level Rossby waves are systematically misrepresented in forecasts from the ECMWF, the Met Office and the National Centre for Environmental

Prediction. The area of ridges in the tropopause and the isentropic gradient in PV across the tropopause in ridges decreases systematically with lead time. Upper-level Rossby wave forecast errors in a case study reminiscent of the systematic error found by Gray et al. (2014) were shown to result from the poor forecast of a WCB in Martínez-Alvarado et al. (2016b). In particular, the modification of θ and PV in the WCB caused the error in Rossby–wave structure. It is important to be able to predict the upper-level flow pattern accurately as the upper-level forcing can induce cyclogenesis (Hoskins et al., 1985) and relatively small errors in the forecast of tropopause level PV features can have a large impact on cyclone representation (Fehlmann and Davies, 1997, 1999).

2.4 Extratropical Cyclones

Much of the focus of the work in this thesis is on the influence extratropical cyclones have on the development and predictability of atmospheric blocking. In this section, an introduction to the structure and development mechanisms of extratropical cyclones is presented. Features of extratropical cyclone dynamics that are known to be important for upper-level flow development and downstream impact are highlighted.

The weather in the midlatitudes is influenced by the passage of cyclones and anticyclones. Cyclones and their associated fronts bring wet and windy conditions whilst conditions are more settled and clear when an anticyclone dominates. Cyclones, or extratropical cyclones as they are often referred to when in the midlatitudes, frequently develop over the oceanic basins and pass over the oceans and across continents steered by the background westerly wind. They transfer considerable heat, moisture and momentum towards the poles (e.g. Holton and Hakim, 2012) and hence are an important feature of the global atmospheric circulation. The structure and typical development of extratropical cyclones have therefore been of great interest to meteorologists for many decades. The Norwegian (Bjerknes, 1922) and Shapiro-Keyser (Shapiro and Keyser, 1990) models are the most famous conceptual models of extratropical cyclone dynamics. The regions where extratropical cyclone activity is most frequent (measured for example by cyclone tracking methods or fields of eddy variance) are termed storm tracks. There are two main storm tracks in the northern hemisphere winter: the Atlantic and Pacific (e.g. Hoskins and Hodges, 2019). Starting at the western edges of the oceanic basins, where cyclones typically form due to strong temperature gradients, and ending east at the continental edges the storm tracks represent an average path of an extratropical cyclone through its

lifecycle.

The typical structure of a mature extratropical cyclone is first described to identify their important features. Development mechanisms for extratropical cyclones are then presented with sections highlighting the role of diabatic processes and the influence of cyclones on the upper–level flow as these are the key mechanisms linking cyclones and atmospheric blocking (the link explored throughout the thesis). The representation of extratropical cyclones in NWP models is briefly reviewed to conclude this section.

2.4.1 Structure

The structure of extratropical cyclones is well known. Numerous studies have attempted to generalise the properties and airflows within extratropical cyclones (e.g. Bjerknes, 1922; Neiman and Shapiro, 1993; Browning and Roberts, 1994). The main features and airflows of a mature extratropical cyclone are summarised as follows and depicted schematically in Figure 2.4 (in a system-relative framework):

- Fronts: an extratropical cyclone has a surface warm front ahead of its direction of motion and a cold front trailing behind the cyclone. In the Shapiro–Keyser model the warm front bends back around the cyclone centre. An occluded front can form in a cyclone near its centre if the cold front catches up with the warm front, and the warm air is lifted above the surface at the cyclone centre.

- Warm conveyor belt (WCB): a warm, moist airflow that travels polewards and upwards ahead of the cold front in the warm sector of the cyclone (Browning, 1971; Harrold, 1973). The WCB transports heat and moisture towards the poles and is often the main cloud and rain-producing flow within the cyclone (Browning, 1990; Pfahl et al., 2014). The WCB has two branches: one anticyclonically turning into the downstream ridge (upper branch) and the other turning cyclonically (lower branch) around the cyclone centre (Browning and Roberts, 1994). Madonna et al. (2014) constructed a climatology of WCBs in ERA-I from 1979 to 2010. WCBs occur more frequently during winter than in summer and typically ascend in the western oceanic basins between 25° and 50° latitude.

- Cold conveyor belt: a characteristically cold air flow that is strongly rearward, relative to the system motion, on the poleward side of the warm front in the lower troposphere (Carlson, 1980; Schultz, 2001).

- Dry intrusion: a stream of dry air descending from the lower stratosphere and upper troposphere in a tropopause fold and down to the cyclone centre.
- Cloud head: a comma-shaped cloud feature extending polewards around the cyclone centre, formed mostly by the ascending air in the WCB as it moves over the warm front and the cold conveyor belt.
- Frontal fracture zone: region in a Shapiro–Keyser type cyclone where there is a horizontal break in the continuous thermal front near the centre of the cyclone (Shapiro and Keyser, 1990); this zone forms when the cyclone has intensified.
- Sting jet: a narrow region of strong low-level winds caused by air descending from the cloud head tip into the frontal fracture zone between the bent-back front and the cold front (Browning, 2004). Note that sting jets exist only in a fraction of extratropical cyclones that intensify according to the Shapiro–Keyser model.

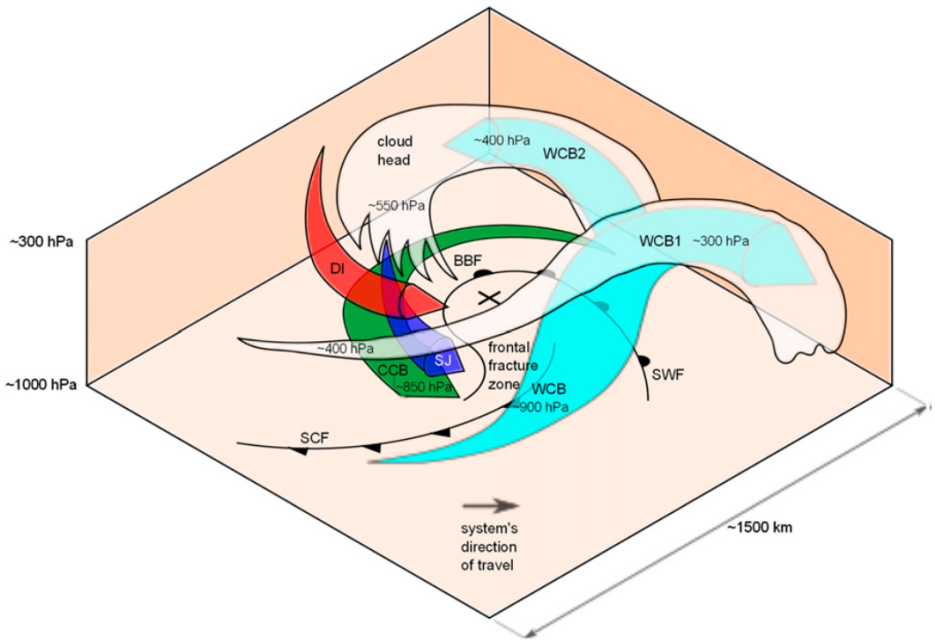

Figure 2.4: The structure of a Northern Hemisphere Shapiro–Keyser cyclone in development stage 3: surface cold front (SCF); surface warm front (SWF); bent-back front (BBF); cold conveyor belt (CCB); sting jet airstream (SJ); dry intrusion (DI); warm conveyor belt (WCB); WCB anticyclonic branch (WCB1); WCB cyclonic branch (WCB2); and the large × represents the cyclone center at the surface, and the gray shading represents cloud top. From Martínez-Alvarado et al. (2014).

The characteristic features of extratropical cyclones described above are useful when evaluating simulations and predictability of extratropical cyclones.

2.4.2 Development

The structural description of an extratropical cyclone of the previous section is given for a cyclone at its mature stage. The typical low-level development of a cyclone can be well described by the Norwegian (Bjerknes, 1922) and Shaprio-Keyser (Shapiro and Keyser, 1990) conceptual models, as many of the features of the models are broadly comparable to those seen in studies of real extratropical cyclones (e.g. Neiman and Shapiro, 1993; Schultz et al., 1998). Cyclones in the real world typically lie somewhere in between the two models and many observed cases of cyclogenesis exhibit significant differences to both models. This is to be expected as they are conceptual, and hence simplifications of the complex reality, and are designed to represent only the key features and processes. The proposal of the Norwegian model by Bjerknes and colleagues is one of the most fundamental breakthroughs in modern meteorology. It describes the development of an extratropical cyclone in three–four stages (Fig 2.5(a)): I) the incipient phase, II) and III) the warm-sector narrowing phase (the cold front moves east faster than the warm front) and eventually catches up, and IV) the occluded phase where the cold front lifts the warm air in the warm front above the Earth's surface. The Norwegian model was found to have certain limitations (e.g Browning, 1990), particularly for rapidly developing cyclones, which led to the development of another conceptual model. The Shapiro-Keyser model splits the development of extratropical cyclones into four phases: I) incipient frontal cyclone, II) frontal fracture, III) frontal T bone and bent back front, and IV) warm-core seclusion. These stages are depicted schematically in Figure 2.5.

Many observed cases of cyclogenesis exhibit similar development stages to those described in the Norwegian and Shapiro-Keyser conceptual models. The mechanisms responsible for the development of extratropical cyclones are also well understood. Extratropical cyclones develop frequently in the atmosphere due to processes associated with baroclinic instability (Hoskins and Valdes, 1990). Barotropic and baroclinic instabilities are prevalent in the atmosphere. An atmosphere is barotropic if the density depends only on pressure and baroclinic if the density depends on pressure and temperature. Perturbations grow due to barotropic instability by extracting kinetic energy from the jet and are associated with horizontal shear of the jet. Baroclinic instability, on the other hand, is associated with vertical shear. Perturbation growth occurs due to the conversion of potential energy associated with the mean horizontal temperature gradient and the vertical shear arising from thermal wind balance. Storm track entrances are regions of strong baro-

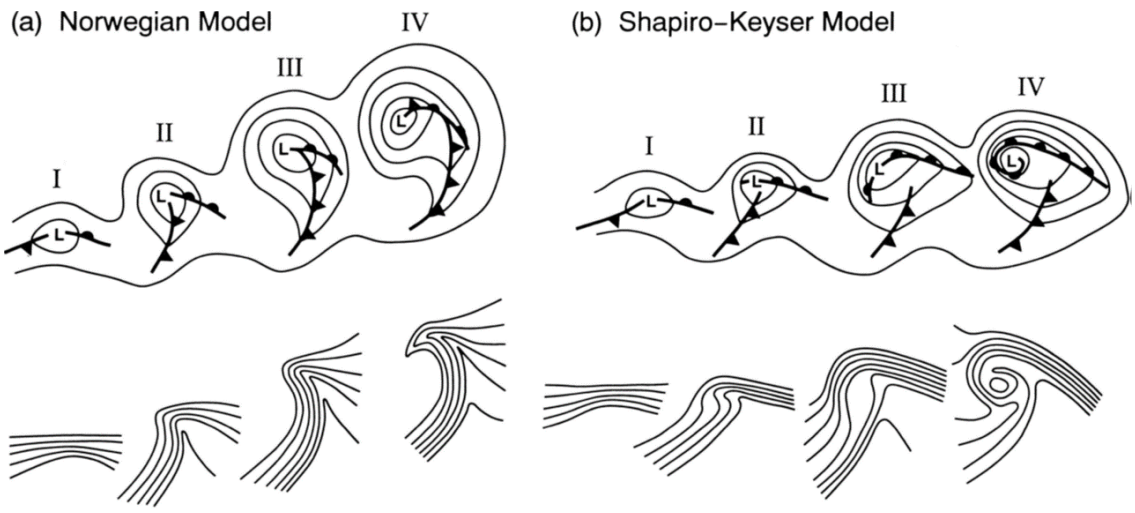

Figure 2.5: Conceptual model of the lifecycle of an extratropical cyclone: (I) incipient frontal cyclone, (II) frontal fracture, (III) bent-back front and frontal T-bone, and (IV) warm-core frontal seclusion. Diagram: sea-level pressure, full lines; fronts, bold lines (upper); lower–tropospheric θ (bottom). From Schultz et al. (1998).

clinicity: strong temperature gradients at the western edges of the oceans produced by the warm western boundary currents and land–sea contrast create vertical shear through thermal wind balance and reduced static stability through ocean–atmosphere moisture fluxes. These conditions are favourable for cyclogenesis (they form the start of the storm tracks).

Analytical models also exist for baroclinic cyclogenesis: the near exponential growth of an initially small amplitude perturbation (baroclinic wave, or cyclone) on a baroclinically-unstable background state (Charney, 1947; Eady, 1949). The Charney (1947) and Eady (1949) models are similar but with a slightly modified background state (f-plane and β-plane, respectively). Though they are limited to dry, inviscid motion, the Eady and Charney models do a remarkable job of predicting the observed growth rate and wavelength of developing cyclones even when they have grown beyond the small amplitude of which they are assumed to be in the theories. Baroclinic disturbances are observed frequently in the real atmosphere (the atmosphere is highly baroclinically unstable). Eady (1949) provide a maximum growth rate for baroclinic disturbances equal to $0.31(f/N)(\partial\bar{u}/\partial z)$, where f is the Coriolis parameter, N the Brunt-Väisälä frequency, and $\bar{u}$ the background zonal wind speed, which tends to be highest in observed cyclogenesis regions (Hoskins and Valdes, 1990; Hoskins and Hodges, 2002a).

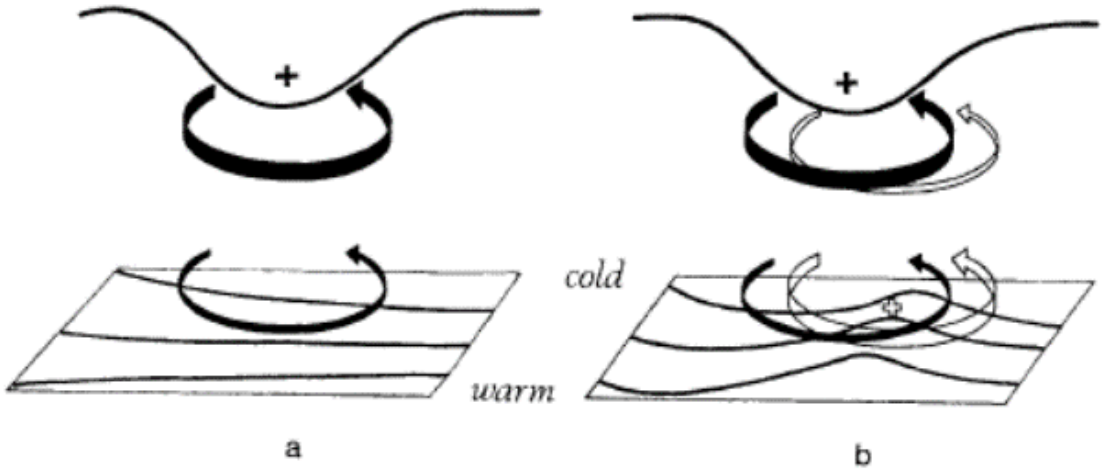

Figure 2.6: A schematic picture of cyclogenesis associated with the arrival of an upper air isentropic PV (IPV) anomaly over a low-level baroclinic region. In (a) the upper air cyclonic IPV anomaly, indicated by a solid plus sign and associated with the low tropopause shown, has just arrived over a region of significant low-level baroclinicity . The circulation induced by the anomaly is indicated by solid arrows, and potential temperature contours are shown on the ground. The low-level circulation is shown above the ground for clarity. The advection by this circulation leads to a warm temperature anomaly somewhat ahead of the upper IPV anomaly as indicated in (b), and marked with an open plus sign. This warm anomaly induces the cyclonic circulation indicated by the open arrows in (b). If the equatorward motion at upper levels advects high-PV polar lower-stratospheric air, and the poleward motion advects low-PV subtropical upper-tropospheric air, then the action of the upper-level circulation induced by the surface potential temperature anomaly will, in effect, reinforce the upper air IPV anomaly and slow down its eastward progression. From Hoskins et al. (1985)

The PV framework has been widely used in the study of extratropical cyclogenesis and dynamics. The principle of invertibility allows us to diagnose the flow induced by a PV anomaly of interest, e.g. a cyclone or a PV anomaly produced by a process within a cyclone. Large-scale gradients in PV support Rossby waves which can be conceptualised as waves in PV and are the fundamental phenomena behind extratropical weather systems. Baroclinic instability can be described by considering upper-level PV features and lower-tropospheric PV and surface θ features interacting with each other. A schematic representing this processes is shown in Figure 2.6. First, consider an upper–level Rossby-wave trough (positive PV anomaly) moving over a surface baroclinic zone (region of strong horizontal temperature gradient). As the upper-level perturbation moves over surface baroclinic zone, PV thinking and action at a distance implies a cyclonic circulation is induced at lower levels by the upper–level feature (Fig 2.6a). This circulation triggers a perturbation at the surface baroclinic front slightly ahead of the upper-level anomaly,

and hence a warm anomaly with its own associated cyclonic circulation is formed. The two circulations mutually reinforce one another (Fig 2.6a) and growth occurs whilst the suitable phase shift of the two PV elements remains (Hoskins et al., 1985). Stronger background winds at upper levels eventually result in the upper-level feature catching up with the surface feature and a breakdown of the feedback mechanism.

The PV framework can be used to describe completely the development of extratropical cyclone development assuming that they are in some kind of balance (which is approximately true for most weather systems (Hoskins et al., 1985; Hoskins and Berrisford, 1988)) and that diabatic and frictional effects are minimal. In the real atmosphere diabatic processes within extratropical cyclones can have a large effect on their development.

2.4.3 Diabatic processes

Diabatic processes in extratropical cyclones, especially latent heating caused by condensation when clouds and precipitation form, can influence their development and can again be understood from a PV-perspective. Returning to the PV tendency equation,

$$\frac{DPV}{Dt} = \frac{1}{\rho}\left[\boldsymbol{\zeta}\cdot\nabla\left(\frac{D\theta}{Dt}\right) + \nabla\theta\cdot\nabla\times\mathbf{F}\right], \tag{2.3}$$

the change in PV associated with latent heating can be calculated. Figure 2.7 shows the tendency in PV resulting from an instantaneous heating (Fig. 2.7a) and the response from a steady source of heating (Fig. 2.7b). PV is created below the region of maximum heating ($\frac{\partial}{\partial z}(D\theta/Dt) > 0$) and destroyed above it. Advection associated with the heating results in a steady-state PV tendency as depicted in (Fig. 2.7b). Equation 2.3 can also be used to quantify the diabatic effect on extratropical cyclone evolution.

The non–conservation of PV can be utilised to diagnose occasions when diabatic or frictional processes are important for cyclone development. The direct effect on the flow can be measured using the invertibility property. Davis and Emanuel (1991) described a diagnostic method based on the conservation and invertibility of PV and used it to diagnose the development of a cyclone from different sources of anomalous PV (upper/lower level). Condensation appeared to produce the low–level positive PV anomaly in their case study that directly acted to increase low–level circulation and advect θ on the tropopause. The low-level feature eventually contributed about 40% of the cyclonic circulation of the cyclone. A favourable phasing between the low-level thermal wave with an upper-level PV

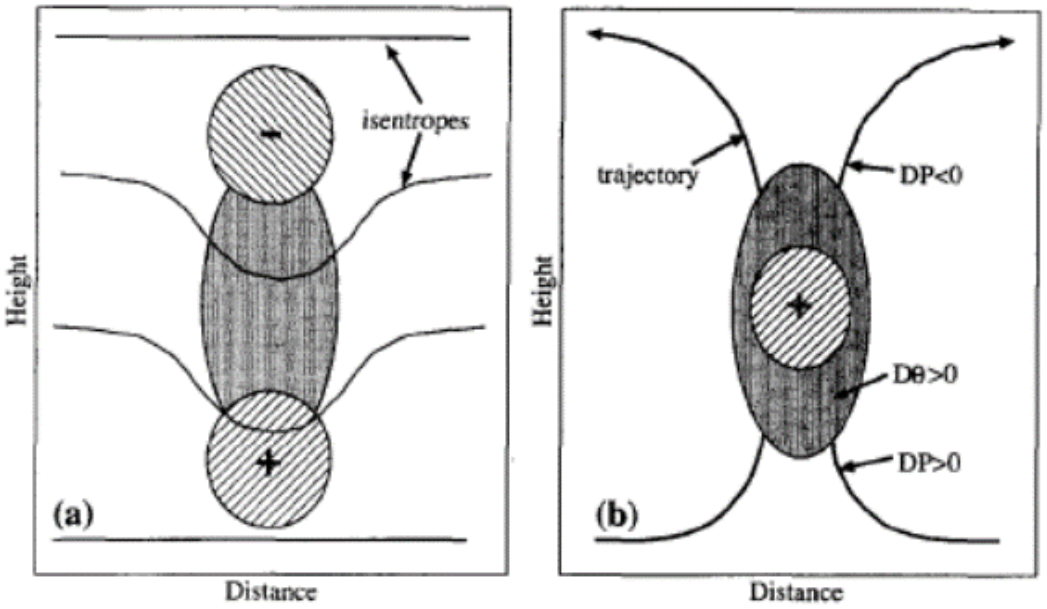

Figure 2.7: Schematic vertical cross-sections showing diabatically produced PV anomalies (hatched regions with a plus or minus sign) for the idealized cases of (a) 'impulsive diabatic heating', and (b) 'steady condensation' in a frontal zone. Shading indicates the region of diabatic heating. In (a) the solid lines are isentropes and in (b) the bold lines with arrows refer to air-parcel trajectories. Dθ and DP denote material tendencies of potential temperature and PV, respectively. From Wernli and Davies (1997)

disturbance occurred during the period of rapid intensification, resembling the schematic mutual reinforcement of Rossby edge waves (Fig. 2.6). Latent-heat release increases the growth rate of baroclinic instabilities (e.g. Kuo et al., 1991; Stoelinga, 1996) and decreases the horizontal scale of the ascent region Kuo et al. (1991). Latent heating can also act to maintain the favourable phase shift between the upper- and lower-level PV anomalies, by slowing the eastward propagation of the upper-level wave (Stoelinga, 1996). Strong ascent in WCBs also causes latent heat release and the modification of PV along WCB trajectories (Wernli, 1997). The reduction of PV above the region of heating can also have an impact on cyclone development (Pomroy and Thorpe, 2000). Using a PV inversion technique, Pomroy and Thorpe (2000) found that the upper-level reduction in PV in a case study of a cyclone weakened the cyclone development. The relative influence of the different PV anomalies associated with cyclogenesis can change from case to case. Cyclogenesis can occur in diabatic Rossby-wave type cases, where a condensation-produced, low-level positive PV anomaly is the main driver of a cyclone, which then interacts with a strong upper-level jet (Wernli et al., 2002). Cases are also common when the contribution to the cyclonic circulation from the surface thermal anomaly is minimal and

the cyclonic intensification is the result of an interaction between a pre-existing upper-level PV anomaly and a diabatically produced mid-level PV anomaly (Plant et al., 2003; Ahmadi-Givi et al., 2004).

2.4.4 Influence on upper-level flow

Extratropical cyclones are known to have a strong impact on the upper-level Rossby wave pattern though the modification of PV near tropopause level (Wernli and Davies, 1997; Pomroy and Thorpe, 2000). Extratropical cyclone influence on block development was discussed in section 2.2.3.1. Diabatic processes embedded in cyclones modify the PV structure near the tropopause (Davis et al., 1993; Ahmadi-Givi et al., 2004; Chagnon et al., 2013) and moist processes can also be essential for realising highly amplified upper-level flow downstream (Grams et al., 2011; Grams and Archambault, 2016). The main feature of extratropical cyclones modifying PV at the tropopause are WCBs (Stoelinga, 1996; Wernli and Davies, 1997). WCBs in extratropical cyclones transport low-valued PV air from low levels to the tropopause level, with WCBs reaching the upper troposphere with PV values roughly equal to that of the inflow air (Methven, 2015) at around 0.5 PVU (Madonna et al., 2014). This can impact the downstream Rossby wave pattern (Joos and Forbes, 2016), particularly in the amplification of ridges (Grams et al., 2011; Archambault et al., 2013), and implies that PV modification in WCBs of extratropical cyclones could be an important mechanism in block development. The development of ridges is particularly affected by the PV destruction above the region of maximum heating in a cyclones WCB. The negative tendency above the region of maximum heating acts to enhance downstream ridges via increased upper-level divergence (Stoelinga, 1996; Pomroy and Thorpe, 2000; Tamarin and Kaspi, 2016). PV modification by diabatic processes also occurs in WCBs (Joos and Wernli, 2012) which in turn suggests diabatic processes could play an important role on block development (Pfahl et al., 2015).

2.4.5 Extratropical cyclones in NWP models

Forecasting extratropical cyclones accurately at the longest possible lead times is necessary because of the heavy rain and damaging winds they can bring to a region (e.g. Buizza and Hollingsworth, 2002) and the large impact this can have on society (Fink et al., 2009; Haylock, 2011). Present day forecasts of synoptic-scale cyclones are reasonably accurate in the short range (e.g. Jung et al., 2006; Walters et al., 2017b),

though forecasting their tracks and intensity at longer lead times is still a challenge (Frame et al., 2015). The forecast of both cyclone track and intensity was found to be generally consistent across ten different NWP centres by Froude (2010) for a six–month period during 2008, though ensembles with lower resolution tended to underestimate the intensity of cyclones and exhibit less ensemble spread. Good horizontal and vertical resolution is necessary to capture the tilt with height in baroclinically developing systems. Cyclone intensification can be incorrectly represented in NWP models because of incorrect coupling between surface and upper-level anomalies (Boettcher and Wernli, 2011). Forecast error can also develop in the representation of the small–scale features within cyclones that can arise from subgrid processes and are hence parameterised (e.g. Ehrendorfer, 1997); these subgrid scale processes are important because they can influence the development of cyclone features (Forbes and Clark, 2003). Increasing horizontal resolution (Jung et al., 2006), better representation of surface fluxes associated with air-sea coupling (Davis and Emanuel, 1988), and improving parameterisations to subgrid processes (Jung et al., 2010) have all been shown to be sources of improvement for forecasts of extratropical cyclones.

Parameterised diabatic processes in simulations of extratropical cyclones can enhance the tropopause-level PV gradient (Chagnon et al., 2013) with negative diabatically produced PV below the tropopause and positive diabatically produced PV above. The parameterisation of longwave radiation, which arises from long–wave cooling at the tropopause (where the humidity falls quickly), generates most of the positive diabatically-produced PV on the stratospheric side of the tropopause. The negative diabatically produced PV below the tropopause is also produced by the long–wave radiation scheme (below the location of the cooling) as well as the convection, large-scale cloud and boundary layer schemes. Chagnon et al. (2013) show that the negative PV is produced by the outflow of the WCB having ascended above the maximum latent heat release region in the mid–troposphere. Parameterised diabatic processes can themselves alter the modification of PV in the WCB (Joos and Wernli, 2012). The same dipole of diabatically-produced PV in three additional simulated extratropical cyclones was found by Chagnon and Gray (2015). Dynamical cores within NWP models can also alter the PV structure near the tropopause, typically smoothing the gradient in PV across the tropopause as they include diffusion (either explicit or implicit) (Gray et al., 2014; Saffin et al., 2016).

The representation of diabatic processes in a NWP model was also shown to be responsible for the forecast under-amplification of a large-amplitude ridge by (Martínez-Alvarado et al., 2016b). In their case study, the WCB in the forecast was too intense

and the outflow located too far south, resulting in an underestimation of the magnitude of the negative PV anomaly in the outflow and subsequent underdeveloped ridge. Martínez-Alvarado et al. (2016b) showed that the error was generally consistent among the ensemble, implying that model error (uncertainty in model formulation) played a large role in this forecast error. WCBs in recent versions of the ECMWF-EPS were shown to not be systematically misrepresented by Madonna et al. (2015), though individual forecasts can show large errors in the location, amplitude and anomalous-PV value of WCBs. The representation of WCBs in NWP models can also be sensitive to the parameterisation of convection (Martínez-Alvarado and Plant, 2014). Operational improvements to parameterisations of diabatic processes in the ECMWF-EPS were shown to change the location of the WCB of an extratropical cyclone and the subsequent development of an upper-level ridge (Joos and Forbes, 2016), again suggesting that the parameterisation of diabatic processes in (WCBs of) extratropical cyclones may be key for the downstream development of blocking.

2.5 Summary

The literature included in this section provides the necessary background to interpret the analysis presented in the remainder of the thesis. Two main ideas were described in detail in various parts of the literature review. First, it was emphasised that the medium–range forecast of atmospheric blocking has been a long–standing issue for many NWP centres and that there is evidence that extratropical cyclones are closely linked to many aspects of block dynamics. Secondly, it was highlighted that model error can be an important source of forecast error in the representation of extratropical cyclones, the upper–level Rossby wave pattern and atmospheric blocking. Diabatic processes were shown to be key in both of these areas. The work included in the following chapters of this thesis aims to further clarify these by investigating the relationships between extratropical cyclones, upper–level Rossby waves and blocks in forecasts from operational NWP centres and quantifying the potential increase in forecast skill gained by reducing model errors.

Chapter 3:

Atmospheric blocking and upper-level Rossby wave forecast skill dependence on model configuration

As described in chapter 2, predicting atmospheric blocking events has been a challenge in medium-range forecasts for many years, particularly predicting the onset of a blocked flow (e.g. Tibaldi and Molteni, 1990; Pelly and Hoskins, 2003a). Predicting atmospheric blocking events accurately is important because of the strong influence they can have on the weather both locally and in regions downstream. Improvements weather forecast models, for example to their parameterisations, have been shown to improve the prediction of atmospheric blocking events (Jung et al., 2010; Pithan et al., 2016) which suggests improvements to other components of the model may also be beneficial for block forecasts. An improvement to a model's dynamical core and its impact on the forecast of atmospheric blocking and upper-level Rossby waves is the focus of this chapter. Atmospheric blocking events are closely linked to the upper-level Rossby wave pattern (Altenhoff et al., 2008) which has been shown to be systematically misrepresented in forecasts (Gray et al., 2014).

This chapter has been published in the Quarterly Journal of the Royal Meteorological Society (Martínez-Alvarado et al., 2018).

3.1 Abstract

Weather models differ in their ability to forecast, at medium range, atmospheric blocking and the associated structure of upper-level Rossby waves. Here, we evaluate the effect of a model's dynamical core on such forecasts. Operational forecasts from the ensemble prediction systems (EPSs) of the European Centre for Medium-range Weather Forecasts (ECMWF), the Met Office (MO) and the Korean Meteorological Administration (KMA) are used. Northern hemisphere model output is analysed from winters before and after a major upgrade to the dynamical core of the MO-EPS. The KMA-EPS acts as a control as it uses the same model as the MO-EPS, but used the older dynamical core throughout. The confounding factor of resolution differences between the MO-EPS and the KMA-EPS is assessed using a MO forecast model hindcast experiment with the more recent dynamical core, but the operational resolution of the KMA-EPS. The introduction of the new dynamical core in the MO-EPS has led to increased forecast blocking frequency, at lead times of five and seven days, counteracting the typically-observed reduction in blocking frequency with lead time. Hit rates of blocking activity, onset and decay are also increased in the main blocking regions (without a corresponding increase in false positive rate). The previously-found reduction of upper-level ridge area and tropopause sharpness (measured by isentropic potential vorticity gradient) with lead time is also reduced with the new dynamical core. This dynamical core improvement (associated with a reduction in implicit damping) is thus demonstrated to be at least as effective as operational resolution improvements in improving forecasts of upper-level Rossby waves and associated blocking.

3.2 Introduction

Atmospheric blocks are nearly stationary large-scale weather patterns that effectively redirect (or block) mobile cyclones. They are often associated with a large-amplitude, synoptic-scale, quasi-stationary anticyclone in the extratropics. This phenomenon has a strong influence on mid-latitude weather as it can lead to high-impact weather events, locally and downstream, due to its scale and persistence. Despite its importance, atmospheric blocking remains difficult to represent in weather and climate models. For example, Schiemann et al. (2017) showed that even though the representation of Euro-Atlantic blocking tends to improve with resolution, models still exhibit large biases, tending to underestimate winter northern European blocking even at a relatively fine 25-km grid

spacing. The purpose of this study is to evaluate the impact of a model's dynamical core on its representation of blocking, specifically a change of dynamical core leading to a reduction in implicit damping.

Medium-range forecasts have demonstrated skill in predicting aspects of blocking for more than a decade. For example, Pelly and Hoskins (2003b) found skill in the European Centre for Medium-Range Weather Forecasts (ECMWF) Ensemble Prediction System (EPS) predictions of (instantaneous) blocking and blocking episodes (with persistence of at least four days) out to 10 days over the Euro-Atlantic sector. They also showed that control forecasts remain skilful for block onset relative to climatology until day five of the forecast in the ECMWF-EPS and concluded that onsets are harder to predict than the decay of blocking. After classifying ECMWF-EPS Euro-Atlantic sector forecasts by weather regimes, Ferranti et al. (2015) found that blocking leads to the least accurate forecasts, with an underestimation of blocking persistence and large ensemble spread in forecasts initiating blocking as well as difficulties in the prediction of the transition to blocking (in agreement with Pelly and Hoskins (2003a) and Tibaldi and Molteni (1990)). Matsueda (2009) found that blocking frequency tended to be underestimated by ensemble forecasts from several operational centres beyond a lead time of five days in winters (December–February: DJF) between 2006/07 and 2009/10. Using single-member hindcasts from the NCEP Climate Forecast System version 2, Jia et al. (2014) found skilful forecasts of wintertime blocking activity in the Northern Hemisphere (NH) at lead times up to nine and seven days over the Euro-Atlantic and Pacific sectors, respectively, but less skill in blocking onset and decay.

Upper-level Rossby waves, manifest in the strong potential vorticity (PV) gradient region along the extratropical (dynamical) tropopause, are associated with mid-latitude tropospheric cyclones and anticyclones. Therefore, Rossby waves greatly influence the generation of mid-latitude weather. Through analysis of seven winters from 2006/07–2012/13 in three EPSs, Gray et al. (2014) found systematic forecast errors in the structure of Rossby waves in terms of a reduction in Rossby-wave amplitude and tropopause sharpness with lead time. In agreement with those results, Giannakaki and Martius (2016) found systematic errors in the area and strength of Rossby waveguides, defined as long and narrow bands of strong isentropic PV gradient, in ECMWF forecasts compared to reanalyses. There is a causal relationship between diabatic processes and ridge development (Davis et al., 1993). Latent heat release is known to have an effect on ridge building by advection of low-PV air into the ridge, which enhances the divergent flow at upper

levels (Riemer and Jones, 2010) and 'tropopause uplifting' (Bosart and Lackmann, 1995). Furthermore, it has been shown that the reduction in Rossby-wave amplitude is linked to diabatic processes through errors in forecasts of warm conveyor belts (Martínez-Alvarado et al., 2016b). Harvey et al. (2016) has also shown that the reduction of isentropic PV gradient can be linked to slower eastward propagation of Rossby waves and to a reduction in Rossby-wave amplitude. The correspondence between errors in the structure of Rossby waves (Gray et al., 2014) and those in the structure of Rossby waveguides (Giannakaki and Martius, 2016), and the relationship of the former with warm conveyor belts (Martínez-Alvarado et al., 2016b) suggest that these errors have a direct impact on the synoptic variability of models. However, their impact on the representation of stationary waves is not known.

Atmospheric blocking and the structure of upper-level Rossby waves are not independent of each other. As well as an anomaly in geopotential height, atmospheric blocking can be conceptualised as a negative anomaly in the PV field (Schwierz et al., 2004; Röthlisberger et al., 2016). Negative PV anomalies can, in turn, be viewed as ridges in Rossby-wave structure. The dynamical association between Rossby-wave ridges and the anticyclones that define blocking imply that changes in the numerical representation of Rossby-wave ridges should lead to changes in the representation of atmospheric blocking. Consistent with this relationship, de Vries et al. (2013) found that future changes of seasonal atmospheric blocking activity can be explained by changes in the strength and variance of the mean upper-level zonal circulation.

The Met Office (MO) introduced a new dynamical core into its operational weather forecast model (the Unified Model: MetUM) in 2014. The new dynamical core is characterised by a reduction in implicit damping with respect to its predecessor. It has been previously shown that the reduced implicit damping has increased extratropical atmospheric variability in the model as measured, for example, by eddy kinetic energy (Walters et al., 2014, 2017b). Consistent with the increase in eddy kinetic energy, the new dynamical core has removed a detected loss in extratropical cyclone intensity with forecast lead time in models based on the previous core (Walters et al., 2017b). Mid-latitude cyclones and jets are more intense with the new dynamical core and, occasionally, too intense in comparison with corresponding analyses (Mittermaier et al., 2016; Walters et al., 2017b).

The MetUM dynamical core upgrade and the availability of The International Grand Global Ensemble (TIGGE, Bougeault et al., 2010), which is an archive of operational forecasts from several forecast centres including the Met Office from 2006 to date, provides an

opportunity to study the effects of the improved representation of extratropical variability and cyclone intensity on large-scale circulation features, using ensemble forecasts from other operational centres as control cases. In this study we focus on atmospheric blocking and the structure of upper-level Rossby waves. Thus, this article aims at answering the following questions: does a reduction in implicit damping in a model's dynamical core change the representation of atmospheric blocking and upper-level Rossby waves? If so, are these changes consistent with the known dynamical link between the two features?

The rest of the article is organised as follows. A description of the new dynamical core features in the MetUM is given in Section 3.3. The data and methodology are presented in Section 3.4. The results are presented as two linked studies: (i) an analysis of atmospheric blocking in EPSs (presented in Section 3.5) and (ii) an analysis of upper-level Rossby waves in EPSs (presented in Section 3.6). Section 3.7 summarises and concludes this work.

3.3 The MetUM dynamical cores

The *NewDynamics* dynamical core (Davies et al., 2005) of the Met Office Unified Model (MetUM) was upgraded to the *ENDGame* (Even Newer Dynamics for General atmospheric modelling of the environment) dynamical core (Wood et al., 2014) in July 2014. Both the NewDynamics and ENDGame dynamical cores use a finite-difference discretisation of the non-hydrostatic deep-atmosphere dynamical equations with semi-implicit, semi-Lagrangian integration schemes (Walters et al., 2017b). Moreover, both cores use Arakawa C-grid staggering in the horizontal (Arakawa and Lamb, 1977) and are terrain-following with a hybrid-height Charney–Phillips (Charney and Phillips, 1953) vertical staggering. The following are the differences between the two cores:

- ENDGame introduces a nested iterative approach for each atmospheric time step reducing the need for off-centring (time weights) used in the calculation of the departure point in the semi-Lagrangian scheme (see e.g. Shutts and Vosper, 2011).
- The special treatment of potential temperature and the continuity equation in New-Dynamics are abandoned for a full semi-Lagrangian discretisation of all prognostic variables in ENDGame.
- The horizontal staggering of variables has been modified in ENDGame to avoid solving the Helmholtz equation at the poles.

- The explicit horizontal and targeted diffusion used in NewDynamics are no longer required in ENDGame.

The introduction of ENDGame, together with improvement to physical parametrizations and increased resolution, compromises the Global Atmosphere 6 (GA6) configuration of the MetUM. Full details on the GA6 configuration and the differences between ENDGame and NewDynamics can be found in Walters et al. (2017b). As discussed in that paper, these changes in the MetUM have improved the accuracy, scalability and numerical stability of the model. The improvement in extratropical circulation with the GA6 configuration seen in Walters et al. (2017b) was attributed to the reduced implicit damping with the ENDGame dynamical core rather than a result of physical parametrization improvements.

3.4 Data and methodology

The operational forecasts used and a bespoke MetUM simulation are presented in Section 3.4.1, and the diagnostics used to assess atmospheric blocking and the structure of Rossby waves are presented in Section 3.4.

3.4.1 Model forecast data

3.4.1.1 Operational forecasts

The present study focuses on four winters, DJF 2012/13–2015/16, motivated by the introduction of ENDGame into the operational version of the Global configuration of the Met Office Global Ensemble Prediction System (MOGREPS-G) (Bowler et al., 2008, 2009; Tennant et al., 2011; Williams et al., 2015) in July 2014. This choice spans two winters before and two winters after the introduction of ENDGame; these periods are hereafter referred to as the NewDynamics and ENDGame eras, respectively

Daily 1200 UTC data from three operational EPSs, namely MOGREPS (Bowler et al., 2008, 2009; Tennant et al., 2011; Williams et al., 2015), the ECMWF EPS (Molteni et al., 1996; Buizza et al., 1999), and the KMA-EPS, are used for both studies (blocking and upper-level Rossby waves). The KMA-EPS is included because its underlying numerical model is the MetUM with NewDynamics throughout the period of analysis; this offers an opportunity to compare the two dynamical cores in operational setups. A comparison between the configuration of the three EPSs in terms of horizontal and vertical resolution and the generation of initial ensemble perturbations is presented in Table 3.1.

Table 3.1: Configurations of the ECMWF-EPS (EC), MOGREPS (MO) and the KMA-EPS (KMA) during the four winter seasons under analysis where 4D Var is four-dimensional variational data assimilation, SV is singular vectors, EDA is ensemble of data assimilations and ETKF is ensemble transform Kalman filter.

Season	Horizontal resolution (zonal grid spacing at 50°N)			#vertical levels (top of model)			Initial perturbation method (data assimilation method)			#ensemble members			Length of forecasts available (days)		
	EC	MO	KMA	EC	MO	KMA	EC	MO	KMA	EC	MO	KMA	EC	MO	KMA
2012/13	T639 (N320) (40 km)	N216 (60 km)	N320 (40 km)	62 ($\approx$ 35 km)	70 (80 km)	70 (80 km)	SV and EDA (4D Var)	ETKF (Hybrid 4D Var)	ETKF (4D Var)	50	23	23	15	15	10
2013/14					85 (85 km)				ETKF (Hybrid 4D Var)						
2014/15		N400 (32 km)		91 ($\approx$ 75 km)	70 (80 km)						11		15	7	
2015/16															

The data were obtained from the TIGGE archive (Park et al., 2008). Geopotential height at 500 hPa (Z_{500}) interpolated onto a regular 2.5° grid is used in the study of atmospheric blocking. PV on the 320-K isentropic surface interpolated onto a regular 1° grid is used in the study of Rossby-wave structure; this particular isentropic surface is often used for the study of Rossby-wave structure and is chosen here because it is the only isentropic surface for which PV is available in the TIGGE archive. Tests using a regular 1° grid (instead of the regular 2.5° grid) for the study of atmospheric blocking showed that the conclusions are not sensitive to the grid resolution within this range (not shown) and the coarser resolution data were used for computational speed.

3.4.1.2 MetUM experiment

Differences in the representation of atmospheric blocking and upper-level Rossby waves are likely to be affected by differences in resolution as well as differences in the dynamical core. To determine the impact of this confounding factor on the comparison of forecasts from MOGREPS and the KMA-EPS, a single-member MetUM run (hereafter ENDGame-RERUN) was performed for the winter 2013/14 with ENDGame and the associated physical parametrization package at a horizontal resolution of N320 (the same resolution as used by the KMA-EPS) and 70 vertical levels (with model top at 80 km). Forecasts were initiated from the Met Office analyses of the day. The output of this run is compared to the operational control-member forecasts from MOGREPS and the KMA-EPS which were both produced using the NewDynamics dynamical core; the resolution of the ENDGame-RERUN is the same as that used by the KMA-EPS and higher than that used by MOGREPS, allowing a relatively clean diagnosis of the relative roles of resolution and dynamical core differences in the atmospheric evolution.

3.4.2 Diagnostic methods

3.4.2.1 Atmospheric blocking

The blocking index proposed by D'Andrea et al. (1998) is used in this study, following Matsueda (2009). This index is one-dimensional, instantaneous (no persistence criteria) and based on the meridional gradients of Z_{500}. Whilst this is a simple index and has several limitations, it is known to be capable of identifying basic blocking features (Barriopedro et al., 2010) and is sufficient for a forecast/reanalysis comparison such as this study. The gradient to the south (GHGS) and north (GHGN) of a central latitude are defined as

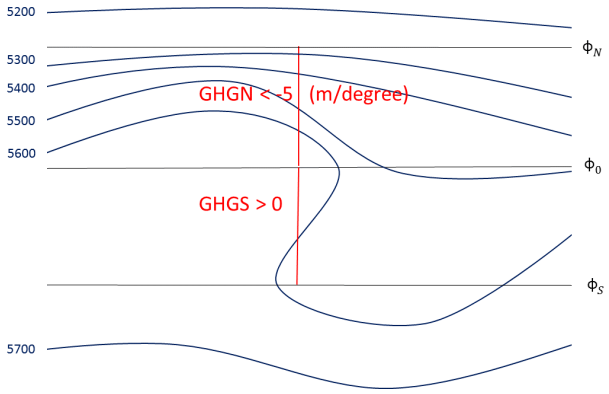

Figure 3.1: The typical configuration of Z_{500} contours (m) during a blocking event. The red line represents a blocked longitude. The quantities ϕ_n, ϕ_0 and ϕ_s as well as GHGN and GHGS are defined in the text.

follows:

$$\begin{aligned} GHGS &= \frac{Z_{500}(\phi_0) - Z_{500}(\phi_s)}{\phi_0 - \phi_s}, \\ GHGN &= \frac{Z_{500}(\phi_n) - Z_{500}(\phi_0)}{\phi_n - \phi_0}, \end{aligned} \tag{3.1}$$

where $\phi_n = 77.5°\text{N} \pm \Delta$, $\phi_0 = 60°\text{N} \pm \Delta$, $\phi_s = 40°\text{N} \pm \Delta$, and $\Delta = 0°, 2.5°, 5°$. These Δ values were chosen because the data are interpolated onto a 2.5° grid following Matsueda (2009). The same Δ is used for ϕ_n, ϕ_0 and ϕ_s.

A specific longitude is defined as blocked if (for at least one value of the same Δ) both

$$GHGS > 0, \tag{3.2}$$

and

$$GHGN < -5 \text{ m } (°)^{-1}. \tag{3.3}$$

Figure 3.1 illustrates an example Z_{500} field that satisfies these conditions. The first condition (3.2) ensures easterly flow to the south of a central blocked latitude, ϕ_0, while the second (3.3) ensures strong westerly flow to the north. Several studies (e.g. Lejenäs and Okland, 1983) provide evidence that these conditions are suitable for identifying the characteristics of a blocked situation.

The regions that are most prone to blocking are defined similarly to Matsueda (2009) as the Euro-Atlantic (EA) sector (27.5°W–40°E) and the Pacific (PA) sector (120°E–140°W). To take into account the longitudinal extent of blocking, a sector is then defined as blocked if three or more adjacent longitudinal grid boxes within the sector are blocked

on a specific day (also following Matsueda (2009)). The *onset* date of a blocked sector is defined as the date when the sector transitions from a non-blocked to a blocked state and the *decay* date is the date when the sector becomes non-blocked after having previously been blocked.

Blocking frequency, defined as the fractional number of blocked days in a winter, was computed from the ensemble-mean forecasts from each EPS for the four winters considered and compared to that calculated using the ECMWF interim reanalysis (ERA-I) reanalyses (Dee et al., 2011) as a reference. Lead times of five, seven and nine days were used for comparison with Matsueda (2009), who found that blocking frequency is well forecast up to a lead time of five days and is under-predicted at longer lead times, taking the Japanese 25-year Reanalysis (Onogi et al., 2007) as the reference.

Table 3.2: Contingency table for the hit rate analysis.

		Analysis	
		yes	no
Forecast	yes	A	B
	no	C	D

To assess the ability of forecasts to predict the timing of blocking, hit rate analyses for blocking activity, block onset and block decay were performed for ensemble forecasts at lead times from three to seven days also using ERA-I as the reference. The hit rate, H, and false positive rate, F, for a given event are defined, using the contingency table in Table 3.2, as follows (e.g. Wilks, 2011; Jia et al., 2014):

$$H = \Pr\{\text{event predicted}|\text{event observed}\} = \frac{A}{A+C}, \tag{3.4}$$

$$F = \Pr\{\text{event not observed}|\text{event predicted}\} = \frac{B}{A+B}. \tag{3.5}$$

A good forecast will have a high hit rate and low false positive rate. Hit rates and false positive rates were also calculated for a randomly generated set of each event (e.g. block onsets) to determine if the operational forecasts performed better than a random forecast. The random sequence of events was constructed by randomly choosing whether an event occurred or not on a day in winter given the probability that it occurred in ERA-I in that period. 10000 random sequences of events were constructed and the hit rates and false positive rates were calculated and then averaged to give a hit rate and false positive rate for random forecasts of each event.

Blocking activity is defined as unity for a day when blocking is present and zero

otherwise. *Blocking onset* is defined as occurring in the ERA-I data if blocking is present on the day being considered, but absent on the previous day. For the ensemble forecasts, onset occurs on a particular day and for a particular lead time if blocking is present on that day for that lead time forecast, but absent in that same forecast on the previous day. *Blocking decay* is defined analogously as occurring on the first day that a block is absent after being present on the previous day. No persistence criteria for blocking events is set to keep the sample size of events as large as possible and for direct comparability with Matsueda (2009). Blocking frequency, hit rates and false positive rates were compared for events occurring in the NewDynamics and ENDGame eras.

Ensemble spread (inter-quartile range) is included for the analysis of blocking forecasts. The forecast of blocking frequency, activity, onset and decay are calculated separately for each ensemble member to calculate the ensemble spread. This assumes that the forecast from a given ensemble member for two different initialisation days are somehow related, which is not necessarily true. To test the representativity of the spread calculated in this way we also calculated the spread by choosing multiple random paths through the different ensemble members for each day to follow possible evolutions the system could have taken. The spread calculated with 10,000 possible random ensemble member sequences is very similar to the spread calculated using consistent ensemble members, supporting the approach taken. For blocking frequency the spread is calculated at the peak of blocking frequency seen in ERA-I within the PA sector. The spread is similar in the EA sector and much smaller where there is infrequent blocking (not shown). For the hit rate analyses, ensemble spread is only plotted for hit rates for clarity of presentation. However, it is of similar magnitude for the false positive rates (not shown).

3.4.2.2 Rossby-wave structure

Following Gray et al. (2014), forecasts of Rossby-wave structure are evaluated via two parameters: Rossby-wave ridge area and isentropic PV gradient at the tropopause. To define these two parameters, we need to first define the concepts of equivalent latitude, the tropopause, Rossby-wave pattern and Rossby-wave ridges on the 320-K isentropic surface used in this work.

Equivalent latitude, ϕ_e, for a given PV contour is the latitudinal circle of a zonally-symmetric background state that contains the same mass and circulation as that contour in the full flow. Computing equivalent latitudes for all PV contours yields a background

state, known as the modified Lagrangian mean (e.g. Nakamura, 1995), given by the latitudinal location of the resulting zonally-symmetric PV contours. Further details on the calculation and interpretation of equivalent latitudes can be found in Methven and Berrisford (2015).

The *tropopause* on the 320-K isentropic surface is defined here as the 2.24 PVU (PV units where 1 PVU = 10^{-6} K m^2 kg^{-1} s^{-1}) contour. The value 2.24 PVU has been chosen because it corresponds to the average location of the strongest PV gradient in the background state (Gray et al., 2014).

A *Rossby-wave pattern* on the 320-K isentropic surface at a given time is defined here as the (unique) tropopause contour that spans every longitude. Contours that span only a limited range of longitudes correspond to cut-off lows or highs depending on their location (south or north) with respect to the Rossby-wave pattern.

Rossby-wave ridges are outlined by all the points along the tropopause contour with a latitude $\phi > \phi_e$; similarly, Rossby-wave troughs are outlined by all the points along the tropopause contour with a latitude $\phi < \phi_e$. Rossby-wave ridge area is defined as the area enclosed between the Rossby-wave ridge outline and ϕ_e.

The same set of equivalent latitudes for the tropopause contour used in Gray et al. (2014) has also been used in this work. This set was computed from the ERA-I reanalyses for the fifteenth day of each month from November to March 2009/10. These values were then linearly interpolated to daily values for each day. The calculated ridge areas will be dependent on the prescribed ϕ_e. However, the conclusions of the present investigation are independent of the precise values chosen for ϕ_e because the ridge areas are classified and compared according to validation times: in a perfect forecast the ridge area would be the same as that in the analysis for the same validation time at all lead times as long as the same ϕ_e is used for both forecast and analysis.

The isentropic PV gradient at the tropopause, calculated as the magnitude of the 2D vector ∇_θPV written in spherical coordinates for an isentropic surface and evaluated at the tropopause, is computed by bi-linearly interpolating the magnitude of the PV gradient onto a set of equally-spaced points along the tropopause contour (this is a different calculation method to that used by Gray et al. (2014)). The uniform spatial separation between tropopause points has been arbitrarily set to 50 km; however, the results are not particularly sensitive to this choice (not shown). The number of points changes from day to day with the length of the tropopause contour. The PV gradient is calculated for a

given validation time as the median of the PV gradients at the tropopause points. The median has been chosen as the statistic that best represents the centre of the resulting skewed distribution (not shown).

The methodology used to characterise Rossby-wave structure in Gray et al. (2014) is here extended in two ways. First, rather than only presenting hemispheric results, a sector analysis is introduced by defining the Greenland–Euro-Atlantic (GEA, 90°W–40°E) and Pacific–North America (PNAm, 120°E–90°W) sectors, akin to those in the atmospheric blocking analysis (see Section 3.4.2.1) but spanning larger longitude ranges under the assumption that a blocked region would be surrounded by a ridge outline. Second, rather than exclusively studying the control members in each EPS, whole ensembles are investigated by computing Rossby-wave ridge area and isentropic PV gradient at the tropopause, hemispherically and sector-by-sector, for each member in each ensemble.

3.5 Atmospheric blocking forecast skill

3.5.1 Blocking frequency

3.5.1.1 ERA-I

The ERA-I data reveals a large inter-annual variability in the pattern of NH blocking frequency (grey shadings in Fig. 3.2). Atmospheric blocking over the EA sector is more frequent than that over the PA sector during winter 2012/13. This pattern is reversed during the next two winters, especially during 2013/14. Among the four winters considered, 2015/16 stands out as a winter with suppressed atmospheric blocking in both the EA and PA sectors in comparison with the three previous years.

3.5.1.2 Operational EPS forecasts

Blocking forecasts are first considered separately for each winter in the study period before synthesizing the results. During 2012/13, every EPS performed reasonably well at predicting blocking frequency over the EA and PA sectors, even at nine days lead time (Fig. 3.2(a–c)). However, the EA maximum was underestimated and the PA maximum was slightly overestimated by every EPS beyond a lead time of seven days.

In five-day forecasts for 2013/14, the ECMWF-EPS and the KMA-EPS accurately predicted blocking frequency over the EA sector (Fig. 3.2d). At that lead time, the

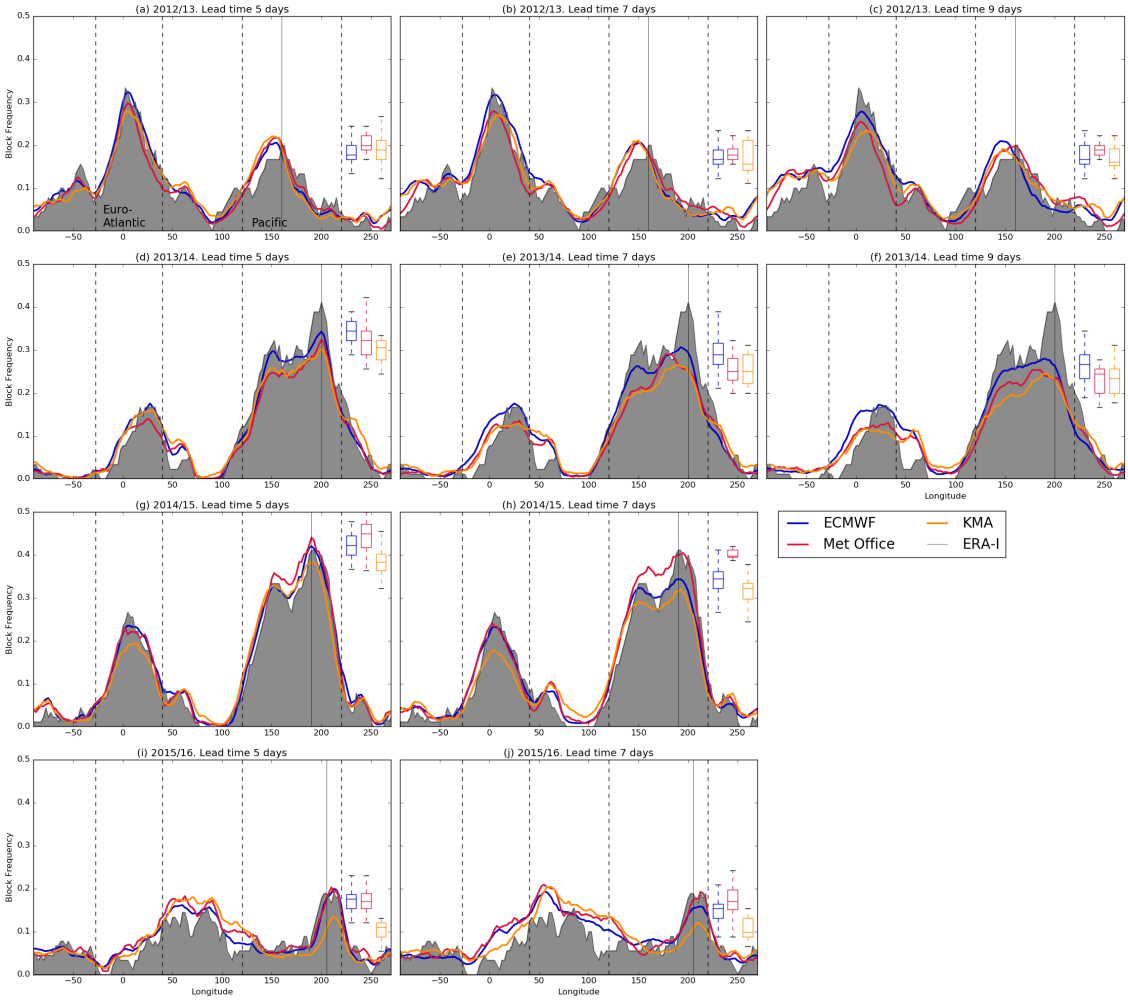

Figure 3.2: Blocking frequency in the NH for ERA-I (grey shading) and for each EPS (colours) for winters (a–c) 2012/13, (d–f) 2013/14, (g–h) 2014/15 and (i–j) 2015/16. The left, middle and right columns represent forecasts of lead times five, seven, and nine days respectively. Data for lead times beyond seven days is not available from the TIGGE archive for MOGREPS after the winter of 2013/14. Vertical dashed lines represent the limits of the EA and PA sectors, as labelled in (a). Box and whisker diagrams indicating ensemble spread for each EPS are included at the right side of each panel for forecasts of blocking frequency at the longitude in the PA sector with the highest blocking frequency in ERA-I. The longitudes where the ensemble spreads are calculated are indicated by the vertical solid lines.

ECMWF-EPS also produced an accurate prediction of the secondary blocking frequency peak over the Pacific (around 150°E), but underestimated the primary peak (around 200°E). The KMA-EPS underestimated blocking frequency over the whole PA sector. During that same winter, five-day MOGREPS forecasts slightly underestimated blocking frequency over both sectors. Nevertheless, every EPS was able to produce the single- and double-peaked patterns observed over the EA and PA sectors, respectively. However, as lead time increased, the quality of the forecasts decreased. Even at seven days lead

time (Fig. 3.2e), a wider sector of blocking activity was forecast over the EA sector than was observed and the forecast maxima in blocking frequency over the Pacific was underestimated by every EPS; this underestimation is worse at nine days lead time.

During 2014/15, every EPS reproduced the hemispheric structure of blocking frequency, mainly given by a single blocking frequency peak over the EA sector and a double peak over the PA sector, at five days lead time (Fig. 3.2g). However, while the ECMWF-EPS accurately predicted blocking frequency over the two sectors, the KMA-EPS underestimated it over the EA sector and MOGREPS overestimated it over the PA sector. In contrast with the previous winter, both the ECMWF-EPS and MOGREPS performed well at seven days lead time even though the overestimation of blocking frequencies by MOGREPS was enhanced and those predicted by the ECMWF-EPS over the PA sector had started to decay by this lead time (Fig. 3.2h). Blocking frequencies forecast by the KMA-EPS, on the other hand, had noticeably reduced over both the EA and PA sectors by seven days lead time.

The suppressed blocking frequency during DJF 2015/16 was slightly over-predicted in the region around 75°E (blocking frequency peaked to the east of the EA region in this winter) by every EPS and well predicted by the ECMWF-EPS and MOGREPS, but slightly under-predicted by the KMA-EPS, over the PA sector at five days lead time (Fig. 3.2). The same forecast error pattern was produced at seven days lead time, but the errors were enhanced with respect to those at five days lead time (Fig. 3.2j).

The spread in the ECMWF-EPS, shown in the box and whisker plots in Figure 3.2, is generally consistent for each winter and lead time considered. The MOGREPS and KMA-EPS have similar ensemble distributions in winters 2012/13–2013/14, consistent with the EPSs having similar ensemble mean forecasts. In winters 2014/15–2015/16 the forecast of blocking frequency is clearly increased in the whole MOGREPS ensemble compared to the KMA-EPS at both five and seven days lead time.

We conclude that the ECMWF-EPS performance was consistent across the four winters despite changes in model configuration (Table 3.1). The performance of the KMA-EPS was similar to that of MOGREPS at all lead times in the NewDynamics era (i.e. before the introduction of ENDGame). This similarity was no longer present in the ENDGame era. Another aspect that highlights the contrasting performance between MOGREPS and the KMA-EPS in the two eras is a change in the tendency of the forecast frequency of frequently blocked regions to decrease with forecast lead time. This blocking

frequency reduction has been a long-standing issue: it was already identified by Tibaldi and Molteni (1990), who showed a reduction in amplitude of the main peaks in blocking frequency with lead time in operational ECMWF winter forecasts between 1980 and 1987. During the NewDynamics era, there is generally a decay in forecast frequency with lead time in all three EPSs (Figs. 3.2(a–c) and 3.2(d–f)). This tendency is absent and even opposite in MOGREPS during the ENDGame era, whereas it is maintained in the other two EPSs (Figs. 3.2(g–h) and 3.2(i–j)).

3.5.1.3 ENDGame-RERUN

The blocking frequency produced by the ENDGame-RERUN, together with that from the control members from the three operational EPSs considered and ERA-I, is presented in Fig. 3.3. Blocking frequency for winter 2013/14 is shown for forecasts at five, seven, and nine days lead time. The control members from MOGREPS and the KMA-EPS show similar features to the ensemble mean forecasts at five days lead time (cf. Fig. 3.3a and Fig. 3.2d). For instance, the maxima in blocking frequency over the Pacific is under-predicted by both control members. However, unlike the MOGREPS ensemble mean, which underestimated the peak in EA-sector blocking frequency, the MOGREPS control member reproduced this feature. The control member from the ECMWF-EPS generally performs better than the ensemble mean, particularly at a lead time of nine days.

At lead times of five and seven days, the control members from the ECMWF-EPS and the ENDGame-RERUN perform better than those from the KMA-EPS and MOGREPS (Fig. 3.3(a,b)). Furthermore, the ENDGame-RERUN forecast the highest peak in blocking frequency over the PA sector more accurately than any other EPS at these lead times; this is consistent with the accurate forecasts from MOGREPS with ENDGame run operationally during 2014/15 and 2015/16 (Fig. 3.2(g–j)). At nine days lead time, the ENDGame-RERUN under-predicts blocking in the PA sector (as does the control member from the ECMWF-EPS), although it performs better than both MOGREPS and the KMA-EPS; in contrast, the ENDGame-RERUN over-predicts blocking over the EA sector and Eastern Europe, although it does not capture the peak blocking frequencies.

3.5.2 Hit rate analysis

In this section, the model representation of the temporal behaviour of blocking in the EA and PA sectors is assessed in terms of blocking activity (Section 3.5.2.1) and

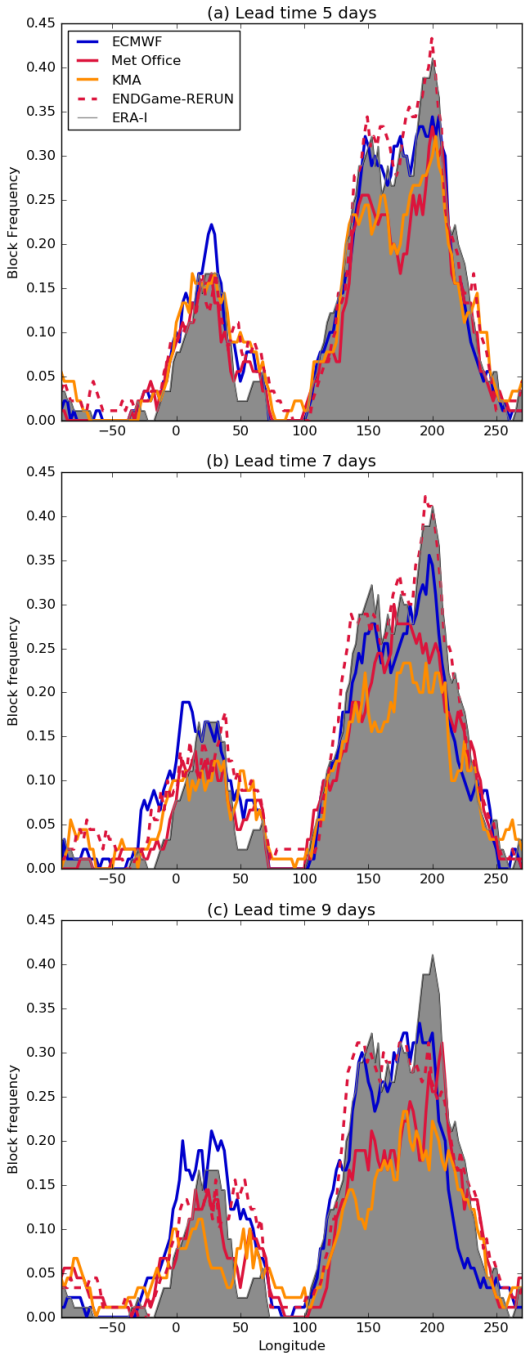

Figure 3.3: Blocking frequency during winter 2013/14 as diagnosed from ERA-I (grey shading). Coloured lines represent the frequency predicted by the control members from the operational forecasts from the ECMWF-EPS, MOGREPS and the KMA-EPS. The dashed line represents the frequency forecast by the control member of the ENDGame-RERUN. Forecasts of lead times five, seven and nine days are shown in panels (a), (b) and (c), respectively.

blocking onset and decay (Section 3.5.2.2). For ease of presentation, results for the two winters during which MOGREPS used the NewDynamics dynamical core (2012/13 and 2013/14) are combined, as are the results for the two winters during which MOGREPS

used the ENDGame dynamical core (2014/15 and 2015/16). It is better to compare the performance of different EPSs within each of these periods than compare how each EPS performs for the two periods because hit rates and false positive rates are sensitive to the observed blocking frequency.

3.5.2.1 Blocking activity

Hit rates and false positive rates as functions of lead time for each EPS are presented in Fig. 3.4, which also includes the hypothetical hit rates and false positive rates for a randomly-generated period of blocking activity with the same probability of blocking as in ERA-I (grey lines in Fig. 3.4). Blocking activity hit rates and false positive rates for all the EPSs remain above the hit rates and below the false positive rates, respectively, for the randomly-generated blocking activity, which implies that the ensemble forecasts have more skill at forecasting blocking activity than a random forecast for lead times up to (at least) seven days.

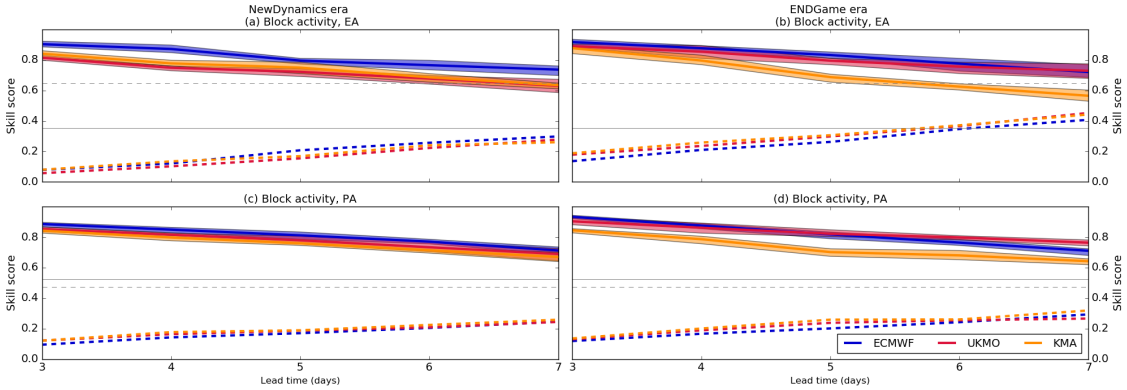

Figure 3.4: Hit rates (solid lines) and false positives rates (dashed lines) for blocking activity in winters (a, c) 2012/13–2013/14 and (b, d) 2014/15–2015/16 in (a, b) the EA and (c, d) PA sectors. Grey lines represent hit rates/false positive rates for a randomly-generated set of events (see text for details). The shading on the hit rate curves represents the ensemble spread.

We first discuss hit rates and false positive rates over the EA sector (Fig. 3.4a,b), followed by those for the PA sector (Fig. 3.4c,d). Over the EA sector, MOGREPS and the KMA-EPS have similar hit rates and false positive rates in the NewDynamics era, which is consistent with the blocking frequency being similar for these two EPSs during those winters (cf. Fig. 3.2). The spread in MOGREPS and KMA-EPS is also similar in the NewDynamics era. The hit rates of both EPSs are well below those of the ECMWF-EPS, which indicates better forecasting skill in the ECMWF-EPS (using ERA-I as the reference). The false positive rates over the EA sector are similar across the EPSs. Moving

to the ENDGame era (Fig. 3.4b) , there is a clear change in MOGREPS performance. MOGREPS hit rates are higher than those of the KMA-EPS (such that the ensemble spreads no longer overlap from five days lead time) and more comparable to those of the ECMWF-EPS for all lead times. False positive rates are similar across both eras for every EPS which, for MOGREPS in particular, implies that the over-estimation of blocking frequency over the EA sector during 2015/16 (Figs. 3.2(i,j) is not worse than it would have been with the NewDynamics dynamical core.

The patterns of hit rates and false positive rates in the PA sector are similar to those in the EA sector (Fig. 3.4c,d). MOGREPS and the KMA-EPS have similar hit rates, which are generally below those of the ECMWF-EPS during the NewDynamics era. During the ENDGame era, MOGREPS has higher hit rates than the KMA-EPS at all lead times and, at lead times of five, six and seven days, MOGREPS exhibits the highest hit rates among the three EPSs considered. In terms of false positive rates, the three EPSs exhibit similar performance during the two eras.

3.5.2.2 Blocking onset and decay

Hit rates and false positive rates are shown in Fig. 3.5 for onset and decay of blocking occurring in the EA (Figs. 3.5(a,b,e,f)) and PA (Figs. 3.5(c,d,g,h)) sectors. Figures 3.5(a–h) also include the hit rates and false positive rates for a randomly-generated set of onset/decay events with the same corresponding probabilities as in ERA-I. Overall, the timescales for accurate prediction of block onset and decay (considered as hit rates above 0.5) by the EPSs are comparable to those found in Pelly and Hoskins (2003b) and Jia et al. (2014) and are an improvement on those found in earlier studies (e.g. Tibaldi and Molteni, 1990).

Hit rates are much lower (and false positive rates higher) for the onset and decay of blocking than for blocking activity. The ensemble spread is also larger for forecasts of onset and decay. In the EA sector, there is a general downward trend with lead time in hit rate for the onset of blocking in the every EPS in both the NewDynamics and ENDGame eras. MOGREPS and the KMA-EPS have similar hit rates for blocking onsets in the NewDynamics era and their ensemble spreads are similar. In contrast, in the ENDGame era, MOGREPS has hit rates greater than the KMA-EPS at all lead times and especially at longer lead times; the ensemble spreads for the forecasts from MOGREPS the KMA-EPS do not overlap at five and six days lead time and only just meet at seven days lead

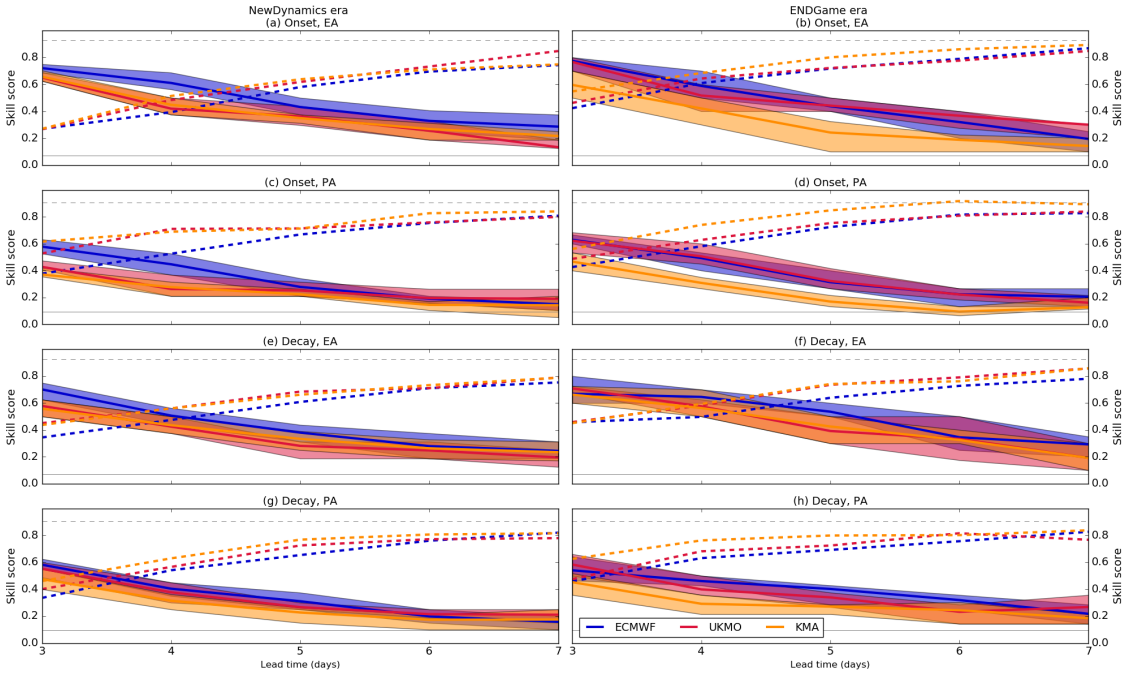

Figure 3.5: Hit rates (solid lines) and false positives rates (dashed lines) for (a, b, c, d) block onset and (e, f, g, h) block decay in (a, c, e, g) winters 2012/13–2013/14 and (b, d, f, h) 2014/15–2015/16 in (a, b, e, f) the EA and (c , d, g, h) PA sectors. Grey lines represent hit rates/false positive rates for a randomly-generated set of events (see text for details). The shading on the hit rate curves represents the ensemble spread.

time. This suggests an improvement in the forecast of block onsets with the ENDGame dynamical core in the EA sector, although analysis of more winters would be needed to confirm this.

For block onsets in the PA sector, hit rates for MOGREPS and the KMA-EPS are again similar in the NewDynamics era and there is an increase in hit rate for MOGREPS in the ENDGame era when compared to the KMA-EPS with separated ensemble spreads at four to six days lead time. This increased hit rate is not associated with an increased false positive rate: false positive rates for MOGREPS in the ENDGame era are lower than for the KMA-EPS and similar to the ECMWF-EPS. Hit rates for the ECMWF-EPS for block onset in the PA sector are similar in both eras. Hit rates for block onset are generally lower in the PA sector than in the EA sector at all lead times and for all EPSs. A possible explanation for this could be the different mechanisms driving the formation of blocking in each sector: block formation in the European region is most dependent on low-frequency dynamics, whereas forcing by transient eddies is crucial for block formation in the Pacific (Nakamura et al., 1997). All EPSs perform better than for a randomly-generated list of onset dates.

Hit rates and false positive rates for the decay of blocking show similar patterns to those for block onset: a general downward trend in hit rate and increase in false positive rate with lead time. The values for each EPS are comparable for onset and decay, implying that EPSs do not clearly forecast either the onset or decay of blocking best. Other studies (e.g. Pelly and Hoskins, 2003b) have found that models tend to predict the decay of blocking events more accurately. In the EA sector, the hit rate and false positive rate for MOGREPS and the KMA-EPS are similar for all lead times and the ECMWF-EPS performs best at short lead times of four and five days in both the NewDynamics and ENDGame eras. In the PA sector, the three EPSs perform similarly in the NewDynamics era. MOGREPS performs better than the KMA-EPS, and more similarly to the ECMWF-EPS, in the ENDGame era at lead times up to five days although the ensemble spreads are not separated: hit rates are generally higher and false positive rates lower than for the KMA-EPS. Apart from this short lead time difference in the PA sector, the hit rates, false positive rates and ensemble spreads for each EPS are consistent in both sectors and both eras. Hence, there has not been a clear impact on the forecast of block decay in MOGREPS due to the introduction of the ENDGame dynamical core.

The improvements in the representation of atmospheric blocking in MOGREPS due to the new dynamical core are hypothesised to be related to the improvement in the representation of upper-level Rossby waves. The changes in the representation of Rossby-waves in MOGREPS are presented in the next section.

3.6 Rossby-wave structure forecast skill

3.6.1 Rossby-wave ridge area

The 320-K Rossby-wave ridge area as a function of forecast lead time is shown in Fig. 3.6 for the NH (Figs. 3.6a–c), and the GEA (Figs. 3.6d–f) and PNAm (Figs. 3.6g–i) sectors (as defined in Section 3.4.2.2). The results in each panel are grouped according to the NewDynamics and ENDGame era winters. The ensemble results are presented in terms of the first, second (median) and third quartiles of all ensemble members across the winter days for each forecast lead time. The control member median over winter is also shown for comparison. The definition of equivalent latitude prevents us from comparing absolute values of ridge areas between two different years (see Section 3.4.2.2). Thus, the results are presented as ridge area normalised by its value at analysis time (T+0).

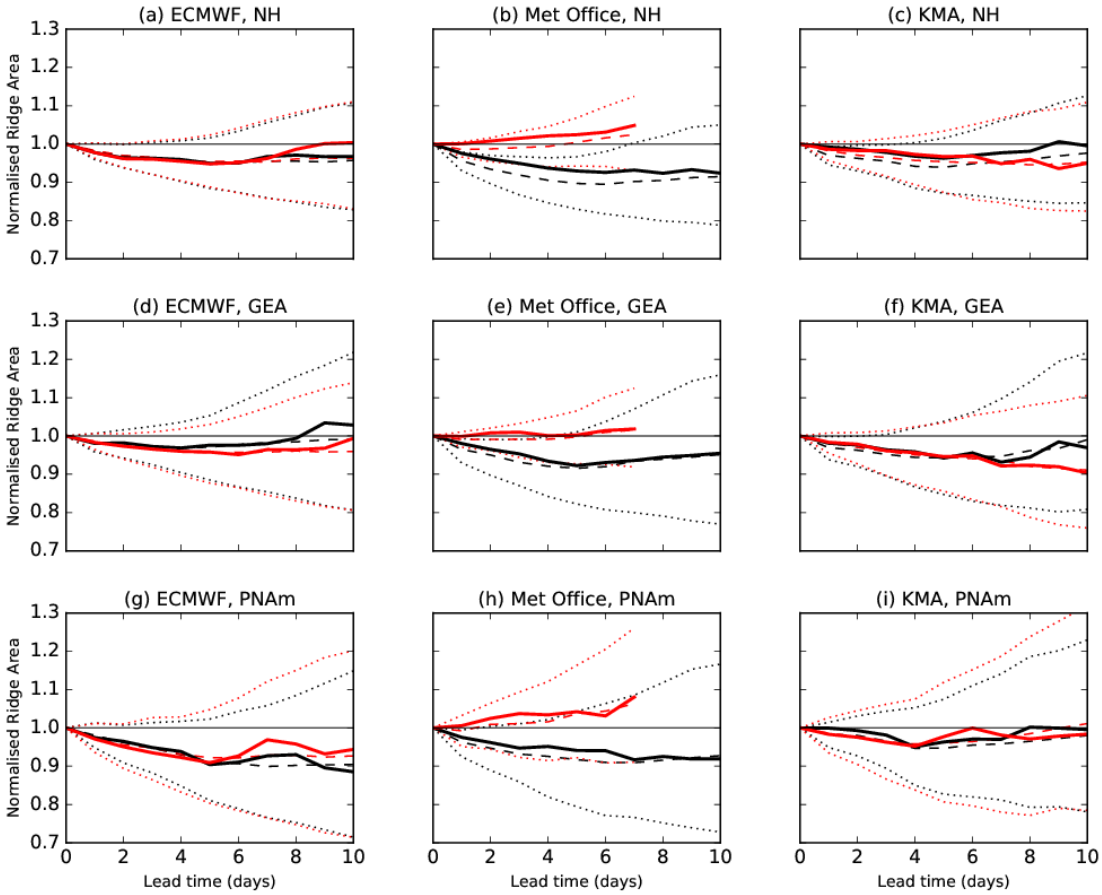

Figure 3.6: Ridge area normalised by its value at analysis time as a function of forecast lead time over (a–c) the NH, (d–f) the GEA sector and (g–i) the PNAm sector for ECMWF (left), Met Office (middle) and KMA (right), showing the control member's median (solid) and the ensemble's median (dashed) and first and third quartiles (dotted) over winters 2012/13–2013/14 (black) and 2014/15–2015/16 (red).

During the NewDynamics era over the NH, the three EPSs exhibit a decrease in ridge area with lead time (as described by Gray et al. (2014) for earlier years in the TIGGE archive) in the medians of both the control member and the ensemble. The decrease in hemispheric ridge area is less evident in the control member of the KMA-EPS, but it is still noticeable in its ensemble median (Fig. 3.6c). Considering only the ensemble data, the ECMWF-EPS and the KMA-EPS display very similar characteristics with a maximum decrease in the median in both EPSs of about 5% with respect to T+0 at ten days lead time, while the first and third quartiles are located at about 80% and 110% of the T+0 value, respectively. In contrast, MOGREPS exhibits the strongest ridge area decrease with a maximum decrease in the median of about 10% with respect to T+0 at ten days lead time; even the third quartile for this EPS only reaches 95% of the T+0 ridge area value at a lead time of five days. Considering that MOGREPS and the KMA-EPS use the same dynamical core during this era, the difference in behaviour between these

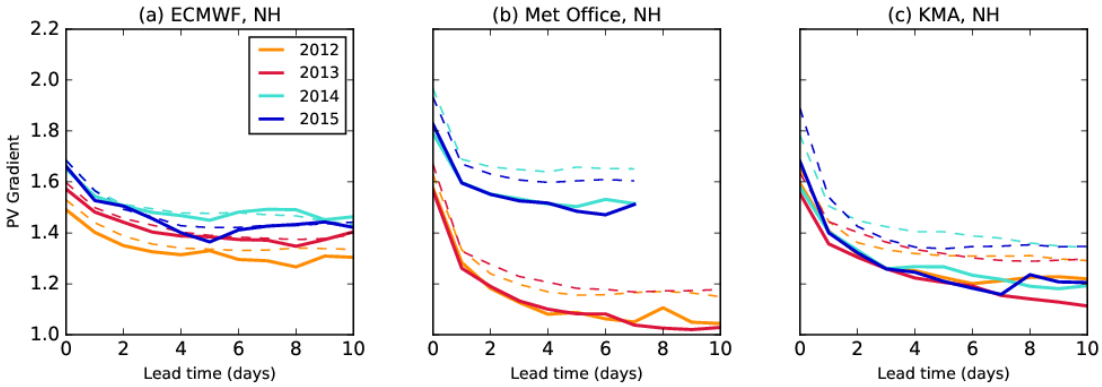

Figure 3.7: NH isentropic PV gradient, in PVU (100 km)$^{-1}$, at the tropopause as a function of forecast lead time for winter 2012/13 (yellow), 2013/14 (red), 2014/15 (turquoise) and 2015/16 (blue) showing the control median (solid) and the ensemble median (dashed) for (a) ECMWF, (b) Met Office and (c) KMA.

two EPSs can be attributed primarily to resolution (see Table 3.1).

During the ENDGame era over the NH, the ECMWF-EPS exhibits strikingly similar statistical behaviour to the NewDynamics era (Fig. 3.6a), both in the control member and in the rest of the ensemble. Similarly, the KMA-EPS exhibits similar behaviour over the NH for the two eras, at least up to six days lead time (Fig. 3.6c) (though the match is not as close as that for the ECMWF-EPS). In clear contrast with the ECMWF-EPS and the KMA-EPS, MOGREPS exhibits large differences in performance over the NH in the two eras (Fig. 3.6b). During the ENDGame era, the ridge area value is maintained above 90% of its value at T+0 even by the first quartile; the median of the control member displays an increase in normalised ridge area as lead time increases. At a lead times exceeding five days, forecast NH ridge area is slightly more likely to be larger than (rather than less than) its T+0 value (Fig. 3.6b).

The sector analysis reveals a longitudinal variation in the systematic forecast errors of Rossby-wave ridge area. However, this longitudinal variation depends on both the EPS and era. There are differences between the GEA and the PNAm sectors in the ECMWF-EPS during the NewDynamics era. In the ECMWF-EPS, the ensemble median over the GEA sector remains above 95% of the T+0 ridge area value (Fig. 3.6d), while in the PNAm sector the ensemble median slowly decreases to reach 90% of the T+0 ridge area value over that sector (Fig. 3.6g). In MOGREPS, the ensemble median and inter-quartile range during the NewDynamics era over the GEA (Fig. 3.6e) and the PNAm (Fig. 3.6h) sectors are similar to each other throughout the ten days of forecast lead time considered with the decrease in the PNAm sector being slightly larger than in the GEA sector. In the

KMA-EPS, the two sectors also behave similarly to each other during the NewDynamics era up to six days lead time (see Figs. 3.6(f,i)).

The statistical behaviour of sector ridge-area forecasts during the ENDGame era is similar to that of the NewDynamics era in both the ECMWF-EPS and the KMA-EPS. However, there is a small displacement towards lower values in the GEA sector and towards higher values in the PNAm sector in the ENDGame era relative to the New-Dynamics era in both EPSs. Considering that there are no significant changes in the configuration of these two EPSs between eras, the statistical differences between eras hint at flow dependence of the development of systematic Rossby-wave forecast error. Consistent with the findings of the hemispheric analysis (cf. Fig. 3.6b and related discussion), sector ridge-area forecasts in MOGREPS during the ENDGame era are very different from those during the NewDynamics era. During the ENDGame era, the median of the normalised ridge area over the GEA sector stays around 1, indicating the virtual absence of systematic forecast error (implying the forecast error is purely random) over this sector throughout the seven-day lead time interval considered (Fig. 3.6e). However, this result should not be interpreted in isolation from the NH and PNAm results. Over the PNAm sector, the median of the normalised ridge area increases during the seven lead-time days so that there is a greater likelihood of an overestimation of ridge area over this sector (Fig. 3.6h). The sector analysis also reveals larger ensemble spread in the sectors than in the hemisphere as a whole, implying that the narrower hemispheric distribution arises as a result of compensations between sectors. This effect is larger for longer lead times, which explains the apparent recovery of ridge area at longer lead times: the forecasts may be displaying total hemispheric ridge area values close to those at T+0. However, the recovery of ridge area may be taking place in localised hemispheric sectors. This effect can be found in both eras in the three EPSs considered.

3.6.2 Isentropic PV gradient at the tropopause

The ensemble representation of the isentropic PV gradient at the NH tropopause for the four individual winters is shown in Fig. 3.7. Unlike ridge area, whose non-normalised values depend on the prescribed equivalent latitude, non-normalised values of isentropic PV gradient do not depend on any arbitrary reference and therefore can be compared directly. The ensemble statistics are represented by the median of all ensemble members over all winter days. The control member median over winter days is also shown for

comparison. The tropopause PV gradient exhibits a decrease with forecast lead time in every year and all the three EPSs considered, similar to that described by Gray et al. (2014) for earlier years in the TIGGE archive. However, there is inter-annual variability in the values. Moreover, there is a lack of agreement in the values of the PV gradient at the tropopause among EPSs even at T+0. For any given year, MOGREPS tends to yield the largest values. There is also a systematic difference between the control member and the rest of the ensemble members in every EPS: the median of the ensemble corresponds to sharper PV gradients than the corresponding control member. This effect is present even at T+0, which suggests that it occurs as the ensemble perturbations are generated, and is most noticeable in MOGREPS. In this EPS (and in the KMA-EPS) the initial condition perturbations are produced using the local ensemble transform Kalman filter (Bowler et al., 2009) and are, therefore, a linear combination of the forecast perturbations. Since the forecast perturbations are affected by the stochastic physics perturbations, these physics perturbations influence the initial condition perturbations (Bowler et al., 2008). In MOGREPS, the stochastic physics perturbations consist of the 'random parameters' and the stochastic kinetic energy backscatter schemes (Bowler et al., 2008, 2009). The latter introduces vorticity perturbations into the forecast to account for kinetic energy dissipated by other model components such as numerical advection errors, horizontal diffusion and parametrization schemes (Bowler et al., 2009). These vorticity perturbations, introduced in regions where gradients are already large such as the tropopause, are a likely source of the stronger PV gradients in the ensemble members (compared to the control member) at T+0.

The tropopause PV gradient normalised by its T+0 value as a function of time is shown in Fig. 3.8. As for the Rossby-wave ridge area, results are presented for the NH (Fig. 3.8a–c) and for the GEA (Fig. 3.8d–f) and the PNAm (Fig. 3.8g–h) sectors and grouped according the NewDynamics and ENDGame eras. During the NewDynamics era over the NH, the ECMWF-EPS (Fig. 3.8a) displayed the smallest decrease in tropopause PV gradient relative to its T+0 value while MOGREPS (Fig. 3.8b) displayed the largest decrease, as indicated by both the control members' medians and the ensembles' inter-quartile ranges. The reduction of PV gradient in the ECMWF-EPS is very similar during the two eras (Fig. 3.8a). The behaviour of the KMA-EPS control member median is very similar during both eras too; however, the ensemble exhibited a slight reduction during the ENDGame era in comparison to the NewDynamics era throughout the ten lead-time days considered, with a difference in medians of about 5% of the T+0 value

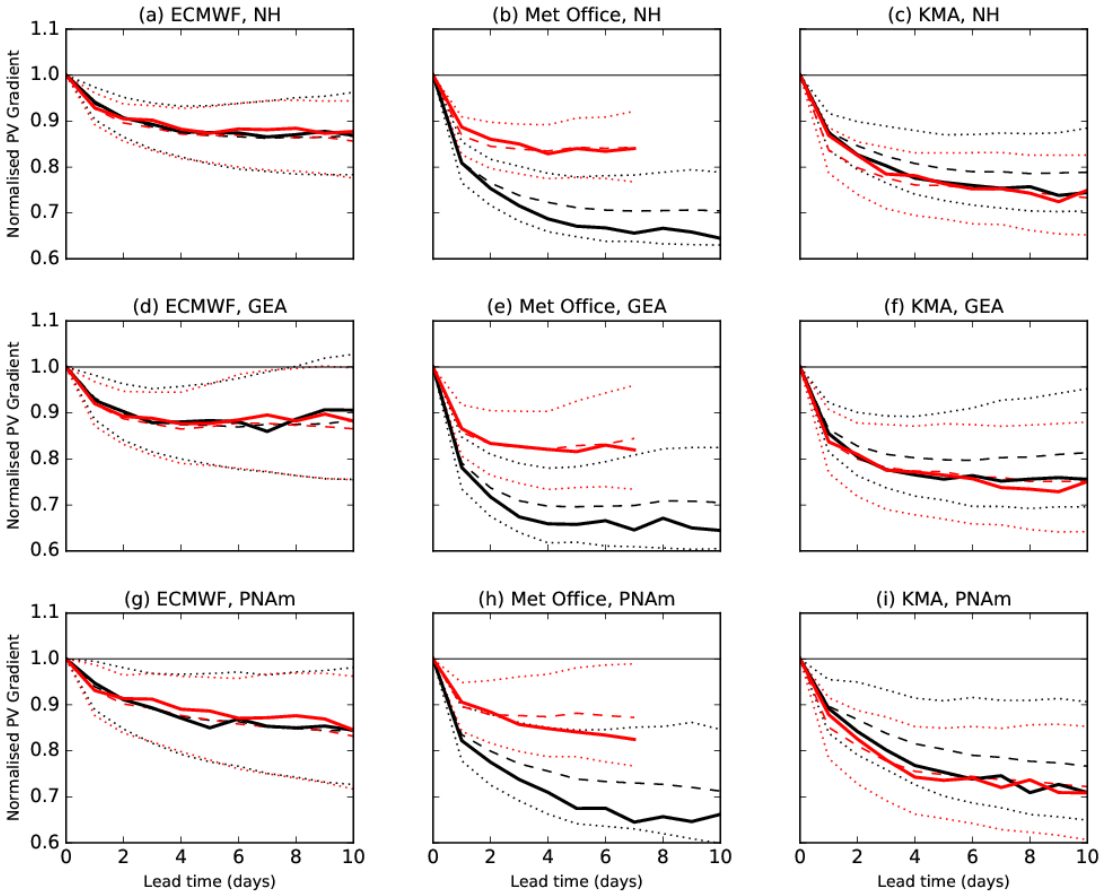

Figure 3.8: As in Fig. 3.6, but for PV gradient at the tropopause normalised by its value at analysis time as a function of forecast lead time.

at ten days lead time. Given the lack of changes in the configuration of the KMA-EPS between eras, the differences in response between eras could be attributed to differences in atmospheric flows. However, given that similar differences in response are not evident in the ECMWF-EPS, this flow-dependent sensitivity might be model dependent.

As for the Rossby-wave ridge area, MOGREPS exhibited clear differences in the forecasts of tropopause PV gradient in the two eras. The ensemble median changed from 70% of the T+0 value at seven-days lead time during the first era to just below 85% of the T+0 value at the same lead time during the second era, making the MOGREPS response more comparable to that of the ECMWF-EPS. Nevertheless, the ECMWF-EPS exhibited the smallest decrease in normalised PV gradient throughout the seven days of comparable lead time. The PV gradient in MOGREPS at T+0 is sharper than in other analyses (Fig. 3.7). Thus, even though the drop with lead time in MOGREPS in the ENDGame era is comparable to that in the ECMWF-EPS (Fig. 3.8a–c), the gradient in MOGREPS at day five is comparable with that of the ECMWF-EPS at T+0 (Fig. 3.7).

It is not possible to compare the analysed PV gradient with observations; indeed, the current lack of observations with which to verify and constrain tropopause PV gradients was one of the motivations for the the recent North Atlantic Waveguide and Downstream Impact Experiment (NAWDEX).

The sector-by-sector analysis shows that even though there is a longitudinal dependence of systematic errors in tropopause PV gradient in the three EPSs considered, the statistical behaviour of each EPS over each sector is consistent with that over the NH. The PV gradient forecasts of the ECMWF-EPS are very consistent across the two eras for both sectors (Figs. 3.8(d,g)). As observed when considering the NH, the PV gradient forecasts from the KMA-EPS exhibit differences across the two eras for both sectors (Figs. 3.8(f,i)). However, these differences are much smaller than those exhibited by MOGREPS, for which there is clearly a reduction in the decrease of tropopause PV gradient with lead time during the ENDGame era relative to the NewDynamics era over both sectors (Figs. 3.8(e,h)).

3.6.3 ENDGame-RERUN

The comparison between MOGREPS and the KMA-EPS leaves open the possibility that the changes seen in the MOGREPS forecasts on the introduction of the ENDGame dynamical core are just due to the increased resolution. To assess this possibility, the results for the ENDGame-RERUN are compared with the EPS control members for winter 2013/14 in Fig. 3.9.

The control members of the ECMWF-EPS, MOGREPS and the KMA-EPS show the same general features during 2013/14 as those discussed previously for the NewDynamics era, both in terms of ridge area (Fig. 3.9a) and tropopause isentropic PV gradient (Fig. 3.9b). Regarding ridge area, the three operational EPSs behaved in a very similar way during this particular winter, even though the KMA-EPS conserves ridge area marginally better than MOGREPS and the ECMWF-EPS (Fig. 3.9a). However, it should be noted that the apparent similarity between MOGREPS and ECMWF-EPS for this winter is not present in winter 2012/13 (not shown). The performance of the ENDGame-RERUN at maintaining ridge area is similar to that of the KMA-EPS control member for the first three days, after which time the median ridge area is greater for the ENDGame-RERUN. The median stays within 97% of the T+0 ridge-area value for up to five-days lead time (Fig. 3.9a) and then increases so that it is about 1% larger than its

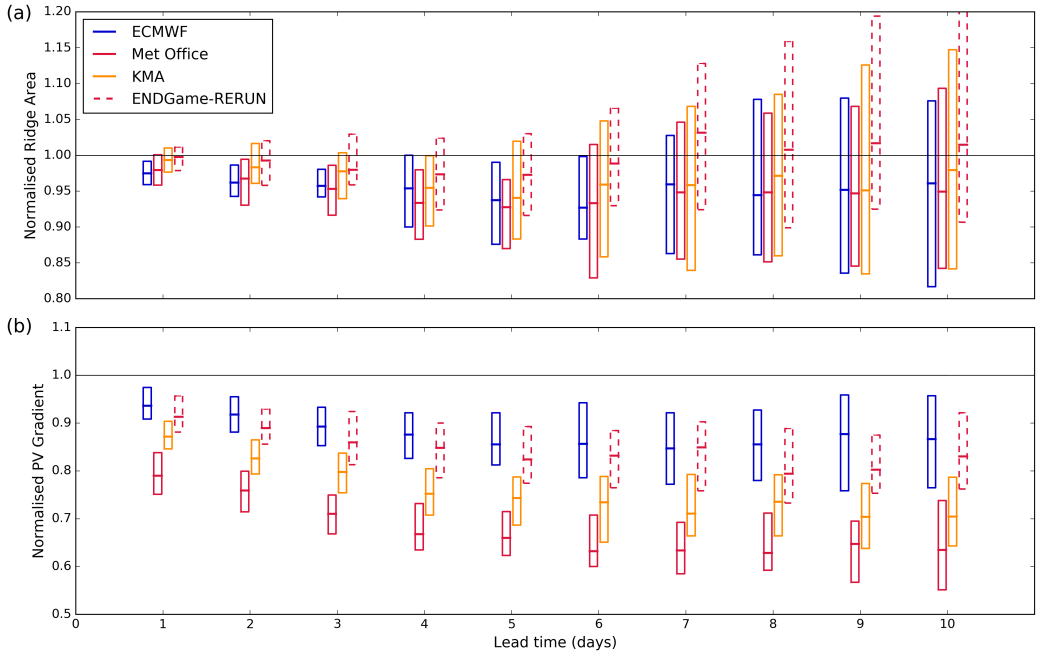

Figure 3.9: (a) Ridge area and (b) isentropic PV gradient at the tropopause, normalised by their values at T+0, as functions of forecast lead time over the NH during winter 2013/14. The boxes indicate the first, second and third quartiles of the control members of the indicated EPSs and the ENDGame-RERUN. Each group of boxes correspond to the central lead time labelled on the horizontal axis.

value at T+0 at ten-days lead time although the spreads for all of the models overlap at all times. This slight increase in normalised ridge area, relative to the T+0 value, by 10-days lead time is consistent with the behaviour found for MOGREPS during the ENDGame era (Fig. 3.6b). Regarding tropopause PV gradient, the ENDGame-RERUN values are comparable, but slightly weaker, than those of the ECMWF-EPS control member and clearly stronger than those of the control members of both MOGREPS and the KMA-EPS (the spreads of the MOGREPS control member and the ENDGame-RERUN do not overlap, and the upper-limit (third quartile) of the spread of KMA control member is below the median of the ENDGame-RERUN).

Direct comparisons between the control members of MOGREPS and the KMA-EPS and between the latter and the ENDGame-RERUN show that the changes in the representation of the ridge area and tropopause isentropic PV gradient are partly due to the changes in the dynamical core and partly due to the resolution increase. Thus, improving the dynamical core can be as important as increasing resolution for the improvement of the representation of upper-level Rossby wave structure as well as blocking, as discussed in Section 3.5.

3.7 Summary and conclusion

We have compared the performance of the ECMWF-EPS, MOGREPS and the KMA-EPS at forecasting two inter-related large-scale aspects of the mid-latitude circulation, atmospheric blocking and upper-level Rossby-wave structure, to assess the impact of changing a model's dynamical core. Forecasts of blocking have been evaluated in terms of blocking frequency and sector hit rate analysis of blocking activity, blocking onset and blocking decay. Forecasts of upper-level Rossby-wave structure have been evaluated in terms of non-conservation of ridge area and isentropic PV gradient at the tropopause with lead time. The study has focused on the winters 2012/13–2015/16. This period was chosen because it includes two years before and two years after the change of dynamical core from NewDynamics to ENDGame in MOGREPS in July 2014. During this same period, the ECMWF-EPS and the KMA-EPS maintained a relatively stable configuration (see Table 3.1) providing an opportunity to examine the impact of the improvements in the dynamical core by using the performance of the ECMWF-EPS and the KMA-EPS as references. The KMA-EPS, in particular, has effectively provided a direct control experiment (apart from resolution differences) as it is based on the same underlying model as MOGREPS, but used the NewDynamics dynamical core throughout the period of analysis. The confounding factor of resolution has been addressed using a single-member hindcast, comparable to a control member run, in which the MetUM was run with ENDGame for winter 2013/14 at N320 resolution, the same resolution as that used by the KMA-EPS.

The long-standing issue that forecast frequency of frequently blocked regions exhibits a tendency to decrease with lead time (e.g. Tibaldi and Molteni, 1990) has been identified in the present study in both the ECMWF-EPS and the KMA-EPS during the four winters included in the analysis. The effect was also identified in MOGREPS during the NewDynamics era, during which the performance of MOGREPS was similar to that of the KMA-EPS at all lead times. However, it has been shown that the introduction of ENDGame into MOGREPS has led to forecast frequency increases with lead time relative to the KMA-EPS and ERA-I in several longitude bands and these changes are robust across the ensemble. The impact of ENDGame was confirmed by the single-member hindcast experiment, which showed that control forecasts with the ENDGame dynamical core performed better than control forecasts with the NewDynamics core (even at the same resolution) for 2013/14.

Consistency was also found in the hit rates and false positive rates for blocking activity in the ECMWF-EPS and the KMA-EPS throughout the four winters considered. The KMA-EPS and MOGREPS exhibited similar hit rates, generally below those of the ECMWF-EPS, during the NewDynamics era. During the ENDGame era, MOGREPS exhibited higher hit rates than the KMA-EPS and similar to the ECMWF-EPS, while maintaining a similar performance in terms of false positive rates throughout the four winters (as did the other two EPSs). Hit rates for onset and decay of blocking were lower than that for blocking activity and the ensemble spread was larger, which highlights that the models struggle to forecast the onset and decay of blocking accurately. The EPSs were found to be more skilful at forecasting onsets in the EA than PA region, while decays were more consistent across the two sectors during the four winters considered. For MOGREPS in the ENDGame era, hit rates for blocking onset were clearly above, and false positives below, those for the KMA-EPS for most lead times; during the NewDynamics era, the performance of the two EPSs was more comparable.

The tendency of the frequency of frequently blocked regions to decrease with lead time is consistent with a reduction in Rossby-wave ridge amplitude with lead time (first identified by Gray et al. (2014)); this tendency has also been found in the present study. The ECMWF-EPS and the KMA-EPS exhibited a decrease in Rossby-wave ridge area with lead time that was consistent across the four winters considered. In contrast, the reduced reduction (or increase) in blocking frequency with lead time in several locations in MOGREPS in the ENDGame era (but not in the NewDynamics era) was associated with a clear improvement in conserving, and even increasing, Rossby-wave ridge area with lead time.

Finally, there is still a tendency for isentropic PV gradient at the tropopause to rapidly decrease with lead time, as previously identified by Gray et al. (2014). However, the introduction of ENDGame has improved the performance of MOGREPS in this respect. There may be a link between this result and the assessment of atmospheric blocking through the mechanism outlined by Harvey et al. (2016): smoothing of the PV gradient was found to lead not only to slower Rossby waves, but also to a decrease in their amplitude.

In summary, the ENDGame dynamical core has led to noticeable changes in forecasts of blocking frequency as well as in blocking activity and the onset of blocking; consistent changes were not seen in the decay of blocking. These results are consistent with those for upper-level Rossby-wave structure, as expected from the relationship between this and

atmospheric blocking.

We conclude with the formulation of a feature chain, linking the physical basis of the changes in the dynamical core to the changes in the large-scale circulation. At the grid-point level, ENDGame has improved the accuracy of the MetUM's large-scale dynamics, leading to a reduction of the model's implicit damping and, as a consequence, to more kinetic energy at mid-latitudes (Walters et al., 2014, 2017b). More mid-latitude kinetic energy has upscaled, leading to synoptic effects such as stronger extratropical cyclones (Walters et al., 2017b). Stronger extratropical cyclones have led to an improved tropopause structure and so improved Rossby-wave structure and development as shown by our results in terms of improvements in the conservation of Rossby-wave ridge area and tropopause sharpness (diagnosed by isentropic PV gradient at the tropopause) with lead time. In turn, the cumulative effect of a better representation of upper-level Rossby waves has led to an improved representation of atmospheric blocking. We hypothesise that a better representation of mid-latitude weather systems will also lead to improvements to the representation of large-scale modes of variability (i.e. NAO, PNA). This hypothesis is supported by Williams et al. (2015), who showed improvement in correlation and variability in the NAO, and Dunstone et al. (2016), who showed that the skill at predicting the NAO in DePreSys3-GC2 (whose atmospheric component is based on ENDGame) is similar to that using GloSea5.

Finally, our study has revealed that changes in a model's dynamical core can be at least as effective as realistic increases in operational model resolution in improving forecasts of upper-level Rossby wave structure and associated atmospheric blocking. This finding is important because the computational cost of dynamical core changes is likely to be substantially less than that associated with typical resolution increases.

Chapter 4:

Upstream cyclone influence on the predictability of block onsets over the Euro-Atlantic region

The improvement in the representation of atmospheric blocking and upper-level Rossby waves in forecasts from a model with an improved dynamical core shown in chapter 3 was hypothesised to originate from an improved representation of extratropical cyclones, owing to increased extratropical atmospheric variability. The relationship between extratropical cyclones and atmospheric blocking events in forecasts is studied in this chapter from a statistical viewpoint to determine if cyclone representation has an impact on block forecasts. Blocks and cyclones have been shown to be closely related in both analyses and a variety of models (Shutts, 1983; Colucci, 1985; Lupo and Smith, 1995; Michel and Rivière, 2011) and important in forecast case studies of block development (Matsueda, 2011; Grams et al., 2018). An association between block development and cyclone representation in forecasts may provide a source of forecast skill improvement as, although the new dynamical core improved forecasts of blocking, the forecasts still had errors in block representation, particularly in the forecast of block onset and decay. Furthermore, blocking remains a key contributor to some of the largest forecast errors in operational forecasting centres (Rodwell et al., 2013).

This chapter has been published in Monthly Weather Review (Maddison et al., 2019).

4.1 Abstract

Atmospheric blocking has been shown to be a phenomenon that models struggle to predict accurately, particularly the onset of a blocked state following a more zonal flow. This struggle is, in part, due to the lack of a complete dynamical theory for block onset and maintenance. Here, we evaluate the impact cyclone representation had on the forecast of block onset in two case studies from the North Atlantic Waveguide and Downstream Impact Experiment field campaign and the 20 most unpredictable block onsets over the Euro-Atlantic region in medium-range forecasts from the ECMWF. The six-day forecast of block onset in the case studies is sensitive to changes in the forecast location and intensity of upstream cyclones (one cyclone for one case and two for the other case) in the days preceding the onset. Ensemble sensitivity analysis reveals that this is often the case in unpredictable block onset cases: a one-standard deviation change in 1000-hPa geopotential height near an upstream cyclone, or 320-K potential vorticity near the tropopause, two or three days prior to block onset is associated with more than a 10% change in block area on the analyzed onset day in 17 of the 20 onset cases. These results imply that improvement in the forecasts of upstream cyclone location and intensity may help improve block onset forecasts.

4.2 Introduction

Atmospheric blocking events are associated with extended periods of anomalous weather (e.g. Rex, 1950; Trigo et al., 2004) and can influence weather in regions downstream (e.g. Carrera et al., 2004; Galarneau Jr et al., 2012). Blocking events can also have severe societal impacts (Kirsch et al., 2012) so forecasting the onset of a blocked period at the longest lead time possible is of large socio-economic interest and has been the focus of much research. However, a complete dynamical theory of blocking does not yet exist (Woollings et al., 2018) so forecasting accurately is a well-documented challenge (e.g. Pelly and Hoskins, 2003b). Ferranti et al. (2015) showed that among large-scale weather regime transitions, the transition to a blocked state following a more zonal flow was the most difficult to predict. The forecast of the frequency of blocking during winter has shown to be underrepresented in several numerical weather prediction (NWP) models and for many years (Tibaldi and Molteni, 1990; Matsueda, 2009). Increasing model resolution (e.g. Matsueda et al., 2009; Anstey et al., 2013; Schiemann et al., 2017), improving the

parameterization of sub-grid physical processes (e.g. Palmer et al., 1986; Jung et al., 2010; Dawson and Palmer, 2015; Pithan et al., 2016) and removing model biases (e.g. Kaas and Branstator, 1993; Scaife et al., 2010; Zappa et al., 2014a) have been shown to improve the representation of blocking in modeling systems, although current models still exhibit errors (Davini and D'Andrea, 2016). The representation of atmospheric blocking has also been shown to be closely related to the representation of upper-level Rossby waves (e.g. Austin, 1980; Altenhoff et al., 2008; Martínez-Alvarado et al., 2018), which have been shown to be systematically misrepresented in several NWP models (Gray et al., 2014). In this study, we explore the relationship between errors in forecasts of block onset over the Euro-Atlantic region and upstream flow features, with a focus on upstream cyclones.

Upstream cyclones are important in the development and maintenance of atmospheric blocking. The thermal and vorticity advection associated with these systems forces geopotential height rises and the anticyclonic growth of incipient blocks (Colucci, 1985; Nakamura and Wallace, 1993). Their continual transfer of momentum and vorticity forcing can act to maintain blocks against dissipation (Shutts, 1983). The phase of synoptic-scale cyclones relative to planetary-scale waves can determine whether a block onset occurs (e.g. Colucci, 1987), with an upstream shift of one-quarter wavelength from the block being favorable (Austin, 1980; Mullen, 1987). Baroclinic instability in the storm track regions is primarily responsible for producing the synoptic-scale cyclones (Mullen, 1987). Additionally, the vast majority of blocking anticyclones are preceded by a cyclone (Colucci and Alberta, 1996). For example, Lupo and Smith (1995) found that *all* of the 63 blocking events in their climatology of northern hemisphere wintertime blocking anticyclones could be identified as having an upstream precursor cyclone. Michel et al. (2012) found that, during the onset of Scandinavian blocking, cyclones move in a straight line northeastward across the Atlantic and have high intensity near Greenland. The background flow during Scandinavian blocking onset is strong enough to prevent the cyclonic wrap up of potential vorticity (PV) around the cyclones, which results in anticyclonic Rossby wave breaking over Europe. Due to the fact that not every intense synoptic-scale cyclone is accompanied by the onset or maintenance of a block, and the highly idealized nature of earlier studies (e.g. Shutts, 1983), Yamazaki and Itoh (2009) proposed a new selective absorption mechanism for block maintenance, whereby blocking highs selectively absorb anticyclonic synoptic-scale eddies, as they are of the same polarity as the blocks, reinforcing their own PV as a result. The selective absorption mechanism is seen as useful because it can be adapted for both dipole- and Ω-type blocks and shifts in the storm track location, and it

has been verified for observed cases of blocking (Yamazaki and Itoh, 2013). The onset of blocking can also be triggered by planetary-scale waves. Forcing from a quasi-stationary Rossby wave train can be the dominant driver of block onset over Europe (Nakamura et al., 1997), with these wave trains frequently emanating from the subtropical western Atlantic (Michel and Rivière, 2011). Interactions between the planetary and synoptic scales were shown to play a substantial role in block formation in an observational case study by Tsou and Smith (1990) and whether a block onset occurs can depend on the phase of background planetary waves relative to the synoptic-scale surface cyclone and their amplitude (Colucci, 1987).

Cyclones have also been studied for their role in the amplification of tropospheric ridges and how their associated moist processes are key for tropopause-level development and realizing highly amplified flow. Diabatic processes embedded in cyclones modify the PV structure in the warm conveyor belt (WCB) (Joos and Wernli, 2012) and around the tropopause (Davis et al., 1993; Ahmadi-Givi et al., 2004; Chagnon et al., 2013), with a negative tendency above the region of maximum heating acting to enhance downstream ridges (Tamarin and Kaspi, 2016). Modifying the PV structure near the tropopause alters Rossby-wave propagation (Harvey et al., 2016). Diabatic processes also amplify upper-level ridge building events downstream of recurving ex-tropical cyclones in the North Atlantic (Grams et al., 2011) and Pacific (Grams and Archambault, 2016). The observed highly-amplified flow that can occur in these cases can only be realized as a result of the cross-isentropic ascent of air mass associated with latent heating in the WCBs of the ex-tropical cyclones. The representation of diabatic processes in a NWP model was also shown to be responsible for the forecast under-amplification of a large-amplitude ridge by Martínez-Alvarado et al. (2016b). Furthermore, air ascending cross isentropically was shown to contribute considerably to blocked air masses by Pfahl et al. (2015), who found that more than 50% of air masses that formed blocking events in the ECMWF Interim Re-Analysis (ERA-I) (Dee et al., 2011) had undergone considerable ascent and diabatic heating in the days prior to arrival in the block. Air ascending into blocking anticyclones at high latitudes in the WCBs of recurrent extratropical cyclones can also be important in driving extreme events (Binder et al., 2017).

Whilst the mechanistic link between upstream cyclones and blocking has been studied, less attention has been paid to their relationship in terms of predictability, or how upstream cyclones affect forecasts of blocking. A few case studies have been analyzed, but little systematic analysis has been performed. For example, Grams et al. (2018) showed

for a block forecast over Europe in the ECMWF ensemble prediction system (EPS), that error in the intensity of the WCB in a cyclone simulated by the ensemble, which was shown to be related to an error in the structure of an upper-level trough, resulted in the poor forecast of the upper-level Rossby wave structure over Europe. For a case study over the Rockies, Matsueda (2011) showed that the forecast of a cut-off cyclone upstream of the block was essential for the accurate development of blocking. The forecast of the block was shown to be sensitive to perturbations in the region of the cut-off cyclone and modifying the perturbations were shown to improve the block development. Forecasting blocking is important because blocks have been shown to be the cause of some of the poorest forecasts, so-called *forecast busts*, for Europe during recent years: occasions when forecasts from one (or several) NWP centers experience a period of unusually low forecast skill. Rodwell et al. (2013) looked at forecast busts occurring over Europe in a 22-year period from forecasts from ERA-I. Their composite 500 hPa geopotential height (Z500, equivalent notation also used hereafter for geopotential height at other pressure levels) field for all the bust cases resembles a block over Europe. Forecast bust cases were shown to be associated with a trough over the Rocky Mountains and increased Convective Available Potential Energy (CAPE) over North America released within mesoscale convective systems (MCSs) in that region, at initialization time six days earlier. Blocking was also shown to be a large contributor to forecast bust cases by Lillo and Parsons (2017). Using the same set of bust cases as Rodwell et al. (2013), they clustered the bust cases into four subsets based on their six-day forecast evolution over the North Atlantic using a clustering algorithm. At the time of forecast initiation, two of the clusters resembled blocking patterns over the USA and Europe and, at the time of verification, the other two clusters resembled blocking features. This implies that transitions to and from a blocked situation are times when the model can have large uncertainties and large forecast errors, consistent with the study by Ferranti et al. (2015). Both Rodwell et al. (2013) and Lillo and Parsons (2017) go further and suggest a relationship between large forecast errors over Europe and upstream Rossby-wave activity forcing. In summer this is typically associated with MCSs, in autumn with re-curving tropical cyclones and in winter with extratropical cyclogenesis. The convection active in each of these cases is not well represented in the ECMWF model and its influence on the downstream propagation of Rossby-waves (via PV modification at upper-levels) can result in large forecast errors.

The relationship between a specific forecast feature of interest and earlier atmospheric features can be quantified using ensemble sensitivity or adjoint sensitivity methods. The

fundamental goal in both methods is to determine where small perturbations in a precursor field can result in large changes in a response function later in the forecast. For example, Yang et al. (1997) used adjoint sensitivity analysis to show blocking over central and eastern Russia was sensitive to upstream perturbations in the stream function field. Sensitivity methods have also been used, for example, to determine sources of initial condition error (Torn and Hakim, 2008), target useful observation locations (Ancell and Hakim, 2007), identify climatological characteristics associated with cyclone development (Dacre and Gray, 2013) and identify the origin of forecast errors in forecast bust cases over Europe (Magnusson, 2017). Magnusson (2017) looked at three particular forecast bust cases in the ECMWF-EPS and identified regions in the Z200 or Z500 fields in which these errors originated. The final case in Magnusson (2017) was a forecast bust resulting from an underestimated blocking ridge over Scandinavia. The error origin was found to be over the western Atlantic, where extratropical cyclone activity is frequent. The error in the block forecast in this case was attributed to error in the WCB representation by Grams et al. (2018). Error growth and forecast sensitivity can also be studied using tangent linear methods. Frederiksen (1998) found that a case of blocking over the North Atlantic was associated with the enhanced development of perturbations located upstream off the east coast of North America, a region where cyclogenesis has been observed to trigger block onset (Colucci, 1985). Cyclogenesis off the east coast of North America was also suggested to trigger the large-scale, baroclinic instability modes of a multi-level quasi-geostrophic model that were associated with the onset of blocking by Frederiksen and Bell (1990).

The two case studies explored in detail here are related to the North Atlantic Waveguide and Downstream Impact Experiment (NAWDEX, Schäfler et al., 2018). This recent international field campaign investigated the role of diabatic processes in modifying the upper-level Rossby wave pattern and the jet stream and influencing high impact weather downstream. Four research aircraft and a host of ground-based instruments were utilized to observe these processes to improve our understanding of Rossby wave dynamics and the role of diabatic processes. During the campaign period, 17 September to 22 October 2016, a wealth of weather phenomena were observed, including tropical cyclone transition into the extratropics, tropopause polar vortices, atmospheric rivers and a large, very-persistent atmospheric block. This block, one of the case studies here, was an important feature in NAWDEX as it persisted over Scandinavia for much of the campaign.

The aim of this study is to systematically investigate the link between forecasts of

block onset and upstream flow features with a focus on the influence of upstream cyclone activity on the forecast of block onset. The question is whether the location and intensity of an upstream cyclone in the days preceding block onset are important for the block appearing in the forecast. In section 4.3, we give details of the forecast data used in this study and describe the blocking index, ensemble sensitivity technique and trajectory calculation. Section 4.4 contains an analysis of the NAWDEX block case study. In section 4.5, a second case study is briefly presented to highlight some case-dependent differences between block onset forecasts and upstream cyclone activity. We extend the analysis to 20 of the most uncertain block onsets occurring in the autumns and winters from 2006 to 2017 in section 4.6. In section 4.7, we summarize the findings of this analysis and discuss some of their implications.

4.3 Data and methods

4.3.1 Operational forecast data

The International Grand Global Ensemble (TIGGE, Bougeault et al., 2010) is an archive containing operational ensemble forecast data from ten NWP centers dating from 2006 to the present that is updated quasi-operationally. Daily 0000 and 1200 UTC forecasts of Z1000, Z500, and potential vorticity on the 320 K isentropic surface (PV320) during autumn and winters (from 1 September 2006 to 28 February 2017) from the ECMWF-EPS (Molteni et al., 1996; Buizza et al., 1999) accessed via the TIGGE archive are used in this study. Potential vorticity is only available at 320 K in TIGGE. However, Madonna et al. (2014) showed that cross isentropic ascent in WCBs can reach at least 315 K in winter (with mean values between 313 and 321 K) so using PV320 to consider WCB outflow in autumn and winter is reasonable, though not optimal for early September cases where WCB outflow may reach higher levels. Block onsets occurring only in autumn and winter were chosen for this study as extratropical cyclones are more frequent and intense over the Euro-Atlantic region during these seasons. ERA-I reanalysis data are used for verification of the ECMWF-EPS forecasts. All forecast and reanalysis data are interpolated onto a common 1° grid. Six-hourly ECMWF operational analysis data (winds, surface pressure and specific humidity) are used in the trajectory calculations (section 4.3.4).

4.3.2 Block onset identification

4.3.2.1 Blocking index

The 2-D Z500 blocking index introduced by Scherrer et al. (2006), based on the 1-D index by Tibaldi and Molteni (1990), is used in this study. The index is calculated using the northern and southern gradients in $Z500$, termed GHGN and GHGS. The gradients are calculated at each longitude for latitudes (ϕ_0) between 35° and 75°N:

GHGN $= \frac{Z(\phi_N)-Z(\phi_0)}{\phi_N-\phi_0}$ and GHGS $= \frac{Z(\phi_0)-Z(\phi_S)}{\phi_0-\phi_S}$, where

$\phi_S = \phi_0 - 15°$ and $\phi_N = \phi_0 + 15°$. A latitude, longitude grid point is then defined as being blocked if GHGS > 0 and GHGN < -10 $(m/°)$. A schematic showing an example $Z500$ field that satisfies these criteria is shown in Fig. 1 of Martínez-Alvarado et al. (2018).

In this study, the blocking index is used to identify the date of block onset in the Euro-Atlantic region (defined as 40–75°N, -60–50°E). This region is chosen to be large with the aim of identifying only true block onsets, rather than blocked areas that move in or out of the domain (though this still can occur). The Euro-Atlantic region is defined as blocked at a given time if the largest area identified as blocked by the index exceeds an arbitrary value. The threshold is chosen to represent the typical area that the index identifies as blocks within large-scale blocking ridges in the tropopause. Considering several cases of blocking events, the threshold chosen is 950,000 km^2 (approximately the area of a circle of 10° at 60°N), though the choice of this threshold is subjective as there is no universally accepted area that defines a block. Woollings et al. (2018) used 500,000 km^2 to define the area of a block whilst earlier studies have defined the scale of a block based on its longitudinal span, ranging from 12° (Tibaldi and Molteni, 1990) to 45° (Rex, 1950). The date of a block onset is then defined as the first day of a period of at least four days identified as blocked in the Euro-Atlantic region that follows four days of the region being not blocked. This criterion gives 34 blocking events during the study period (defined in section 4.3.1).

4.3.2.2 Uncertain block onsets

Block onsets that had large uncertainty in their six-day forecast were chosen for analysis in this study. Uncertainty was measured using the area identified as blocked by the index in six-day ensemble forecasts from the ECMWF-EPS for the date of block onset in ERA-I. The 25 most uncertain onsets, defined as those with the largest inter-quartile range of block area in the ensemble, were chosen for analysis in this study. We focus on the most uncertain cases because a large range of block areas within the ensemble improves the reliability of the ensemble sensitivity analysis. However, five of the onsets were discarded: three for being blocking events moving in and out of the North-Atlantic/European domain and hence not considered real block onsets and two because the index identified features that a synoptician would not call a block. In one of the false cases the index was triggered over Greenland to the north of a large-scale trough with no ridge feature in that region. The other false case was caused by a large trough over Scandinavia to the west of a ridge that extended outside of the domain.

4.3.3 Ensemble sensitivity

4.3.3.1 Calculation

The ensemble sensitivity method used here follows the approach of Garcies and Homar (2009). The response function, J, is chosen here to be the area diagnosed as blocked by the blocking index. It is calculated for each ensemble member (51 members) for forecasts of a chosen lead time, here six days. The sensitivity, $S_{i,j}$, is calculated as

$$S_{i,j} = m_{i,j} \times \sigma_{i,j} \times \alpha_{i,j} = \frac{cov(x_{i,j},J)}{\sigma_{i,j}} \times \alpha_{i,j},$$

where

$$m_{i,j} = (\frac{\partial J}{\partial x})_{i,j},$$

and $x_{i,j} = X_{i,j} - \bar{x}_{i,j}$ (the difference between the forecast field (X) and the mean of the ensemble forecast ($\bar{x}$) at grid point i,j), $\sigma_{i,j}$ is the standard deviation of the precursor field in the ensemble at each grid point and $\alpha_{i,j}$ is a correction factor applied to filter out weak correlations (the method assumes linearity) between the response function and the precursor minus mean field:

$$\alpha_{i,j} = \begin{cases} 1, \text{ if } r^2_{i,j} \geq r^2_{min} \\ \frac{r^2_{i,j}}{r^2_{min}}, \text{ if } r^2_{i,j} \leq r^2_{min} \end{cases},$$

where $r_{i,j}$ is the correlation coefficient and r^2_{min} is the minimum correlation coefficient for which the raw sensitivities remain unaltered. Here r^2_{min} is chosen as 0.15 to only retain reliable sensitivity information and to produce clear sensitivity fields, but the conclusions are robust with $r^2_{min} = 0.05$. We have used the property

$$m_{i,j} = \frac{cov(x_{i,j},J)}{var(x_{i,j})},$$

resulting from the least-squares regression calculation in the above (note that $J = J_{i,j}\ \forall\ i,j,$). Note that we use the original expression given for $m_{i,j}$ in our calculations.

The sensitivity has the same units as the response function, in this case meters squared. The sensitivity value can be interpreted as the change in response function due to a one standard deviation increase in the precursor field. Multiplication by the standard deviation also takes into account the climatologically lower variance at lower latitudes and prevents misleading climatological sensitivity values (see Garcies and Homar, 2009, for more details). For this study, the sensitivity values detail how the area of the block in the ensemble (six days into forecast run) changes as a result of a one standard deviation change in a given precursor field (three–four days into forecast run).

Magnusson (2017) used a similar ensemble sensitivity calculation in their evaluation of three forecast bust cases over Europe. They calculated the sensitivity as the correlation between the response function and precursor field,

$$S_{i,j} = \frac{cov(J,x_{i,j})}{\sigma_{i,j}\sigma_J},$$

which differs from our calculation by a factor of $\sigma_J\alpha_{i,j}$, where σ_J is the standard deviation of the response function in the ensemble. The $\alpha_{i,j}$ term is simply a damping term so the patterns (and signs) of the sensitivity fields will not change on its application, but sensitivity values in regions where the correlation between the response function and precursor field is weak will be reduced in magnitude. The σ_J term takes into account the size and spread of the response function in the ensemble. Here, we present the sensitivities as percentage departures from the response function value in ERA-I, so information about the response function is included in our calculation and the resulting sensitivities are very comparable with the method used in Magnusson (2017).

4.3.3.2 Choice of response function

Ensemble sensitivity analysis results are presented here using the area blocked in the blocking index as the response function as this provides easily interpretable information

about changes in block area due to earlier changes in the forecast evolution. Ensemble sensitivity is also briefly discussed for two other response functions for comparison and to determine the robustness of the results. The first additional response function used is the root mean square error (RMSE) of Z500 over the blocked region. The blocked region is defined as the region between 40 and 80°N and between 30°W–30°E, 0–60°E and 60°W–0°E for blocks over the UK, Scandinavia and Greenland, respectively. Using RMSE of Z500 as the response function gives sensitivity values that detail where earlier changes in a given forecast field are associated with increased or decreased forecast error. The second additional response function used is a measure of ridge area. Ridges are defined as regions north of 55°N, in the same longitudinal bands defined above, where PV320 is less than 2 PVU (1 PVU= 10^{-6} $m^2\,s^{-1}\,K\,kg^{-1}$). The ridge area response function is used to investigate the relationship between the Z500 based blocking index and ridges in PV320. Whilst the RMSE of Z500 and ridge area response functions provide useful information about forecast sensitivity, they will be affected by processes separate from block dynamics because other features, e.g. cyclonic regions upstream or downstream of the blocking high pressure, may dominate their values. This means that the sensitivity cannot be interpreted in terms of blocking directly.

4.3.3.3 Interpretation of ensemble sensitivity

In this study ensemble sensitivity analysis is used to determine how the representation of upstream cyclones affect downstream block forecasts. For each block onset forecast, each ensemble member will forecast a different location and intensity of the upstream cyclone (if present). Here, simple idealized sensitivities for a small ensemble are calculated to determine the sensitivity patterns we expect when it is the forecast of the cyclones strength and/or location that is most important for the downstream block forecast. In each case the ensemble consists of three members, each with a prescribed cyclone location and intensity (minimum Z1000) as well as a value for the response function, J (block area). Cyclones are constructed using an idealized Z1000 field modeled as a 2D-Gaussian distribution with values of Z1000>-0.5 m set to zero. The prescribed differences in cyclone location, cyclone intensity and response function value were chosen based on those seen in the ECMWF-EPS forecasts.

Four simple idealizations of cyclone forecast, response function and sensitivity field are presented in Fig. 4.1. In the first three examples the response function is chosen so

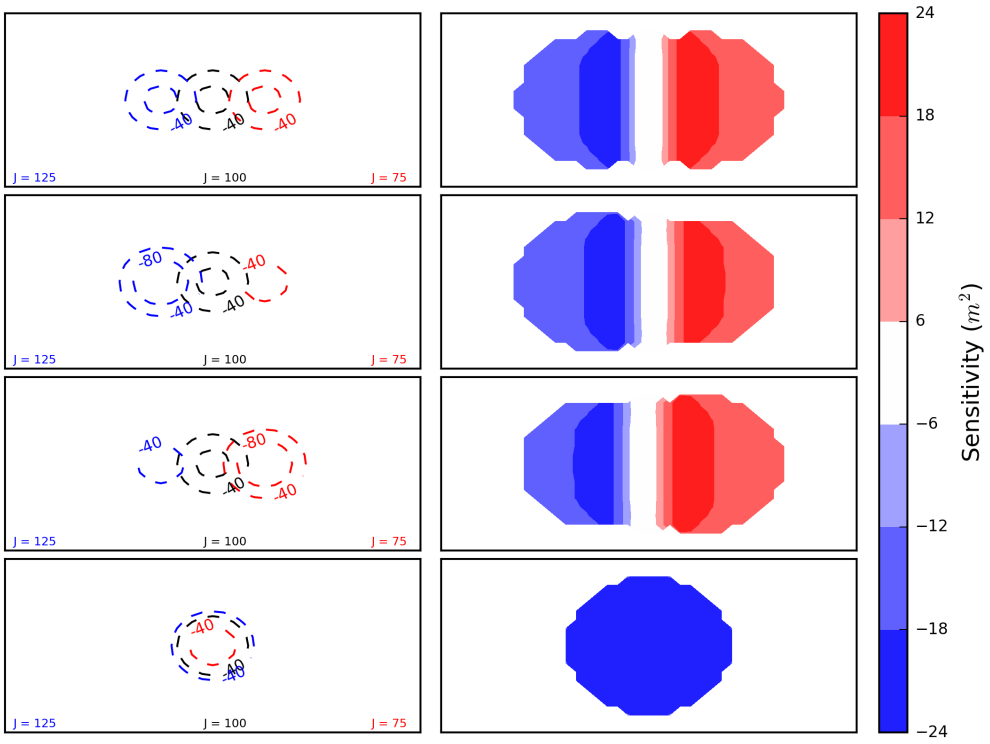

Figure 4.1: Four idealized three-member ensemble forecasts of a cyclone and response function, J (left column), and the corresponding sensitivity field for each ensemble forecast (right column). Contour values of -40 and -80 m Z1000 are presented to identify the cyclones in each ensemble member.

that the cyclone located furthest to the west has the largest block develop downstream and the cyclone furthest to the east has the smallest; in the last example the ensemble members all have same location and the ensemble member with the deepest cyclone has the largest forecast block.

In the first example only the cyclone location changes among the ensemble (the three cyclones all have the same intensity). In this example the sensitivity pattern is a dipole centered on the middle of the three cyclones. The dipole is symmetric along the axis of cyclone location change with a negative/positive orientation. The negative sensitivity to the west implies increasing Z1000 in this region is associated with a smaller block. This is equivalent (by linearity) to a deeper cyclone in this location being associated with a larger block, as we expected by construction.

In the second example, the cyclone intensity and location are both changed among the ensemble. The western cyclone is made deeper, the central cyclone remains the same and the eastern cyclone (associated with the smallest block) is weakened. The same

negative/positive dipole in sensitivity as for example 1 remains. However, the region of negative sensitivity expands and increases slightly in magnitude whilst the region of positive sensitivity is reduced.

In the third example, the cyclone furthest east is the strongest cyclone among the ensemble, still with the smallest block. The negative/positive dipole remains, but the positive region of sensitivity is larger and stronger and the negative region of sensitivity is reduced compared to examples 1 and 2. If we had constructed the ensembles in the above examples such that it was the cyclone furthest east that resulted in a larger block, the dipoles would be identical, but with orientation positive/negative, i.e. rotated by 180° (not shown).

Finally, in the fourth example we construct an ensemble in which the location of the cyclone is the same in each ensemble member, but the intensity changes. The resultant sensitivity field is a monopole of negative sensitivity around the location of the cyclones. Had we chosen the response function such that the ensemble member with the weakest (rather than the strongest) cyclone had the largest block then the monopole would be positive.

Together, the idealized scenarios presented suggest that changes in response function resulting from differences in cyclone location in the ensemble forecast leads to the sensitivity field to have a dipole structure. Any asymmetries in the dipole are associated with sensitivity to cyclone intensity. If the negative lobe of the sensitivity pattern dominates in the dipole, the deeper cyclones in the ensemble are associated with larger blocks developing downstream; if it is the positive lobe that dominates, then it is the weaker cyclones. This relationship does not depend on the dipole orientation. These results also suggest that a monopole in the sensitivity pattern is associated with larger importance of the intensity of the cyclone in the ensemble forecast rather than its location. The idealized sensitivity fields presented here aid in the interpretation of the results presented in the remainder of this article.

4.3.4 Trajectory calculation

Air that has ascended into the blocking ridges in each case is traced backwards to an upstream cyclone using trajectories calculated with the Lagrangian Analysis Tool (LAGRANTO, Wernli and Davies, 1997; Sprenger and Wernli, 2015). Back trajectories are started within the blocking ridge (in the region where the blocking index is satisfied)

every 25 hPa from 400 hPa to 200 hPa at 1200 UTC on the date of block onset in ERA-I. The trajectories are calculated backwards using the ECMWF operational analysis wind fields for 84 hours. Those that descend more than 500 hPa in the first 72 hours are classed as part of the WCB and used to identify the cyclone(s) associated with ridge building and block onset. Previous studies (e.g. Grams and Archambault, 2016) have used 600 hPa ascent in 48 hours to define a WCB. This criterion is slightly modified here to take into account the fact that we do not *a priori* know when strong ascent occurred in each case relative to the date of block onset in ERA-I. The cyclone identified is termed here the block's *feeder cyclone*, as it is feeding the blocked air mass. In the case that the back trajectories identify multiple cyclones feeding the blocking ridge then the cyclone with the larger number of trajectories entering the block is chosen. This identification provides a dynamical link between the upstream cyclone and the block and allows us to focus the ensemble sensitivity analysis in the region of the upstream feeder cyclone.

4.4 Case study I. NAWDEX

The first case study of a block onset that was associated with large uncertainty occurred on 4 October 2016 during the NAWDEX field campaign. In this section, a description of the synoptic evolution in the days preceding block onset is given together with an analysis of the operational ensemble forecast performance of the ECMWF-EPS in the days leading to the onset of the block. An illustration of the role an upstream cyclone had on the forecast evolution in the days leading to block onset is presented together with ensemble sensitivity analysis results for the block onset to conclude this section.

4.4.1 Overview of synoptic situation

The days preceding the block onset were a period of intense weather activity over the Euro-Atlantic region. A block had been situated over Scandinavia since the beginning of September and broke down around the 25 September. A deep cyclone, named the Stalactite cyclone during the NAWDEX campaign because of the very deep, narrow, stalactite-like tropopause trough associated with it, was located over the North Atlantic Ocean (to be discussed in Section 4.4.2) on 1 October and was moving towards Iceland (Fig. 4.2g). The system had a strong WCB (to be discussed in Section 4.4.2) that amplified the upper-level ridge ahead of it and on 2 October 2016 there was a large amplitude ridge in the tropopause extending across a large part of the North Atlantic (Fig. 4.2d). This

ridge became the blocking ridge that formed over Scandinavia on 4 October (Fig. 4.2a). The block persisted over Scandinavia for several weeks. The development of the Stalactite cyclone and the subsequent onset of blocking was identified as a highlight of the NAWDEX field campaign in Schäfler et al. (2018) (see their Sequence B for more details) and the Stalactite cyclone and its WCB were observed by the campaign aircraft during several phases of their development.

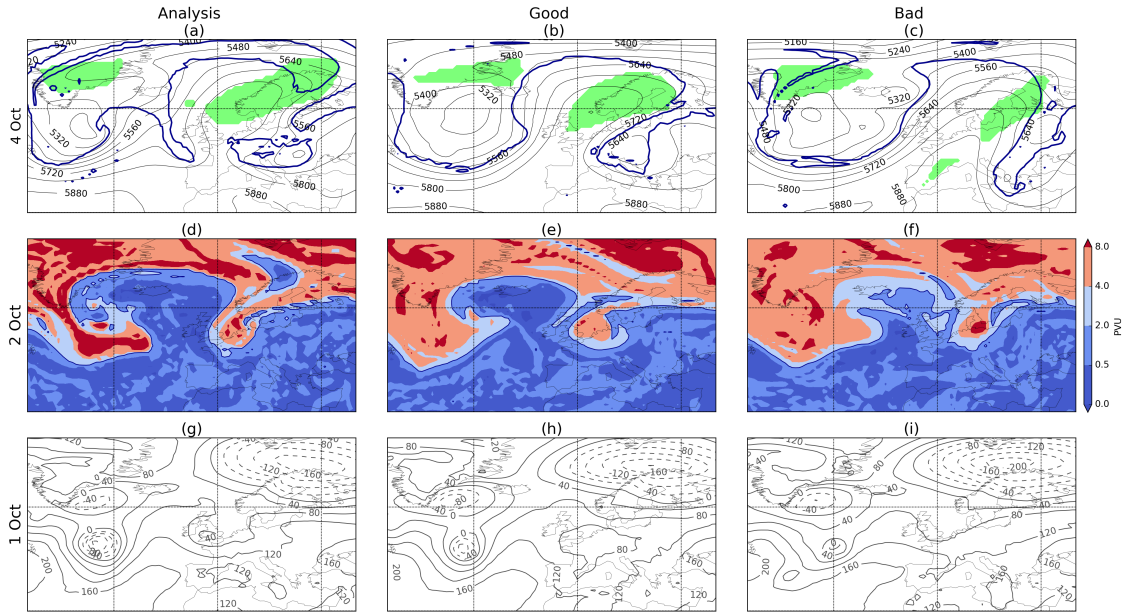

Figure 4.2: (a–c) Z500, the 2-PVU contour and blocking index (green shading) on 4 October 2016, (d–f) PV320 on 2 October 2016 showing tropospheric (blues) and stratospheric (reds) air, and (g–i) Z1000 on 1 October from (left column) ERA-I and (middle and right columns) in the forecast initiated on the 28 September 2016 from two members of the ECMWF-EPS.

4.4.2 Forecast representation

The onset of the NAWDEX block was associated with large forecast uncertainty: forecasts valid for the time of block onset experienced an extended reduction in anomaly correlation coefficient of Z500 over Europe (Schäfler et al., 2018). The six-day forecast of the area identified as blocked over Europe had large spread among the ensemble. The size of the largest area identified as blocked in each ensemble member of the ECMWF-EPS as the forecast evolves is presented in Fig. 4.3. The area in each ensemble member and the control forecast is calculated in the region of the block in the analysis (40–50°N,10°W–40°E). The majority of the ensemble members underpredicted the area of the block that formed compared to ERA-I, or did not predict a block onset at all. The control member

matches the evolution seen in ERA-I reasonably well, apart from the underestimation of the size of block on the onset date and a delay in the increase in block area that occurs after 96 hours in ERA-I. The ensemble members show large spread: some members have a large area blocked early into the forecast run and nearly all under-predict the block area on block onset date.

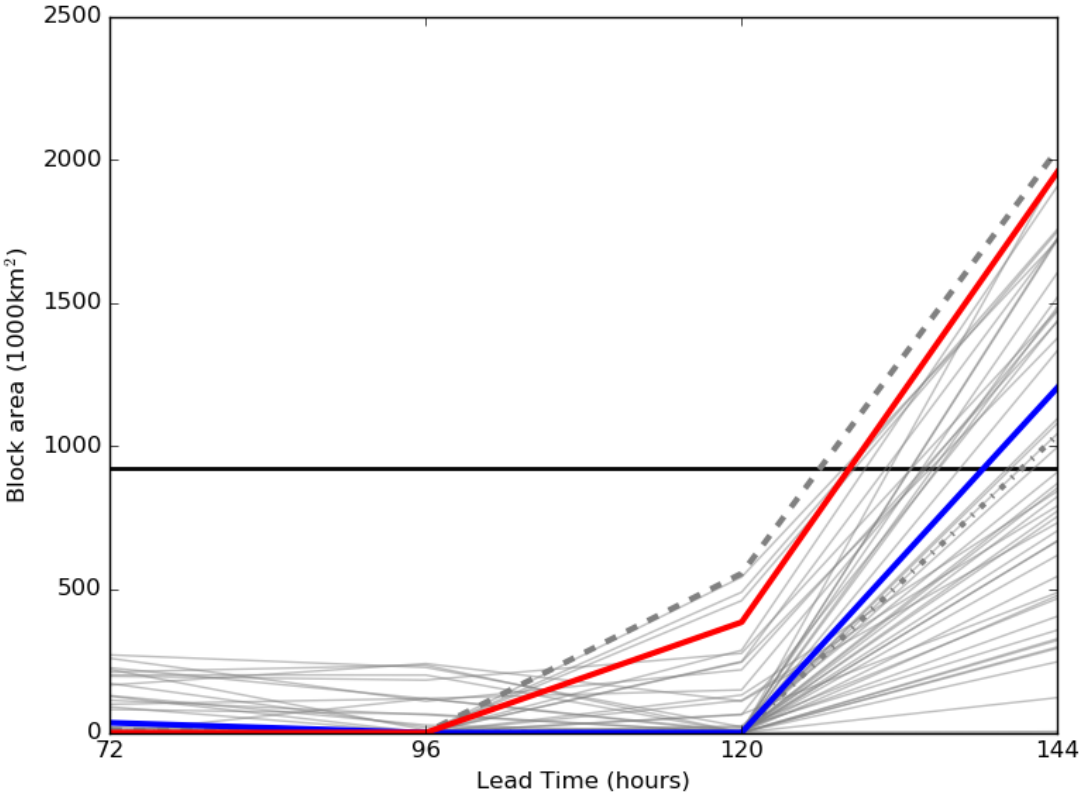

Figure 4.3: Area of the largest object identified as a block between 72 and 144 hours lead time in the forecast initiated on 28 September 2016 (forecast valid dates between 1 and 4 October 2016) from the ECMWF-EPS for the NAWDEX case study. The area is shown for each ensemble member (gray lines), the control member (blue line) and in ERA-I on the corresponding date (red line). The good and bad ensemble member (see text) are shown with the dashed and dash-dotted lines respectively.

We hypothesize that this misrepresentation was caused by the earlier poor forecast of the upstream Stalactite cyclone. To demonstrate that this may be the case it is helpful to consider the flow evolution in two ensemble members from this ECMWF-EPS forecast and compare their development to that seen in ERA-I. The two ensemble members were chosen as having either similar or different block representation to ERA-I six days into their forecast (based on RMSE of Z500 averaged over Europe, 62 m and 139 m for the chosen members, and similarity of block area to ERA-I): hereafter these are named the good and bad ensemble members, respectively, though both represent possible evolutions

of the system. The area identified as blocked in the good and bad ensemble members is highlighted in Fig. 4.3. In Fig. 4.2, Z1000 on 1 October 2016, PV320 on 2 October 2016 and Z500, the tropopause at 320 K (taken as the 2 PVU surface) and blocking index on 4 October 2016 are shown for the analysis and forecasts of the corresponding date from the good and bad ensemble members. The block is clearly identifiable in the analysis as a large-scale tropospheric ridge in both the tropopause contour and Z500 field (Fig 4.2a). The index identifies the block of interest over a large region from the north of the UK to Scandinavia as well as a second center of blocking action over Greenland. The blocking ridge in PV320 is also present in both ensemble members but is less amplified, particularly in the bad ensemble member in which the ridge extends less far to the north and spans fewer longitudes. Two days prior to block onset the under amplification of the ridge in the forecasts is more obvious. The ridge in the analysis extends much further poleward than in either of the ensemble members and a PV streamer has formed on the western flank of the ridge which is not present in either ensemble member. The good ensemble member has a larger, more coherent ridge than the bad ensemble member, but it is still not as amplified as in the analysis and in the bad member this results in a delay in the block onset (Fig. 4.3).

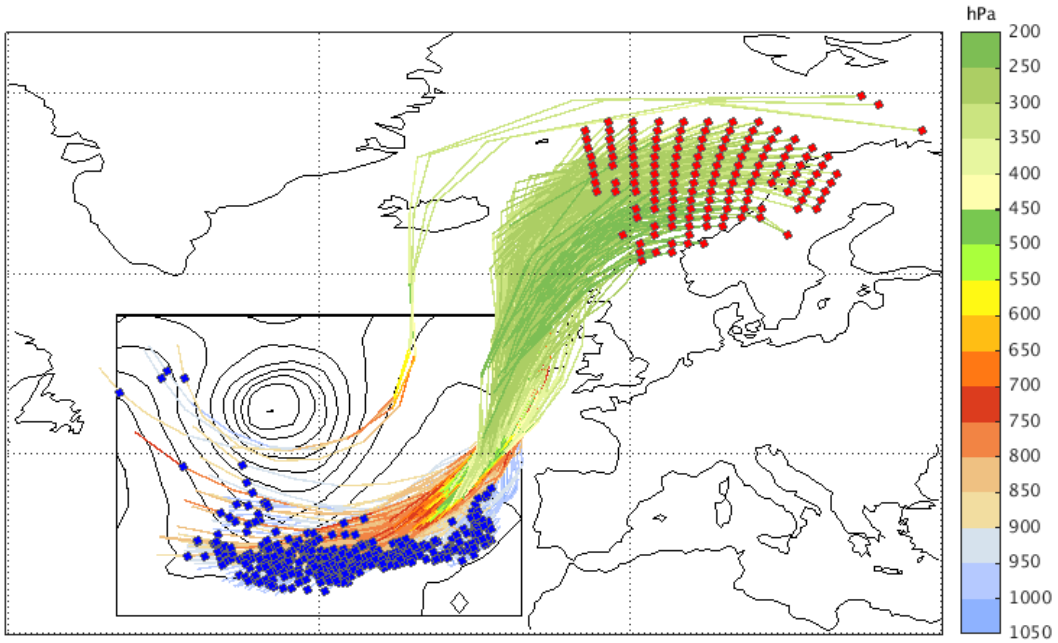

Figure 4.4: Backward trajectories initialized within the block (red points) at 1200 UTC 4 October 2016 and calculated for 84 hours. Trajectory locations are shown for the start points (red points) and at -72 hrs (1200 UTC 1 October 2016, blue points). The surface pressure in the region of the cyclone at the time of the blue points is shown by the contours in the region around the cyclone (black box).

The smaller ridges in the ensemble member forecasts are consistent with the underestimation of the Stalactite cyclone intensity and incorrect location of the cyclone relative to the upper-level features. In the analysis the cyclone was much deeper and located further west than in either of the ensemble members. We hypothesize that this affected the development of the upper-level ridge. A stronger system could amplify the ridge more due to a number of mechanisms. A stronger WCB with stronger latent heating will lead to inflow air arriving at higher altitudes and having a larger negative PV anomaly relative to the background PV. Because the average PV of the outflow of a WCB almost equals that of the inflow (Methven, 2015). It will thus be associated with stronger upper-level divergence. A stronger system will also have greater advection of low-valued PV air from the south to the north. The WCB of the Stalactite cyclone as represented in the ECMWF analysis is shown in Fig. 4.4. The Stalactite cyclone's WCB transported a large air-mass poleward and upwards into the blocking ridge. It is hypothesized that the different WCBs in the ensemble member forecasts are responsible for the different ridge developments. The good ensemble member had a deeper cyclone located further to the west than the bad member, though not as far west as in the analysis, which is consistent with its more amplified ridge on 2 October. Therefore the forecast of the Stalactite cyclone on 1 October 2016 is likely to have been important for the forecast of the block onset on 4 October 2016. To quantify the extent to which upstream cyclone representation is modifying block representation, ensemble sensitivity analysis is calculated for this onset case.

4.4.3 Ensemble sensitivity

We calculate sensitivity to Z1000 and PV320 in the days prior to block onset as these fields can describe upstream flow features, cyclone characteristics and upper-level development.

The sensitivity of block area at 144 hours into the forecast evolution to the earlier forecast of Z1000 is shown in Fig. 4.5. Sensitivity fields at 72 and 96 hours into the forecast evolution are presented with the control forecast overlain to identify features of interest. The region of highest sensitivity is located upstream of block location in a dipole around the Stalactite cyclone in the Atlantic, with a region of positive sensitivity to the east of the cyclone center and negative sensitivity to the west of the cyclone in the control forecast. A one standard deviation change in Z1000 is associated with a 15–20% change in

block area forecast relative to the block area in ERA-I. The maximum sensitivity region moves with the cyclone as the forecast evolves (Fig. 4.5). Recall that positive/negative sensitivity values do not mean that the forecast was better or worse, but instead that there was more or less blocking in the ensemble members.

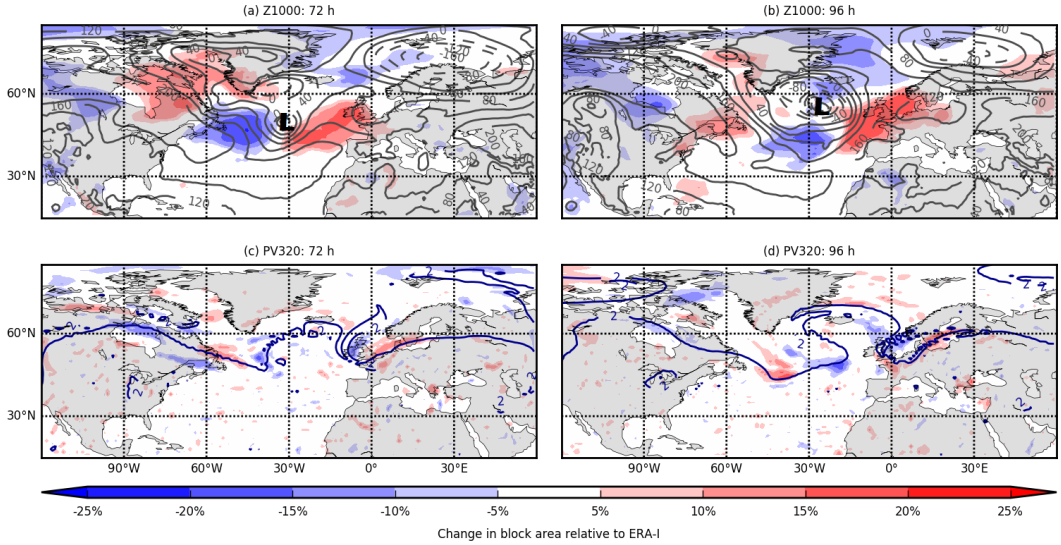

Figure 4.5: Sensitivity of the response function 144 hours into the forecast initiated at 1200 UTC on 28 September 2016 to Z1000 at 72 (a) and 96 (b) hours lead time and PV320 at 72 (c) and 96 (d) hours lead time. Sensitivities presented at 72 and 96 hours represent 1 and 2 October 2016, respectively. The control member forecast of Z1000 (a–b) or the 2-PVU contour (c–d) is overlain.

The dipole structure of sensitivity in the region of the cyclone can be understood by comparison to the idealized results in Section 4.3.3.3. The positive region to the east of the center of the Stalactite cyclone in the control forecast indicates that higher pressure there results in more blocking. The idealized examples show that this is achieved when the cyclones in the ensemble members leading to the largest blocks are located further west. The sizes and strengths of the poles are dependent on lead time. At 72 h lead time the negative pole of the dipole is stronger than the positive pole (Figs. 4.5a) which implies the ensemble members with the cyclones further west and more intense have larger blocks than those further east and less intense. The conclusion that ensemble members that had more intense cyclones located further to the west (than the cyclone in the control forecast) had a larger blocked area on onset day is consistent with our initial two-member analysis (comparing the good and bad ensemble members for which the good member had the largest block and was closest to the analysis). These results suggest that changes to the location and intensity of the Stalactite cyclone among the ensemble are important for block forecast downstream and we hypothesize that it is changes to the cyclone's WCB

structure that lead to the different block structures. Consistent with this hypothesized link between cyclone and WCB intensity, Binder et al. (2016) found a moderate to strong correlation between cyclone intensification and WCB strength.

The sensitivities to PV320 for the same lead times are also shown in Fig. 4.5. The sensitivity to PV320 is centered on the tropopause and is generally weaker than the sensitivity to Z1000. Sensitivity along the tropopause indicates that the phasing and structure of the upstream Rossby wave pattern is associated with differing representation of the blocking ridge, as we might expect. The increased localized sensitivity around the edge of the blocking ridge and near the upstream trough at both lead times (Fig. 4.5c,d) implies that the location and extent of the building ridge and upstream trough in the ensemble are associated with changes in the ensemble for block forecast. A region of negative sensitivity on the western flank of the ridge is present at both lead times: increased PV in this region results in a smaller block developing. By linearity, this indicates that if the PV in that region is decreased (i.e. that region becomes part of the ridge) then the area blocked will be larger. It is hypothesized that the ridge building in this case is associated with the divergent outflow from the Stalactite cyclone. There is a region of negative PV advection by the divergent wind on the northern and western flank of the ridge in the deterministic forecast at 96 hours and at 250 hPa (not shown), suggesting that the sensitivity in this region could be associated with the representation of the cyclone in the ensemble. The other main region of sensitivity is positive and is present in the location of a shortwave trough (located near 40°N, 40°W at 96 hours) upstream of the blocking ridge. Consistent with this sensitivity, the increased cyclonic circulation from a stronger trough would steer the Stalactite cyclone further to the north and allow for a larger ridge to build.

In summary, for the NAWDEX block onset ensemble sensitivity analysis reveals that an upstream cyclone is clearly identifiable as the main feature influencing the block forecast. Consistent conclusions can be made looking at sensitivity to Z1000 and PV320.

4.5 Case study II. NAWDEX dryrun

The second case study of block onset, referred to here as the NAWDEX dryrun block, occurred a year prior to the NAWDEX campaign, during a campaign forecast and flight planning test period. It is included briefly here to demonstrate a more complicated link between block onset and upstream cyclone activity than found for the first case study. The NAWDEX dryrun block formed on 27 September 2015, downstream of a merging of

a cyclone propagating across the North Atlantic and another near Greenland (the two merging cyclones are visible in the control forecast of Z1000 in Figs. 4.6a,b).

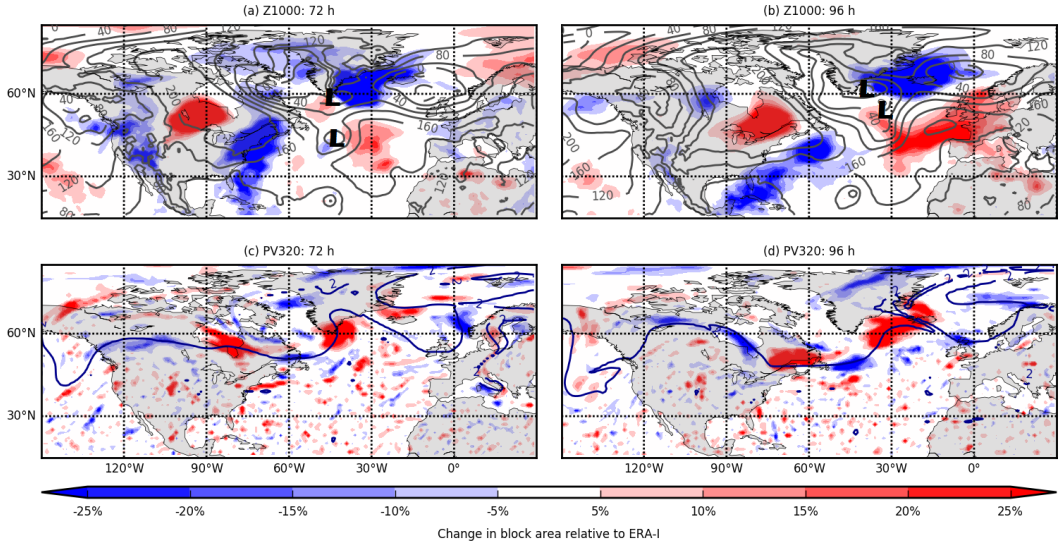

Figure 4.6: Sensitivity of the response function 144 hours into the forecast initiated at 1200 UTC on 21 September 2015 to Z1000 at 72 (a) and 96 (b) hours lead time and PV320 at 72 (c) and 96 (d) hours lead time. The control member forecast of Z1000 (a–b) or the 2-PVU contour (c–d) is overlain.

The sensitivity of the block area to Z1000 and PV320 in the days preceding block onset is shown in Fig. 4.6 for the forecast initiated at 1200 UTC on 21 September 2015. At 72 hours into the forecast (Fig. 4.6a), the regions of highest sensitivity extend further upstream than in the first case study and the highest values are located over North America and between Greenland and Iceland. There is increased localized sensitivity in a dipole around a cyclone propagating across the Atlantic that had a WCB feeding into the block (WCB trajectories not shown). At 96 hours into the forecast (Fig. 4.6b), the high-sensitivity region is now oriented in a dipole with stronger negative sensitivity ahead of the merging cyclones, implying a more intense merging of the two cyclones results in more blocking. The increased sensitivity to Z1000 over North America could be associated with convection in that region: areas of strong convection were present to the west of the Great Lakes and to the northeast of Florida between 24 and 25 September (not shown). The intensity of convection, as inferred from large values of CAPE, was shown to be associated with large forecast errors in Rodwell et al. (2013), though further investigation of the role of this convection is beyond the scope of this study.

The regions of highest sensitivity to PV320 are located in the region near the tropopause: on the western flank of the developing blocking ridge that forms over the

UK and also over North America in similar locations to those of the high sensitivity to Z1000. The sensitivity to PV320 for this case is much stronger than in the NAWDEX case study (compare Fig. 4.6c,d with Fig. 4.5c,d). At 72 hours into the forecast (Fig. 4.6c), the region of large positive sensitivity on the western flank of the blocking ridge over the Atlantic implies that ensemble members with larger magnitude PV320 in this region than in the control member have a larger block form over the UK in the forecast. Larger PV320 in this region could be associated with a smaller ridge or an enhanced cyclonic overturning of the PV contour. By 96 hours (Fig. 4.6d), the ridge–trough system over Canada has amplified and the sensitivity in the region has increased. The region of negative–positive sensitivity in the ridge–trough system suggests that a more amplified ridge–trough feature over Canada is associated with a larger block developing downstream over the United Kingdom.

In summary, ensemble sensitivity analysis indicates that the uncertainty in the ECMWF-EPS for the NAWDEX dryrun onset was associated with several upstream features. The area of the block forecast in the ensemble was sensitive to the following: Z1000 upstream over the Atlantic in the region of several low pressure systems; Z1000 over North America; PV320 along the western flank of the blocking ridge where WCB outflow from an upstream cyclone was located; and PV320 further upstream in the region of another large scale ridge–trough system.

4.6 Uncertain TIGGE block onsets

Ensemble sensitivities are now calculated for the 20 most uncertain block onsets over the Euro-Atlantic region during the study period (defined in section 4.3). The most uncertain block onsets were defined as those that had the largest spread in the six-day forecast of the area blocked in the forecast from the ECMWF-EPS on the date of block onset in the analysis (section 4.3). The two case studies included in the previous sections are among this list of 20 uncertain block onset forecasts.

4.6.1 Hemispheric sensitivity

The sensitivity of the response function in each case to Z1000 two days prior to block onset is shown in Fig. 4.7. Note that in each case the blocked region corresponds to the upper-right corner of the figure (marked by the black box in Fig. 4.7a) and that the cases are grouped, as described, according to the location of the block: Greenland, the UK

or Scandinavia. The feeder cyclones that amplified the blocking ridges, identified using trajectory analysis, are indicated with an 'L'.

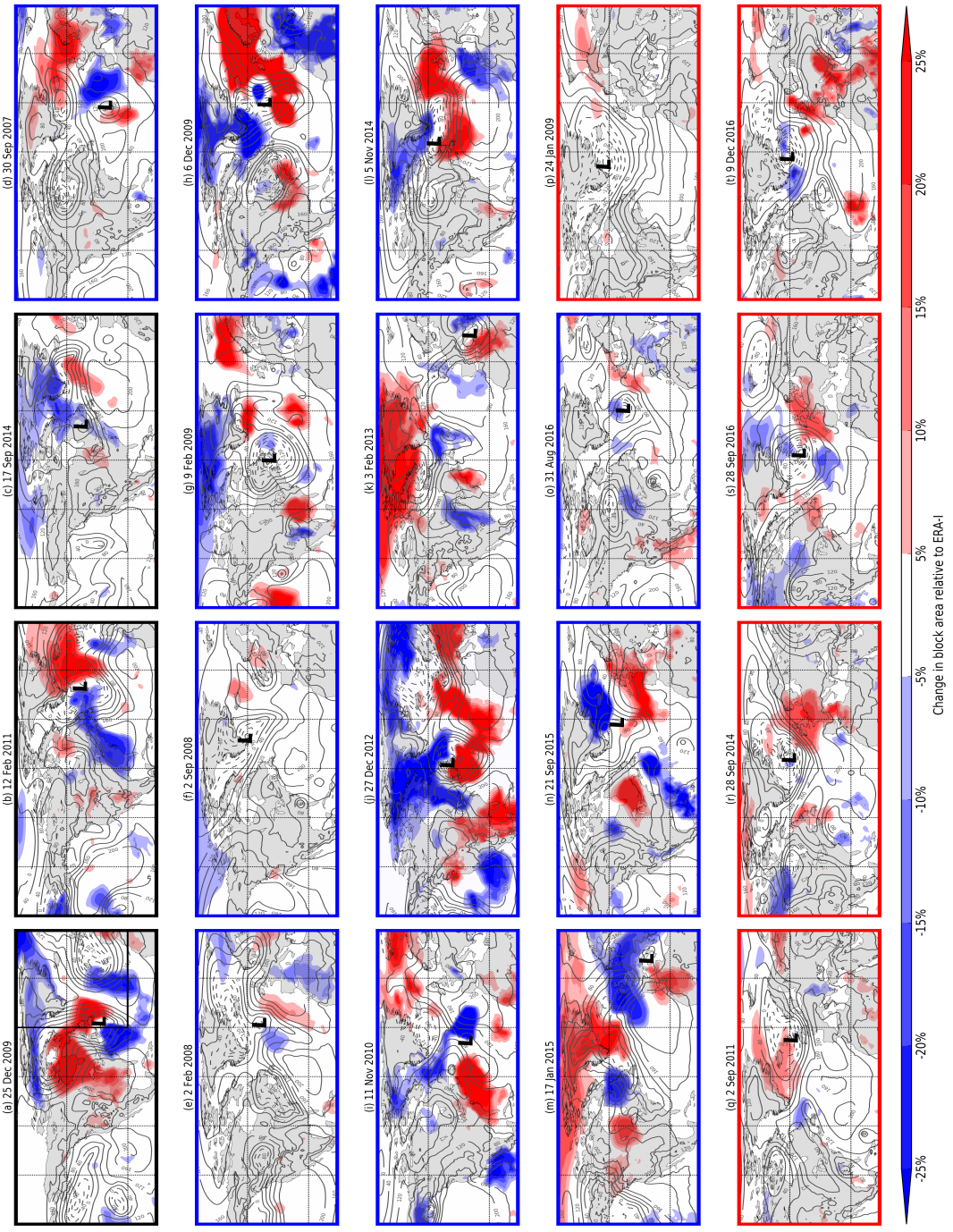

Figure 4.7: Sensitivity of the block area in the ensemble at 144 hours to Z1000 at 96 hours for the 20 onset cases. Block onsets are separated into those occurring over Greenland (black map boundary), the UK (blue map boundary) and Scandinavia (red map boundary). The control member forecast of Z1000 is overlain in contours (every 40 m). The date shown for each onset date is the date that the forecast was initiated.

The patterns and magnitudes of sensitivity are different in each onset case. The magnitude of the sensitivity values is dependent on the area of the block in ERA-I because we present the results as a percentage change in this area to reflect the relative influence of the cyclone in each onset case. Presenting the sensitivity as an absolute value of block area change does not change the interpretation of the results included in this section. Although the patterns are different, common features exist: the region of highest sensitivity is located upstream of the block location, rather than over a large part of the northern hemisphere, and there is usually a cyclone (or cyclones) located upstream over the Atlantic ocean. Three sensitivity patterns occur: (i) large-scale wave-train-like patterns extending far upstream (Figs. 4.7g,h,i,j,k,m,n); (ii) more localized sensitivity just upstream of where the block forms (Figs. 4.7a,b,c,d,e,l,o,q,r,s,t); and (iii) little sensitivity across the whole domain (Figs. 4.7f,p). In several onset cases there is also increased sensitivity to cyclone activity in the Mediterranean. Because the ensemble sensitivity analysis shows an association (rather than causality) between the representation of blocking and an earlier forecast of Z1000, it is no surprise that in some cases the sensitivity extends far upstream in a wave-like feature (Figs. 4.7g,h,i,j,k,m,n). For the Rossby-wave structure (including the block) to be well represented over Europe, the large-scale trough-ridge structure will have to be in the correct location and phase as well. Block onsets over Europe are frequently supported by a quasi-stationary Rossby-wave train coming from the subtropical western Atlantic (Nakamura et al., 1997). This pattern would be associated with surface activity (such as cyclones) in several upstream regions.

The sensitivity to PV320 two days prior to block onset in each case is shown in Fig. 4.8. Again, the pattern and magnitude of sensitivity is different in each case. The commonality between cases is that the sensitivity is focused generally along the 320-K tropopause, often in bands aligned with the tropopause, and that it generally has maximum magnitude around the ridge that becomes the block. The sensitivity to PV320 on either side of the tropopause indicates spread in the ensemble forecast in this location has a large downstream effect. Spread in the ensemble in PV320 near the tropopause could develop from the one or more of the five mechanisms of proposed near-tropopause PV error growth found in a case study by Davies and Didone (2013). We expect diabatic processes to modify the PV structure near the tropopause (e.g. Joos and Wernli, 2012; Chagnon et al., 2013) so the increased sensitivity in each case near the tropopause could also imply that the diabatic processes within each ensemble representation of the cyclones are the cause of this sensitivity. Furthermore, this increased sensitivity to PV is

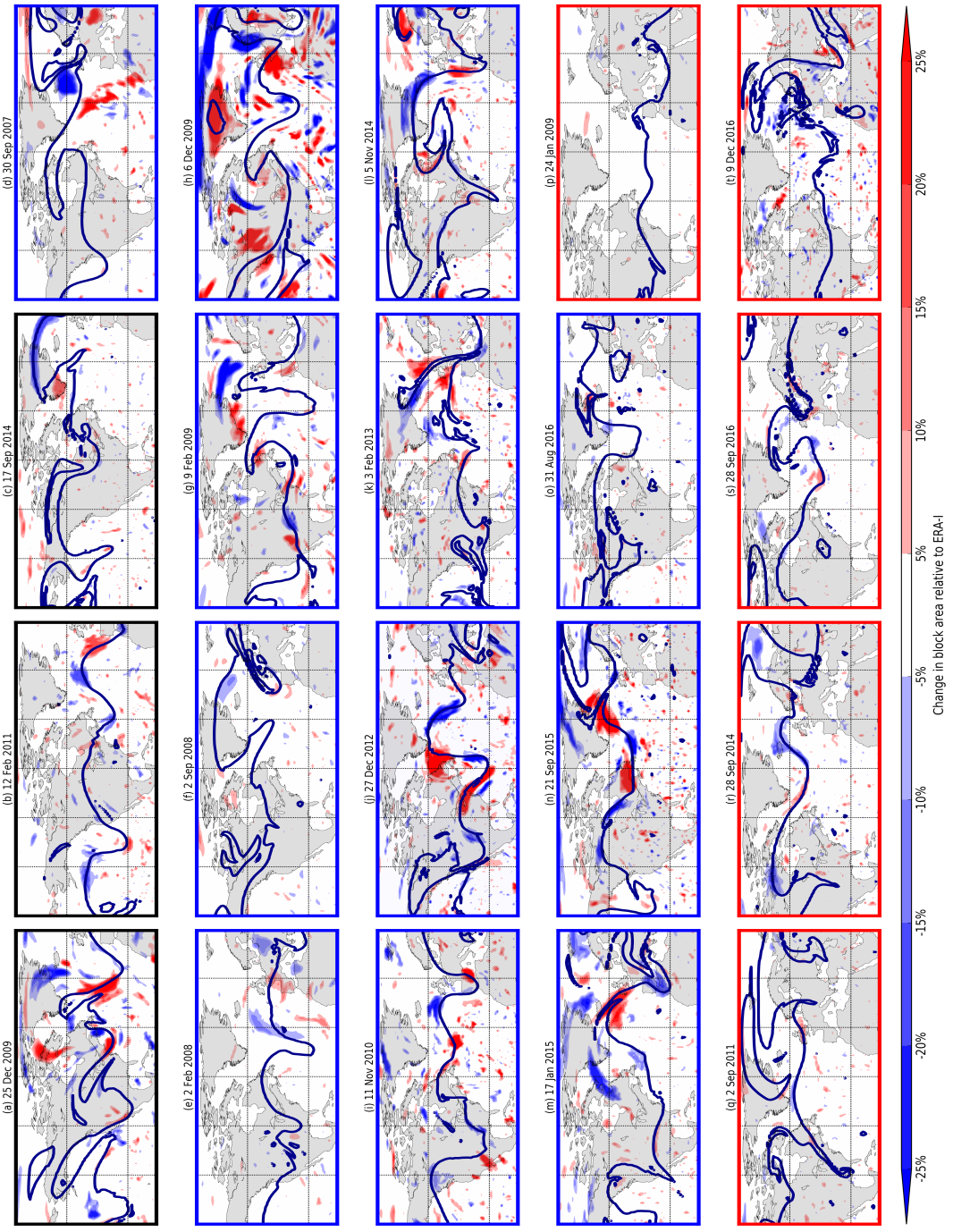

Figure 4.8: As in Fig. 4.7 but for sensitivity to PV320. The control member forecast of the 2-PVU contour is overlain.

often in the ridge ahead of the surface cyclone that was associated with large sensitivity, implying the sensitivities are highlighting real dynamical features that are important for block formation and not spurious sensitivities occurring as a consequence of our relatively

small ensemble. The sensitivity of block onset to upstream cyclone representation in the ensemble can be inferred from both sensitivity fields. However, some onsets show little sensitivity to either field. This implies that the uncertainty in the ensemble forecast of these onsets of blocking at six days lead time was not associated with increased spread in the earlier forecast of Z1000 or PV320. This does not necessarily imply that the forecast was not sensitive to cyclone structure because Z1000 and PV320 cannot describe a cyclone's structure fully. Influence from the stratosphere or more local effects could also be important in these cases. There are also some onsets that show sensitivity to one field but not the other, e.g. for the onset forecast from 2 September 2011 (Figs. 4.7q, 4.8q).

The aim of this part of the study was to determine the impact of the forecast of upstream cyclones on the downstream representation of blocking in uncertain medium-range forecasts. Even though in many of the block onset cases there is large sensitivity in the region upstream of the block around one or more cyclones, the sensitivity in the region of the feeder cyclone for the majority of the block onset cases is as large (or larger) than sensitivity in other regions. This indicates that cyclone representation is of first-order importance for downstream block forecast.

4.6.2 Ensemble sensitivity for alternative function results

Sensitivity to Z1000 and PV320 for each onset case was also calculated for the RMSE of Z500 and ridge area response functions described in section 4.3.3.2. The general features identified using the block area as the response function are present in both other response functions: the sensitivity field to Z1000 resembles either a large wave-train pattern extending far upstream, a localized region of sensitivity near an upstream cyclone or reduced sensitivity across the domain; and the sensitivity to PV320 is focused along the tropopause. Results of the ensemble sensitivity analysis are summarized in Table 4.1. The majority of block onset cases have similar patterns in sensitivity to those shown in Figs 4.7 and 4.8 for both the RMSE of Z500 and ridge area response functions. Similarity between patterns is based on large-scale sensitivity patterns identified by eye. Large sensitivity near the upstream feeder cyclones and around the upper-level blocking ridges is also found for both additional response functions, though in fewer of the cases than with the block area response function. The consistency in sensitivity patterns between response functions used in the sensitivity analysis demonstrate that the result that the forecast of block onset is sensitive to the representation of upstream cyclones is robust to

the definition of response function.

4.6.3 Feeder cyclone sensitivity

To analyze the sensitivity to each block's feeder cyclone in more detail, the sensitivity maps are now restricted to a $30^\circ \times 30^\circ$ domain centered on the cyclone at the lead time for which the sensitivity was greatest; this time is either two or three days prior to the analyzed block onset (i.e. at 72 or 96 h), and so differs from Fig 4.7 for which 96 h is used for all panels. The ordering of panels is also changed and is grouped based on the type of sensitivity pattern found in the feeder cyclone restricted domains. In the cases where more than one cyclone was identified as ridge building, the cyclone with most trajectories ending in the block was selected. In most cases the feeder cyclones are located to the west of the block over the Atlantic. However, in the forecasts of block onset valid on the 3 February 2013 (Fig. 4.9e) and 17 January 2015 (Fig. 4.9g) it is a Mediterranean cyclone to the south of the block that contributed most to ridge building and was associated with the large sensitivity. Three characteristic patterns of sensitivity to the upstream cyclone emerge from Fig. 4.9. The block onsets have sensitivity to an upstream cyclone with any of the following:

(i) a dipole of sensitivity either side of the cyclone center (panels a–n). These can be oriented with positive sensitivity to the east of the cyclone and negative to the west or vice versa, as well as with positive sensitivity to the north and negative to the south and vice versa. There is no obvious dominant orientation;

(ii) a monopole of sensitivity in the location around the cyclone (panels o–q); or

(iii) little sensitivity in the location of the cyclone (panels r–t).

The block onsets that have a dipole in sensitivity around the feeder cyclone were influenced by the earlier forecast of the location and/or intensity of their feeder cyclone as can be inferred using the results of the idealized sensitivities (Section 4.3.3.3) as follows. For the onsets that have quasi-symmetric dipoles around the cyclone (e.g. Figs. 4.9f,i) it was the forecast location of the cyclone among the ensemble that was associated with the biggest change in block area forecast. Onsets with one lobe of the dipole larger or of greater magnitude were sensitive to both the location and the intensity of the cyclone in the forecast: if the positive lobe dominates it is the less intense systems that result in more blocking, and vice versa. If the dipole is oriented with negative sensitivity ahead of the cyclone it is the systems further to the east that result in a large block; positive

Table 4.1: The sensitivity patterns using RMSE Z500 and ridge area as the response functions are compared to those using block area as the response function. The numbers indicate the number of cases (of the 20 studied) for which the sensitivity fields are similar (1st and 3rd columns of numbers) and the number of cases, for all three response functions, where there is locally increased sensitivity near to a specific feature (2nd and 4th columns).

Response function	Similar pattern in sensitivity to Z1000 as block area	Increased sensitivity near upstream cyclone	Similar pattern in sensitivity to PV320 as block area	Increased sensitivity to upper-level ridge
Block area	——	17	——	16
RMSE Z500	13	14	16	12
Ridge area	14	13	16	14

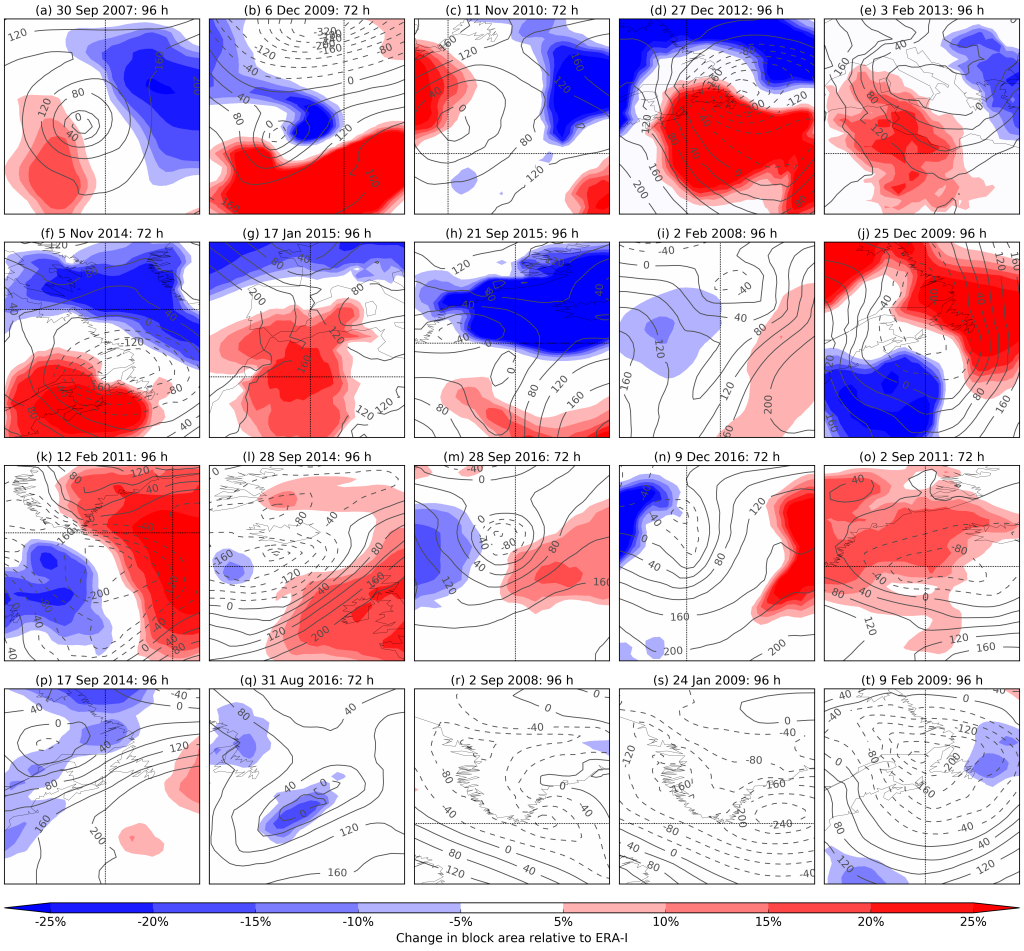

Figure 4.9: Sensitivity of the block area at 144 hours to Z1000 in the region of the upstream feeder cyclone at 72 or 96 hours lead time (whichever time the sensitivity was greater). For the onsets that have maximum sensitivity at 96 hours the data shown is a zoomed in version of that shown in Fig. 4.7. The control forecast of Z1000 is overlain in contours.

sensitivity ahead implies it is the cyclones further west. When there is a monopole in sensitivity near the location of the feeder cyclone this implies the cyclone's intensity was most important for downstream block development sensitivity. Of the 20 block onset cases considered, 14 have a dipole in sensitivity (8 with positive-negative orientation, 6 with negative-positive), 3 onsets resemble monopoles and 3 onsets have little sensitivity to the upstream feeder cyclone.

These patterns of sensitivity demonstrate that the location or intensity (or both) of an upstream cyclone two or three days prior to block onset is important in the forecast of blocks that showed largest uncertainty during recent years. Of the 20 onsets that had the largest spread in their six-day forecast of block onset, 17 had large sensitivity to an upstream feeder cyclone: a one standard deviation change in Z1000 is associated with

a 20-25% change in block area. The results also show that upstream cyclones are not always important for unpredictable block onsets over the North Atlantic and Europe.

4.6.4 The relationship between cyclone characteristics and ensemble sensitivity

In this section we assess the relationship between characteristics of the feeder cyclones and total ensemble sensitivities in each of the 20 block onset cases. For each case we correlate spatially summed ensemble sensitivities for Z1000 and PV320 and also correlate these sensitivities with feeder cyclone characteristics. The sum over the domain of the magnitude of the sensitivity at each grid point (termed 'total sensitivity') is our sensitivity metric. For example, the total sensitivity to Z1000 at 96 h for the first case shown in Fig. 4.7 is calculated by summing the magnitude of the sensitivity values at each grid point in Fig. 4.7a. This simple metric provides a single value of total sensitivity (i.e. uncertainty in block area associated with Z1000 or PV320) for each of the onset cases at each lead time. We use magnitude of minimum Z1000 (in the control forecast) at 72 and 96 h as measures of cyclone intensity and number of WCB trajectories within the 72 h before block onset (in the ECMWF operational analysis) as a measure of WCB intensity. Total sensitivity to Z1000 and PV320 are highly correlated with themselves (significant at the 10% level) for different lead times as well as with each other at the same and different lead times. PV320 has higher correlation when comparing its sensitivity at 72 and 96 h (0.964) than Z1000 (0.834). When comparing the different fields, the correlation between sensitivity to Z1000 at 72 h and sensitivity to PV320 at 96 h is the highest (0.938), with the correlation between sensitivity to PV320 at 72 h to Z1000 at 96 h the lowest (0.792). This result supports the hypothesis that in the block onset cases sensitivity to surface cyclones evolves with the flow to become sensitivity to the upper-level Rossby wave pattern (likely via changes to WCB representation).

Total sensitivity to either Z1000 or PV320 is not significantly correlated with cyclone intensity at either lead time. This implies that the degree of uncertainty in block size associated with feeder cyclone location and/or intensity, or upper-level Rossby wave pattern, does not depend on feeder cyclone intensity in our 20 cases. Total sensitivity to PV320 at 72 and 96 h are both significantly correlated to WCB intensity (0.438 and 0.384 respectively), whereas total sensitivity to Z1000 is not significantly correlated with WCB intensity at either lead time. The significant correlations found between WCB intensity

and total sensitivity to PV320 further support our hypothesis that the high sensitivity of block area to PV320 in the ensemble arises from the modification of the upper-level Rossby wave structure by WCBs.

4.7 Conclusions

The importance of cyclone representation in uncertain medium-range forecasts of block onset over the Euro-Atlantic region in the ECMWF-EPS has been assessed systematically over many forecasts here for the first time using ensemble sensitivity analysis. The onset of blocking has been shown to be sensitive to upstream features previously in several different models and using a variety of methods (e.g. Yang et al., 1997; Frederiksen, 1998; Frederiksen et al., 2004; Matsueda, 2011), though normally for single case study events. In this study we focus on the relationship between uncertainty in operational NWP model forecasts of blocking and upstream cyclones in a larger set of case studies. The effect surface cyclone representation can have on the downstream block forecast has been illustrated in two case studies of block onset over Europe related to the NAWDEX field campaign (Schäfler et al., 2018). Differing cyclone intensity and location among the ensemble in the days prior to block onset was associated with different Rossby wave evolution and block formation (or not). Ensemble sensitivity analysis was used to verify that the ensemble forecast of the block onsets was sensitive to changes in the upstream surface geopotential height pattern as well as to changes in PV in the region around the tropopause. The sensitivity to PV was generally strongest around the edge of ridges, which is where we expect diabatic outflow of WCBs to have a strong impact.

To investigate this case dependence in more detail, the relationship between block onset and upstream cyclone activity has been studied using ensemble sensitivity analysis for 20 cases (including the two cases described above) of block onset over the Euro-Atlantic region that had large ensemble spread in their six-day forecasts. The forecasts of block onset were shown to be generally sensitive to the upstream surface geopotential height pattern and upper-level PV field in the days preceding the block onset. The sensitivity to Z1000 was largest upstream of the block location and typically associated with a surface cyclone, usually over the North Atlantic though in two cases over the Mediterranean. The sensitivity pattern sometimes extended far upstream implying, as to be expected, that the hemispheric phasing of Rossby-waves associated with surface weather upstream is important for block formation in a given region. The sensitivity to PV320 was generally

greatest near the tropopause (2-PVU contour), where diabatic processes in extratropical cyclones modify the PV structure. Significant correlations were found between the total sensitivity to Z1000 and PV320 in the 20 cases. The total sensitivity to PV320 in the ensemble was shown to be positively correlated to the intensity of the WCB of the feeder cyclone in the ECMWF operational analysis. However, the total sensitivity to PV320 and Z1000 did not depend on the intensity of the feeder cyclone in the control forecasts.

To focus on the importance of upstream cyclone forecasts, the sensitivities were calculated in the region of each block onset's upstream feeder cyclone (established from the WCBs identified by back-trajectories from within the block) at the time the block area exhibited maximum sensitivity to the cyclone. Blocks associated with more than one cyclone were prescribed a primary feeder cyclone based on the WCB that had the most trajectories. The forecast location and intensity of the upstream cyclone is shown to strongly influence block formation in 17 of the 20 onset cases considered. Changes in the ensemble forecast of geopotential height in the region of an upstream cyclone in the Atlantic were shown to be associated with a large change in the forecast block area: 20-25% of the area of the block in ERA-I. The pattern of sensitivity is different for each case, suggesting that there is no systematic error in block onset related to upstream cyclone forecast. The relative importance of cyclone intensity and location for block formation was interpreted using sensitivity patterns generated using idealized cyclones: 14 of the 20 block onset cases had a dipole in sensitivity around their feeder cyclone implying that the forecast location dominated the impact on downstream block development with some importance of intensity of the cyclone for asymmetric dipoles; 3 of the cases had a monopole in sensitivity implying that the forecast of cyclone intensity was most important; and the remaining 3 cases had little sensitivity near the cyclone.

The results presented in this study are generally consistent with the large body of work investigating upstream influences on block dynamics. The demonstrated sensitivity to large-scale wave-train like features extending from the subtropics suggest that the importance of low-frequency Rossby wave trains in analyzed blocking events over Europe (Nakamura et al., 1997) is also important in the forecast of block onset over Europe. The sensitivity of block formation over the North Atlantic to upstream perturbations off the coast of North America, found when examining instabilities of the flow in quasi-geostrophic models (Frederiksen and Bell, 1990; Frederiksen, 1998), is consistent with the sensitivity in operational EPS found here. Colucci (1987) and Lupo and Smith (1995) highlight the existence of an upstream cyclone in all their considered cases of analyzed

blocking events: we find this is also true for the forecast of the 20 block onset cases included here. The conclusion that uncertain forecasts of block onset are sensitive to upstream cyclones is directly comparable with Magnusson (2017). The sensitivity of a blocking event (a forecast bust in ERA-I) to Z500 was highest upstream in the western Atlantic and was linked to the poor forecast of a cyclone developing in the same region. Here we have looked at the sensitivity of many block onset cases to Z1000 and demonstrated that cyclone representation is associated with large forecast sensitivity in the majority of cases. This result implies that cyclone representation could have a large influence on forecast busts over Europe and that better representation of the cyclones could help reduce the frequency of forecast busts that are associated with block onset. The results presented here are also consistent with Matsueda (2011) who showed that a block over the Rockies was sensitive to an upstream cut-off cyclone in the Pacific.

Using ensemble sensitivity analysis we have shown that block onset forecasts are often limited by the forecast of an upstream surface cyclone. The question then arises of why the cyclone forecasts are uncertain. Sensitivity along the wave guide further upstream of the cyclones in many cases suggests that transient upper-level features may also be associated with the increased uncertainty in the cyclone development and downstream influence. Diabatic processes are often intense in the WCBs of extratropical cyclones and have also been shown to affect cyclone development (e.g. Joos and Wernli, 2012). For example, the low-level, diabatically-produced positive PV anomaly beneath the region of maximum heating was shown to contribute about 40% to the circulation in a mature cyclone by Davis and Emanuel (1991). In NWP models diabatic processes need to be parametrized and different parameterizations have also been shown to result in different WCB development (Martínez-Alvarado and Plant, 2014). The parametrization of diabatic processes in extratropical cyclones are a source of model uncertainty in addition to initial condition, boundary condition and other model uncertainties. Future work should investigate the relationship between parameterized physical processes in NWP models and the downstream development of blocking and determine if different or better parameterizations can reduce the uncertainty in forecasts of block onset.

Chapter 5:

Impact of model upgrades on diabatic processes in extratropical cyclones and downstream forecast evolution

In chapter 4, forecasts for the onset of blocking events that had large uncertainty were shown to be often sensitive to the earlier forecast of upstream cyclones. The technique utilized in chapter 4 to demonstrate this sensitivity was purely statistical so no causal dynamical mechanism behind the sensitivity could be proven. The dynamical mechanism behind the sensitivity of block forecasts to upstream cyclones was hypothesised to be warm conveyor belts, as these are known to transport air within cyclones into blocking ridges (Pfahl et al., 2015) and have been shown to cause forecast error in case studies of blocking events (Martínez-Alvarado et al., 2016b; Grams et al., 2018). In this chapter, model upgrades to the parameterisation of diabatic processes are used to investigate the link between diabatic heating in warm conveyor belts and the downstream amplification of ridges and block development. This is motivated by the known influence of parameterised diabatic processes on the development of warm conveyor belts and downstream flow evolution (Martínez-Alvarado and Plant, 2014; Joos and Forbes, 2016).

This chapter has been submitted to the Quarterly Journal of the Royal Meteorological Society.

5.1 Abstract

Models are continuously developed at numerical weather prediction (NWP) centres to improve forecast skill, with new operational model configurations adopted every few years. The parameterisations of diabatic processes are probably the most frequently updated part of NWP models as they are crucial for accurate weather predictions and contain uncertainties in their formulation. The impact of model developments is assessed here in forecasts from the Met Office's weather forecast model initialised throughout the North Atlantic Waveguide and Downstream Impact Experiment field campaign period in autumn 2016. Planned model parameterisation developments are considered, together with an 'inexpensive coupled' forecast with daily updating of the sea surface temperature and sea-ice fraction. Forecasts produced from the coupled system have, on average, indistinguishable skill from the control forecasts, suggesting the benefits of coupled atmosphere-ocean NWP systems can be small. In contrast, a reduction in forecast error ($\sim$4%) is identified in forecasts produced using an upgraded convection scheme. Periods of low forecast skill during the study period are shown to be associated with the onset and decay of blocking events and increased diabatic heating of air masses reaching the upper troposphere. In forecasts of a specific block development case that was not accurately predicted in any of the experiments or in the operational ensemble forecast from the Met Office, the representation of diabatic heating in the warm conveyor belt of an upstream cyclone is shown to moderate the subsequent block development: forecasts in which the heating is stronger generally have a more-amplified blocking ridge and amplified heating contributions from all parameterisations as diagnosed using diabatic tracers. Hence, we demonstrate that plausible changes to the representation of several different diabatic processes in models can impact forecast block development via changes within upstream cyclones.

5.2 Introduction

Numerical weather prediction (NWP) centres across the globe routinely produce forecasts of the weather for the coming days, weeks and even months, with the use of highly complex numerical models of the atmosphere. The models generally consist of a dynamical core that is used to numerically solve the atmosphere's equations of motion; a data assimilation system that ingests millions of observations into the model to produce

an initial state of the atmosphere; a set of parameterisation schemes needed to represent processes occurring on scales smaller than those producible by the model; and boundary conditions for the model such as a description of roughness length, sea surface temperature (SST), soil moisture and vegetation cover. Each component of the NWP model is being constantly developed in an effort to improve the forecasts and new model configurations, consisting of many changes to its various parts, become operational every few years. The parameterisations within the model, representing processes occurring on scales smaller than the grid scale, are one of the most frequently updated components of the model. They are known to have a large impact on forecast error (e.g. Bauer et al., 2015), and contain uncertain parameters that need to be tuned to correspond with changes elsewhere in the model. The purpose of this article is to quantify the relative impact of several operational improvements to parameterisations that affect diabatic processes on forecasts of extratropical circulation features.

Weather forecasts can have errors that arise from uncertainty in defining an initial state of the atmosphere and imperfections in NWP model formulation. These are commonly termed initial condition (or analysis) and model errors, respectively. Ensemble prediction systems (EPSs) have been introduced at many operational NWP centres in recent decades to account for both initial condition and model error (Buizza et al., 2005). To represent initial condition uncertainty, the probability distribution function (PDF) of possible initial conditions is sampled by adding dynamically-defined perturbations to the model's analysis (e.g. Molteni et al., 1996; Bowler et al., 2008); an ensemble of simulations is produced giving a probabilistic description of the weather. Model error is typically accounted for by the addition of stochasticity to parameterisation schemes (Buizza et al., 1999). Initial condition error is typically larger than model error in medium-range weather forecasts (Arpe et al., 1985; Rabier et al., 1996), though several studies have shown that model error cannot be ignored (Harrison et al., 1999; Buizza et al., 1999; Stensrud et al., 2000; Orrell et al., 2001), and both initial condition and model error can depend on geographical region and weather pattern. Forecast uncertainty in operational NWP models is generally highest for the transition to, and maintenance of, a blocked state (Ferranti et al., 2015; Matsueda and Palmer, 2018). Improvements to the models' parameterisation schemes (Jung et al., 2010; Dawson and Palmer, 2015; Joos and Forbes, 2016) and dynamical cores (Martínez-Alvarado et al., 2018), as well as increased resolution (Matsueda, 2009; Davini and D'Andrea, 2016; Schiemann et al., 2017), have been shown to improve forecasts of extratropical circulation features and atmospheric blocking in NWP

and climate models. Boundary conditions, in particular SST, have also been shown to affect block development (Scaife et al., 2011; O'Reilly et al., 2016) and increasing the spatial resolution of SST can improve operational forecasts from the European Centre for Medium-range Weather Forecasts (ECMWF, Chelton, 2005).

Diabatic processes active in extratropical cyclones typically occur on scales smaller than the grid in global weather forecast models and hence must be parameterised. These diabatic processes, especially latent heat released by the condensation of water vapor, can contribute considerably to the intensification of extratropical cyclones (Davis and Emanuel, 1991; Stoelinga, 1996). Therefore their parameterisation is key for the accurate forecast of these systems. Latent heat release in the mid-troposphere produces a positive low-level potential vorticity (PV) anomaly which can induce rapid cyclogenesis if it favorably interacts with an upper-level positive PV anomaly (Wernli et al., 2002; Ahmadi-Givi et al., 2004). One effect of parameterised diabatic processes in extratropical cyclones is to enhance the tropopause-level PV gradient (Chagnon et al., 2013) where a sharp increase from low PV values in the troposphere to high PV values in the stratosphere is observed. Warm conveyor belts (WCBs), the broad cloudy ascending airstreams flowing poleward in the warm sector of extratropical cyclones, are the regions of primary latent heat release in cyclones (Browning and Roberts, 1994). The representation of WCBs in extratropical cyclones is also sensitive to the parameterisation of diabatic processes (Joos and Wernli, 2012; Joos and Forbes, 2016) which, in turn, can affect the upper-tropospheric PV structure and downstream flow development (Pomroy and Thorpe, 2000). This relationship suggests that the parameterisation of diabatic processes could also be important for the representation of the upper-tropospheric negative PV anomalies that define blocks. We investigate the impact of model physics uncertainty on the representation of upper-tropospheric ridge amplification and atmospheric blocking here.

Extratropical cyclones force the geopotential height rises in developing blocks through thermal and vorticity advection (Colucci, 1985; Nakamura and Wallace, 1993) and the repeated transfer of low-PV air polewards and upwards within cyclones into blocking ridges can act to maintain them against dissipation (Shutts, 1983; Yamazaki and Itoh, 2013; Luo et al., 2014). Diabatically-heated air masses can contribute considerably (>50%) to the total mass of blocked regions in the northern hemisphere (Pfahl et al., 2015). Atmospheric blocks are notoriously difficult to forecast in NWP models (e.g. Tibaldi and Molteni, 1990; Pelly and Hoskins, 2003a; Matsueda, 2009) and are the cause of some of the worst forecasts produced at operational NWP centres (Rodwell et al., 2013; Lillo

and Parsons, 2017). Grams et al. (2018) showed in a case study of a large forecast error originating from a missed blocking event that it was the poor forecast of an upstream cyclone's WCB that was the cause of the error. Forecasts of the most uncertain block onset cases in recent years were shown to be strongly influenced by the representation of upstream extratropical cyclones by Maddison et al. (2019). Furthermore, ridges in the tropopause are systematically misrepresented in operational NWP models (Gray et al., 2014) with the area and isentropic PV gradient of ridges decreasing with lead time. The sharpening of the isentropic PV gradient by parameterised diabatic processes can be too weak to maintain the strong PV-gradients in forecasts (Saffin et al., 2017). A case study that had an error representative of this systematic bias was caused by the poor forecast (too weak and too far south) of WCB outflow (Martínez-Alvarado et al., 2016b).

Previous studies investigating the sensitivity of extratropical cyclones and atmospheric blocking to model physics or boundary conditions have often made large changes in parts of the model to obtain a large response in the representation of the feature of interest, such as removing moisture (Davis et al., 1993; Wernli et al., 2002; Coronel et al., 2015), changing parameterisation schemes (Carrera et al., 1999; Dearden et al., 2016) and reducing the physical tendencies from parameterisations (Martínez-Alvarado and Plant, 2014). Generally, cyclones are less intense and downstream upper-level ridges smaller when the diabatic effects are reduced. Smoothing the SST gradient near the Gulf Stream, or reducing the SST and maintaining the sharp front, can also reduce the intensity of cyclones (Sheldon et al., 2017) and reduce the frequency of blocking over Europe (O'Reilly et al., 2016). The approach taken here is different: we make small changes to various parameterisation schemes that constitute (or could constitute) an operational upgrade to the scheme. Joos and Forbes (2016) showed that an operational upgrade to the microphysical parameterisation in the ECMWF Integrated Forecasting System (IFS) had an impact on the simulation of a cyclone's WCB and downstream ridge building. Whilst changes to the forecast evolution were initially small, they were advected with and amplified by the flow resulting in marked differences in the upper-tropospheric PV pattern. An operational improvement to the radiation scheme in the IFS was also shown to systematically improve the skill of medium-range weather forecasts of geopotential at 200, 500 and 1000 hPa (Morcrette et al., 2008). A new operational version (cycle) of the ECMWF model, that differed primarily in its parameterisations of physical processes, was shown to improve the representation of blocking in seasonal forecasts (Branković and Molteni, 1996). In this article, planned operational upgrades to the Met Office Unified

Model (MetUM) to various physical parameterisations are introduced separately to assess the impact of each parameterisation on the forecast evolution.

The research presented in this article addresses the following research questions.

1. Do model upgrades to physical parameterisations and boundary conditions have a systematic effect on forecasts of upper-tropospheric Rossby wave development and blocking?

2. How does the effect on the forecast evolution from model changes compare to initial condition uncertainty?

3. Does the previously found error in block forecasts associated with upstream cyclone representation and WCB structure (e.g. Matsueda, 2011; Grams et al., 2018; Maddison et al., 2019) originate from uncertainty in the representation of diabatic processes in extratropical cyclones?

These questions are motivated by relatively new results showing that the dynamics and predictability of upper-tropospheric Rossby waves and atmospheric blocking events are influenced strongly by diabatic processes within extratropical cyclones (Pfahl et al., 2015), especially those active in their WCBs (Martínez-Alvarado et al., 2016b; Grams et al., 2018). In this article we follow forecast evolution changes that are triggered by the model upgrade's effect on parameterised diabatic heating from cyclone and WCB development to upper-level Rossby wave amplification and blocking.

The article is organised as follows. Details of the model simulations used in this study are given in section 5.3 and the methods used to analyse them are described in section 5.4. An overview of the results from forecasts initialised across the study period are presented in section 5.5. In section 5.6, a particular case study of block onset following extratropical cyclone intensification is described together with a verification of the operational forecast of the case and its representation in the study experiments. The sensitivity experiments are compared with the control simulation in section 5.7, with a focus on the role of diabatic processes in the sensitivity of upper-tropospheric flow to parameterised physical processes. We summarise the results and give conclusions in section 5.8.

5.3 Met Office Unified model experiments

In this section, details are given of the sensitivity experiments that are performed with the MetUM and analysed in this study. The MetUM is the numerical model developed and used by the Met Office for both weather and climate modelling. The model is continuously developed with new configurations being implemented operationally every few years. The experiments used in this study are mainly based around an operational upgrade in the MetUM from configuration Global Atmosphere (GA)6.1 to GA7.0, which is scheduled for November 2019. Experiments implementing the GA7 cloud, microphysics and boundary layer schemes into the GA6.1 configuration of the model are performed as well as a convection parameterisation experiment and a SST updating experiment. The control run is a MetUM GA 6.1 (Walters et al., 2017b) run at N768 resolution with 70 model levels and an 80 km top. This is a rerun of the operational configuration of the MetUM that was used during the study period (autumn 2016). The experiments are summarised in Table 5.1 and a more detailed description of the MetUM and each of the sensitivity experiments is given in the Appendix.

The sensitivity experiments are separated into two groups: (1) the SST-update and Prog-ent experiments and (2) the experiments in which the different schemes are modified to their GA7 versions. The Prog-ent and SST-update experiment have been initialised every 12 hours (at 00 and 12 UTC) during the North Atlantic Wave and Downstream impact EXperiment (NAWDEX, Schäfler et al., 2018) field campaign period (20 September–16 October 2016) and integrated for 12 days, giving a total set of 54 12–day runs. NAWDEX was a field campaign investigating the diabatic influence on the jet stream and high impact weather over Europe. The NAWDEX campaign period included several extratropical cyclones and upper-level ridge building events which make it an ideal study period for this work. Whilst the SST-update experiment could never be implemented to produce an operational forecast, it is used to provide insight into the potential benefit of using a coupled model system for NWP. The GA7 physics experiments (GA7Mp, GA7Cl, GA7Bl) have been run for a single chosen forecast initiation date to determine their impact for a blocking case study. All of the experiments are global model runs with output of certain diagnostics restricted to every 12 hours and in the Euro-Atlantic region (defined as 20.25°–80.55°N, 79.875°W–40.725°E, which covers the region of interest for the NAWDEX campaign period).

Table 5.1: Summary of forecast experiments.

Name	Experiment description
SST-update	SST and sea-ice fractions are updated daily during the forecast evolution to the Operational Sea Surface Temperature and Sea Ice Analysis (OSTIA, Donlon et al., 2012)
Prog-ent	The convection scheme in the GA6.1 configuration is changed to the prognostic entrainment convection scheme that has been developed at the Met Office to include memory of recent convective activity
GA7Mp	The modifications to the microphysical parameterisation scheme for the GA7 configuration are implemented, including a new treatment of sub-grid cloud water content variability; a change to the warm rain microphysics; and a change to the turbulent production of liquid water in mixed-phase clouds
GA7Cl	The modifications to the large-scale cloud parameterisation scheme for the GA7 configuration are implemented, including a representation of convective core radiative effect; a new critical relative humidity based on turbulence; and the removal of complexity when dealing with ice cloud
GA7Bl	The modifications to the boundary layer parameterisation scheme for the GA7 configuration are implemented, including a dependence on coupling for boundary layer entrainment; a representation of clouds forming at boundary layer top; and a retuned cloud threshold used to diagnose a shear dominated boundary layer

5.4 Methods

5.4.1 Block identification

Blocking is identified in this study using a modified version of the 2D 500 hPa geopotential height (Z500) blocking index introduced by Scherrer et al. (2006), an extension of the 1D index of Tibaldi and Molteni (1990). The index is calculated using meridional gradients in $Z500$, termed GHGN and GHGS for northern and southern gradients respectively. The gradients are calculated at each longitude for latitudes (ϕ_0) between 35° and 75°N:

GHGN $= \frac{Z(\phi_N)-Z(\phi_0)}{\phi_N-\phi_0}$ and GHGS $= \frac{Z(\phi_0)-Z(\phi_S)}{\phi_0-\phi_S}$, where

$\phi_S = \phi_0 - 15°$ and $\phi_N = \phi_0 + 15°$. A latitude, longitude grid point is then defined as being blocked if GHGS > 0 and GHGN < -10 $(m/°)$. A schematic showing an example $Z500$ field that satisfies these criteria is shown in Fig. 1 of Martínez-Alvarado et al. (2018). The index is extended here to identify blocks north of 75°N. For latitudes north of 75°N, GHGN is calculated using the remaining latitudes to ϕ_N at the pole; and the threshold on GHGN to identify a block is scaled relative to the distance to the pole. GHGS is calculated in the normal way.

5.4.2 Anticyclone tracking

Anticyclones are tracked using the objective feature tracking algorithm, TRACK (Hodges, 1994, 1995, 1999), which has been used extensively to track tropical (e.g. Hodges and Emerton, 2015) and extratropical cyclones (e.g. Hoskins and Hodges, 2002b, 2005, 2019), polar lows (Zappa et al., 2014b) and Tibetan plateau vortices (Curio et al., 2018) using relative vorticity to identify these features.

In this work, TRACK is used to identify anticyclones corresponding to positive Z500 anomalies with respect to the instantaneous zonal mean component. Small scales are removed by spectral filtering, lowering the original resolution of the data to T42 resolution. Once the maxima in Z500 anomaly field are identified, a track is constructed by finding nearest neighbours in consecutive time steps (Hodges, 1994, 1999). Anticyclones are tracked in the forecasts initiated at 1200 UTC 27 September 2016 in the control simulation, model physics experiments, and the analysis. The location of the anticyclones in

the analysis corresponds well with the blocking centre.

5.4.3 Trajectory calculation

WCBs are identified in this article using a Lagrangian trajectory method. Air parcel trajectories are calculated with the Lagrangian Analysis Tool (LAGRANTO, Wernli and Davies, 1997; Sprenger and Wernli, 2015). Forward trajectories are started at every horizontal grid point over the North Atlantic (in the region of an extratropical cyclone) and vertically every 20 hPa from 1010 hPa to 790 hPa for various times throughout the cyclone evolution. The trajectories are calculated forward using the output from the MetUM experiments using the 3D wind field, temperature, specific humidity and surface pressure. Air parcel trajectories that ascend by more than a chosen ascent threshold in a given time period are defined as part of the WCB and used to compare WCB features among the experiments. The ascent thresholds are varied between 500 and 600 hPa in either 48 or 72 hour forecast periods to provide comparisons of WCB ascent rates in different forecast periods.

5.4.4 Block forecast verification

Forecasts of atmospheric blocking are verified using a version of the Structure Amplitude Location (SAL) diagnostic introduced by Wernli et al. (2008) for verification of precipitation forecasts and adapted here for block forecasts. Block forecasts are compared against the analysis fields, and experiment forecasts against the control forecast, using amplitude (A) and location (L) values calculated from the output of the blocking index. We do not compute the structure (S) component of the SAL diagnostic in Wernli et al. (2008). The S component takes into account the 3D structure of the field, looking for differences between the forecast and observations in the intensity and coverage of precipitation. Because the values used here for block forecasts lie between zero and unity the S component does not provide any additional useful information not obtained from the A and L components. The A and L components are calculated for blocked regions within the Euro-Atlantic domain (D) as follows. The A component is given by

$$A = \frac{D(B_{fc}) - D(B_{an})}{0.5[D(B_{fc}) + D(B_{an})]}, \tag{5.1}$$

where $D(B)$ denotes the domain sum of the blocking index (scaled for latitude) and subscripts fc and an represent forecast and analysis fields respectively (

$$D(B) = \sum_{(i,j)\in\mathcal{D}} B_{i,j}, \tag{5.2}$$

and $B_{i,j}$ is either $cos(\phi)$ if the grid point at latitude ϕ is blocked or zero if it is not blocked). The A score provides a measure of the accuracy of the area blocked in the forecast within a region $\mathcal{D}$. A values are between -2 and 2, and $A = 0$ indicates the total area blocked across the region in the forecast was equal to that in the analysis.

The L component is constructed using the sum of two separate metrics (L_1 and L_2). L_1 is equal to the normalised distance between the centres of mass of the blocking index fields in the forecasts and analysis,

$$L_1 = \frac{|\mathbf{x}(B_{fc}) - \mathbf{x}(B_{an})|}{d}, \tag{5.3}$$

where d is the largest distance between two points in $\mathcal{D}$ and $\mathbf{x}(B)$ denotes the centre of mass of the blocking index field within $\mathcal{D}$. L_1 can have values between 0 and 1. $L_1 = 0$ implies that the centre of mass of the forecast and analysis blocking fields are equal, though this does not mean the forecast was perfect because many different blocking index fields can have the same centre of mass. The purpose of L_2 is to try and identify situations when two different blocking index fields may have the same centre of mass. L_2 is calculated as the difference between the forecast and analysis in the averaged distance between the centre of mass of the total blocking field and individual blocked regions within $\mathcal{D}$. For each blocked region ($\mathcal{B}_n$) within the domain its area, B_n, is calculated as

$$B_n = \sum_{(i,j)\in\mathcal{B}_n} B_{i,j}. \tag{5.4}$$

The area-weighted averaged distance between the centres of mass of the individual blocked regions, $\mathbf{x}_n$, and the centre of mass of the total blocking index field, $\mathbf{x}$, is then calculated as

$$b = \frac{\sum_{n=1}^{M} B_n|\mathbf{x} - \mathbf{x}_n|}{\sum_{n=1}^{M} B_n}, \tag{5.5}$$

where M is the total number of blocking regions. b can range from 0 to $d/2$. If the blocking index only identifies one blocked region (which will frequently be the case for

large, mature blocks) $b = 0$. L_2 is then calculated as the difference in b between the forecast and analysis blocking index fields:

$$L_2 = 2\left[\frac{|b(B_{fc}) - b(B_{an})|}{d}\right]. \tag{5.6}$$

L_2 then also has values between 0 and 1 and thus L, equal to $L_1 + L_2$, can have values between 0 and 2. An L value of zero does not necessarily imply a perfect forecast because the definition of L is not sensitive to rotation around the centre of mass.

5.4.5 Potential temperature tracers

To study how the parameterisations of diabatic processes are affecting the flow and contributing to model error a set of θ-tracers has been incorporated in the MetUM. The method is similar to that described in Martínez-Alvarado and Plant (2014) and uses the temperature increments for several physical processes that are converted into θ increments. The tracer method utilises the conservation property of θ by writing it in terms of a conserved component (θ_0) and a non-conserved component ($\Delta\theta$). θ_0 is advected with the flow but not altered by the parameterisation schemes and gives the isentropic origin of air masses at the start of the forecast. $\Delta\theta$ is advected as well but also accumulates the effect of the parameterisation schemes throughout the integration. The increments to θ are calculated from the thermodynamic equation of the MetUM:

$$\frac{D\theta_{vd}}{Dt} = S_\theta, \tag{5.7}$$

where θ_{vd} is the prognostic variable of virtual dry potential temperature (hereafter referred to as θ for convenience) and S_θ represents diabatic sources. θ at a grid point x and time t can then be written as

$$\theta(x,t) = \theta_0(x,t) + \Delta\theta(x,t) + \epsilon_\theta(x,t), \tag{5.8}$$

where $\epsilon_\theta(x,t)$ is an error term originating from numerical diffusion modifying θ. The non-conserved term can be separated into terms for each parameterised process (i)

$$\Delta\theta(x,t) = \sum_i \Delta\theta_i(x,t), \tag{5.9}$$

where $\Delta\theta_i(x,t)$ represents the cumulative contribution to θ due to parameterisation i. The parameterisations contributing to θ that are considered in this study are:

- $\Delta\theta_{slow-phys}$: θ contribution from the slow physics scheme. This includes both the short and long wave radiation increments as well as the microphysics increments;
- $\Delta\theta_{BL}$: θ contribution from the boundary layer parameterisation;
- $\Delta\theta_{conv}$: θ contribution from the convection parameterisation;
- $\Delta\theta_{cloud-rebal}$: θ contribution from the cloud rebalancing scheme. This scheme calculates condensate and cloud fraction changes due to change in the temperature in a grid box that occurs due to condensation from adiabatically cooling ascending air (see Wilson et al. (2008b) for more details).

The θ-tracers are calculated online within the model simulation code from the transport equation using 5.7:

$$\frac{D\theta}{Dt} = \frac{\partial\theta}{\partial t} + \mathbf{v}\cdot\nabla\theta = \sum_i S_{\theta_i}, \tag{5.10}$$

where S_{θ_i} is the source from each diabatic process (parameterisation) and $S_{\theta_0} \equiv 0$ by definition. Substituting (5.8) into (5.10) and collecting like terms yields

$$\frac{D\theta_0}{Dt} = \frac{\partial\theta_0}{\partial t} + \mathbf{v}\cdot\nabla\theta_0 = 0, \tag{5.11}$$

and

$$\frac{D\Delta\theta_i}{Dt} = \frac{\partial\Delta\theta_i}{\partial t} + \mathbf{v}\cdot\nabla\Delta\theta_i = S_{\theta_i}. \tag{5.12}$$

The θ at the start of the model integration is used as the initial condition for (5.11), i.e. $\theta_0(t=0) = \theta(t=0)$. Each of the $\Delta\theta_i$ is set to zero at the initial time for all of the parameterisations so that the tracers describe the cumulative effect of each source term. The error ϵ_θ also satisfies an equation of this form but it is instead computed as

$$\epsilon_\theta = \theta - \theta_0 - \Delta\theta. \tag{5.13}$$

The source terms in (5.12) can be calculated by differencing θ before and after each parameterisation call because the parameterisations included here are called sequentially within the MetUM. The advection terms are computed using a semi-Lagrangian scheme that is inbuilt in the model for calculating the advection of tracer fields (Davies et al.,

2005). θ_0 and each $\Delta\theta_i$ are output as model diagnostics. The total non-conserved part of θ (neglecting the tracer error) can then be calculated as the difference between θ and θ_0 (or $\sum_i \Delta\theta_i$) and illustrates where diabatic processes have heated or cooled air masses during the model integration.

The θ-tracer diagnostic can be used to quantify how important diabatic heating is in the development of blocking in the forecast evolution and assess how strongly air masses that arrive in blocks have been heated in the preceding days. An example of the θ-tracer diagnostic is shown in Fig. 5.1. The θ, θ_0, $\Delta\theta$ and ϵ terms are shown at a forecast lead time of seven days and at model level 34 (8634 m) from a model run initiated at 1200 UTC on 27 September 2016. At this time there is a large-scale blocking ridge present over Northern Europe. Generally, we expect regions of diabatic heating to be located in ridges as air parcels arriving in them have ascended from lower levels and have experienced diabatic heating (Pfahl et al., 2015). The conserved part of θ, that has just been advected by the flow (Fig. 5.1(b)), shows the value of θ that air masses arriving at each grid points had at the start of the forecast. The field highlights where diabatic or frictional processes have modified θ and the scales at which these processes are active. The non-conserved component of the θ field shows regions that have been heated or cooled during the integration and can be used to trace air masses. For example, the region of strong heating to the north of the UK depicts an air mass that has ascended and undergone latent heating in the WCB of a cyclone before arriving at the model level shown. Air in the cut-off region over central Europe has experienced descent and cooling. The θ-tracer error term is shown in Fig. 5.1(d). The error is generally small across the entire domain and considerably smaller than the non-conserved θ shown in Fig. 5.1c (note that the colour bars in panels c and d are different). The error at even seven days into the forecast evolution is generally <10% of the non-conserved θ and hence we can neglect error in our analysis and consider the term $\theta - \theta_0$ as the change in θ due to diabatic processes (termed the total diabatic heating here).

5.5 NAWDEX campaign period

In this section, results are presented from the control forecast together with the SST-update and Prog-ent experiments for forecasts from the whole of the NAWDEX period. Forecasts from the operational ensemble are also included to compare the magnitude of the change in skill due to initial condition uncertainty and model uncertainty. The skill

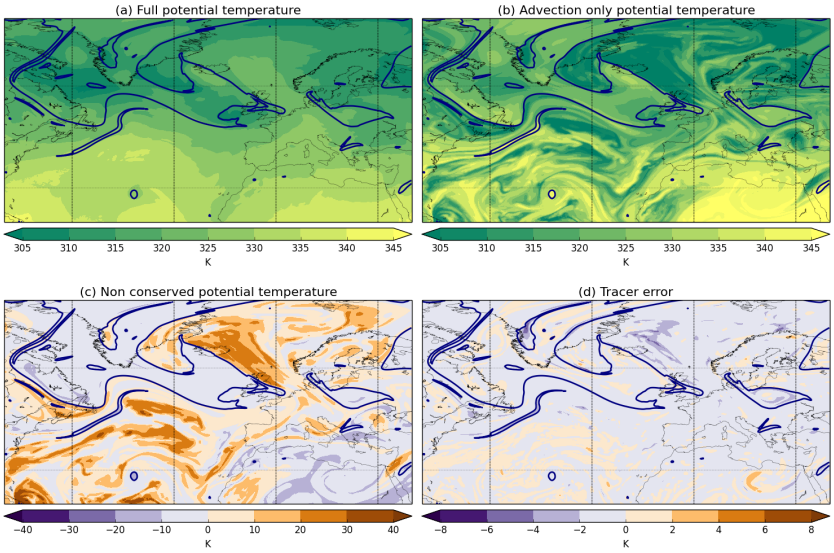

Figure 5.1: (a) Full field (θ), (b) advected initial field (θ_0), (c) the non-conserved θ ($\theta - \theta_0$) and (d) the tracer error ($\theta - (\theta_0 + \sum_i \Delta\theta_i)$) from the θ-tracer output on model level 34 (8634 m) in the forecast of 12 UTC 4 October 2016 at a lead time of 7 days. Note that the colour bar in (d) is one fifth of the scale in (c). The 2 PVU contour is plotted in each case to show Rossby-wave structure.

of the forecasts is assessed using the Root Mean Square Error (RMSE) of the mean sea level pressure (MSLP) and Z500. The variability in forecast skill is also related to weather patterns and diabatic heating, and the representation of blocking in forecasts during the NAWDEX period is assessed.

5.5.1 Overview of forecast performance

The average RMSE of Z500 and MSLP over the Euro-Atlantic region (the domain shown in Fig. 5.1) is shown for forecasts during NAWDEX from the control forecast, SST-update and Prog-ent experiments and the operational ensemble mean forecast as a function of forecast lead time in Fig. 5.2. At early lead times, the average RMSE in all the forecasts are almost identical for both MSLP and Z500. For forecasts longer than five days, the ensemble mean out-performs the control forecast and both model experiments, as expected (e.g. Toth and Kalnay, 1997). The RMSE is lower in the Prog-ent experiment than in the control forecasts for forecasts between five and ten days lead time for both fields. The RMSEs remain nearly indistinguishable between the control forecast and SST-update experiment until the longest lead times. It is clear from Figure 5.2 that running a forecast model with SST updating daily did not improve or degrade the forecast skill on

average for this period. This suggests that running a coupled atmosphere-ocean model for medium-range forecasts may not be beneficial for this period and region, though having SST changing on only daily timescales may limit the potential impact. There was a slight improvement in skill with the Prog-ent experiment with a maximum reduction in RMSE of around 4% in both fields at nine days lead time. The reduction in RMSE is not insignificant in the operational forecast context, with similar reductions in RMSE found with the full GA7.0 implementation (Walters et al., 2017a).

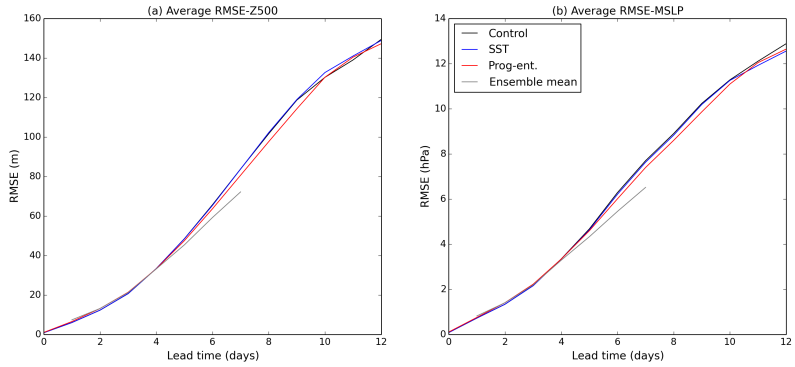

Figure 5.2: Average RMSE as a function of lead time for the control forecast, SST-update experiment, Prog-ent experiment and the mean of the operational ensemble for all of the forecasts initiated during the NAWDEX period. The RMSE of Z500 (a) and MSLP (b) are shown throughout the operational and experiment forecast integrations (7 and 12 days, respectively). Note that the black and blue lines are nearly indistinguishable until the longest lead times.

Forecast skill can also vary depending on the weather pattern (Ferranti et al., 2015; Matsueda and Palmer, 2018) so it can be insightful to consider how the RMSE values vary throughout the NAWDEX period. We now only consider RMSE of Z500 as this can be used to describe the general flow pattern, or weather regime, and relate this to periods of high and low forecast skill. The RMSE of Z500 for forecasts valid on dates during the NAWDEX period is shown in Fig. 5.3(a) together with a measure of blocking activity (the area blocked in the analysis). Both measures are calculated over the Euro-Atlantic domain defined above. The RMSE on the given valid date is averaged for forecasts of that date for all lead times between six and ten days inclusive.

Periods of low forecast skill (high RMSE) during the NAWDEX period are associated with the onset and decay of blocked periods. The average RMSE increases quickly before the onset of a blocked period around 12 UTC on 4 October 2016, suggesting that the onset of this block was poorly forecast in the control and model experiments. The RMSE of Z500 then decreases dramatically once the block is mature and remains low during the

maintenance period of this block. The RMSEs in all forecasts increases again before the block decays, highlighting the difficulty in forecasting the decay, as well as the onset, of blocked periods. The variation in RMSE throughout the NAWDEX period is similar in the control and SST-update experiment, consistent with their almost identical average Z500 RMSEs. There is a larger difference between the RMSE in the control forecast and the Prog-ent experiment; the RMSE in the Prog-ent experiment is generally lowest, except for forecasts for the period of block onset at the start of the NAWDEX period.

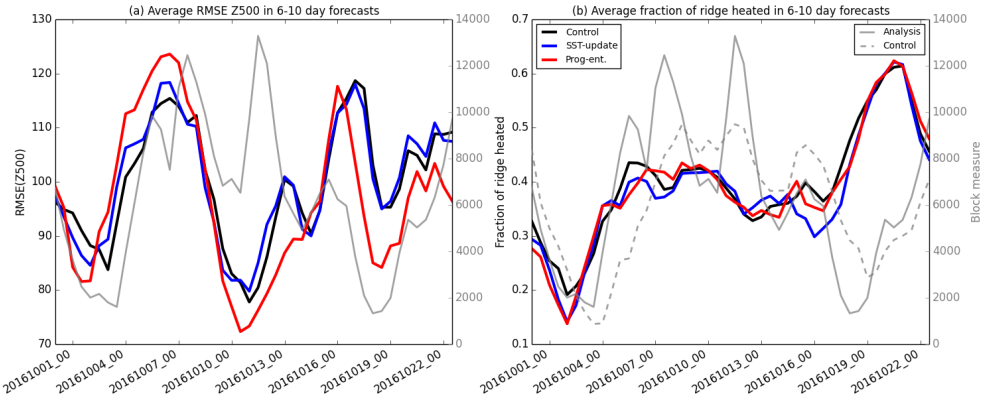

Figure 5.3: (a) RMSE of Z500 in the Euro-Atlantic region for forecasts valid on days during the NAWDEX period, averaged for all forecast lead times between six and ten days lead time inclusive. The area blocked over the Euro-Atlantic domain during the NAWDEX period in the analysis as also shown (grey line). (b) The fraction of ridges that have been heated ($\theta - \theta_0 > 2$) for forecasts valid on days during NAWDEX period, averaged in forecasts of that date between six and ten days lead time. Again the area blocked in the analysis is given by the grey line and additionally the area blocked in the control forecast (averaged between six and ten days lead time) is given by the grey dashed line. Note that the right hand axis corresponds to the grey lines in both panels.

The fraction of the ridges that have undergone heating (FH) is calculated as

$$\mathrm{FH} = \frac{\sum_{i,j \in \hat{R}} cos\phi_j}{\sum_{i,j \in R} cos\phi_j}, \tag{5.14}$$

where R are ridges (points on the 315 K isentropic surface north of 51.33°N and with a PV value less than 2 PVU), $\hat{R}$ represents the regions within R with total diabatic heating $(\theta - \theta_0)$ greater than 2 K (the same value used in Pfahl et al. (2015)) and ϕ is the latitude of grid point i, j. Note that the results presented in this section are not sensitive to the arbitrary choice of latitude used to define ridges. The mean fraction of ridges heated in all forecasts between six and ten days lead time inclusive for forecasts valid on days during the NAWDEX period is shown in Fig. 5.3(b), as well as the area blocked in the

analysis and the average area blocked in the control forecasts of the same lead times. The onset of the first blocked period in the control forecast is preceded by an increase in the fraction of the ridges heated. This is a result of air masses being heated and arriving at upper-levels as the ridge is amplifying before the block develops fully and is identified by the blocking index. The increase in the fraction of the ridges heated coincides with the increase in RMSE prior to block development. This supports the hypothesis that the uncertainty in block forecast (diagnosed as RMSE in Z500) is originating from lower levels and associated with diabatic heating and its representation by the parameterisation schemes. The uncertainty in the block forecast could also be due to uncertainty in the strength and location of the WCB due to initial condition uncertainty. The FH then remains relatively constant during the maintenance phase of the blocked period. There is an increase in the FH as this block decays, this increase is associated with heating in an amplifying ridge that develops into the blocked area towards the end of the NAWDEX period (not shown).

Low forecast skill during the NAWDEX period was related to an increase in diabatic heating (rather than a large net fraction of the ridge heated). This is partly a property of the θ-tracer calculation as it is the accumulated heating that is measured and a large heated fraction of a ridge does not necessarily mean that diabatic processes were active recently. However, an increase in the heated ridge fraction does imply recent diabatic heating which is uncertain in the model and potentially causing the low forecast skill. The increase in RMSE Z500 and total diabatic heating generally precedes block onset reflecting the model's known difficulty in transitioning to a blocked state (Matsueda, 2009; Martínez-Alvarado et al., 2018). The representation of blocking during the NAWDEX period in the control forecasts, model experiments and operational ensemble is now reviewed.

5.5.2 Predictability of blocking during NAWDEX

Block representation in the forecasts is now compared to that in the analysis during the NAWDEX period. The average area difference in block area between the analysis and each of the forecasts and the operational ensemble forecast is shown together with the inter-quartile range in block area difference among each individual forecasts from the control and model experiments in Fig. 5.4(a). All the forecasts (both operational and experiments) exhibit the longstanding model deficiency of a reduction in block area with lead time (Tibaldi and Molteni, 1990; Matsueda, 2009; Martínez-Alvarado et al., 2018),

though the reduction is not large for forecasts during this period especially compared to the spread in the individual forecasts. The difference in block area in all experiments and in the ensemble mean is small until after five days lead time, consistent with other studies (e.g Tibaldi and Molteni, 1990; Pelly and Hoskins, 2003a; Matsueda, 2009). As the lead time increases, the average difference then becomes increasingly negative (the blocks are smaller in the forecasts) with the error generally similar in the control forecast, SST-update and Prog-ent experiments and smaller in the average of the operational ensemble. There is a large spread in block area difference between the forecasts and analysis for specific forecast initiation dates (thin dashed lines).

Block forecasts are now verified using the modified version of the SAL technique (Wernli et al., 2008) described in section 5.4.4 to provide additional information about the error in both amplitude and location of the forecast blocks. A and L values are calculated for each of the operational ensemble members for forecasts of seven days lead time, and in the control simulation, SST-update and Prog-ent experiments at seven and ten days lead time, for every forecast initiated during the NAWDEX period. These lead times were chosen as they span the lead times at which block onset forecast typically deteriorates. The means (points) and the standard errors (lines) in A and L are plotted for values calculated against the analysis (Fig. 5.4(b)). Recall that a perfect forecast will have A and L values equal to zero. The mean amplitude values are close to zero for all the simulations, reflecting the small average area difference shown in Fig. 5.4(a). The mean of the operational ensemble forecast has the lowest A value. The mean L values in the control, model experiments and operational ensemble lie between 0.2 and 0.3 which suggests some systematic error in the location of blocking events. The A and L values can also be used to contrast the SST-update and Prog-ent experiments against the control forecasts (Fig. 5.4(c)) to better quantify how much impact the experiments are having on the simulation of blocking. In general, the sensitivity experiments are more similar to the control forecast than all the forecasts are to the analysis (the points are closer to the origin). The Prog-ent experiment has more of an effect on block forecasts than the SST-update, consistent with the larger effect seen in RMSE MSLP and Z500 values (Figs. 5.2 and 5.3). The difference in amplitude of the blocks in the simulations is much smaller than the difference in their locations. This is true for their means and standard errors, suggesting verifying block forecasts based only on their amplitudes might hide some of the forecast differences.

In this section, it has been shown that updating SST daily into the forecast inte-

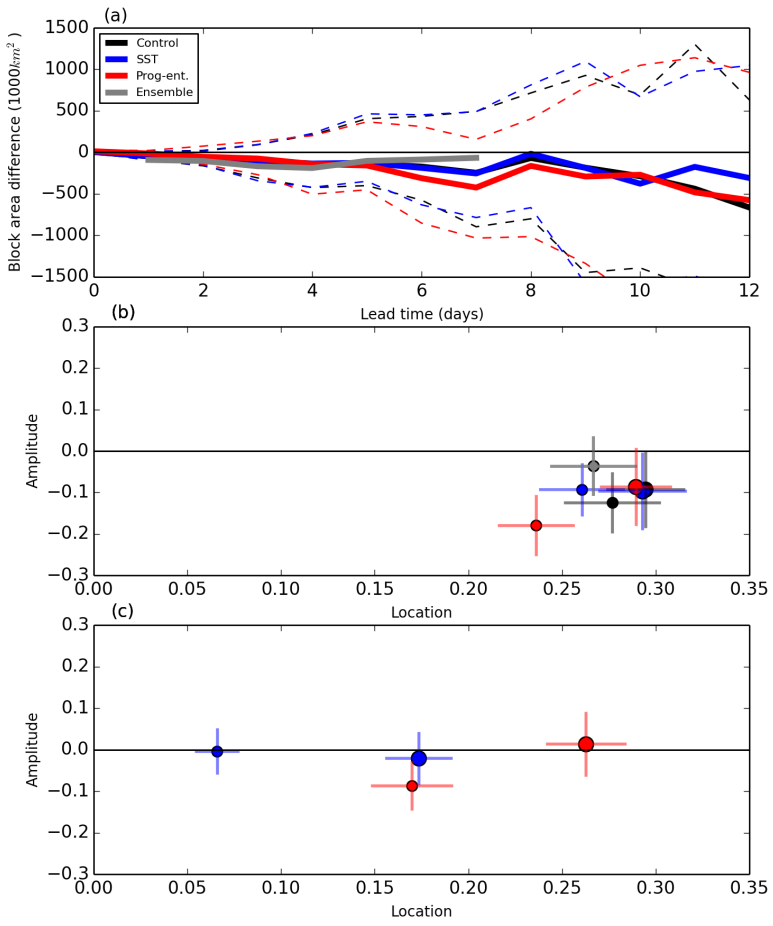

Figure 5.4: (a) The average difference in block area between the analysis and forecasts from the control, SST-update and Prog-ent experiments, and operational ensemble as a function of forecast lead time. The difference is shown in the mean (thick lines) and the interquartile range (thin dashed lines) of the forecasts for the control, model experiments and the operational ensemble mean. (b) AL diagram for forecasts of blocking during the NAWDEX period compared to the analysis in the control, model experiment and operational ensemble forecasts. Mean (points) and standard errors (lines) of A and L values are shown for forecasts of 7 (small dots) and 10 (big dots) days lead time. (c) As in (b) for forecasts from the model experiments compared to the control forecasts.

gration to their observed values did not systematically improve or degrade the forecasts during NAWDEX. Running the forecast model with a new convection scheme had a larger impact and generated a slight reduction in average forecast error. Both the SST-update and Prog-ent experiments had different representations of blocking events than in the control simulation. In the next section, we will show in a case study that the SST-update and Prog-ent experiments, together with the GA7 parameterisation experiments, can nevertheless have a large impact on the evolution of individual forecasts and make use of the

θ-tracers to explain the evolution changes observed.

5.6 Block case study: forecasts versus analysis

The case study is introduced first in this section after which the operational forecast and the full set of model experiments (GA7 parameterisation experiments as well as the SST-update and Prog-ent experiments) are compared against the analysis. The case study is focused on the block onset around 12 UTC on 4 October 2018 over Scandinavia following a cyclone known as the Stalactite cyclone (Schäfler et al., 2018). The forecast initiation time (1200 UTC on 27 September 2016, a week prior to block onset) is chosen to be far enough in advance of the block onset so that the experiments have diverged considerably. This is a lead time at which models are known to poorly predict the onset of a blocked flow (e.g. Pelly and Hoskins, 2003a; Matsueda, 2011; Martínez-Alvarado et al., 2018).

5.6.1 Synoptic overview

In Fig. 5.5, the synoptic situation is presented for the days preceding block onset. The analysed MSLP and Z500 fields as well as the 2-PVU contour on the 315 K isentropic surface (Tp315, representing the tropopause) and the location of the Stalactite cyclone are shown between 1–4 October 2016. On 1 October 2016, the Stalactite cyclone is identified in the central North Atlantic with an upper-tropospheric trough above it and to the west. An amplifying ridge is also visible in both the Tp315 and Z500 contours downstream of the cyclone, with a more zonal flow further downstream and upstream (Fig. 5.5(a)). On 2 October, the Stalactite cyclone has intensified and moved north-eastward toward Iceland and the ridge in the tropopause has amplified. An upper-level PV streamer is formed to the south of the Stalactite cyclone as the cyclone interacts with the upper-level trough and the streamer cyclonically wraps up around the cyclone centre. Z500 has risen over the UK associated with the incipient block and warm air advection in the Stalactite cyclone. By 3 October, the ridge has expanded dramatically and now extends over a large part of the North Atlantic, Z500 has risen further over UK and towards Scandinavia as the transition to a blocked state continues. The Stalactite cyclone has now reached maximum intensity and moved nearer to Iceland with the upper-level trough completely wrapped around the cyclone centre. At this time there is a sign of a secondary cyclone developing as a kink in the MSLP contours in the Gulf Stream region off the coast of North America. On 4 October, the analysed block onset date over Scandinavia, the block is clear in Z500

(almost a cut off high region) and Tp315 (a large ridge over Scandinavia). The Stalactite cyclone has dissipated by this time and a secondary cyclone has intensified leading to a secondary ridge ahead of it. This synoptic evolution provides a clear example of regime transition to a blocked state following extratropical cyclogenesis similar to those presented in previous studies (e.g. Colucci, 1985; McLeod and Mote, 2015; Grams et al., 2018). The flow evolution in this case is now assessed in the forecasts from the chosen initiation date.

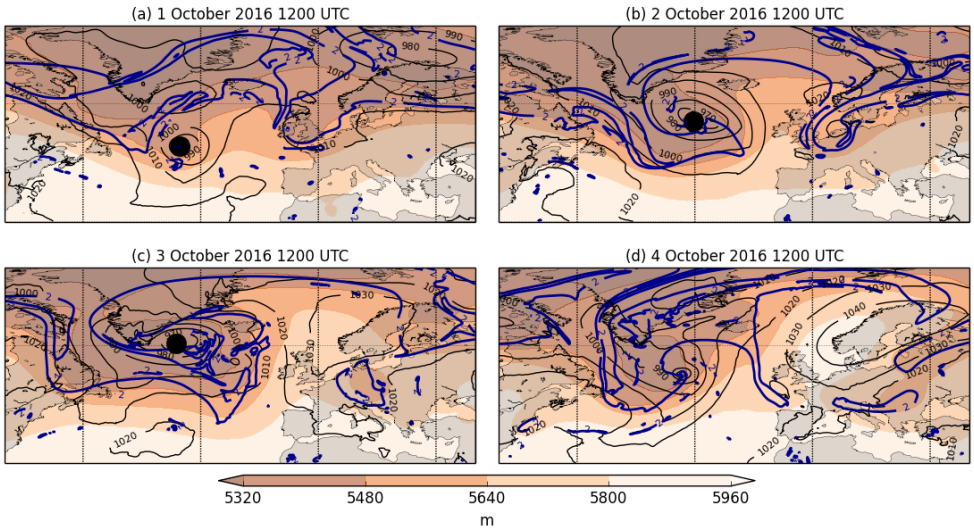

Figure 5.5: Synoptic overview for days preceding block initiation. MSLP (contours), Z500 (filled contours) and the Tp315 contour (thick blue contour) from the Met Office analyses are shown for (a) 1, (b) 2, (c) 3 and (d) 4 October 2016. The location of the Stalactite cyclone when present is shown by the black circle.

5.6.2 Forecast verification

The track of the Stalactite cyclone and its minimum MSLP as seen in the analysis, operational ensemble and model physics experiments are shown in Fig. 5.6(a),(c). The tracks and intensities are shown between 12 UTC 30 September 2016 and 12 UTC 4 October 2016, which corresponds to lead times between three and six days for the forecasts initiated on 12 UTC 27 September 2016. The tracks and intensities (diagnosed by the associated positive Z500 anomalies) of the downstream block are also shown in Fig. 5.6 for the control forecast and model experiments.

All of the forecasts (control, model experiments and operational ensemble) have a clear eastward shift in the track of the cyclone compared to the analysis when it is present in the forecast between three and six days lead time (Fig. 5.6(a)). None of the model experiments result in a large change in the cyclone track forecast in this case and they

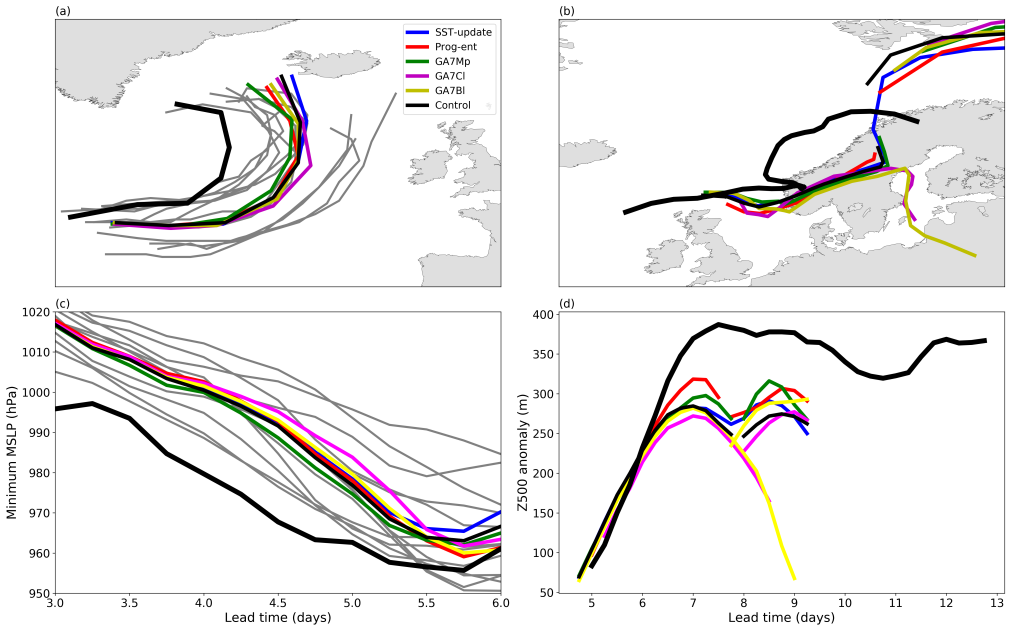

Figure 5.6: Stalactite cyclone and downstream block tracks and intensities for the forecast initiated at 1200 UTC 27 September 2016 from the control simulation (thin black), model physics experiments (colours), operational ensemble (grey, for the cyclone only) and the analysis (thick black): (a) cyclone tracks, (b) anticyclone tracks, (c) cyclone minimum MSLP, and (d) Z500 anomaly. Cyclone tracks and intensities are shown for forecast valid dates between 1200 UTC 1 and 1200 UTC 4 October 2016. Anticyclone tracks are shown for forecast valid dates between 1800 UTC 2 and 1800 UTC 10 October 2016.

are spread about the control (thin black line). All of the model experiments and the control forecast also forecast a less intense Stalactite cyclone than analysed (Fig. 5.6(b)), particularly at earlier lead times. The rate of MSLP drop and minimum MSLP reached is quite similar in the experiments to that analysed but starts from an incorrect value (at three days lead time). Again, the control forecast of minimum MSLP is in the middle of forecasts in the ensemble of experiments. There is larger spread among the operational ensemble than the model experiments (initial condition uncertainty develops quicker than model physics uncertainty in this case) in both the track and intensity of the cyclone, although the analysis still generally remains outside the ensemble spread in both track and intensity of the Stalactite cyclone. The cyclone in the analysis was further west than any ensemble member, and had a deeper MSLP than any member, at nearly all lead times. As none of the operational ensemble or model experiments were able to capture the development of the Stalactite cyclone it could be that there exists a deficiency somewhere in the model, e.g. in the dynamical core or set of physics parameterisations, which meant the model could never predict this evolution. Alternatively, the PDF of possible initial conditions may not have been sampled sufficiently and the ensemble may not have enough

members.

Similar errors in the track and intensity are identified for the block that develops downstream of the Stalactite cyclone. The tracks of the block centre are located further east in the forecasts (thin lines) than the analysis (thick line), the same error as in the track of the Stalactite cyclone. The intensity (maximum Z500 anomaly) of the block is less in the forecasts than the analysis, the same error as in the intensity of the Stalactite cyclone. Whilst this does not prove a causal relationship between the development of the Stalactite cyclone and downstream block it is highly suggestive of one and motivates the analysis in the subsequent sections of this article. The tracks of the blocking anticyclone are not continuous in all of the forecasts because the anomaly in Z500 did not always exceed the threshold for block detection, though these gaps are generally less than 12 hours long.

The misrepresentation of the track and intensity of the Stalactite cyclone and downstream block in the forecasts is consistent with errors in the forecast of the upper-tropospheric flow pattern. This can be summarised by looking at the Tp315 contour and the location of the Stalactite cyclone in the analysis and model experiments, as shown in Fig. 5.7, for the same dates as those in Fig. 5.5 to allow a direct comparison. On 1 October 2016, four days into the forecast evolution, the developing ridge is generally well represented in all of the experiments except for the upstream trough to the south of Greenland which is shifted too far east. This is consistent with the position of the Stalactite cyclone being too far east. Over the next 48 hours, the amplification both northward and westward of the ridge is underestimated in all of the experiments. By 3 October 2016, six days into the forecast evolution, the ridge in the analysis extends across Greenland which is not reproduced in any of the forecasts. The ridge position in the forecasts being further east than the analysis is also consistent with the eastward shift in the block tracks in the forecast. The position of the Stalactite cyclone remains too far east at this time. On 4 October, seven days into the forecast, the Stalactite cyclone has weakened and there is a large-scale blocking ridge present in all of the forecasts. The location and shape of the upper-level ridge in the control and model experiments does not match the analysis. The analysed blocking ridge has formed over Scandinavia and the secondary ridge has amplified over the North Atlantic. In the forecasts, the primary ridge is extending too far over Greenland (resembling the analysed ridge on the previous day). The developing ridge ahead of the secondary cyclone is completely missed in all the experiments. In this case, the forecasts do predict the onset of a blocking ridge following the Stalactite cyclone

but are not able to predict the exact timing and location of the features accurately.

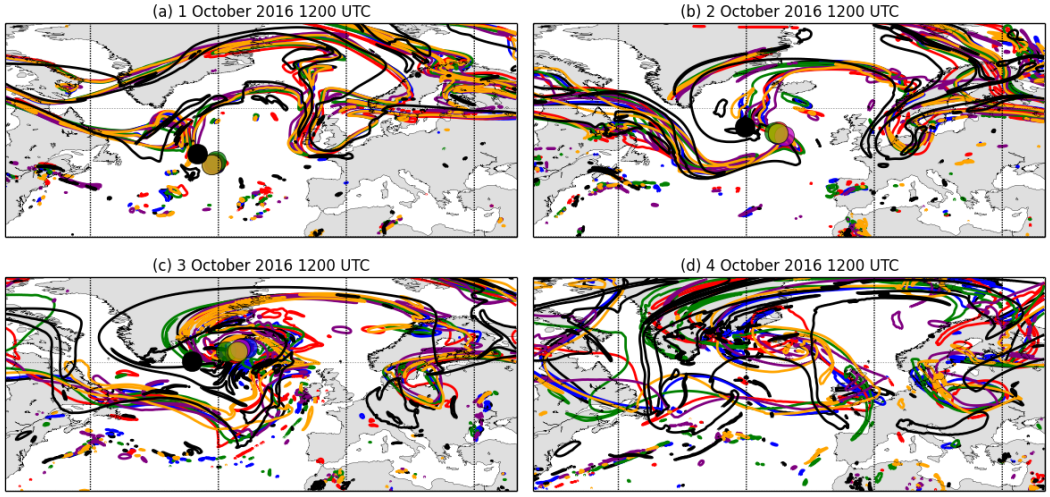

Figure 5.7: Tropopause location (Tp315 contour) in the analysis (thick black line) and model experiment forecasts (coloured lines) initialised at 1200 UTC 27 September 2016 and valid on the same date for (a) 1, (b) 2, (c) 3 and (d) 4 October 2016. The location of the Stalactite cyclone in the analysis is marked by the black circle and in the model experiments by the coloured circles.

The poor forecast of the upper-level ridge and associated block can be analysed from a different perspective using the blocking index. The area identified as blocked within the Euro-Atlantic region in the forecasts as a function of lead time, and on the corresponding date in the analysis, is shown in Fig. 5.8(a). The control forecast and model experiments do a reasonable job of capturing the analysed blocked area in the region. All forecasts exhibit an increase in block area around 160 hours lead time at roughly the same rate as that in the analysis. The spread in the operational ensemble (grey shading) is larger than the spread among the physics ensemble and the operational ensemble shows a tendency to underestimate the area blocked. The control forecast and SST-update experiment remain similar, with their forecast of block area nearly identical. There is greater spread among the parameterisation experiments, particularly at later lead times, with the analysis generally lying among the forecasts. The clear error in the forecast of the Stalactite cyclone and upper-tropospheric ridge highlighted previously is not evident in the forecast of block area over the Euro-Atlantic. A large-scale blocking ridge is clearly evident in all of the forecasts (Figs.5.7(c),(d)) and the blocking index reveals the block areas forecast are similar to that in the analysis. The error in the location of the block apparent in Fig. 5.7 is now quantified using the modified SAL diagnostic described in section 5.4.4.

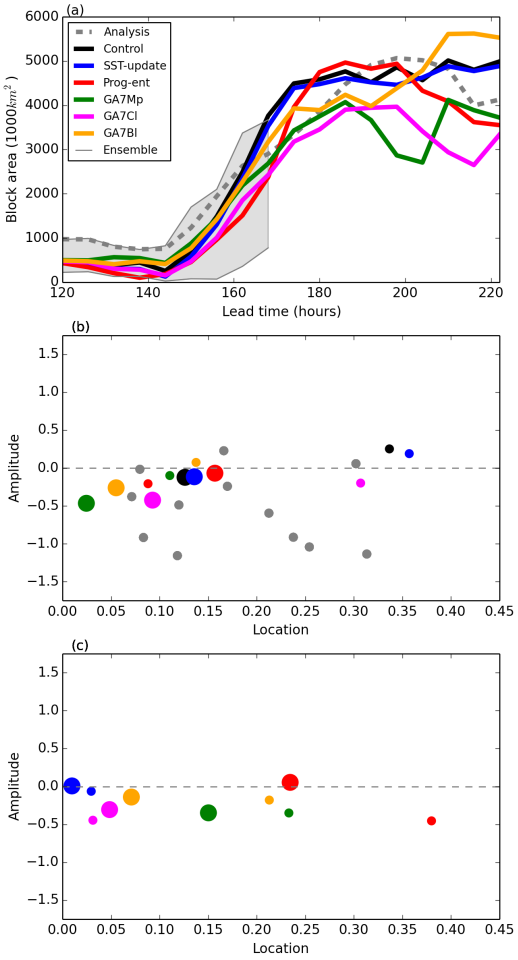

Figure 5.8: (a) Block area as a function of lead time in forecast initiated on the specified date in the control simulation and the model physics experiments and block area in the analysis on the corresponding day. (b) Diagram showing the A and L components of the modified SAL diagnostic for blocks in the operational ensemble at seven days lead time (grey dots) and each of the experiments at 7 (small coloured dots) and 8 (large) days lead time calculated against the analysis. (c) as in (b) but calculated against the control simulation and for the experiments only. Lead times of 7 and 8 days represent forecasts valid at 1200 UTC on 5 and 6 October 2016, respectively.

A and L values calculated against the analysis are presented in Fig. 5.8(b). Values are calculated for forecasts from the operational ensemble, control and model experiment forecasts. A and L values are calculated at forecast lead times of seven (small dots) and eight days (big dots) lead time for the control and physics experiments and at seven days lead time for the operational ensemble forecasts. These lead times were chosen because they are the times of block development in the forecast (recall the operational

ensemble only extends to seven days). In the control forecast and model experiments, A values are generally low at both forecast lead times implying that the forecasts did a reasonable job in predicting the total area blocked in the region. However, A values of less than -0.4 are found for some of the physics experiments at eight days lead time, representing an underestimation by more than a factor of 1.5 in the area blocked. L values are also non-zero, highlighting the error in the blocked location in this forecast. Whilst the GA7 parameterisation experiments resulted in a smaller area blocked than in the control forecast (increased error), they have smaller L values than the control forecast (particularly in the GA7Mp experiment) at both lead times and hence reduced error in the predicted location of the block. L values are typically larger at seven days lead time, consistent with the error in upper-level ridge location at this lead time (Fig 5.7(d)). A values in the operational ensemble members are typically more negative and span a greater range of values than those in the physics experiments. A and L values are also calculated in each of the model experiments using the control forecast as a reference. If two forecast's A and L values are similar when compared to the analysis but different when compared to the control (e.g. the SST-update and Prog-ent experiments at eight days lead time) it suggests they were similar to the analysis in different ways. Not all of the model experiments are closer to the control forecast than to the analysis in this case.

This case study of block onset, following the development of the Stalactite cyclone, was very unpredictable (none of the ensemble or physics experiments did well, Schäfler et al., 2018) for forecasts beyond four days lead time. The location and intensity of the Stalactite cyclone appear to be important for the block development in this case. This association has been confirmed using ensemble sensitivity analysis (using ECMWF operational ensemble forecasts in Maddison et al. (2019)). In that paper it was hypothesised that the sensitivity of block development to upstream cyclones originated from diabatic heating in WCBs. This hypothesis is investigated in the next section by comparing the model physics experiments to the control run. Although all these forecasts diverge from reality, insight can still be gained into how diabatic processes in the Stalactite cyclone affect the large-scale development, and in particular the block. An advantage of restricting our analysis to the model forecasts is that the θ diagnostic can be used to assess the diabatic influence on dynamical evolution; this diagnostic is not available for the analysis.

5.7 Block case study: impact of model upgrades

The block onset case study is now compared in each of the model experiments to the control (operational) forecast to quantify how much model uncertainty can affect the dynamical evolution. The θ tracers are used to determine the role that diabatic heating in the WCB of the Stalactite cyclone had on the upper-level Rossby wave pattern and block development. It was shown in Fig. 5.6 that there was some spread in the intensity ($\approx$ 10 hPa) and location ($\approx 5°$) of the Stalactite cyclone among the model experiments. But how much did the model experiments change the WCB of the Stalactite cyclone? WCB trajectories have been computed in the control forecast and each of the model experiments in the forecast initialised at 12 UTC on 27 September 2016 and are shown as an example in Fig. 5.9 for the control forecast only. The trajectories shown start at three days into the forecast evolution, finish at six days into the forecast and have ascended more than 500 hPa in that period. The end points of the trajectories are at 12 UTC on 3 October 2016 (cf. Fig. 5.7.(c)) when the blocking ridge is amplifying in the control forecast.

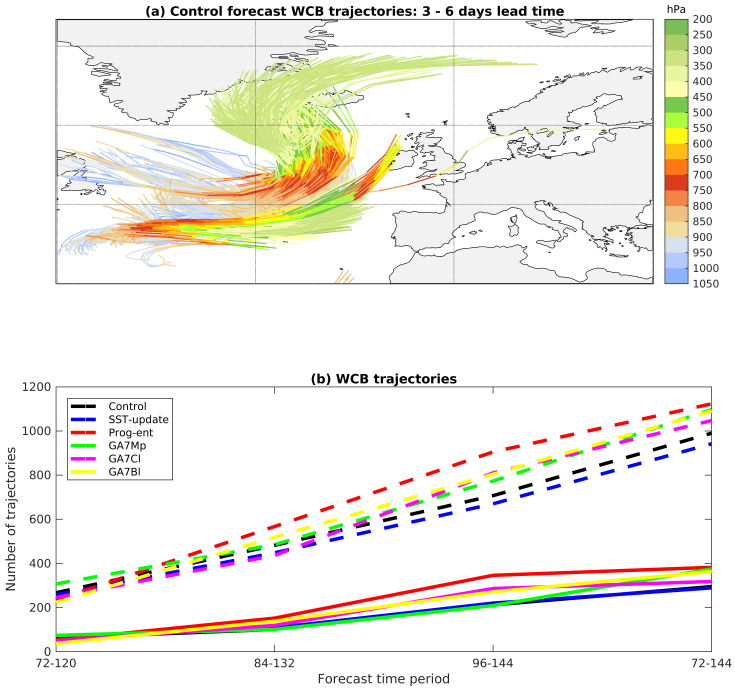

Figure 5.9: (a) WCB trajectories (having ascended more than 500 hPa) in the control forecast initiated on 12 UTC 27 September 2016 between three and six days lead time. (b) The total number of identified WCB trajectories (see text) during different forecast periods in the control forecast and model experiments for ascent thresholds of 500 hPa (dashed lines) and 600 hPa (solid lines).

A large air mass ascends from the central northern Atlantic in the WCB of the Stalactite cyclone into the upper-level ridge, linking the Stalactite cyclone and the downstream block development. To quantify the intensity of the WCB in each of the experiments the number of trajectories classified as part of the WCB are compared for different time periods during the forecast run and for different ascent thresholds. The comparison is presented in Fig. 5.9(b). The Prog-ent experiment has the highest number of WCB trajectories for the majority of the different selection time periods and ascent thresholds; the control forecast and SST-update experiment often have the least. The Prog-ent and SST-update experiments were not outliers in the experiments when considering the track and intensity of the cyclone (Fig. 5.6). This suggests that whilst neither the track nor the intensity of the cyclone changed considerably in the physics experiments the WCB intensity differed because of the changes to the latent heating from the parameterised diabatic processes that were modified in the physics experiments. We expect the convection scheme to be active in the WCB of a deep extratropical cyclone so this may explain why we see the largest change in the Prog-ent experiment.

The experiments modifying parameterisations of physical processes also had different developments of the upper-level Rossby wave pattern and block. The difference in PV on the 315 K isentropic surface (PV315) between each of the model experiments and control forecast (experiment minus control) is shown in Fig. 5.10, together with the Tp315 contour in both the control (solid black contour) and experiment (dashed black contour). The forecasts are shown at seven days lead time (cf. Fig 5.7(d)), which is when the block first formed over Scandinavia and was identified in the blocking index. There are clear differences in the amplitude and phase of the Rossby-wave pattern among the experiments. The main differences are in the northern extent of the ridge, the structure of the PV streamer forming on the upstream trough, and the phase and amplitude of the smaller ridge to the south of Greenland. The northern extent of the ridge and cyclonic wrap up of the upstream trough are coupled to the development of the Stalactite cyclone and the divergent outflow in its WCB. The Prog-ent and GA7Cl experiments have a ridge that extends further to the north (extending out of the domain shown), consistent with the increased number of WCB trajectories compared to the control in these experiments, and different structure of the PV streamer. The GA7Bl experiment has a larger ridge extent in the north eastern corner of the domain. The PV difference between the experiments and control forecasts is much smaller than the difference compared to the analysis (not shown). We now use the θ-tracers to investigate if the difference in PV is originating from

changes to the parameterised diabatic heating in the WCB of the cyclone.

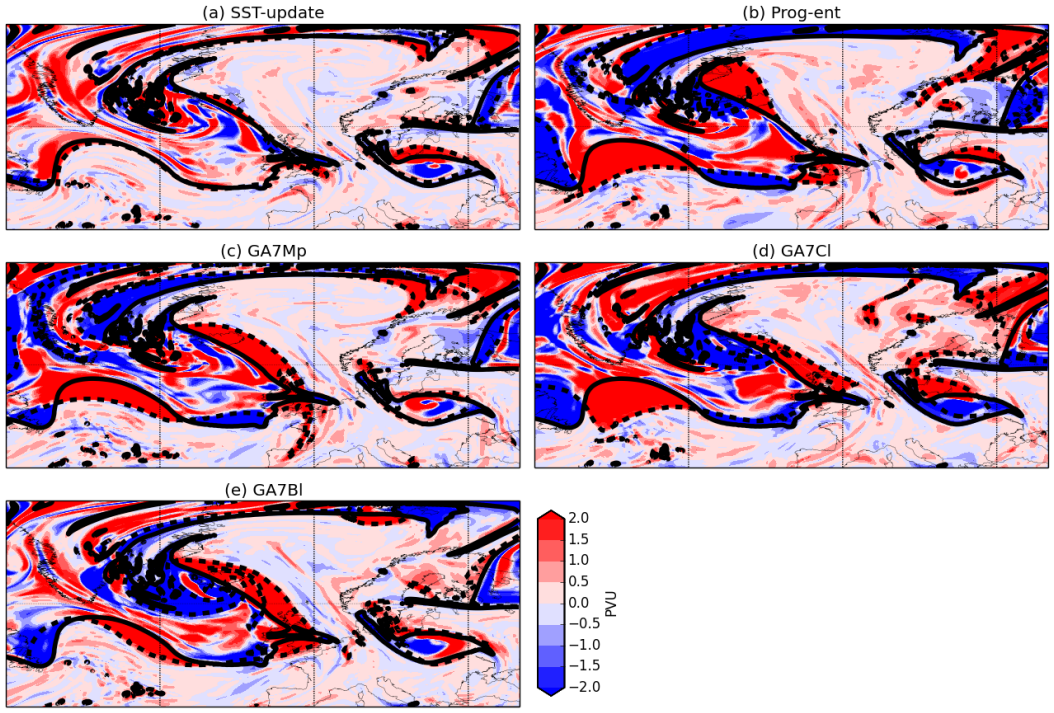

Figure 5.10: Difference (experiment - control) in PV315 in the (a) SST-update, (b) Prog-ent, (c) GA7Mp, (d) GA7Cl and (e) GA7Bl experiments. The Tp315 contour in the experiments (dashed contour) and control forecast (black contour) are plotted also. The difference is shown at seven days into the forecast initiated on the specified start date.

5.7.1 Role of heating

The difference in total diabatic heating (as defined in section 5.4.5) on the 315 K surface between each experiment and the control simulation is plotted at seven days lead time in Fig. 5.11 so the results can be directly compared to the PV315 differences shown in Fig. 5.10. The heating represents the non-conserved part of θ and indicates where diabatic processes are active and air masses have undergone ascent or descent. There are large differences in the total diabatic heating of air parcels on the 315 K isentropic surface during the first seven days of forecast integration. The structure of the difference in PV315 between the control and each experiments clearly resembles that of that difference in total diabatic heating (which can exceed 20 K). Given that the total diabatic heating in the control forecast is generally less than 30 K (Fig. 5.1), these differences are considerable. There is generally more heating within the large-scale ridge for each of the experiments when compared to the control. In particular, the GA7Cl and Prog-ent experiments exhibit more heating across the ridge interior and as well as in the region where the ridge is

extending further north. This suggests that the ridge is more amplified because of the increased ascent of air masses resulting in the air masses reaching higher levels and the ridge becoming larger. The regions of largest difference in heating between the control simulation and the model physics ensemble are in the location of the WCB ascent and outflow as shown for the control experiment in Fig. 5.9(a). This suggests that changes to the heating in the WCB of the cyclone arising from the changes to the parameterised diabatic processes in our experiments are causing the different amplifications of the ridge. Note that here we are using a large threshold of $\theta - \theta_0$ (as defined in section 5.4.5) as a proxy for WCB air masses (they have experienced strong ascent and heating). For example, in the Prog-ent experiment, $\theta - \theta_0$ is increased meaning there is greater latent heat release in the WCB which results in its outflow reaching higher isentropic levels and the ridge being larger than in the control simulation. The region of negative difference in heating on the western flank of the ridge that is present in nearly all of the experiments is likely a result of a shift in the WCB ascent region in the experiments.

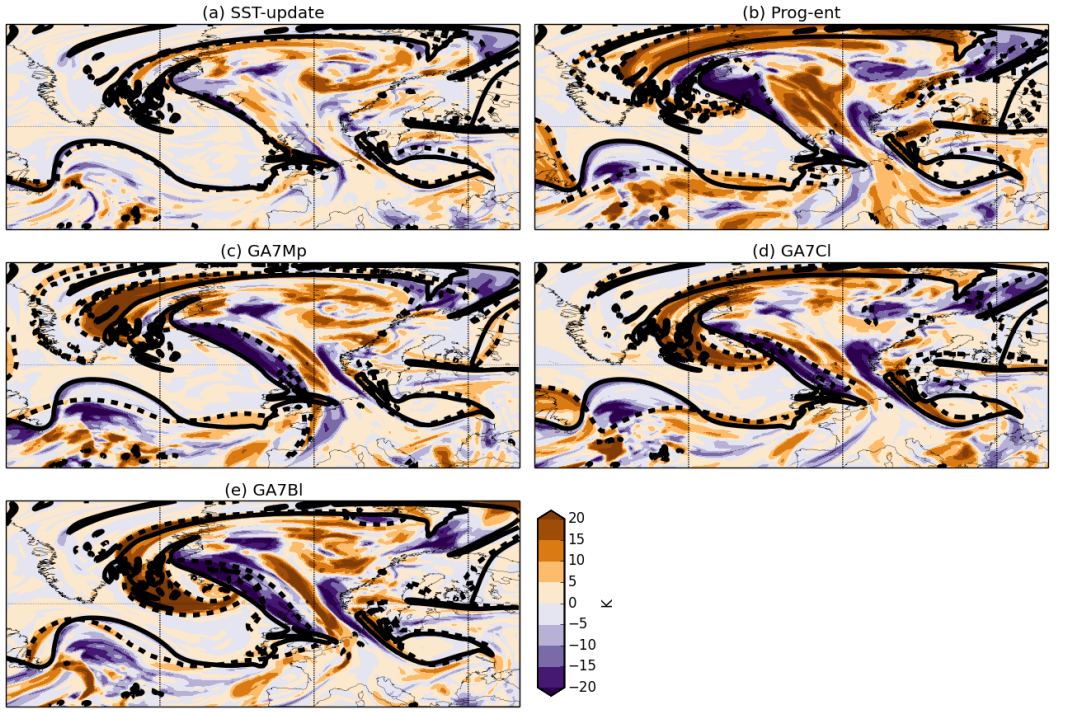

Figure 5.11: Difference (experiment - control) in total diabatic heating at 315 K in the (a) SST-update, (b) Prog-ent, (c) GA7Mp, (d) GA7Cl and (e) GA7Bl experiments. The Tp315 contour for the experiments (dashed line) and control forecast (solid) are plotted also. The fields plotted are from the forecast initiated on the specified initiation date at a lead time of seven days.

The WCB intensities in the control simulation and experiments are consistent with

the difference in heating in the ridges observed in Fig. 5.11: experiments with more WCB trajectories have more heating in the ridge when compared to the control and also a ridge that extends further north. To quantify this relationship the area of the ridges in the experiments was calculated as the area of regions north of 51.33°N with PVU values on the 315 K isentropic surface less than 2 PVU (not shown). The difference between each of the model experiments and the control forecast in the number of WCB trajectories, diabatic heating at 315 K, and ridge area appear to be highly correlated (correlations greater than 0.7), though the small sample size does not allow for a robust statement regarding these correlations. It is clear however that modifying the model parameterisations have an effect on WCB intensity and experiments with stronger WCBs had increased total diabatic heating and larger ridges.

5.7.2 Vertical structure of heating

Vertical cross sections of the total diabatic heating between 40-80°N in each of the simulations are shown in Fig. 5.12, averaged between 60°W and 40°E (the domain shown in Fig. 5.11), with the averaged 2 PVU contour overlain for tropopause identification. The region used to average the heating captures the WCB region and its outflow into the upper-level ridge. The blocking ridge is evident in all simulations to the north of 55°N as a slight increase in average tropopause height with latitude.

The general vertical structure of heating in the control and each model experiment is similar. There is a positive total diabatic heating throughout most of the upper-troposphere in the blocking ridge in all the simulations. The strongest regions of diabatic heating are generally near the tropopause (or above the average location of the tropopause) north of 60°N and extending towards the pole. This shows that air masses have been heated (in the WCBs of the cyclone) in the simulations prior to their arrival at upper levels in the blocking ridge. The average heating throughout this cross section is strongest in the Prog-ent, GA7Cl and GA7Mp experiments. This is consistent with these experiments having more heating throughout the ridge on the 315 K isentropic surface and more intense WCBs than in the control (Figs 5.11 and 5.9). We would expect the convection, cloud and microphysics parameterisation schemes to be active in the cloudy, ascending air of the WCB and changing these schemes to result in different diabatic heating rates. Figures 5.11 and 5.12 show only snapshots of the heating structure in the simulations for one lead time and for particular isentropic surfaces or longitude bands.

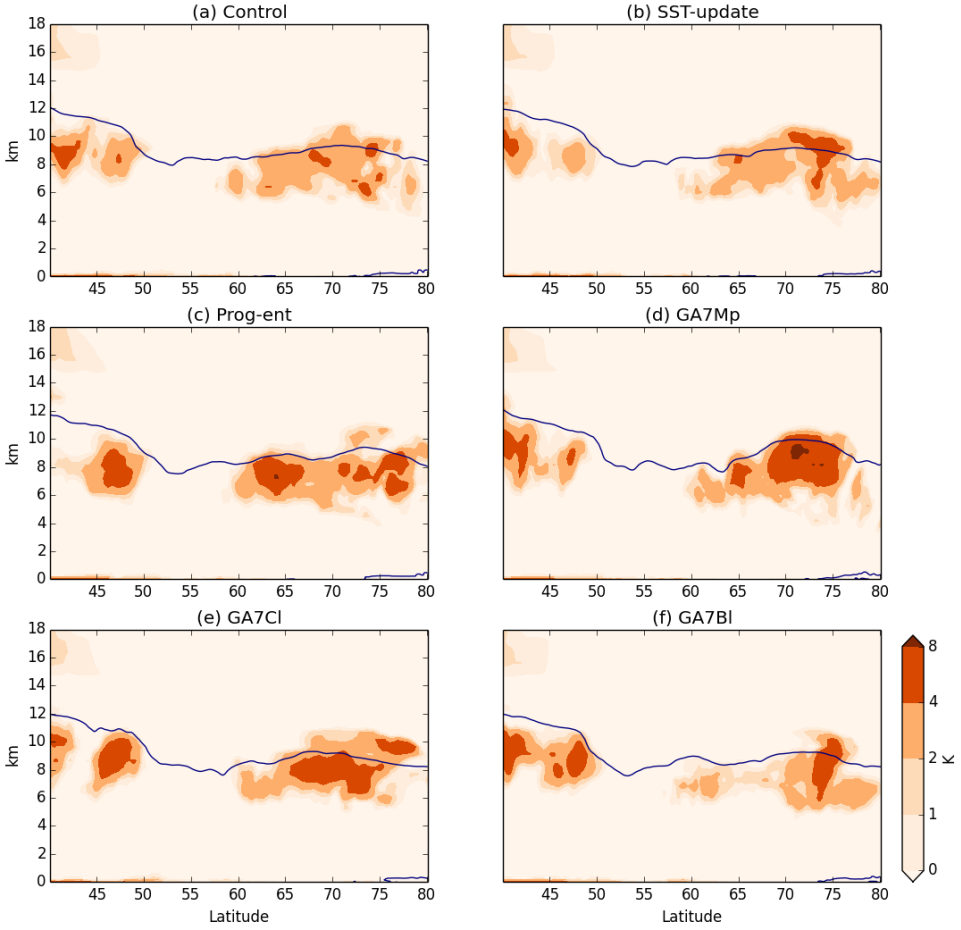

Figure 5.12: Cross section of total diabatic heating between 40 and 80° averaged between 60°W and 40°E in the (a) control forecast and the (b) SST-update, (c) Prog-ent, (d) GA7Mp, (e) GA7Cl and (f) GA7Bl experiments at 1200 UTC 4 October 2016 (168 hours lead time).

To quantify how the total heating in the WCB during the forecast evolution is changing in the experiments, and to verify that this is driving the ridge amplification differences, an integrated measure of the diabatic heating is now calculated.

5.7.3 Integrated heating

The θ-tracer technique accumulates the diabatic heating along Lagrangian-trajectories throughout the forecast integration. The $\theta - \theta_0$ output at t days lead time therefore represents the total heating that air parcels arriving at each grid point have undergone throughout the t days of the simulation. To determine how much diabatic heating has occurred during the WCB ascent we can integrate the heating term in the

region of WCB outflow at the time it reaches the upper-troposphere. The θ-tracer diagnostic then gives us the heating the WCB trajectories have experienced since the start of the forecast. This calculation assumes the integration only covers the WCB period, i.e. there was not strong heating in the early part of the forecast, which is true for this case (the WCB started around two days into the forecast). Furthermore, the forecast evolution in the control forecast and model experiments is very similar for the first two days (prior to WCB development) meaning differences in total heating in the first seven days of forecast integration are due to differences in the diabatic heating associated with the WCB ascent. It has been seen using trajectory analysis that the WCB outflow is within the ridge and hence we can integrate the diabatic heating over the ridge at various isentropic levels to quantify the total heating of air parcels arriving in the upper-level ridge.

We calculate the integrated heating measure (IHM), which represents the total heating in grid boxes within the WCB outflow (grid boxes that have strong ascent) normalised by the ridge area at a certain lead time, as

$$IHM(t) = \frac{\sum_{i,j \in W \cap R} cos(\phi_j)(\theta - \theta_0)_{i,j}}{(\sum_{i,j \in R} cos(\phi_j)) \times t}, \tag{5.15}$$

where W is the WCB outflow region ($\theta - \theta_0 > 10\ K$), R is the ridge ($PVU < 2$ and north of 51.33°N within the domain shown in Figure 5.11) and ϕ is the latitude of grid point i, j. Note the conclusions presented in this section are robust to the choice of latitude used to define a ridge. This gives IHM units of K/day. The IHM is calculated on isentropic surfaces between 310 and 340 K to measure the strength of heating of the air parcels in the WCB outflow within the ridge reaching (passing through) the different levels.

The IHM is shown in Fig. 5.13 at a forecast lead time of seven days. The total diabatic heating, and level at which the heating is maximum, is different in each of the experiments. The Prog-ent and GA7Cl experiments generally have the strongest heating in the WCB air parcels when looking at the different θ levels; the GA7Bl experiment and the control forecast generally have the least. The control simulation has the least integrated heating at 315 K, consistent with Fig. 5.11. The θ surface for which the integrated heating is strongest depends on experiment, though is between 315 and 330 K, with the experiments with larger total diabatic heating in the WCB having the maximum heating at higher levels, illustrating the link between WCB diabatic heating and ascent. The large range of θ surfaces at which diabatic heating in the WCBs is maximum reflects the

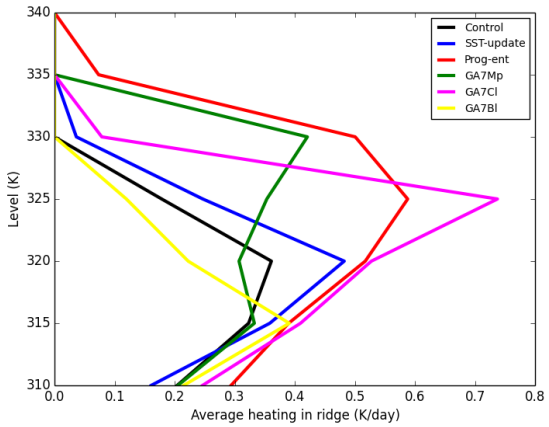

Figure 5.13: IHM as a function of isentropic level in the control forecast and model experiments. The total accumulated heating is averaged over the seven days of forecast evolution.

uncertainty in WCB dynamics and the level their outflows reach. The control simulation and GA7Bl experiment have no outflow reaching 330 K; the SST-update, GA7Cl and GA7Mp have no outflow reaching 335 K. The Prog-ent experiment has outflow reaching the highest isentropic level among the experiments. Averaging the IHM for the different WCB outflow levels yields an estimation of the total heating of WCB air parcels reaching the upper troposphere in the ridge. Averaged values were smallest for the GA7Bl experiment and control forecast (0.135 K/day and 0.152 K/day, respectively) and largest in the Prog-ent and GA7Cl experiments (0.338 K/day and 0.286 K/day, respectively). The vertically averaged heating rates are also shown in the first column of Fig. 5.14.

The IHM calculated provides consistent results with the analysis previously presented and the hypothesis introduced in the introduction of this article. The Prog-ent and GA7Cl experiments have larger ridges, forced by increased heating across the ridge at 315 K, stronger heating meridionally throughout the troposphere across the WCB region and stronger heating throughout the WCB outflow reaching most isentropic levels. The results demonstrate that the diabatic heating in the WCB trajectories is driving the amplification of the upper-level ridge. The GA7Bl experiment for example had a large number of WCB trajectories, but the diabatic heating was not strong, its WCB did not reach high altitudes and its ridge was not amplified. The Prog-ent and GA7Cl experiments had increased diabatic heating in their WCB developments, the outflow from their WCBs reached higher isentropic levels and their ridges were larger. This demonstrates that by changing the parameterisations of convection and cloud, the diabatic heating in the WCB ascent was increased which resulted in its outflow reaching higher levels and a

more amplified upper-level ridge developing in the forecasts. The picture is not as clear when looking at the block metrics: whilst the Prog-ent experiment had a similar area blocked to the control forecast (slightly larger at certain lead times) the GA7Cl experiment had a smaller area blocked. The block index only considers geopotential height at 500 hPa and may be less sensitive to changing ridge amplitudes at higher levels.

5.7.4 Dominant processes

The total diabatic heating for air parcels arriving in the block as part of the WCB outflow can be separated into the diabatic heating from each parameterisation. By doing this, it is possible to quantify how much diabatic heating is added by each process and which parameterisation scheme is contributing most to the total diabatic heating. The IHM can be computed for each parameterisation by replacing the $(\theta - \theta_0)$ term in (5.15) with the $\Delta\theta_i$ terms listed in section 5.4.5.

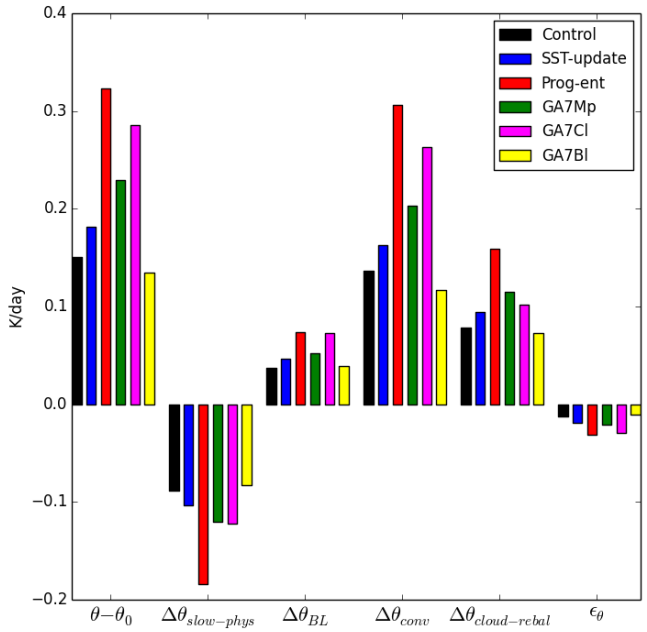

Figure 5.14: Contributions to the total IHM from the different physical parameterisations and for the different experiments at seven days lead time.

The IHM from each parameterisation considered is shown averaged for isentropic surfaces between 310 and 340 K and at seven days lead time in Fig. 5.14. The total diabatic heating $(\theta - \theta_0)$ and θ-tracer error $(\theta - (\theta_0 + \sum_i \Delta\theta_i))$ are also shown. In the control forecast and each of the experiments, the convection parameterisation contributes

most to the total diabatic heating along the WCB trajectories, followed by the cloud rebalancing scheme. The accumulated tendencies for each of the parameterisation schemes are larger than the tracer error in all experiments, despite the long forecast lead time. The amount of heating from the different parameterised processes in each experiment scales approximately linearly with total heating. For example, the Prog-ent experiment has the highest magnitude of total heating rate as well as heating from each parameterisation scheme, rather than a disproportionately large increase in heating coming from the convection scheme. This implies that the changes to the individual parameterisation schemes in the experiments are changing the evolution of the cyclone and its WCB and not just the heating increments from the modified scheme.

5.8 Conclusions

We have quantified the effects of operational changes to parameterisation schemes that impact diabatic processes, and those of running a forecast with updating SST, on midlatitude forecast evolution and compared this effect to the forecast evolution change from different initial conditions. We have also used the forecast evolution changes identified when modifying the parameterisations to show that upper-level ridge amplification depends on parameterised diabatic heating rates in the WCB of an extratropical cyclone. The forecast experiments were performed for the time period of the NAWDEX field campaign (Schäfler et al., 2018) because this included a variety of interesting weather events including a case study of block onset downstream of extratropical cyclogenesis that was the main focus of this study. The development of atmospheric blocks has been related to upstream cyclones since some of the earliest studies of blocking (e.g. Berggren et al., 1949; Colucci, 1985; Lupo and Smith, 1995). More recently, forecasts of atmospheric blocking and upper-level ridges have been shown to depend on the forecast of upstream cyclones (Maddison et al., 2019), the representation of their WCBs (Grams et al., 2018), and their parameterised diabatic processes (Joos and Forbes, 2016; Martínez-Alvarado et al., 2016b). Here it is demonstrated that this sensitivity can arise from diabatic heating from parameterised processes.

In forecasts initialised every 12 hours during the NAWDEX campaign period, updating the SST at daily intervals during the forecast evolution did not have a systematic effect on the forecast skill. SST is important for the evolution of the overlying atmosphere because of the influence surface fluxes have on the stability of the marine boundary layer

and near surface winds (Park et al., 2006; Donlon et al., 2012). Coupling the atmospheric model to an ocean model is known to improve prediction on subseasonal to seasonal timescales (Palmer and Anderson, 1994; Goddard et al., 2001; de Andrade et al., 2019). The small impact of evolving SST shown here suggests that running a coupled model may be less important in medium-range forecasts, where initial condition uncertainty usually dominates (Rabier et al., 1996; Kalnay, 2003), though giving the forecasts analysed SST and the relatively small sample of forecasts used here are caveats. Forecasts from the model with an improved convection scheme (one including memory about recent convective activity) led to an average reduction in forecast error. Periods of low forecast skill during the NAWDEX campaign period were associated with the onset and decay of atmospheric blocking events. The poor prediction of the transition to and from a blocked state has been a persistent problem in NWP (e.g. Tibaldi and Molteni, 1990; Pelly and Hoskins, 2003b; Ferranti et al., 2015; Lillo and Parsons, 2017). Periods of low forecast skill also tended to be associated with an increase in the amount of diabatic heating in upper-level ridges, consistent with previous studies showing that parameterised diabatic processes can be important for forecast skill (Rodwell et al., 2013; Martínez-Alvarado et al., 2016b). The forecast error for atmospheric blocking events during the NAWDEX period was characterised by an underestimation of block area. This was the case in forecasts from both the model experiments performed for this article and the operational ensemble forecasts. The location of the predicted blocking events was also assessed using a modified version of the SAL technique introduced in Wernli et al. (2008). The location of blocks in the analysis were systematically misforecast with the mean values far from zero even when taking into account the standard error.

The impact of the model upgrades on forecast evolution was considered in detail for a particular forecast initiation date preceding the intensification of an extratropical cyclone and the downstream development of a block. The cyclone development, between three and six days lead time, and downstream block development, after six days lead time, was missed in the control forecast, model experiments and operational ensemble. Forecasts of this event were identified as those having some of the least skill during the NAWDEX period in Schäfler et al. (2018). The cyclone in all of the forecasts was located too far east throughout its lifecycle. The downstream block error was forecast dependent, either misplaced or too small (or both) in the control and model experiment forecasts and in the operational ensemble forecasts. The development of blocking in this case was very unpredictable: forecast runs with different initial conditions, updated SST, and improved

parameterisations of diabatic processes were not able to capture the evolution of the flow that really happened. In the forecast of the cyclone and downstream block, there was more spread among the operational ensemble than the model experiments, particularly at early lead times. Initial condition uncertainty normally is larger for medium-range forecasts than model uncertainty (Lorenz, 1963; Rabier et al., 1996), though the small model experiment ensemble size and the method of modifying the model here were not intended to represent fully model uncertainty. The model experiments did however diverge from the control forecast considerably by six or seven days lead time.

A set of θ-tracers implemented in the MetUM was used to attribute the different upper-level forecast evolutions to the different diabatic heating rates from parameterised processes. The implemented new versions of the parameterisation schemes in the MetUM resulted in differences in the phase and amplitude of the upper-level blocking ridge. The different amplitudes of the upper-level ridge in the experiments resulted from differences in the total diabatic heating of air parcels arriving in the ridge in the WCB of an extratropical cyclone. Forecasts that produced larger-amplitude ridges had stronger diabatic heating throughout the WCB development. Changing the parameterisation of convection was shown to have the biggest increase in number of WCB trajectories, the diabatic heating of air masses in the upper-level ridge and downstream block forecast. The model experiments changed the cyclone location and intensity by approximately 5° (zonally) and 10 hPa, respectively, but the diabatic heating changed by more than 20 K. We hypothesise that the small changes in the cyclone location and intensity resulted from the changes to the parameterised diabatic processes which then resulted in large changes in the total diabatic heating in the ascending WCB. WCB ascent is sensitive to diabatic heating (Joos and Wernli, 2012) and errors have shown to amplify rapidly on the arrival of the WCB at upper levels (Davies and Didone, 2013; Martínez-Alvarado et al., 2016b; Grams et al., 2018). For this case study we have demonstrated that modifying parameterised diabatic processes changed the properties of the WCB, the diabatic heating of air parcels in the WCB ascent, and the upper-level ridge amplification and block forecast. Hence, model error attributable to the parameterisation of diabatic processes contributes to the documented role of extratropical cyclones and WCBs on the forecast uncertainty of upper-level ridges and blocking events (Grams et al., 2018; Maddison et al., 2019) and the large forecast errors associated with some blocking events (Rodwell et al., 2013; Ferranti et al., 2015). While this relationship was demonstrated by Joos and Forbes (2016) by implementing a new microphysical parameterisation in the IFS model and assessing the heating rate from

each microphysical process with consistent results to those found here, this is the first time (to the authors' knowledge) that this relationship has been quantified and compared for several parameterisation modifications and using all contributions to the total diabatic heating (such that the heating budget is closed). This study thus provides strong evidence that improving the representation of diabatic processes could reduce the frequency of poor forecasts associated with blocking events. Future work should try to investigate if the relationship between parameterised diabatic heating in WCBs and upper-level ridges in the case study included here is systematic across case studies and contributing to poor forecast skill.

5.9 Appendix

The forecast experiments performed for this article are described in detail in this appendix.

5.9.1 The MetUM

The MetUM GA6.1 uses the ENDGame dynamical core to solve the non-hydrostatic, fully compressible deep-atmosphere equations of motion with a semi-implicit semi-Lagrangian formulation (Wood et al., 2014). The prognostic fields are the three-dimensional wind components, virtual dry potential temperature, Exner pressure and dry density. Moist prognostic fields (e.g. mass mixing ratio of water vapour and prognostic cloud fields) are advected as free tracers. Prognostic fields are discretised horizontally onto a regular latitude-longitude grid with Arakawa C-grid staggering (Arakawa and Lamb, 1977). A Charney-Phillips staggering is used in the vertical (Charney and Phillips, 1953) with terrain-following hybrid height coordinates. ENDGame uses a nested iterative approach at each atmospheric time step with processes split into an outer loop and an inner loop (see Wood et al. (2014) for details). Processes that are parameterised in the MetUM include solar and terrestrial radiation, large-scale precipitation, large-scale cloud, sub-grid orographic drag, non-orographic gravity wave drag, the boundary layer, convection, and atmospheric aerosols and chemistry. The MetUM is coupled to the Joint UK Land Environment Simulator (JULES) land-surface model (Clark et al., 2011). For a full description of the MetUM GA6.1 the reader is referred to Walters et al. (2017b).

5.9.2 Sensitivity experiments

5.9.2.1 Prognostic entrainment

In the Prog-ent experiment, the convection scheme in GA6.1 is changed to a scheme that includes prognostic entrainment rates, designed to give the convection scheme memory about recent convective activity. The change to the Prog-ent scheme also includes the change to the 6A convection scheme that is part of the GA7 convection scheme (Walters et al., 2017a). The numerics of the convection scheme were revised for the 6A scheme. A convection parameterisation represents sub-grid scale cumulus clouds within a grid box and their associated transport of heat, moisture and momentum. The MetUM GA6.1 uses a mass flux convection scheme that is an extension of Gregory and Rowntree (1990). The scheme consists of three steps: (i) initial convective diagnosis of whether convection is possible given boundary layer properties; (ii) a call to either the shallow or deep convection schemes at all points diagnosed as shallow or deep from step (i); and (iii) a call to the mid-level convection scheme at all grid points.

In the GA6.1 scheme fully developed, deep convective clouds can appear within a single timestep without any gradual development, which is not usually realistic. This can occur because the entrainment rate given to a cloud diagnosed as a deep convective cloud is one that is appropriate for deep convection that is fully developed, as there is no option in the scheme for using higher entrainment rates appropriate for developing cumulus. In the real world, regions with a small amount of convective activity would be likely to have relatively small convective clouds with relatively high entrainment rates (if convection was present) and regions with lots of recent convective activity the opposite. A scheme has been developed at the Met Office that accounts for this difference by adding an additional 3D model prognostic ($\bar{P}$) that is a measure of recent convective activity (described in Willett and Whitall (2017)). It is defined as

$$\frac{D\bar{P}}{Dt} = \frac{1}{\tau}(\tilde{p}_{surf}^{conv} - \bar{P}), \tag{5.16}$$

where

$$\tilde{p}_{surf}^{conv}(x, y, z) = C(x, y, z)\max[p_{min}, p_{surf}^{conv}(x, y)] \tag{5.17}$$

is a 3D extension of the 2D surface convective precipitation rate (p_{surf}^{conv}). This equation gives $\bar{P}$ the same units as precipitation rate. $C(x, y, z)$ is defined as equal to unity at a

given point if convection is active and zero if not, p_{min} is an arbitrarily small precipitation rate (set to 10^{-5} kg m^{-2} s^{-1}) allowing non-precipitating clouds to contribute to $\bar{P}$, and τ is the e-folding time (set to three hours) that defines the memory timescale. $\bar{P}$ is related to the entrainment rate such that grid points that have had relatively little amounts of recent convection have higher entrainment rates and vice versa. To do this, the standard entrainment rate is scaled by the 3D factor

$$F = C_{grad} \log_{10} \left(\bar{P} \frac{q_s^{ref}}{q_s^{LCL}} \right) + C_{int}, \tag{5.18}$$

where $C_{grad} = -1.1$ is a constant controlling the strength of the coupling between the entrainment and $\bar{P}$, $C_{int} = -2.9$ is an intercept, q_s^{LCL} is the specific humidity of an undilute parcel-ascent to the lifting condensation level (LCL) calculated in the convective diagnostics, which is normalised by a reference value $q_s^{ref} = 20$ g kg^{-1}. Estimates of the range of tropical precipitation rates and associated entrainment rates (from observations and model data) were used to derive the values of C_{grad} and C_{int}. The scaling factor F is limited to the range 0.5–2.5 which requires the scaling to have a logarithmic dependence on $\bar{P}$ because precipitation rates can vary over several orders of magnitude. The dependence on q_s^{LCL} reflects the strong control temperature has on precipitation rates. The Prog-ent scheme has been tested for several cases over tropical regions for a variety of tropical processes (Willett and Whitall, 2017), and its performance assessed in terms of mean climate and average NWP scores across the globe. The impact that the Prog-ent scheme has in simulations of extratropical cyclones is investigated here.

5.9.2.2 Evolving SST

The SST-update experiment is designed to mimic a coupled NWP model that has evolving SST. The SST of the atmospheric model is updated at daily intervals in the forecast evolution. The sea-ice fraction is also updated each day as these fields both contribute to the surface fluxes we are trying to evolve. The SST are updated daily at 12 UTC using the OSTIA analysis (Donlon et al., 2012) produced by the Met Office for the corresponding date in the forecast evolution. The OSTIA analysis is a global SST and sea-ice fraction field at a resolution of 1/20° produced using several different sources of both satellite data and in-situ measurements of SST and sea-ice fraction. The product is described fully in Donlon et al. (2012). Operational forecasts produced at the Met Office are initialised with the OSTIA analysis of that date and the fields are not updated during

the forecast integrations.

5.9.3 GA7 parameterisations

The parameterisations that are modified to their GA7 versions in the experiments are now described: the microphysics, large-scale cloud and boundary layer parameterisation schemes. These processes are likely to have an impact on cyclone and WCB development and hence will likely affect PV modification near the tropopause and have an impact on the downstream forecast flow pattern. The convection scheme is also likely to have an impact here, but we will use the Prog-ent convection scheme described above to elucidate the effects that a new convection scheme can have. Details of each of the schemes being modified are first given, followed by the specific GA7 changes that are made to the scheme from the GA6.1 control run (a full description of the MetUM GA6.0/6.1 configuration can be found in Walters et al. (2017b) and of GA7.0/7.1 in Walters et al. (2017a)). The GA ticket numbers (#GA) used in the GA7.0/7.1 development and documentation are included here for reference.

5.9.3.1 Microphysics

The microphysics (also known as the large-scale precipitation) scheme is responsible for the formation and evolution of precipitation due to grid scale processes, including phase changes between vapour, liquid water and ice and their vertical advection. The GA6.1 (control) scheme is an extensively modified version of the Wilson and Ballard (1999) scheme. The individual changes made to the microphysics scheme that constitute the GA7 upgrade are summarised below.

- **New sub-grid scale cloud water content variability treatment (#GA15)**: the standard deviation of cloud water content in a grid box (divided by its mean value) is now used to represent the sub-grid scale water content variability effect on radiation in the microphysics scheme. This has been changed from a globally constant value to a more realistic one dependent on cloud fraction, vertical layer thickness and whether the cloud is convective or not.

- **Change to warm rain microphysics (#GA52)**: within the microphysics scheme the warm rain microphysics part has been nearly totally rewritten for GA7. The autoconversion and accretion parameterisations are changed and the evaporation

and sedimentation code have been improved. The new scheme also explicitly represents how sub-grid variability affects microphysical process rates. Sub-grid rain fraction is now consistently set by either the fraction of autoconverting cloud or melting snow when rain is created.

- **Turbulent production of liquid water in mixed-phase clouds (#GA120)**: the parameterisation of liquid water production in mixed-phase clouds is changed to improve the production and maintenance of super-cooled liquid and mixed-phase clouds, which is a known problem across many models (Illingworth et al., 2007). A probability distribution of supersaturation is calculated and then the liquid-cloud properties are calculated as moments of this distribution. A lack of super-cooled liquid in cold clouds has been shown to contribute to model biases in, for example, surface radiative fluxes (Curry et al., 2000) and liquid water path (Klein et al., 2009).

5.9.3.2 Large-scale cloud

Clouds form on scales smaller than the grid scale before the grid box average humidity reaches saturation. The large-scale cloud scheme is required to determine how much of the grid box is covered by cloud and how much condensed water is contained in those clouds. Within a grid box, the cloud scheme calculates the amount and phase of condensation at each time step and calculates or updates the cloud fractions. The cloud scheme can create latent heat release when it converts water vapour into liquid or ice. The calculated cloud cover and ice water contents are passed to the radiation and microphysics schemes to calculate the radiative impact of the clouds and determine if any precipitation has formed. The prognostic cloud and prognostic condensate (PC2) scheme is used (Wilson et al., 2008b,a) in both GA6 and GA7. Modifications to the GA6.1 scheme for the upgrade to GA7 are made as follows:

- **Representation of the radiative impact of convective cores (#GA44)**: for some convective cloud types, e.g. shallow fair-weather cumulus, detrainment into the environment may be small but the radiative impact of the convective core considerable and needs to be represented. The impacts of these clouds are included using a convective cloud model that includes the radiative effects of the convective cores. Previously it was assumed a convective plume rises and mixes with the environment and it is only once condensate has detrained from the plume that it

will have a radiative effect.

- **New critical relative humidity value that is based on turbulence (#GA89)**: the critical relative humidity used to determine the initiation of cloud in grid boxes that are cloud free, but with increasing (in time) relative humidity, is changed from a constant global value for each model level to a value based on turbulence. This new value is also used for the removal of cloud from grid boxes that are full of cloud when relative humidity is decreasing. The value is calculated using the resolved vertical gradients in temperature and humidity as well as the sub-grid mixing length, eddy diffusivity and turbulent kinetic energy calculated from the boundary layer scheme.

- **Removal of unnecessary complexity when dealing with ice cloud (#GA98)**: the value of the cirrus spreading rate has been reduced from $1.0 \times 10^{-3}s^{-1}$ to $1.0 \times 10^{-5}s^{-1}$. The cirrus spreading rate acts to increase the frozen cloud fraction and was introduced into an earlier configuration of the MetUM to counteract an unrealistic reduction in mean ice cloud fraction.

5.9.3.3 Boundary layer

The atmospheric boundary layer scheme parameterises vertical turbulent transports of heat, moisture and horizontal momentum. These turbulent motions are not resolved in global NWP models but are important for producing realistic vertical structure in wind and thermodynamic profiles. The scheme primarily handles the lowest layers in the MetUM, but does include a free-tropospheric component that can extend to model levels approaching the tropopause. The boundary layer scheme is based on Lock et al. (2000), with the modifications of Lock (2001) and Brown et al. (2008). Upgrades from the GA6 boundary layer parameterisation for GA7 are described below.

- **A boundary layer entrainment dependence on decoupling (#GA13)**: surface driven turbulence entrainment at cloud top is restricted when the cloud layer is decoupled from the surface so the parameter value diagnosing decoupling is increased in GA7 and a linear weighting is introduced to better match large eddy simulations. The boundary layer scheme includes the parameterisation of turbulent entrainment at the top of cloudy boundary layers. There are sources from both the cloud top (radiative and evaporative cooling) and the surface (positive buoyancy

fluxes and wind shear).

- **Forced convective clouds and resolved mixing across the top of the boundary layer (#GA83)**: a new parameterisation of the profile of cloud fraction for clouds forming in the capping inversion is implemented that varies linearly in height between the cloud base and cloud top. Forced convective clouds can form in undulations of the top of convective boundary layers when the capping inversion thickness is parameterised. These are too shallow to reach the level of free convection and become cumulus clouds. Previously, capping inversions at the top of convective boundary layers were assumed to be thin enough to be unresolved by the model so the entrainment flux across the boundary layer could be applied at one vertical level. As the model resolution increases this is no longer the case.

- **Retuned cloud threshold for diagnosing a shear dominated boundary layer (#GA162)**: the fraction of the cloud layer through which the Richardson number is calculated to diagnose a shear-dominated boundary layer is changed from 0.3 to 0.4. This change was not scientifically formulated but instead is a tuning change implemented in GA7.

Chapter 6:

Conclusions

In this chapter, the key results presented in this thesis are summarised in light of the research questions highlighted in chapter 1 and some of the limitations and implications of the thesis and ideas for future work are discussed. First, the main topics of the work presented in this thesis are recapped.

Atmospheric blocks occur frequently in the northern hemisphere midlatitudes and have a profound effect on the weather in these regions. This means it is of large socio–economic interest to be able to accurately predict blocking events as far in advance as possible. Until even now however, atmospheric blocks have been a situation that numerical weather prediction (NWP) centres struggle to predict accurately (Tibaldi and Molteni, 1990; Pelly and Hoskins, 2003a; Matsueda, 2009). The transition to a blocked flow and the frequency of blocking occurring in a given period are known to be particularly difficult to predict. The poor representation of blocks in NWP models partly results from the lack of a complete dynamical theory for their development (e.g. Woollings et al., 2018). Many theories proposed to explain the dynamics of blocking suggest (either explicitly or implicitly) that there is a strong influence of upstream extratropical cyclones, or cyclonic synoptic–scale eddies as they can be otherwise known, on a block's lifecycle (Shutts, 1983; Illari, 1984; Colucci, 1987; Nakamura et al., 1997; Pelly and Hoskins, 2003b; Yamazaki and Itoh, 2013; Luo et al., 2014; Pfahl et al., 2015). There are two hypotheses addressed in this thesis. The first hypothesis, which motivates the analysis included in chapters 4 and 5, is that upstream cyclones play an important role in the forecast of upper–level Rossby waves and atmospheric blocking.

The mechanistic link between cyclones and upper–level Rossby waves and blocking in NWP simulations can be summarised using potential vorticity (PV). The parameteri-

sations of various diabatic processes are known to have an effect on cyclone development (Forbes and Clark, 2003), warm conveyor belt (WCB) intensity (Joos and Wernli, 2012; Martínez-Alvarado et al., 2016b), the PV pattern near the tropopause (Chagnon et al., 2013), the structure of the upper–level Rossby wave pattern (Chagnon and Gray, 2015; Joos and Forbes, 2016), and the downstream propagation of Rossby waves (Harvey et al., 2016). This suggests parameterisations of diabatic processes active in cyclones, and particularly in their WCBs, are important for the accurate forecast of blocking. Inaccurate representations of WCBs have been shown to result in the poor forecast of upper-level ridges and atmospheric blocks (Martínez-Alvarado et al., 2016a; Grams et al., 2018) which further supports this hypothesis.

A main source of forecast error in NWP originates from the numerical model used to represent the atmosphere (e.g. Harrison et al., 1999; Orrell et al., 2001; Simmons and Hollingsworth, 2002). Model error can originate from any part of the atmospheric model and is sometimes considered harder to deal with than initial condition error (Buizza et al., 2005). Sources of model error considered in this thesis are the model's dynamical core and its set of parameterisation schemes representing subgrid scale processes. The parameterisation schemes together represent the gridscale effect of all the subgrid processes and how they interact non–linearly with the large–scale flow. They are physically based, but contain assumptions and uncertainties which can be approximately accounted for by adding stochasticity (e.g. Buizza et al., 1999). A model's dynamical core numerically solves the fundamental equations of motion and they vary across NWP centres in their grid geometry, numerical method and resolution. Changing the dynamical core of a model can have a large impact on its forecast evolution (e.g. Walters et al., 2017b). The second motivating hypothesis of the thesis is that reducing model error arising from a NWP centre model's dynamical core and parameterisation schemes will lead to improved forecasts of atmospheric blocking. This hypothesis is tested in chapters 3 and 5.

6.1 Key results

In this section the key results that were presented in chapters 3 through 5 are discussed. Chapters 3 and 4 were included in the versions in which they were published in Martínez-Alvarado et al. (2018) and Maddison et al. (2019), respectively. Chapter 5 was included in the form that it had been submitted to the Quarterly Journal of the Royal Meteorological Society. The two research questions posed for each chapter in section 1.1 are

addressed individually then synthesised to address the main overarching research question posed initially in section 1.1.

Chapter 3

1. **What impact did the introduction of a new dynamical core in the Met Office Unified Model (MetUM) have on the forecast of atmospheric blocking?**

   In chapter 3, forecasts of atmospheric blocking in three currently (recently) operational configurations of NWP models were assessed and the impact that a new dynamical core in a NWP centre model can have on forecasts of atmospheric blocking was investigated. The effect of the dynamical core change in the MetUM on block forecasts was identified by comparing forecasts from two winter seasons before and after its introduction in the Met Office Global and Regional Ensemble Systems (MOGREPS). The new dynamical core was designed to improve the accuracy, scalability and stability of the MetUM by introducing (among other things) a nested iterative structure for each time step, with processes split into an inner and outer loop which is shown to improve many of the calculations performed within the time step (see Walters et al. (2017a) for full details). Forecasts from the European Centre for Medium–range Weather Forecasts (ECMWF) ensemble prediction System (EPS) and the Korean Meteorological Administration (KMA)-EPS were also analysed as the EPSs from these centres remained relatively consistent across these four winters and therefore acted as controls to measure the effect of the new dynamical core in the MetUM. The KMA-EPS in particular provided a useful comparison as it used the same underlying model as in the MOGREPS (the MetUM), during the time period considered, but did not change to the configuration with the new dynamical core.

   Forecasts from all three centres during the first two study winters exhibited a general underestimation of peak blocking frequencies across the northern hemisphere for forecast lead times greater than five days. This is consistent with many earlier studies assessing block predictability (e.g Tibaldi and Molteni, 1990; Matsueda, 2009). The predicted frequencies from the MOGREPS and the KMA-EPS were similar (and more different than the ECMWF-EPS) in forecasts from the first two winters. The spread among the ensemble forecasts from the MOGREPS and the KMA-EPS was also similar during this time period. A hit rate analysis was performed to assess

the models' ability to predict timing of blocking events. Generally all the models had accurate predictions (hit rates greater than 0.5) of block onset and decay out to forecast lead times of around 3–4 days, again showing no clear improvement for forecasts from the models in earlier time periods (Pelly and Hoskins, 2003a; Jia et al., 2014). Forecasts of block onset and decay were also similar for the MOGREPS and the KMA-EPS and different (in this case worse) than the ECMWF-EPS.

Considering forecasts from the two winters after the introduction of the new dynamical core in the MOGREPS there was a clear and consistent improvement in the model's ability to predict the frequency and timing of blocking events. Regional peaks in the observed blocking frequency were better forecast with the new dynamical core in both the control and ensemble member forecast spread. Hit rates for the timing of blocking events remained higher for longer lead times without a corresponding rise in false positives, also consistent across the ensemble. Comparing forecasts from MOGREPS during these two winters to forecasts from the KMA-EPS revealed this improvement was not due to inter–annual variability as now the MOGREPS and KMA-EPS had larger differences and the MOGREPS was closer to the ECMWF-EPS. This analysis showed a clear improvement in block representation with the new dynamical core.

2. **How are the errors in the forecast of blocking related to the systematic errors in Rossby wave structure?**

   Gray et al. (2014) identified a systematic bias in the forecast of upper–level Rossby waves in several NWP models: the area of ridges in the tropopause and the isentropic gradient in PV in ridges both decrease with lead time. The decrease in ridge area with lead time is consistent with the long–standing bias of under–predicted block frequency with lead time because blocks are a subset of tropospheric ridges and there exists a close relationship between blocks and upper–level Rossby waves (Austin, 1980; Altenhoff et al., 2008; Masato et al., 2012).

   In the first two winters analysed in chapter 3, all three NWP models exhibited a general reduction in both ridge area and PV gradient as well as a decrease in predicted blocking frequency with lead time, confirming that these features are closely linked in the forecasts. Forecasts from the models in the two winters after the new dynamical core was introduced in the MetUM further supported this relationship as well as highlighting the improvement gained from the new dynamical core. In forecasts

from the KMA– and ECMWF–EPSs there remained a similar reduction in ridge area, PV gradient and block frequency with lead time. In the MOGREPS however, there was now a slight increase in ridge area with lead time, less of a strong reduction in PV gradient with lead time and a more constant predicted block frequency. The new dynamical core had a better representation of upper–level Rossby waves as well as blocking. Gray et al. (2014) suggested the systematic error in Rossby wave structure could originate from model error associated with the parameterisation of diabatic processes. The results presented in chapter 3 imply these processes could also be important for block forecasts.

One uncertainty in the results obtained in chapter 3 was whether the improvement in forecasts from the MetUM described above could be attributed to the dynamical core change directly because there was also a resolution increase (as well as minor parameterisation changes). This uncertainty was addressed in two ways. Firstly, it was noted that the KMA-EPS ran at a higher resolution than the MetUM in the first two winter periods and, in spite of this, both models produced very similar forecasts of blocking events. Secondly, one winter of hindcasts was produced in which the MetUM was run with the new dynamical core but at the lower resolution used with the old dynamical core. The hindcasts showed a clear improvement with the new dynamical core compared to the MOGREPS and KMA-EPS in both block and upper-level ridge representation. It was thus concluded that the dynamical core was having the biggest impact on the forecast improvements seen.

Chapter 3 was concluded with a feature chain linking the improved accuracy of the MetUM's new dynamical core with the improved upper–level Rossby wave and block representation via improvements to extratropical cyclone intensity. This feature chain assumes there exists a link between cyclone and block development in the forecasts. This assumption is supported by the known effects of cyclones on the upper–level PV structure (e.g. Wernli and Davies, 1997; Ahmadi-Givi et al., 2004; Chagnon et al., 2013) and the block theories involving upstream cyclones mentioned at the start of this chapter and in chapter 2. The aim of the fourth chapter is to determine if this relationship exists in a statistical sense and is summarised using the two research questions below.

Chapter 4

1. **How much of the difference seen in the ensemble forecast of block area can be attributed to the earlier forecast of an upstream cyclone?**

Forecasts of block area in the ECMWF-EPS were considered for the 20 most unpredictable cases between September 2006 and March 2017. The 20 most unpredictable cases were chosen based on the inter–quartile range in the ensemble spread of block area at a forecast lead time of six days. Ensemble sensitivity analysis was performed to answer this question. The technique provides a quantified change in a chosen response function, here block area, given a one standard deviation (σ) change in the ensemble forecast of a chosen precursor variable, here geopotential height at 1000 hPa (Z1000) and PV on the 320 K isentropic surface (PV320). Z1000 and PV320 were chosen as these fields can be used to infer cyclone and WCB structure. In each case the upstream 'feeder cyclone' was identified using WCB trajectory analysis.

A 1σ change among the ensemble in the forecast of Z1000 two–three days prior to block onset was associated with between a 10 and 25% change in the block area relative to the block area in ERA-I on the block onset date in 18 out of the 20 cases (90%). In 17 out of the 20 cases (85%) there was increased forecast sensitivity upstream of the block location near an extratropical cyclone. Implying the representation of the cyclone two–three days prior to block onset had a strong control over the downstream block development. The cyclone representation and downstream block formation were dynamically linked using WCB trajectories. Forecasts of blocking that had large errors have previously been found to result from the forecast of upstream features (Rodwell et al., 2013; Magnusson, 2017), and in particular cyclones (Matsueda, 2011) and WCBs (Grams et al., 2018). The uncertainty in block forecast was shown to be associated with upstream cyclones more systematically here. In some cases (35%) the sensitivity to Z1000 extended farther upstream in a wavetrain–like pattern. This implies that the different block developments in the ensemble members in these cases were also associated to changes in the hemispheric Rossby-wave pattern and the associated influence on Z1000. Large–scale Rossby-wave trains are known to drive block onsets (Tsou and Smith, 1990; Nakamura et al., 1997; Michel and Rivière, 2011).

The sensitivity of the forecast block area to PV320 was generally weaker and smaller in scale than the sensitivity to Z1000: 15 of the cases had between 10 and 25% change in the block area for a 1σ change in PV320. The smaller–scales present in the sensitivity field reflect the nature of the precursor variable, PV320, which is inherently fine-scale in nature. The sensitivity to PV320 is nearly always confined to regions either side of the tropopause. This implies changes among the ensemble in

the location of the tropopause are associated with the biggest change in block area. Diabatic processes in extratropical cyclones modify the PV near the tropopause (e.g. Wernli and Davies, 1997; Chagnon et al., 2013) which suggests that the increased sensitivity in these regions could be associated with model uncertainty arising from the parameterised diabatic processes. This association is tested in the final work chapter of this thesis.

Whilst there was commonality between the patterns in sensitivity to both Z1000 and PV320 across the 20 cases, there was no systematic sensitivity of block area in the ensemble to either Z1000 or PV320, i.e. the signs, spatial scales and magnitudes of the sensitivity patterns and their location relative to the block changed in each case. The sensitivity patterns in onset cases that had strongest sensitivity to Z1000 near the upstream feeder cyclone, and strongest sensitivity to PV320 in the trough–ridge above the feeder cyclone, indicate that the ensemble spread in block area was dominated by the earlier forecast of the feeder cyclone. This is in agreement with previous studies documenting the strong link between blocks and upstream cyclone activity (e.g. Lupo and Smith, 1995; Colucci and Alberta, 1996; Michel et al., 2012; McLeod and Mote, 2015). Ensemble spread was influenced by weather systems further upstream in the cases of larger wave–train–like sensitivities. These cases could be interpreted as consistent with global theories for block onset (e.g. Hoskins and Karoly, 1981; Nakamura et al., 1997; Altenhoff et al., 2008) or they could simply arise due to the linked positions of cyclones forced via Rossby wave trains. The many different flow configurations that can be defined as atmospheric blocks may cause the lack of systematic sensitivity pattern for block onset forecasts.

2. **What are the cyclone characteristics (in particular location and intensity) that are associated with the differing development of blocking in the ensemble?**

   To address this question, sensitivity patterns were studied in the region around the location of the upstream feeder cyclone (though no additional sensitivity calculation was made) at the lead time of maximum sensitivity. The feeder cyclone was identified as the cyclone having the most WCB trajectories arriving in the block at upper levels on onset date. Idealised calculations demonstrated that dipoles of equal magnitude in the sensitivity pattern to Z1000 imply that the forecast of the upstream cyclone's location was the most important for the ensemble representation

of block area. Monopoles in sensitivity imply it was changes among the ensemble in the cyclone's intensity that was associated with the largest change among the ensemble in block area. Dipoles in sensitivity that had poles that were different in magnitude suggest both location and intensity changes in the cyclone forecast were associated with changes in block area.

In light of these idealised results, it was determined that from the 17 of 20 onset cases that had large sensitivity to the feeder cyclone, the majority (14/17) had uncertainty associated with changes to both the feeder cyclone's intensity and location. The remaining six cases were evenly split between having ensemble spread in block area associated with change to cyclone intensity only, and those not associated with feeder cyclone changes. There exists a (moderate) correlation between cyclone intensity and WCB intensity (Binder et al., 2017) which supports the hypothesised mechanism behind the sensitivity patterns presented in the chapter: changes in the ensemble forecast of the cyclone also change the structure of its WCB and this results in differing block representation. The cyclone's location would also be expected to impact the upper–level development as coupling between the cyclone and upper–level PV features is important for cyclone and upper–level development (e.g. Hoskins et al., 1985).

It was shown in chapter 4 that there is an association between cyclone representation and downstream block development and it was hypothesised that this association was caused by different WCB developments in the ensemble and could be related to the parameterisation of diabatic processes. The hypothesis was based on the fact that diabatic heating in the WCBs of extratropical cyclones modifies the PV structure at upper–levels (Joos and Wernli, 2012; Chagnon et al., 2013) and the amplification and propagation of Rossby waves (Grams et al., 2011; Joos and Forbes, 2016). Earlier studies have shown that various steps in the hypothesised causal sequence starting from the parameterisation of diabatic process and ending in block development are valid. Diabatic processes can have a strong influence on cyclone intensification (Davis et al., 1993; Rossa et al., 2000). Latent heating and PV modification from parameterised diabatic processes are intense in numerical simulations of WCBs (Joos and Wernli, 2012). The outflow of WCBs reaches the upper troposphere with low values of PV (Wernli and Davies, 1997; Methven, 2015) and can therefore produce or amplify upper–level ridges (Pomroy and Thorpe, 2000; Grams et al., 2011). Different WCB representations can lead to different upper–level

Rossby wave structure (Martínez-Alvarado et al., 2016b; Joos and Forbes, 2016), and blocks forecast (Grams et al., 2018). Different parameterisation schemes can also cause different diabatic heating rates in the WCBs of extratropical cyclones (Martínez-Alvarado et al., 2016b; Joos and Forbes, 2016).

The work presented in chapter 5 followed this causal sequence from parameterisation change to block development change in a case study of blocking. Sensitivity experiments with the MetUM were used to demonstrate that forecast evolution changes can arise from different diabatic heating rates from parameterised diabatic processes within the WCB of an extratropical cyclone and the subsequent upper-level flow modification.

Chapter 5

1. **What is the impact of model physics uncertainty on medium–long range forecasts of atmospheric blocking and how does it compare to initial condition uncertainty?**

   A set of model upgrade experiments were utilised in chapter 5 to quantify the impact of model physics uncertainty on WCB development and downstream block development. Model error, including that resulting from model physics uncertainty, is known to be important for forecast evolution (Buizza et al., 1999; Stensrud et al., 2000; Simmons and Hollingsworth, 2002) and can in some cases be as important as initial condition error. Though initial condition error is normally the dominant cause of error in NWP (Rabier et al., 1996; Bowler et al., 2008) and reducing initial condition uncertainty remains a promising source of forecast skill improvement in current high resolution NWP models (Zhang et al., 2019). Forecast uncertainty arising from initial condition error was compared to model physics uncertainty by comparing the model upgrade experiments with the operational ensemble with perturbed initial conditions and stochastic model physics perturbations. Model physics uncertainty was explored in the experiments by implementing different parameterisation schemes, or planned operational upgrades to various schemes at the Met Office, or running forecasts with evolving sea surface temperatures (SST) (thus reducing boundary condition error). Two sets of experiments were performed for this chapter. An experiment with a new convection scheme and an experiment with daily evolving SST that were run for many forecasts initialised during the North Atlantic and Downstream Impact Experiment period. And a set of additional experiments modifying different parameterisation schemes that was run for a single

initialisation date.

Model physics uncertainty, represented by either changing the parameterisation of convection or changing the model's boundary conditions with SST that are updated daily into the forecast integration, did not have a large systematic effect on the average forecast error in a set of 54 forecasts from autumn 2016. The experiment with an improved representation of SST in the forecast evolution had RMSE values nearly identical to the control (operational–rerun) experiment. Improving the parameterisation of convection reduced the average RMSE slightly for lead times greater than six days, though perhaps not insignificantly from an operational weather forecaster's perspective. The ensemble mean is expected to perform better than any individual member on average (Toth and Kalnay, 1997; Ebert, 2001; Christiansen, 2019). This was also shown to be the case in the 54 forecasts analysed here.

In individual forecasts from specific initiation dates, there was a clear impact on the forecast evolution resulting from model uncertainty. Model uncertainty arising from the cloud, boundary layer and microphysics parameterisation schemes was also analysed for the case study included in chapter 5. The case study of cyclone intensification and downstream block development was presented to demonstrate the model uncertainty effect. The model physics experiments did not diverge considerably from the control simulation until after 5–6 days into the forecast evolution, after this time there was considerable difference in the evolution of the flow between the experiments. The effect of model uncertainty was smaller than initial condition uncertainty for early lead times. The case study cyclone that developed between 3 and 6 days lead time in the forecasts was not captured by any member of either the perturbed initial conditions or model physics experiments. The entire ensemble being wrong implies that either there was not enough ensemble members to capture the true evolution or the initial condition perturbations were not large enough and even a larger ensemble would not improve the forecast, or, alternatively, there existed a model deficiency that means the true evolution would be missed regardless of the ensemble size or magnitude of initial condition perturbation. In this case the model upgrade experiments performed may not have been large enough to account for this potential model deficiency.

2. **Is block development sensitive to the heating structure and potential vorticity modification from parameterised diabatic processes near the**

tropopause?

A suite of potential temperature (θ)-tracers were used to answer this question in chapter 5. The diagnostic was used to calculate the total non–conserved part of θ (that produced by diabatic or frictional processes) and show that it contributed to the development of the WCB and its subsequent outflow into the upper–level developing blocking ridge. The net effect of diabatic heating during the model integrations was compared in the model physics experiments for the same case study of block development downstream of the extratropical cyclone mentioned previously.

The model physics changes had some impact on the location and intensity of the cyclone between four and six days lead time: some experiments predicted the cyclone to be further west than in the control experiment, some further east, and there was some spread in the maximum intensity of the cyclone (≈10 hPa). There was a larger change in the number of WCB trajectories in the experiments (a difference of more than 200 trajectories out of around 1000) which suggests that whilst the grid–scale structure of the cyclones was similar, the modified parameterisation schemes had different diabatic heating tendencies and this had a bigger effect on the WCB development. Stronger diabatic heating in WCBs, particularly latent heat release, generally results in more intense ascent in the WCBs. There is a feedback loop involved here: stronger diabatic heating causes increased ascent which results in more cloud formation and more diabatic heating (Grams et al., 2018). The experiment modifying the convection scheme had the biggest increase in number of WCB trajectories. The representation of WCBs is known to be sensitive to the parameterisation of convection (Martínez-Alvarado and Plant, 2014) and microphysics (Joos and Forbes, 2016). The convection scheme is active in the WCB ascent and can contribute strongly to the total diabatic heating, so the change in total diabatic heating and hence the total strength of the WCB would be largest in the experiment with the modified convection scheme.

The relatively small changes in cyclone location and intensity, and larger change in WCB intensity, resulted in considerable changes in the upper–level PV pattern by six days into the forecast evolution and the total diabatic heating along trajectories arriving in the upper-level blocking ridge. The experiments with more intense WCBs generally had stronger total diabatic heating in the ridge occurring throughout the mid and upper troposphere, which caused a more amplified upper–level

blocking ridge. The change in total diabatic heating, arising from the changes to parameterised processes and their affect on the WCB intensity, resulted in a different upper-level Rossby wave amplification and block development. Diabatic processes were shown to contribute considerably to blocked air masses in Pfahl et al. (2015), and block forecast error was shown to be caused by the wrong forecast of WCB ascent, and associated latent heat errors, in Grams et al. (2018). Inaccurate WCB ascent and resulting changes in parameterised diabatic heating were also shown to cause an under amplification of a ridge by Martínez-Alvarado et al. (2016a). The different upper–level developments were shown to be directly related to the parameterisation of diabatic processes here.

The key results just described can now be reflected on in light of the main research question of the thesis.

Do uncertainties in the representation of diabatic processes in extratropical cyclones lead to error in the downstream development of blocking?

In a case study of a blocking event it was shown that modifying the parameterisation of various diabatic processes in the MetUM resulted in differences in the upper–level Rossby wave pattern and block forecast. Forecasts of upper–level Rossby wave structure and blocking during four winter seasons were also shown to depend considerably on the model's dynamical core, demonstrating that model uncertainty has the potential to strongly influence block forecasts. However, the changes in the upper–level PV pattern around the time of block onset in the parameterisation experiments were relatively small when compared to the difference between the forecast and the analysed PV structure. This means that, in this case, the forecast error was not changed substantially by the subtle reduction of model uncertainty. However, the modifications made to the parameterisations in the experiments were not large, representing a typical operational upgrade, so their individual impact on forecast error being small is not surprising. The experiments did however allow us to identify the processes linking parameterised diabatic heating and eventual downstream impact in a case study. Modifying the parameterised diabatic heating changed the development of the cyclone and allowed the non–linear feedback between WCB evolution and latent heat release (Grams et al., 2018) to produce considerable changes in the upper–level Rossby wave evolution. This case study was one of the 17 out of 20 cases of uncertain block onset forecasts shown to be sensitive to the representation of an upstream cyclone that had a WCB feeding the blocking ridge in chapter 4. This

could imply that the parameterised diabatic heating in the WCBs of the other cases was also important for the uncertainty in the block onset forecasts. A greater impact on block error in this case would require larger changes to the parameterisations than made here, though these may not be realistic and there may exist another model deficiency that is prohibiting accurate medium–range forecasts of block onset.

6.2 Thesis limitations

There are three note–worthy limitations to the analysis and results presented in chapters 3–5. The first limitation is that chapters 3 and 5 were primarily based on forecasts from the MetUM (though chapter 3 did include forecasts from two other EPSs) whereas chapter 4 used only forecasts from the ECMWF-EPS. The statistical results of chapter 4 were used to provide evidence for hypotheses resulting from chapter 3 as well as motivation for experiments in chapter 5. The use of forecasts from the ECMWF-EPS was necessary because it has a 51 member ensemble: the ensemble sensitivity analysis technique utilised in chapter 4 calculates a correlation between a response function and precursor field using ensemble members and hence a large number of members is required to ensure the results are statistically valid. Ensemble sensitivity was also calculated in the MOGREPS (using two 12–member sets lagged in forecast initiation time) for one of the block onset cases and the general sensitivity patterns highlighted in chapter 4 were present in the MOGREPS. Systematic errors in PV gradient and ridge error (Gray et al., 2014) as well as block representation (Matsueda, 2009) are also very similar in the two ensemble systems (Martínez-Alvarado et al., 2018). It is therefore reasonable to assume the statistical link between feeder cyclone and downstream block forecasts identified in the ECMWF-EPS is likely to be similar in the Met Office ensemble. Furthermore, the link was present in a case study from the MetUM and explained in detail in chapter 5.

The impact a new dynamical core had on upper–level Rossby wave and block representation was deduced in chapter 3 by comparing forecasts from before and after a major operational upgrade to the MetUM. The operational upgrade not only included the new dynamical core, but also changes to parameterisations and a resolution increase (Walters et al., 2017a). The importance of resolution was shown to be small by using hindcast simulations and in a comparison of the MOGREPS with the KMA-EPS (both of which used the MetUM). The influence of the parameterisation changes was not quantified. However, the changes to the parameterisations in the new operational configuration were much

smaller than the change to the dynamical core, which was completely rewritten (Walters et al., 2017a). The changes to the schemes are comparable to those implemented in chapter 5 in which no systematic effect on forecast skill was seen, implying the improvement identified in chapter 3 resulted primarily from the new dynamical core. The changes to the parameterisations were also very minor compared to the changes in the study of Jung et al. (2010) which were shown to have a large effect on the model climate.

A final limitation relates to the model physics experiments included in chapter 5. In the results presented, there was a clear mechanism linking model physics uncertainty to downstream block development via changes to the diabatic heating parameterised by various schemes. Further insight could be gained if there existed a set of θ–tracers for the observed (analysed) flow. This would allow a comparison between the total effect of diabatic processes in the forecasts and the real world and reveal if the forecasts could be more drastically improved if the total diabatic heating in the various stages of the WCB development matched that in reality. Martínez-Alvarado et al. (2016b) used a proxy to the real world (using sequential short range forecasts) to estimate a total 'real' diabatic effect. However, as the forecasts here were of longer lead time and the evolution so far away from what occurred in reality the method was not appropriate.

6.3 Implications and future work

Atmospheric blocks have been shown to be the dominant cause of forecast bust cases over Europe in the ECMWF-EPS (Rodwell et al., 2013; Lillo and Parsons, 2017). Forecast busts are cases when the medium–range forecast for Europe was considerably inaccurate and are a major cause for concern at NWP centres as the forecasts give no benefit to the users and potentially expose society to weather related risks. The strong relationship between the development of atmospheric blocking in forecasts and the preceding representation of extratropical cyclones implies a method to reduce the number of forecast busts that occur could focus on improving the forecasts of the preceding cyclones. Indeed a cyclone and its WCB development was identified as the source of a forecast bust case by Grams et al. (2018). Reducing the number of forecast bust cases would improve a forecasting centre's average skill scores and prevent the potential societal impacts of the forecast busts.

Diabatic processes need to be parameterised in extratropical cyclones, so can be a source of model error and offer a source of potential model improvement (e.g. Simmons

and Hollingsworth, 2002; Jung et al., 2010). The mechanistic link between cyclones and upper–level Rossby waves and block development identified in this thesis and in previous studies (e.g. Grams et al., 2011; Martínez-Alvarado et al., 2016a; Joos and Forbes, 2016; Grams et al., 2018) is centred around the diabatic processes active in WCBs modifying the PV structure near the tropopause and the downstream implications. This suggests an improvement to cyclone development that is designed to improve block forecasts could be found in further parameterisation improvements. Parameterisation improvements also offer the benefit of being much cheaper to implement than resolution increases or increasing ensemble size.

Atmospheric blocking is known not only to be an issue in NWP models but also a source of large model bias in seasonal and climate integrations (e.g. D'Andrea et al., 1998; Scaife et al., 2010; Anstey et al., 2013). The models' reluctance to form blocked flows is common across the modelling timescales. Hence it may be the case that improvements to block representations could be gained from a common source, i.e. improved extratropical cyclone forecasts. Seasonal, and especially climate integrations, are typically run at much lower resolution than NWP forecasts which means the physics parameterisation impact on blocking may be larger in climate models. Extratropical cyclones are systematically misrepresented in climate models (Zappa et al., 2013) though a high resolution climate model can produce extratropical cyclones that have reasonably accurate synoptic scale structure but not intensity (Catto et al., 2010). Physical parameterisation improvements have shown to improve block forecasts in climate models (Tibaldi et al., 1997; Dawson and Palmer, 2015; Pithan et al., 2016) which may have come from better extratropical cyclone characteristics. Improved statistics of extratropical cyclones and an increase in block frequency were obtained by substantial modifications to the physics parameterisations in Jung et al. (2010).

The key findings presented in this thesis and the implications previously discussed highlight several avenues for future research. Three possible avenues are posed as research questions and are given with a possible method to answer them and a hypothesised outcome.

1. **Is the sensitivity of block onset forecast to upstream cyclones systematic across NWP models?**

   In chapter 4, the ECMWF-EPS was used to show block forecasts were sensitive to upstream cyclones. The same ensemble prediction system has been used to show

that a forecast bust case associated with a block resulted from the poor representation of an upstream cyclone (Grams et al., 2018) and that blocks occurring over Greenland were sensitive to upper–level perturbations, particularly from the tropics (Parker et al., 2018). The TIGGE archive (Bougeault et al., 2010) contains operational ensemble forecasts from 10 NWP centres dating back to 2006. The analysis in chapter 4 could be repeated using ensemble members from all of the centres to perform a *super*–ensemble sensitivity analysis. The analysis could also be repeated for subsets of various models based on, for example, the model's resolution or dynamical core. The relative role of initial condition and model error could be discovered comparing sensitivity results across the models and in the *super*–ensemble. If sensitivity features were common across individual model analyses, various subsets of the models and in the *super*–ensemble this would imply initial condition error was dominant. If they were more different model error would be more important. Quandt et al. (2019) recently performed ensemble sensitivity analysis using the ensemble from three NWP models for the Russian block of summer 2010. They found significant sensitivities for block onset, maintenance and decay to upstream mean sea level pressure in the multi–model ensemble that were generally similar in each of the separate EPSs, suggesting initial condition error was more important in this case.

2. **Is the sequence linking diabatic heating changes to block forecast error that was shown in a case study systematic?**

   A case study of a forecast of block development was shown to depend on the parameterised diabatic heating occurring in the WCB of an upstream cyclone in chapter 5. Other single case studies of error in forecasts of upper-level ridge amplification and blocking have also been attributed to general WCB error previously (Martínez-Alvarado et al., 2016a; Grams et al., 2018). It is unknown whether diabatic heating in WCBs is systematically having an effect on block forecasts. The systematic reduction in PV gradient in upper–level ridges with lead time is consistent with insufficient PV modification by diabatic processes which act to sharpen tropopause–level PV gradients (Chagnon et al., 2013; Gray et al., 2014). The θ–tracer diagnostic could be used in a larger set of block forecasts and for both model physics experiments and perturbed initial condition runs. This would allow for a statistical comparison of diabatic heating in WCBs and downstream block developments in medium–range forecasts. It has already been shown that diabatic heating is crucial for blocked air

masses in a reanalysis dataset (Pfahl et al., 2015). A θ–tracer diagnostic calculated for the observed or analysed developments of blocks would help identify if the diabatic heating from the parameterised processes is contributing to block error in a systematic way.

3. **What are uncertain predictions of summer blocking events sensitive to?**

   Blocking events in summer are known to be as equally unpredictable as those in autumn/winter (e.g. Pelly and Hoskins, 2003a; Matsueda, 2011). The impacts of blocking in summer may even be more severe, with some of the most memorable and damaging heatwaves in recent times (e.g. Europe in 2003 and Russia in 2010) caused by atmospheric blocking events. Blocks in summer, like autumn and winter, are typically associated with upstream cyclone activity (Lupo and Smith, 1995; McLeod and Mote, 2015) and the forecast of the Russian 2010 block was sensitive to the upstream mean sea level pressure pattern and vapour transport in a cyclone (Quandt et al., 2019). An analysis of a larger set of blocking events occurring in summer using ensemble sensitivity analysis would reveal whether this is normally the case. The different climatological features of blocking in different seasons might suggest the forecast of blocking would be sensitive to different features and/or regions, and hence forecast improvements for summer blocks may need to be found in different places. Answering this question could also shed light on the appropriateness of blocking theories covering blocks occurring year round.

REFERENCES

Abbe, C., 1901: The physical basis of long-range weather forecasts. *Mon. Weather Rev.*, **29**, 551–561.

Ahmadi-Givi, F., G. Graig, and R. Plant, 2004: The dynamics of a midlatitude cyclone with very strong latent-heat release. *Quart. J. Roy. Meteor. Soc.*, **130**, 295–323.

Altenhoff, A. M., O. Martius, M. Croci-Maspoli, C. Schwierz, and H. C. Davies, 2008: Linkage of atmospheric blocks and synoptic-scale Rossby waves: a climatological analysis. *Tellus A*, **60**, 1053–1063.

Ancell, B. and G. J. Hakim, 2007: Comparing adjoint-and ensemble-sensitivity analysis with applications to observation targeting. *Mon. Weather Rev.*, **135**, 4117–4134.

Anderson, J. L., 1993: The climatology of blocking in a numerical forecast model. *J. Climate*, **6**, 1041–1056.

Anstey, J. A., P. Davini, L. J. Gray, T. J. Woollings, N. Butchart, C. Cagnazzo, B. Christiansen, S. C. Hardiman, S. M. Osprey, and S. Yang, 2013: Multi-model analysis of Northern Hemisphere winter blocking: Model biases and the role of resolution. *Journal of Geophysical Research: Atmospheres*, **118**, 3956–3971.

Arai, M. and H. Mukougawa, 2002: On the effectiveness of the eddy straining mechanism for the maintenance of blocking flows. *Journal of the Meteorological Society of Japan. Ser. II*, **80**, 1089–1102.

Arakawa, A. and V. Lamb, 1977: Computational design of the basic dynamical processes of the UCLA General Circulation Model. *Methods Comput. Phys.*, **17**, 173–265.

Archambault, H. M., L. F. Bosart, D. Keyser, and J. M. Cordeira, 2013: A climatological analysis of the extratropical flow response to recurving western North Pacific tropical cyclones. *Mon. Weather Rev.*, **141**, 2325–2346.

Arpe, K., A. Hollingsworth, M. Tracton, A. Lorenc, S. Uppala, and P. Kållberg, 1985: The response of numerical weather prediction systems to FGGE level IIb data. Part II: Forecast verifications and implications for predictability. *Quart. J. Roy. Meteor. Soc.*, **111**, 67–101.

Austin, J., 1980: The blocking of middle latitude westerly winds by planetary waves. *Quart. J. Roy. Meteor. Soc.*, **106**, 327–350.

Barnston, A. G. and R. E. Livezey, 1987: Classification, seasonality and persistence of low-frequency atmospheric circulation patterns. *Mon. Weather Rev.*, **115**, 1083–1126.

Barriopedro, D., E. M. Fischer, J. Luterbacher, R. M. Trigo, and R. García-Herrera, 2011: The hot summer of 2010: redrawing the temperature record map of Europe. *Science*, **332**, 220–224.

Barriopedro, D., R. García-Herrera, and R. M. Trigo, 2010: Application of blocking diagnosis methods to General Circulation Models. Part I: a novel detection scheme. *Climate Dyn.*, **35**, 1373–1391, doi:10.1007/s00382-010-0767-5.

Bauer, P., A. Thorpe, and G. Brunet, 2015: The quiet revolution of numerical weather prediction. *Nature*, **525**, 47.

Berggren, R., B. Bolin, and C.-G. Rossby, 1949: An aerological study of zonal motion, its perturbations and break-down. *Tellus*, **1**, 14–37.

Berry, F., W. Haggard, and P. M. Wolff, 1953: 500-millibar studies at Project AROWA. *Bull. Amer. Meteor. Soc.*, 444–453.

Binder, H., M. Boettcher, C. M. Grams, H. Joos, S. Pfahl, and H. Wernli, 2017: Exceptional air mass transport and dynamical drivers of an extreme wintertime Arctic warm event. *Geophys. Res. Lett.*, **44**, 3997–4020.

Binder, H., M. Boettcher, H. Joos, and H. Wernli, 2016: The role of warm conveyor belts for the intensification of extratropical cyclones in Northern Hemisphere winter. *J. Atmos. Sci.*, **73**, 3997–4020.

Bjerknes, J., 1922: Life cycle of cyclones and the polar front theory of atmospheric circulation. *Geophys. Publik.*, **3**, 1–18.

Bjerknes, V., 1904: Das Problem der Wettervorhers-age, betrachtet vom Standpunkte der Mechanik und der Physik. *Meteor. Z.*, **21**, 1–7.

Black, E., M. Blackburn, G. Harrison, B. Hoskins, and J. Methven, 2004: Factors contributing to the summer 2003 European heatwave. *Weather*, **59**, 217–223.

Boettcher, M. and H. Wernli, 2011: Life cycle study of a diabatic Rossby wave as a precursor to rapid cyclogenesis in the North Atlantic—Dynamics and forecast performance. *Mon. Weather Rev.*, **139**, 1861–1878.

Bosart, L. F. and G. M. Lackmann, 1995: Postlandfall Tropical Cyclone Reintensification in a Weakly Baroclinic Environment: A Case Study of Hurrica ne David (September 1979). *Mon. Weather Rev.*, **123**, 3268–3291, doi:10.1175/1520-0493(1995)123¡3268:PTCRIA¿2.0.CO;2.

Bougeault, P., Z. Toth, C. Bishop, B. Brown, D. Burridge, D. H. Chen, B. Ebert, M. Fuentes, T. M. Hamill, K. Mylne, et al., 2010: The THORPEX interactive grand global ensemble. *Bull. Amer. Meteor. Soc.*, **91**, 1059–1072.

Bowler, N. E., A. Arribas, S. E. Beare, K. R. Mylne, and G. J. Shutts, 2009: The local ETKF and SKEB: Upgrades to the MOGREPS short-range ensemble prediction system. *Q. J. R. Meteorol. Soc.*, **135**, 767–776.

Bowler, N. E., A. Arribas, K. R. Mylne, K. B. Robertson, and S. E. Beare, 2008: The MOGREPS short-range ensemble prediction system. *Q. J. R. Meteorol. Soc.*, **134**, 703–722.

Branković, Č. and F. Molteni, 1996: Sensitivity of the ECMWF model northern winter climate to model formulation. *Climate Dyn.*, **13**, 75–101.

Brown, A., R. Beare, J. Edwards, A. Lock, S. Keogh, S. Milton, and D. Walters, 2008: Upgrades to the boundary-layer scheme in the Met Office numerical weather prediction model. *Boundary Layer Meteorol.*, **128**, 117–132.

Browning, K., 1971: Radar measurements of air motion near fronts. *Weather*, **26**, 320–340.

— 2004: The sting at the end of the tail: Damaging winds associated with extratropical cyclones. *Quart. J. Roy. Meteor. Soc.*, **130**, 375–399.

Browning, K. and N. Roberts, 1994: Structure of a frontal cyclone. *Quart. J. Roy. Meteor. Soc.*, **120**, 1535–1557.

Browning, K. A., 1990: Organization of clouds and precipitation in extratropical cyclones. *Extratropical cyclones*, Springer, 129–153.

Buehler, T., C. C. Raible, and T. F. Stocker, 2011: The relationship of winter season North Atlantic blocking frequencies to extreme cold or dry spells in the ERA-40. *Tellus A: Dynamic Meteorology and Oceanography*, **63**, 174–187.

Buizza, R. and A. Hollingsworth, 2002: Storm prediction over Europe using the ECMWF ensemble prediction system. *Meteorol. Appl.*, **9**, 289–305.

Buizza, R., P. Houtekamer, G. Pellerin, Z. Toth, Y. Zhu, and M. Wei, 2005: A comparison of the ECMWF, MSC, and NCEP global ensemble prediction systems. *Mon. Weather Rev.*, **133**, 1076–1097.

Buizza, R., M. Milleer, and T. Palmer, 1999: Stochastic representation of model uncertainties in the ECMWF ensemble prediction system. *Q. J. R. Meteorol. Soc.*, **125**, 2887–2908.

Carlson, T. N., 1980: Airflow through midlatitude cyclones and the comma cloud pattern. *Mon. Weather Rev.*, **108**, 1498–1509.

Carrera, M., R. Higgins, and V. Kousky, 2004: Downstream weather impacts associated with atmospheric blocking over the northeast Pacific. *J. Climate*, **17**, 4823–4839.

Carrera, M. L., J. R. Gyakum, and D.-L. Zhang, 1999: A numerical case study of secondary marine cyclogenesis sensitivity to initial error and varying physical processes. *Mon. Weather Rev.*, **127**, 641–660.

Cassou, C., 2008: Intraseasonal interaction between the Madden–Julian oscillation and the North Atlantic Oscillation. *Nature*, **455**, 523.

Cattiaux, J., B. Quesada, A. Arakélian, F. Codron, R. Vautard, and P. Yiou, 2013: North-Atlantic dynamics and European temperature extremes in the IPSL model: sensitivity to atmospheric resolution. *Climate Dyn.*, **40**, 2293–2310.

Catto, J. L., L. C. Shaffrey, and K. I. Hodges, 2010: Can climate models capture the structure of extratropical cyclones? *J. Climate*, **23**, 1621–1635.

Chagnon, J., S. Gray, and J. Methven, 2013: Diabatic processes modifying potential vorticity in a North Atlantic cyclone. *Q. J. R. Meteorol. Soc.*, **139**, 1270–1282.

Chagnon, J. M. and S. L. Gray, 2015: A diabatically generated potential vorticity structure near the extratropical tropopause in three simulated extratropical cyclones. *Mon. Weather Rev.*, **143**, 2337–2347.

Charney, J., J. Shukla, and K. Mo, 1981: Comparison of a barotropic blocking theory with observation. *J. Atmos. Sci.*, **38**, 762–779.

Charney, J. G., 1947: The dynamics of long waves in a baroclinic westerly current. *J. Meteor.*, **4**, 136–162.

Charney, J. G. and J. G. DeVore, 1979: Multiple flow equilibria in the atmosphere and blocking. *J. Atmos. Sci.*, **36**, 1205–1216.

Charney, J. G. and N. A. Phillips, 1953: Numerical integration of the quasi-geostrophic equations for barotropic and simple baroclinic flows. *J. Meteor.*, **10**, 71–99.

Chelton, D. B., 2005: The Impact of SST Specification on ECMWF Surface Wind Stress Fields in the Eastern Tropical Pacific. *J. Climate*, **18**, 530–550, doi:10.1175/JCLI-3275.1.

Christiansen, B., 2019: Analysis of ensemble mean forecasts: The blessings of high dimensionality. *Mon. Weather Rev.*.

Ciais, P., M. Reichstein, N. Viovy, A. Granier, J. Ogée, V. Allard, M. Aubinet, N. Buchmann, C. Bernhofer, A. Carrara, et al., 2005: Europe-wide reduction in primary productivity caused by the heat and drought in 2003. *Nature*, **437**, 529.

Clark, D., L. Mercado, S. Sitch, C. Jones, N. Gedney, M. Best, M. Pryor, G. Rooney, R. Essery, E. Blyth, et al., 2011: The Joint UK Land Environment Simulator (JULES), model description–Part 2: carbon fluxes and vegetation dynamics. *Geosci. Model Dev.*, **4**, 701–722.

Colucci, S. J., 1985: Explosive cyclogenesis and large-scale circulation changes: Implications for atmospheric blocking. *J. Atmos. Sci.*, **42**, 2701–2717.

— 1987: Comparative diagnosis of blocking versus nonblocking planetary-scale circulation changes during synoptic-scale cyclogenesis. *J. Atmos. Sci.*, **44**, 124–139.

Colucci, S. J. and T. L. Alberta, 1996: Planetary-scale climatology of explosive cyclogenesis and blocking. *Mon. Weather Rev.*, **124**, 2509–2520.

Coronel, B., D. Ricard, G. Rivière, and P. Arbogast, 2015: Role of Moist Processes in the Tracks of Idealized Midlatitude Surface Cyclones. *J. Atmos. Sci.*, **72**, 2979–2996, doi:10.1175/JAS-D-14-0337.1.

Curio, J., Y. Chen, R. Schiemann, A. G. Turner, K. C. Wong, K. Hodges, and Y. Li, 2018: Comparison of a manual and an automated tracking method for Tibetan Plateau vortices. *Adv. Atmos. Sci.*, **35**, 965–980.

Curry, J., P. Hobbs, M. King, D. Randall, P. Minnis, G. Isaac, J. Pinto, T. Uttal, A. Bucholtz, D. Cripe, et al., 2000: FIRE Arctic clouds experiment. *Bull. Amer. Meteor. Soc.*, **81**, 5–30.

Cushman-Roisin, B. and J.-M. Beckers, 2011: *Introduction to geophysical fluid dynamics: physical and numerical aspects*, volume 101. Academic press.

Dacre, H. F. and S. L. Gray, 2013: Quantifying the climatological relationship between extratropical cyclone intensity and atmospheric precursors. *Geophys. Res. Lett.*, **40**, 2322–2327.

D'Andrea, F., S. Tibaldi, M. Blackburn, G. Boer, M. Déqué, M. Dix, B. Dugas, L. Ferranti, T. Iwasaki, A. Kitoh, et al., 1998: Northern Hemisphere atmospheric blocking as simulated by 15 atmospheric general circulation models in the period 1979-1988. *Climate Dyn.*, **14**, 385–407.

Davies, H. C. and M. Didone, 2013: Diagnosis and dynamics of forecast error growth. *Mon. Weather Rev.*, **141**, 2483–2501.

Davies, T., M. J. P. Cullen, A. J. Malcolm, M. H. Mawson, A. Staniforth, A. A. White, and N. Wood, 2005: A new dynamical core for the Met Office's global and regional modelling of the atmosphere. *Q. J. R. Meteorol. Soc.*, **131**, 1759–1782.

Davini, P. and F. D'Andrea, 2016: Northern Hemisphere atmospheric blocking representation in global climate models: Twenty years of improvements? *J. Climate*, **29**, 8823–8840.

Davis, C. A., 1992: Piecewise potential vorticity inversion. *J. Atmos. Sci.*, **49**, 1397–1411.

Davis, C. A. and K. A. Emanuel, 1988: Observational evidence for the influence of surface heat fluxes on rapid maritime cyclogenesis. *Mon. Weather Rev.*, **116**, 2649–2659.

— 1991: Potential vorticity diagnostics of cyclogenesis. *Mon. Weather Rev.*, **119**, 1929–1953.

Davis, C. A., M. T. Stoelinga, and Y.-H. Kuo, 1993: The integrated effect of condensation in numerical simulations of extratropical cyclogenesis. *Mon. Weather Rev.*, **121**, 2309–2330.

Dawson, A. and T. Palmer, 2015: Simulating weather regimes: Impact of model resolution and stochastic parameterization. *Climate Dyn.*, **44**, 2177–2193.

de Andrade, F. M., C. A. Coelho, and I. F. Cavalcanti, 2019: Global precipitation hindcast quality assessment of the Subseasonal to Seasonal (S2S) prediction project models. *Climate Dyn.*, **52**, 5451–5475.

de Vries, H., T. Woollings, J. Anstey, R. J. Haarsma, and W. Hazeleger, 2013: Atmospheric blocking and its relation to jet changes in a future climate. *Climate Dyn.*, **41**, 2643–2654.

Dearden, C., G. Vaughan, T. Tsai, and J.-P. Chen, 2016: Exploring the diabatic role of ice microphysical processes in two North Atlantic summer cyclones. *Mon. Weather Rev.*, **144**, 1249–1272.

Dee, D., M. Balmaseda, G. Balsamo, R. Engelen, A. Simmons, and J.-N. Thépaut, 2014: Toward a consistent reanalysis of the climate system. *Bull. Amer. Meteor. Soc.*, **95**, 1235–1248.

Dee, D. P., S. Uppala, A. Simmons, P. Berrisford, P. Poli, S. Kobayashi, U. Andrae, M. Balmaseda, G. Balsamo, P. Bauer, et al., 2011: The ERA-Interim reanalysis: Configuration and performance of the data assimilation system. *Q. J. R. Meteorol. Soc.*, **137**, 553–597.

Dirren, S., M. Didone, and H. Davies, 2003: Diagnosis of "forecast-analysis" differences of a weather prediction system. *Geophys. Res. Lett.*, **30**.

Doblas-Reyes, F., A. Weisheimer, M. Déqué, N. Keenlyside, M. McVean, J. Murphy, P. Rogel, D. Smith, and T. Palmer, 2009: Addressing model uncertainty in seasonal and annual dynamical ensemble forecasts. *Quart. J. Roy. Meteor. Soc.*, **135**, 1538–1559.

Dole, R. M., 1986: Persistent anomalies of the extratropical northern hemisphere wintertime circulation: Structure. *Monthly weather review*, **114**, 178–207.

Donlon, C. J., M. Martin, J. Stark, J. Roberts-Jones, E. Fiedler, and W. Wimmer, 2012: The operational sea surface temperature and sea ice analysis (OSTIA) system. *Remote Sens. Environ.*, **116**, 140–158.

Dunstone, N., D. Smith, A. Scaife, L. Hermanson, R. Eade, N. Robinson, M. Andrews, and J. Knight, 2016: Skilful predictions of the winter North Atlantic Oscillation one year ahead. *Nat. Geosci.*, **9**, 809–814, doi:10.1038/ngeo2824.

Eady, E. T., 1949: Long waves and cyclone waves. *Tellus*, **1**, 33–52.

Ebert, E. E., 2001: Ability of a poor man's ensemble to predict the probability and distribution of precipitation. *Mon. Weather Rev.*, **129**, 2461–2480.

Ehrendorfer, M., 1997: Predicting the uncertainty of numerical weather forecasts: A review. *METEOROLOGISCHE ZEITSCHRIFT-BERLIN-*, **6**, 147–183.

Ertel, H., 1942: Ein neuer hydrodynamischer wirbelsatz. *Meteor. Z.*, 271–281.

Fehlmann, R. and H. C. Davies, 1997: Misforecasts of synoptic systems: Diagnosis via PV retrodiction. *Mon. Weather Rev.*, **125**, 2247–2264.

— 1999: Role of salient potential-vorticity elements in an event of frontal-wave cyclogenesis. *Quart. J. Roy. Meteor. Soc.*, **125**, 1801–1824.

Ferranti, L., S. Corti, and M. Janousek, 2015: Flow-dependent verification of the ECMWF ensemble over the Euro-Atlantic sector. *Q. J. R. Meteorol. Soc.*, **141**, 916–924.

Ferranti, L., F. Molteni, and T. Palmer, 1994: Impact of localized tropical and extratropical SST anomalies in ensembles of seasonal GCM integrations. *Quart. J. Roy. Meteor. Soc.*, **120**, 1613–1645.

Fink, A. H., T. Brücher, V. Ermert, A. Krüger, and J. G. Pinto, 2009: The European storm Kyrill in January 2007: synoptic evolution, meteorological impacts and some considerations with respect to climate change. *Nat. Hazards Earth Syst. Sci.*, **9**, 405–423.

Forbes, R. M. and P. A. Clark, 2003: Sensitivity of extratropical cyclone mesoscale structure to the parametrization of ice microphysical processes. *Quart. J. Roy. Meteor. Soc.*, **129**, 1123–1148.

Forbes, R. M. and R. J. Hogan, 2006: Observations of the depth of ice particle evaporation beneath frontal cloud to improve NWP modelling. *Quart. J. Roy. Meteor. Soc.*, **132**, 865–883.

Frame, T. H., J. Methven, N. M. Roberts, and H. A. Titley, 2015: Predictability of frontal waves and cyclones. *Weather Forecasting*, **30**, 1291–1302.

Frederiksen, J., 1982: A unified three-dimensional instability theory of the onset of blocking and cyclogenesis. *J. Atmos. Sci.*, **39**, 969–982.

— 1983: A unified three-dimensional instability theory of the onset of blocking and cyclogenesis. II. Teleconnection patterns. *J. Atmos. Sci.*, **40**, 2593–2609.

— 1989: The role of instability during the onset of blocking and cyclogenesis in Northern Hemisphere synoptic flows. *J. Atmos. Sci.*, **46**, 1076–1092.

Frederiksen, J. and R. Bell, 1990: North Atlantic blocking during January 1979: linear theory. *Quart. J. Roy. Meteor. Soc.*, **116**, 1289–1313.

Frederiksen, J. S., 1998: Precursors to blocking anomalies: The tangent linear and inverse problems. *J. Atmos. Sci.*, **55**, 2419–2436.

Frederiksen, J. S., M. A. Collier, and A. B. Watkins, 2004: Ensemble prediction of blocking regime transitions. *Tellus A*, **56**, 485–500.

Frederiksen, J. S. and P. J. Webster, 1988: Alternative theories of atmospheric teleconnections and low-frequency fluctuations. *Rev. Geophys.*, **26**, 459–494.

Froude, L. S., 2010: TIGGE: Comparison of the prediction of Northern Hemisphere extratropical cyclones by different ensemble prediction systems. *Weather Forecasting*, **25**, 819–836.

Galarneau Jr, T. J., T. M. Hamill, R. M. Dole, and J. Perlwitz, 2012: A multiscale analysis of the extreme weather events over western Russia and northern Pakistan during July 2010. *Mon. Weather Rev.*, **140**, 1639–1664.

García-Herrera, R., J. Díaz, R. M. Trigo, J. Luterbacher, and E. M. Fischer, 2010: A review of the European summer heat wave of 2003. *Critical Reviews in Environmental Science and Technology*, **40**, 267–306.

Garcies, L. and V. Homar, 2009: Ensemble sensitivities of the real atmosphere: application to Mediterranean intense cyclones. *Tellus A*, **61**, 394–406.

Garriott, E., 1904: Long range forecasts. *US Weather Bureau Bulletin*, **35**.

Giannakaki, P. and O. Martius, 2016: An Object-Based Forecast Verification Tool for Synoptic-Scale Rossby Waveguides. *Weather Forecast.*, **31**, 937–946, doi:10.1175/WAF-D-15-0147.1.

Goddard, L., S. J. Mason, S. E. Zebiak, C. F. Ropelewski, R. Basher, and M. A. Cane, 2001: Current approaches to seasonal to interannual climate predictions. *Int. J. Climatol.*, **21**, 1111–1152.

Grams, C. M. and H. M. Archambault, 2016: The key role of diabatic outflow in amplifying the midlatitude flow: A representative case study of weather systems surrounding western North Pacific extratropical transition. *Mon. Weather Rev.*, **144**, 3847–3869.

Grams, C. M., L. Magnusson, and E. Madonna, 2018: An atmospheric dynamics 'perspective on the amplification and propagation of forecast error in numerical weather prediction models: a case study. *Quart. J. Roy. Meteor. Soc.*, **144**, 2577–2591.

Grams, C. M., H. Wernli, M. Böttcher, J. Čampa, U. Corsmeier, S. C. Jones, J. H. Keller, C.-J. Lenz, and L. Wiegand, 2011: The key role of diabatic processes in modifying the upper-tropospheric wave guide: a North Atlantic case-study. *Q. J. R. Meteorol. Soc.*, **137**, 2174–2193.

Gray, S. L., C. Dunning, J. Methven, G. Masato, and J. M. Chagnon, 2014: Systematic model forecast error in Rossby wave structure. *Geophys. Res. Lett.*, **41**, 2979–2987.

Green, J., 1977: The weather during July 1976: Some dynamical considerations of the drought. *Weather*, **32**, 120–126.

Gregory, D. and P. Rowntree, 1990: A mass flux convection scheme with representation of cloud ensemble characteristics and stability-dependent closure. *Mon. Weather Rev.*, **118**, 1483–1506.

Grose, W. L. and B. J. Hoskins, 1979: On the influence of orography on large-scale atmospheric flow. *J. Atmos. Sci.*, **36**, 223–234.

Grumm, R. H., 2011: The central European and Russian heat event of July–August 2010. *Bull. Amer. Meteor. Soc.*, **92**, 1285–1296.

Haines, K. and J. Marshall, 1987: Eddy-forced coherent structures as a prototype of atmospheric blocking. *Quart. J. Roy. Meteor. Soc.*, **113**, 681–704.

Hansen, A. R. and A. Sutera, 1993: A comparison between planetary-wave flow regimes and blocking. *Tellus A: Dynamic Meteorology and Oceanography*, **45**, 281–288.

Harrison, M., T. Palmer, D. Richardson, and R. Buizza, 1999: Analysis and model dependencies in medium-range ensembles: Two transplant case-studies. *Quart. J. Roy. Meteor. Soc.*, **125**, 2487–2515.

Harrold, T. W., 1973: Mechanisms influencing the distribution of precipitation within baroclinic disturbances. *Quart. J. Roy. Meteor. Soc.*, **99**, 232–251, doi:10.1002/qj.49709942003.

Harvey, B. J., J. Methven, and M. H. Ambaum, 2016: Rossby wave propagation on potential vorticity fronts with finite width. *J. Fluid Mech.*, **794**, 775–797.

Haylock, M., 2011: European extra-tropical storm damage risk from a multi-model ensemble of dynamically-downscaled global climate models. *Nat. Hazards Earth Syst. Sci.*, **11**, 2847–2857.

Held, I. M. and A. Y. Hou, 1980: Nonlinear axially symmetric circulations in a nearly inviscid atmosphere. *J. Atmos. Sci.*, **37**, 515–533.

Higgins, R. and S. Schubert, 1994: Simulated life cycles of persistent anticyclonic anomalies over the North Pacific: Role of synoptic-scale eddies. *J. Atmos. Sci.*, **51**, 3238–3260.

Hodges, K. I., 1994: A general method for tracking analysis and its application to meteorological data. *Mon. Weather Rev.*, **122**, 2573–2586.

— 1995: Feature tracking on the unit sphere. *Mon. Weather Rev.*, **123**, 3458–3465.

— 1999: Adaptive constraints for feature tracking. *Mon. Weather Rev.*, **127**, 1362–1373.

Hodges, K. I. and R. Emerton, 2015: The prediction of Northern Hemisphere tropical cyclone extended life cycles by the ECMWF ensemble and deterministic prediction systems. Part I: Tropical cyclone stage. *Mon. Weather Rev.*, **143**, 5091–5114.

Holland, W. R. and P. B. Rhines, 1980: An example of eddy-induced ocean circulation. *J. Phys. Oceanogr.*, **10**, 1010–1031.

Holton, J. R. and G. J. Hakim, 2012: *An introduction to dynamic meteorology*, volume 88. Academic press.

Hoskins, B. and P. Berrisford, 1988: A potential vorticity perspective of the storm of 15–16 October 1987. *Weather*, **43**, 122–129.

Hoskins, B. and K. Hodges, 2019: The annual cycle of Northern Hemisphere storm tracks. Part I: Seasons. *J. Climate*, **32**, 1743–1760.

Hoskins, B. J. and K. I. Hodges, 2002a: New perspectives on the Northern Hemisphere winter storm tracks. *J. Atmos. Sci.*, **59**, 1041–1061.

— 2002b: New perspectives on the Northern Hemisphere winter storm tracks. *J. Atmos. Sci.*, **59**, 1041–1061.

— 2005: A new perspective on Southern Hemisphere storm tracks. *J. Climate*, **18**, 4108–4129.

Hoskins, B. J., I. N. James, and G. H. White, 1983: The shape, propagation and mean-flow interaction of large-scale weather systems. *J. Atmos. Sci.*, **40**, 1595–1612.

Hoskins, B. J. and D. J. Karoly, 1981: The steady linear response of a spherical atmosphere to thermal and orographic forcing. *J. Atmos. Sci.*, **38**, 1179–1196.

Hoskins, B. J., M. McIntyre, and A. W. Robertson, 1985: On the use and significance of isentropic potential vorticity maps. *Quart. J. Roy. Meteor. Soc.*, **111**, 877–946.

Hoskins, B. J. and P. D. Sardeshmukh, 1987: A Diagnostic Study of the Dynamics of the Northern Hemisphere Winter of 1985-86. *Quart. J. Roy. Meteor. Soc.*, **113**, 759–778.

Hoskins, B. J. and P. J. Valdes, 1990: On the existence of storm-tracks. *J. Atmos. Sci.*, **47**, 1854–1864.

Hurrell, J. W., Y. Kushnir, G. Ottersen, and M. Visbeck, 2003: *An Overview of the North Atlantic Oscillation*, American Geophysical Union (AGU). 1–35.

Hurrell, J. W., Y. Kushnir, and M. Visbeck, 2001: The North Atlantic oscillation. *Science*, **291**, 603–605.

Illari, L., 1984: A diagnostic study of the potential vorticity in a warm blocking anticyclone. *J. Atmos. Sci.*, **41**, 3518–3526.

Illari, L. and J. C. Marshall, 1983: On the interpretation of eddy fluxes during a blocking episode. *J. Atmos. Sci.*, **40**, 2232–2242.

Illingworth, A., R. Hogan, E. O'connor, D. Bouniol, M. Brooks, J. Delanoë, D. Donovan, J. Eastment, N. Gaussiat, J. Goddard, et al., 2007: Cloudnet: Continuous evaluation of cloud profiles in seven operational models using ground-based observations. *Bull. Amer. Meteor. Soc.*, **88**, 883–898.

Jia, X., S. Yang, W. Song, and B. He, 2014: Prediction of Wintertime Northern Hemisphere Blocking by the NCEP Climate Forecast System. *Journal of Meteorological Research*, **28**, 76–90.

Joos, H. and R. M. Forbes, 2016: Impact of different IFS microphysics on a warm conveyor belt and the downstream flow evolution. *Quart. J. Roy. Meteor. Soc.*, **142**, 2727–2739.

Joos, H. and H. Wernli, 2012: Influence of microphysical processes on the potential vorticity development in a warm conveyor belt: A case-study with the limited-area model COSMO. *Quart. J. Roy. Meteor. Soc.*, **138**, 407–418.

Jung, T., G. Balsamo, P. Bechtold, A. Beljaars, M. Köhler, M. Miller, J.-J. Morcrette, A. Orr, M. Rodwell, and A. Tompkins, 2010: The ECMWF model climate: Recent progress through improved physical parametrizations. *Quart. J. Roy. Meteor. Soc.*, **136**, 1145–1160.

Jung, T., S. Gulev, I. Rudeva, and V. Soloviov, 2006: Sensitivity of extratropical cyclone characteristics to horizontal resolution in the ECMWF model. *Quart. J. Roy. Meteor. Soc.*, **132**, 1839–1857.

Kaas, E. and G. Branstator, 1993: The relationship between a zonal index and blocking activity. *J. Atmos. Sci.*, **50**, 3061–3077.

Kalnay, E., 2003: *Atmospheric modeling, data assimilation and predictability*. Cambridge university press.

Kelly, G., J.-N. Thépaut, R. Buizza, and C. Cardinali, 2007: The value of observations. I: Data denial experiments for the Atlantic and the Pacific. *Quart. J. Roy. Meteor. Soc.*, **133**, 1803–1815.

Kimoto, M. and M. Ghil, 1993a: Multiple flow regimes in the Northern Hemisphere winter. Part I: Methodology and hemispheric regimes. *J. Atmos. Sci.*, **50**, 2625–2644.

— 1993b: Multiple flow regimes in the Northern Hemisphere winter. Part II: Sectorial regimes and preferred transitions. *J. Atmos. Sci.*, **50**, 2645–2673.

Kimoto, M., H. Mukougawa, and S. Yoden, 1992: Medium-range forecast skill variation and blocking transition. A case study. *Mon. Weather Rev.*, **120**, 1616–1627.

Kirsch, T. D., C. Wadhwani, L. Sauer, S. Doocy, and C. Catlett, 2012: Impact of the 2010 Pakistan floods on rural and urban populations at six months. *PLoS currents*, **4**.

Klein, S. A., R. B. McCoy, H. Morrison, A. S. Ackerman, A. Avramov, G. d. Boer, M. Chen, J. N. Cole, A. D. Del Genio, M. Falk, et al., 2009: Intercomparison of model simulations of mixed-phase clouds observed during the ARM Mixed-Phase Arctic Cloud Experiment. I: Single-layer cloud. *Quart. J. Roy. Meteor. Soc.*, **135**, 979–1002.

Konrad, C. E. and S. J. Colucci, 1988: Synoptic climatology of 500 mb circulation changes during explosive cyclogenesis. *Mon. Weather Rev.*, **116**, 1431–1443.

Kuo, Y.-H., M. Shapiro, and E. G. Donall, 1991: The interaction between baroclinic and diabatic processes in a numerical simulation of a rapidly intensifying extratropical marine cyclone. *Mon. Weather Rev.*, **119**, 368–384.

Lau, W. K. and K.-M. Kim, 2012: The 2010 Pakistan flood and Russian heat wave: Teleconnection of hydrometeorological extremes. *J. Hydrometeorol.*, **13**, 392–403.

Legras, B. and M. Ghil, 1985: Persistent anomalies, blocking and variations in atmospheric predictability. *J. Atmos. Sci.*, **42**, 433–471.

Lejenäs, H., 1984: Characteristics of Southern Hemisphere blocking as determined from a time series of observational data. *Quart. J. Roy. Meteor. Soc.*, **110**, 967–979.

Lejenäs, H. and H. Okland, 1983: Characteristics of Northern Hemisphere blocking as determined from a long time series of observational data. *Tellus A*, **35**, 350–362.

Lillo, S. P. and D. B. Parsons, 2017: Investigating the dynamics of error growth in ECMWF medium-range forecast busts. *Q. J. R. Meteorol. Soc.*, **143**, 1211–1226.

Lock, A., 2001: The numerical representation of entrainment in parameterizations of boundary layer turbulent mixing. *Mon. Weather Rev.*, **129**, 1148–1163.

Lock, A., A. Brown, M. Bush, G. Martin, and R. Smith, 2000: A new boundary layer mixing scheme. Part I: Scheme description and single-column model tests. *Mon. Weather Rev.*, **128**, 3187–3199.

Lorenz, D. J. and D. L. Hartmann, 2003: Eddy–zonal flow feedback in the Northern Hemisphere winter. *J. Climate*, **16**, 1212–1227.

Lorenz, E. N., 1963: Deterministic nonperiodic flow. *J. Atmos. Sci.*, **20**, 130–141.

— 1993: *The essence of chaos*. University of Washington Press.

Luo, D., 2000: Planetary-scale baroclinic envelope Rossby solitons in a two-layer model and their interaction with synoptic-scale eddies. *Dyn. Atmos. Oceans*, **32**, 27–74.

— 2005: A barotropic envelope Rossby soliton model for block–eddy interaction. Part I: Effect of topography. *J. Atmos. Sci.*, **62**, 5–21.

Luo, D., J. Cha, L. Zhong, and A. Dai, 2014: A nonlinear multiscale interaction model for atmospheric blocking: The eddy-blocking matching mechanism. *Quart. J. Roy. Meteor. Soc.*, **140**, 1785–1808.

Luo, D. and Z. Chen, 2006: The role of land–sea topography in blocking formation in a block–eddy interaction model. *J. Atmos. Sci.*, **63**, 3056–3065.

Lupo, A. R. and P. J. Smith, 1995: Climatological features of blocking anticyclones in the Northern Hemisphere. *Tellus A*, **47**, 439–456.

Maddison, J. W., S. L. Gray, O. Martínez-Alvarado, and K. D. Williams, 2019: Upstream Cyclone Influence on the Predictability of Block Onsets over the Euro-Atlantic Region. *Mon. Weather Rev.*, **147**, 1277–1296, doi:10.1175/MWR-D-18-0226.1.

Madonna, E., M. Boettcher, C. M. Grams, H. Joos, O. Martius, and H. Wernli, 2015: Verification of North Atlantic warm conveyor belt outflows in ECMWF forecasts. *Q. J. R. Meteorol. Soc.*, **141**, 1333–1344.

Madonna, E., H. Wernli, H. Joos, and O. Martius, 2014: Warm conveyor belts in the ERA-Interim dataset (1979–2010). Part I: Climatology and potential vorticity evolution. *J. Climate*, **27**, 3–26.

Maeda, S., C. Kobayashi, K. Takano, and T. Tsuyuki, 2000: Relationship between singular modes of blocking flow and high-frequency eddies. *Journal of the Meteorological Society of Japan. Ser. II*, **78**, 631–646.

Magnusson, L., 2017: Diagnostic methods for understanding the origin of forecast errors. *Q. J. R. Meteorol. Soc.*.

Malguzzi, P. and P. Malanotte-Rizzoli, 1984: Nonlinear stationary Rossby waves on nonuniform zonal winds and atmospheric blocking. Part I: The analytical theory. *J. Atmos. Sci.*, **41**, 2620–2628.

Malguzzi, P. and A. Speranza, 1981: Local multiple equilibria and regional atmospheric blocking. *J. Atmos. Sci.*, **38**, 1939–1948.

Martínez-Alvarado, O., L. H. Baker, S. L. Gray, J. Methven, and R. S. Plant, 2014: Distinguishing the cold conveyor belt and sting jet airstreams in an intense extratropical cyclone. *Mon. Weather Rev.*, **142**, 2571–2595.

Martínez-Alvarado, O., S. L. Gray, and J. Methven, 2016a: Diabatic processes and the evolution of two contrasting summer extratropical cyclones. *Mon. Weather Rev.*, **144**, 3251–3276.

Martínez-Alvarado, O., J. W. Maddison, S. L. Gray, and K. D. Williams, 2018: Atmospheric blocking and upper-level Rossby-wave forecast skill dependence on model configuration. *Quart. J. Roy. Meteor. Soc.*, **144**, 2165–2181.

Martínez-Alvarado, O., E. Madonna, S. Gray, and H. Joos, 2016b: A route to systematic error in forecasts of Rossby waves. *Quart. J. Roy. Meteor. Soc.*, **142**, 196–210.

Martínez-Alvarado, O. and R. Plant, 2014: Parametrized diabatic processes in numerical simulations of an extratropical cyclone. *Q. J. R. Meteorol. Soc.*, **140**, 1742–1755.

Martius, O., C. Schwierz, and H. Davies, 2010: Tropopause-level waveguides. *J. Atmos. Sci.*, **67**, 866–879.

Masato, G., B. Hoskins, and T. J. Woollings, 2012: Wave-breaking characteristics of midlatitude blocking. *Quart. J. Roy. Meteor. Soc.*, **138**, 1285–1296.

Matsueda, M., 2009: Blocking predictability in operational medium-range ensemble forecasts. *Sola*, **5**, 113–116.

— 2011: Predictability of Euro-Russian blocking in summer of 2010. *Geophys. Res. Lett.*, **38**.

Matsueda, M., R. Mizuta, and S. Kusunoki, 2009: Future change in wintertime atmospheric blocking simulated using a 20-km-mesh atmospheric global circulation model. *Journal of Geophysical Research: Atmospheres*, **114**, 114.

Matsueda, M. and T. Palmer, 2018: Estimates of flow-dependent predictability of wintertime Euro-Atlantic weather regimes in medium-range forecasts. *Quart. J. Roy. Meteor. Soc.*.

McLeod, J. T. and T. L. Mote, 2015: Assessing the role of precursor cyclones on the formation of extreme Greenland blocking episodes and their impact on summer melting across the Greenland ice sheet. *Journal of Geophysical Research: Atmospheres*, **120**, 12357–12377.

McWilliams, J. C., 1980: An application of equivalent modons to atmospheric blocking. *Dyn. Atmos. Oceans*, **5**, 43–66.

Methven, J., 2015: Potential vorticity in warm conveyor belt outflow. *Quart. J. Roy. Meteor. Soc.*, **141**, 1065–1071.

Methven, J. and P. Berrisford, 2015: The slowly evolving background state of the atmosphere. *Q. J. R. Meteorol. Soc.*, **141**, 2237–2258, doi:10.1002/qj.2518.

Michel, C. and G. Rivière, 2011: The link between Rossby wave breakings and weather regime transitions. *J. Atmos. Sci.*, **68**, 1730–1748.

Michel, C., G. Rivière, L. Terray, and B. Joly, 2012: The dynamical link between surface cyclones, upper-tropospheric Rossby wave breaking and the life cycle of the Scandinavian blocking. *Geophys. Res. Lett.*, **39**.

Michelangeli, P.-A., R. Vautard, and B. Legras, 1995: Weather regimes: Recurrence and quasi stationarity. *J. Atmos. Sci.*, **52**, 1237–1256.

Mittermaier, M., R. North, A. Semple, and R. Bullock, 2016: Feature-based diagnostic evaluation of global NWP forecasts. *Mon. Wea. Rev.*, **144**, 3871–3893.

Molteni, F., R. Buizza, T. N. Palmer, and T. Petroliagis, 1996: The ECMWF ensemble prediction system: Methodology and validation. *Q. J. R. Meteorol. Soc.*, **122**, 73–119.

Morcrette, J.-J., H. W. Barker, J. N. S. Cole, M. J. Iacono, and R. Pincus, 2008: Impact of a New Radiation Package, McRad, in the ECMWF Integrated Forecasting System. *Mon. Weather Rev.*, **136**, 4773–4798, doi:10.1175/2008MWR2363.1.

Mullen, S. L., 1987: Transient eddy forcing of blocking flows. *J. Atmos. Sci.*, **44**, 3–22.

Nakamura, H., M. Nakamura, and J. L. Anderson, 1997: The role of high-and low-frequency dynamics in blocking formation. *Mon. Weather Rev.*, **125**, 2074–2093.

Nakamura, H. and J. M. Wallace, 1990: Observed changes in baroclinic wave activity during the life cycles of low-frequency circulation anomalies. *J. Atmos. Sci.*, **47**, 1100–1116.

— 1993: Synoptic behavior of baroclinic eddies during the blocking onset. *Mon. Weather Rev.*, **121**, 1892–1903.

Nakamura, M. and R. A. Plumb, 1994: The effects of flow asymmetry on the direction of Rossby wave breaking. *J. Atmos. Sci.*, **51**, 2031–2045.

Nakamura, N., 1995: Modified Lagrangian-mean diagnostics of the stratospheric polar vortices. Part I. Formulation and analysis of GFDL SKYHI GCM. *J. Atmos. Sci.*, **52**, 2096–2108.

Neiman, P. J. and M. Shapiro, 1993: The life cycle of an extratropical marine cyclone. Part I: Frontal-cyclone evolution and thermodynamic air-sea interaction. *Mon. Weather Rev.*, **121**, 2153–2176.

Nezlin, M. V. and E. N. Snezhkin, 1993: *Rossby vortices, spiral structures, solitons: astrophysics and plasma physics in shallow water experiments*. Springer Science & Business Media.

Onogi, K., J. Tsutsui, H. Koide, M. Sakamoto, S. Kobayashi, H. Hatsushika, T. Matsumoto, N. Yamazaki, H. Kamahori, K. Takahashi, S. Kadokura, K. Wada, K. Kato, R. Oyama, T. Ose, N. Mannoji, and R. Taira, 2007: The JRA-25 Reanalysis. *J. Meteorol. Soc. Jpn. Ser. 2*, **85**, 369–432, doi:10.2151/jmsj.85.369.

Oortwijn, J., 1998: Predictability of the onset of blocking and strong zonal flow regimes. *J. Atmos. Sci.*, **55**, 973–994.

O'Reilly, C. H., S. Minobe, and A. Kuwano-Yoshida, 2016: The influence of the Gulf Stream on wintertime European blocking. *Climate Dyn.*, **47**, 1545–1567.

Orrell, D., L. Smith, J. Barkmeijer, and T. Palmer, 2001: Model error in weather forecasting. *Nonlinear Processes Geophys.*, **8**, 357–371.

Palmer, T., G. Shutts, and R. Swinbank, 1986: Alleviation of a systematic westerly bias in general circulation and numerical weather prediction models through an orographic gravity wave drag parametrization. *Quart. J. Roy. Meteor. Soc.*, **112**, 1001–1039.

Palmer, T. N., 1993: Extended-range atmospheric prediction and the Lorenz model. *Bull. Amer. Meteor. Soc.*, **74**, 49–66.

— 2000: Predicting uncertainty in forecasts of weather and climate. *Rep. Prog. Phys.*, **63**, 71.

Palmer, T. N. and D. L. T. Anderson, 1994: The prospects for seasonal forecasting—A review paper. *Quart. J. Roy. Meteor. Soc.*, **120**, 755–793.

Park, K., P. Cornillon, and D. L. Codiga, 2006: Modification of surface winds near ocean fronts: Effects of Gulf Stream rings on scatterometer (QuikSCAT, NSCAT) wind observations. *Journal of Geophysical Research: Oceans*, **111**.

Park, Y.-Y., R. Buizza, and M. Leutbecher, 2008: TIGGE: preliminary results on comparing and combining ensembles. *Q. J. R. Meteorol. Soc.*, **134**, 2029–2050, doi:10.1002/qj.334.

Parker, T., T. Woollings, and A. Weisheimer, 2018: Ensemble sensitivity analysis of Greenland blocking in medium-range forecasts. *Quart. J. Roy. Meteor. Soc.*, **144**, 2358–2379.

Pelly, J. L. and B. J. Hoskins, 2003a: How well does the ECMWF Ensemble Prediction System predict blocking? *Q. J. R. Meteorol. Soc.*, **129**, 1683–1702.

— 2003b: A new perspective on blocking. *J. Atmos. Sci.*, **60**, 743–755.

Pfahl, S., E. Madonna, M. Boettcher, H. Joos, and H. Wernli, 2014: Warm conveyor belts in the ERA-Interim dataset (1979–2010). Part II: Moisture origin and relevance for precipitation. *J. Climate*, **27**, 27–40.

Pfahl, S., C. Schwierz, M. Croci-Maspoli, C. Grams, and H. Wernli, 2015: Importance of latent heat release in ascending air streams for atmospheric blocking. *Nat. Geosci.*, **8**, 610–614.

Pfahl, S. and H. Wernli, 2012: Quantifying the relevance of atmospheric blocking for co-located temperature extremes in the Northern Hemisphere on (sub-) daily time scales. *Geophys. Res. Lett.*, **39**.

Pithan, F., T. G. Shepherd, G. Zappa, and I. Sandu, 2016: Climate model biases in jet streams, blocking and storm tracks resulting from missing orographic drag. *Geophys. Res. Lett.*, **43**, 7231–7240.

Plant, R., G. C. Craig, and S. Gray, 2003: On a threefold classification of extratropical cyclogenesis. *Quart. J. Roy. Meteor. Soc.*, **129**, 2989–3012.

Pomroy, H. R. and A. J. Thorpe, 2000: The evolution and dynamical role of reduced upper-tropospheric potential vorticity in intensive observing period one of FASTEX. *Mon. Weather Rev.*, **128**, 1817–1834.

Quandt, L.-A., J. H. Keller, O. Martius, J. G. Pinto, and S. C. Jones, 2019: Ensemble Sensitivity Analysis of the Blocking System over Russia in Summer 2010. *Mon. Weather Rev.*, **147**, 657–675.

Rabier, F., E. Klinker, P. Courtier, and A. Hollingsworth, 1996: Sensitivity of forecast errors to initial conditions. *Quart. J. Roy. Meteor. Soc.*, **122**, 121–150.

Reinhold, B. B. and R. T. Pierrehumbert, 1982: Dynamics of weather regimes: Quasi-stationary waves and blocking. *Mon. Weather Rev.*, **110**, 1105–1145.

Rex, D. F., 1950: Blocking action in the middle troposphere and its effect upon regional climate: I. An aerological study of blocking action. *Tellus*, **2**, 196–211.

— 1951: The effect of Atlantic blocking action upon European climate. *Tellus*, **3**, 100–112.

Riemer, M. and S. C. Jones, 2010: The downstream impact of tropical cyclones on a developing baroclinic wave in idealized scenarios of extratropical transition. *Q. J. R. Meteorol. Soc*, **136**, 617–637.

Robine, J.-M., S. L. K. Cheung, S. Le Roy, H. Van Oyen, C. Griffiths, J.-P. Michel, and F. R. Herrmann, 2008: Death toll exceeded 70,000 in Europe during the summer of 2003. *C.R. Biol.*, **331**, 171–178.

Rodwell, M. J., L. Magnusson, P. Bauer, P. Bechtold, M. Bonavita, C. Cardinali, M. Diamantakis, P. Earnshaw, A. Garcia-Mendez, L. Isaksen, et al., 2013: Characteristics of occasional poor medium-range weather forecasts for Europe. *Bull. Amer. Meteor. Soc.*, **94**, 1393–1405.

Roeckner, E., G. Bäuml, L. Bonaventura, R. Brokopf, M. Esch, M. Giorgetta, S. Hagemann, I. Kirchner, L. Kornblueh, E. Manzini, et al., 2003: The atmospheric general circulation model ECHAM 5. PART I: Model description.

Rossa, A., H. Wernli, and H. Davies, 2000: Growth and decay of an extra-tropical cyclone's PV-tower. *Meteorol. Atmos. Phys.*, **73**, 139–156.

Rossby, C.-G., 1940: Planetary flow patterns in the atmosphere. *Quart. J. Roy. Meteor. Soc.*.

Röthlisberger, M., S. Pfahl, and O. Martius, 2016: Regional-scale jet waviness modulates the occurrence of midlatitude weather extremes. *Geophys. Res. Lett.*, **43**, doi:10.1002/2016GL070944.

Saffin, L., S. Gray, J. Methven, and K. Williams, 2017: Processes maintaining tropopause sharpness in numerical models. *Journal of Geophysical Research: Atmospheres*, **122**, 9611–9627.

Saffin, L., J. Methven, and S. Gray, 2016: The non-conservation of potential vorticity by a dynamical core compared with the effects of parametrized physical processes. *Q. J. R. Meteorol. Soc.*.

Scaife, A. A., D. Copsey, C. Gordon, C. Harris, T. Hinton, S. Keeley, A. O'Neill, M. Roberts, and K. Williams, 2011: Improved Atlantic winter blocking in a climate model. *Geophys. Res. Lett.*, **38**.

Scaife, A. A., T. Woollings, J. Knight, G. Martin, and T. Hinton, 2010: Atmospheric blocking and mean biases in climate models. *J. Climate*, **23**, 6143–6152.

Schäfler, A., G. Craig, H. Wernli, P. Arbogast, J. D. Doyle, R. McTaggart-Cowan, J. Methven, G. Rivière, F. Ament, M. Boettcher, et al., 2018: The North Atlantic Waveguide and Downstream Impact Experiment. *Bull. Amer. Meteor. Soc.*.

Scherrer, S. C., M. Croci-Maspoli, C. Schwierz, and C. Appenzeller, 2006: Two-dimensional indices of atmospheric blocking and their statistical relationship with winter climate patterns in the Euro-Atlantic region. *Int. J. Climatol.*, **26**, 233–250.

Schiemann, R., M.-E. Demory, L. C. Shaffrey, J. Strachan, P. L. Vidale, M. S. Mizielinski, M. J. Roberts, M. Matsueda, M. F. Wehner, and T. Jung, 2017: The resolution sensitivity of Northern Hemisphere blocking in four 25-km atmospheric global circulation models. *J. Clim.*, **30**, 337–358, doi:10.1175/JCLI-D-16-0100.1.

Schultz, D. M., 2001: Reexamining the cold conveyor belt. *Mon. Weather Rev.*, **129**, 2205–2225.

Schultz, D. M., D. Keyser, and L. F. Bosart, 1998: The effect of large-scale flow on low-level frontal structure and evolution in midlatitude cyclones. *Mon. Weather Rev.*, **126**, 1767–1791.

Schwierz, C., M. Croci-Maspoli, and H. C. Davies, 2004: Perspicacious indicators of atmospheric blocking. *Geophys. Res. Lett.*, **31**, doi:10.1029/2003GL019341.

Shapiro, M. A. and D. Keyser, 1990: Fronts, jet streams and the tropopause. *Extratropical cyclones*, Springer, 167–191.

Sheldon, L., A. Czaja, B. Vannière, C. Morcrette, B. Sohet, M. Casado, and D. Smith, 2017: A 'warm path' for Gulf Stream–troposphere interactions. *Tellus A: Dynamic Meteorology and Oceanography*, **69**, 1299397.

Shutts, G., 1983: The propagation of eddies in diffluent jetstreams: Eddy vorticity forcing of 'blocking'flow fields. *Q. J. R. Meteorol. Soc.*, **109**, 737–761.

— 1986: A case study of eddy forcing during an Atlantic blocking episode. *Advances in Geophysics*, **29**, 135–162.

Shutts, G. J. and S. B. Vosper, 2011: Stratospheric gravity waves revealed in NWP model forecasts. *Q. J. R. Meteorol. Soc.*, **137**, 303–317, doi:10.1002/qj.763.

Simmons, A. J. and A. Hollingsworth, 2002: Some aspects of the improvement in skill of numerical weather prediction. *Quart. J. Roy. Meteor. Soc.*, **128**, 647–677.

Sousa, P. M., R. M. Trigo, D. Barriopedro, P. M. Soares, and J. A. Santos, 2018: European temperature responses to blocking and ridge regional patterns. *Climate Dyn.*, **50**, 457–477.

Sprenger, M. and H. Wernli, 2015: The LAGRANTO Lagrangian analysis tool–version 2.0. *Geosci. Model Dev.*, **8**, 2569–2586.

Stensrud, D. J., J.-W. Bao, and T. T. Warner, 2000: Using initial condition and model physics perturbations in short-range ensemble simulations of mesoscale convective systems. *Mon. Weather Rev.*, **128**, 2077–2107.

Stoelinga, M. T., 1996: A potential vorticity-based study of the role of diabatic heating and friction in a numerically simulated baroclinic cyclone. *Mon. Weather Rev.*, **124**, 849–874.

Tamarin, T. and Y. Kaspi, 2016: The poleward motion of extratropical cyclones from a potential vorticity tendency analysis. *J. Atmos. Sci.*, **73**, 1687–1707.

Tennant, W. J., G. J. Shutts, A. Arribas, and S. A. Thompson, 2011: Using a stochastic kinetic energy backscatter scheme to improve MOGREPS probabilistic forecast skill. *Mon. Wea. Rev.*, **139**, 1190–1206.

Tibaldi, S., F. d'Andrea, E. Tosi, and E. Roeckner, 1997: Climatology of Northern Hemisphere blocking in the ECHAM model. *Climate Dyn.*, **13**, 649–666.

Tibaldi, S. and F. Molteni, 1990: On the operational predictability of blocking. *Tellus A*, **42**, 343–365.

Tibaldi, S., E. Tosi, A. Navarra, and L. Pedulli, 1994: Northern and Southern Hemisphere seasonal variability of blocking frequency and predictability. *Mon. Weather Rev.*, **122**, 1971–2003.

Torn, R. D. and G. J. Hakim, 2008: Ensemble-based sensitivity analysis. *Mon. Weather Rev.*, **136**, 663–677.

Toth, Z. and E. Kalnay, 1993: Ensemble forecasting at NMC: The generation of perturbations. *Bull. Amer. Meteor. Soc.*, **74**, 2317–2330.

— 1997: Ensemble forecasting at NCEP and the breeding method. *Mon. Weather Rev.*, **125**, 3297–3319.

Trigo, R., I. Trigo, C. DaCamara, and T. Osborn, 2004: Climate impact of the European winter blocking episodes from the NCEP/NCAR Reanalyses. *Climate Dyn.*, **23**, 17–28.

Tsou, C.-H. and P. J. Smith, 1990: The role of synoptic/planetary–scale interactions during the development of a blocking anticyclone. *Tellus A*, **42**, 174–193.

Tung, K. K. and R. Lindzen, 1979: A theory of stationary long waves. Part I: A simple theory of blocking. *Mon. Weather Rev.*, **107**, 714–734.

Tyrlis, E. and B. Hoskins, 2008: Aspects of a Northern Hemisphere atmospheric blocking climatology. *J. Atmos. Sci.*, **72**.

Uppala, S. M., P. Kållberg, A. Simmons, U. Andrae, V. D. C. Bechtold, M. Fiorino, J. Gibson, J. Haseler, A. Hernandez, G. Kelly, et al., 2005: The ERA-40 re-analysis. *Quart. J. Roy. Meteor. Soc.*, **131**, 2961–3012.

Vautard, R., 1990: Multiple weather regimes over the North Atlantic: Analysis of precursors and successors. *Mon. Weather Rev.*, **118**, 2056–2081.

Vautard, R. and B. Legras, 1988: On the source of midlatitude low-frequency variability. Part II: Nonlinear equilibration of weather regimes. *J. Atmos. Sci.*, **45**, 2845–2867.

Walters, D., A. Baran, I. Boutle, M. Brooks, P. Earnshaw, J. Edwards, K. Furtado, P. Hill, A. Lock, J. Manners, C. Morcrette, J. Mulcahy, C. Sanchez, C. Smith, R. Stratton, W. Tennant, L. Tomassini, K. Van Weverberg, S. Vosper, M. Willett, J. Browse, A. Bushell, M. Dalvi, R. Essery, N. Gedney, S. Hardiman, B. Johnson, C. Johnson, A. Jones, G. Mann, S. Milton, H. Rumbold, A. Sellar, M. Ujiie, M. Whitall, K. Williams, and M. Zerroukat, 2017a: The Met Office Unified Model Global Atmosphere 7.0/7.1 and JULES Global Land 7.0 configurations. *Geosci. Model Dev. Discuss.*, **2017**, 1–78, doi:10.5194/gmd-2017-291.

Walters, D., I. Boutle, M. Brooks, T. Melvin, R. Stratton, S. Vosper, H. Wells, K. Williams, N. Wood, T. Allen, et al., 2017b: The Met Office Unified Model Global Atmosphere 6.0/6.1 and JULES Global Land 6.0/6.1 configurations. *Geosci. Model Dev.*, **10**.

Walters, D., N. Wood, S. Vosper, and S. Milton, 2014: ENDGame: A new dynamical core for seamless atmospheric prediction. *Met Office documentation. can be consulted at http://www. metoffice. gov. uk/media/pdf/s/h/ENDGameGOVSci v2. 0. pdf*.

Wernli, B. H. and H. C. Davies, 1997: A Lagrangian-based analysis of extratropical cyclones. I: The method and some applications. *Q. J. R. Meteorol. Soc.*, **123**, 467–489.

Wernli, H., 1997: A Lagrangian-based analysis of extratropical cyclones. II: A detailed case-study. *Quart. J. Roy. Meteor. Soc.*, **123**, 1677–1706.

Wernli, H., S. Dirren, M. A. Liniger, and M. Zillig, 2002: Dynamical aspects of the life cycle of the winter storm 'Lothar'(24–26 December 1999). *Quart. J. Roy. Meteor. Soc.*, **128**, 405–429.

Wernli, H., M. Paulat, M. Hagen, and C. Frei, 2008: SAL—A novel quality measure for the verification of quantitative precipitation forecasts. *Mon. Weather Rev.*, **136**, 4470–4487.

Wilks, D. S., 2011: *Statistical methods in the atmospheric sciences*, volume 100. Academic press.

Willett, M. R. and M. A. Whitall, 2017: A Simple Prognostic based Convective Entrainment Rate for the Unified Model: Description and Tests. Technical report, Met Office.

Williams, K. D., C. M. Harris, A. Bodas-Salcedo, J. Camp, R. E. Comer, D. Copsey, D. Fereday, T. Graham, R. Hill, T. Hinton, P. Hyder, S. Ineson, G. Masato, S. F. Milton, M. J. Roberts, D. P. Rowell, C. Sanchez, A. Shelly, B. Sinha, D. N. Walters, A. West, T. Woollings, and P. K. Xavier, 2015: The Met Office Global Coupled model 2.0 (GC2) configuration. *Geosci. Model Dev.*, **8**, 1509–1524, doi:10.5194/gmd-8-1509-2015.

Wilson, D. R. and S. P. Ballard, 1999: A microphysically based precipitation scheme for the UK Meteorological Office Unified Model. *Quart. J. Roy. Meteor. Soc.*, **125**, 1607–1636.

Wilson, D. R., A. Bushell, A. M. Kerr-Munslow, J. D. Price, C. J. Morcrette, A. Bodas-Salcedo, et al., 2008a: PC2: A prognostic cloud fraction and condensation scheme. II: Climate model simulations. *Quart. J. Roy. Meteor. Soc.*, **134**, 2109–2125.

Wilson, D. R., A. C. Bushell, A. M. Kerr-Munslow, J. D. Price, and C. J. Morcrette, 2008b: PC2: A prognostic cloud fraction and condensation scheme. I: Scheme description. *Quart. J. Roy. Meteor. Soc.*, **134**, 2093–2107.

Wood, N., A. Staniforth, A. White, T. Allen, M. Diamantakis, M. Gross, T. Melvin, C. Smith, S. Vosper, M. Zerroukat, et al., 2014: An inherently mass-conserving semi-implicit semi-Lagrangian discretization of the deep-atmosphere global non-hydrostatic equations. *Q. J. R. Meteorol. Soc.*, **140**, 1505–1520.

Woollings, T., D. Barriopedro, J. Methven, S.-W. Son, O. Martius, B. Harvey, J. Sillmann, A. R. Lupo, and S. Seneviratne, 2018: Blocking and its response to climate change. *Current Climate Change Reports*, **4**, 287–300.

Woollings, T., A. Hannachi, and B. Hoskins, 2010: Variability of the North Atlantic eddy-driven jet stream. *Quart. J. Roy. Meteor. Soc.*, **136**, 856–868.

Yamazaki, A. and H. Itoh, 2009: Selective absorption mechanism for the maintenance of blocking. *Geophys. Res. Lett.*, **36**, L05803.

— 2013: Vortex–vortex interactions for the maintenance of blocking. Part I: The selective absorption mechanism and a case study. *J. Atmos. Sci.*, **70**, 725–742.

Yang, Y., Z. Li, and L. Ji, 1997: Adjoint sensitivity analyses on the anomalous circulation features in East Asian summer monsoon. *Adv. Atmos. Sci.*, **14**, 111–123.

Zappa, G., G. Masato, L. Shaffrey, T. Woollings, and K. Hodges, 2014a: Linking Northern Hemisphere blocking and storm track biases in the CMIP5 climate models. *Geophys. Res. Lett.*, **41**, 135–139.

Zappa, G., L. Shaffrey, and K. Hodges, 2014b: Can polar lows be objectively identified and tracked in the ECMWF operational analysis and the ERA-Interim reanalysis? *Mon. Weather Rev.*, **142**, 2596–2608.

Zappa, G., L. C. Shaffrey, and K. I. Hodges, 2013: The ability of CMIP5 models to simulate North Atlantic extratropical cyclones. *J. Climate*, **26**, 5379–5396.

Zhang, F., Y. Q. Sun, L. Magnusson, R. Buizza, S.-J. Lin, J.-H. Chen, and K. Emanuel, 2019: What is the predictability limit of midlatitude weather? *Journal of the Atmospheric Sciences*, **76**, 1077–1091.